BetonKalender

Concrete Structures for Wind Turbines

Jürgen Grünberg, Joachim Göhlmann

WILEY

Ernst & Sohn
A Wiley Brand

Jürgen Grünberg,
Joachim Göhlmann

Concrete Structures
for Wind Turbines

Jürgen Grünberg, Joachim Göhlmann

Concrete Structures for Wind Turbines

Ernst & Sohn
A Wiley Brand

The Authors

Prof. Dr.-Ing. Jürgen Grünberg
Flerrentwiete 79
22559 Hamburg
Germany

Dr.-Ing. Joachim Göhlmann
grbv Ingenieure im Bauwesen GmbH & Co. KG
Expo Plaza 10
30539 Hannover
Germany

The Editors of Beton-Kalender

Prof. Dipl.-Ing. Dr.-Ing. Konrad Bergmeister
Ingenieurbüro Bergmeister
Peter-Jordan-Straße 113
1190 Vienna
Austria

Dr.-Ing. Frank Fingerloos
German Society for Concrete and Construction Technology
Kurfürstenstr. 129
10178 Berlin
Germany

Prof. Dr.-Ing. Dr. h.c. mult. Johann-Dietrich Wörner
German Aerospace Center
Linder Höhe
51145 Cologne
Germany

Translation by: *Philip Thrift, Hannover,* Germany

Coverphoto: Mathias Euler, Stuttgart, Germany

The original German text is published in Beton-Kalender 2011, ISBN 978-3-433-02954-1, and titled "*Windenergieanlagen in Stahlbeton- und Spannbetonbauweise*"

Library of Congress Card No.: applied for

British Library Cataloguing-in-Publication Data
A catalogue record for this book is available from the British Library.

Bibliographic information published by the Deutsche Nationalbibliothek
The Deutsche Nationalbibliothek lists this publication in the Deutsche Nationalbibliografie; detailed bibliographic data are available on the Internet at <http://dnb.d-nb.de>.

Print ISBN: 978-3-433-03041-7
ePDF ISBN: 978-3-433-60331-4
ePub ISBN: 978-3-433-60330-7
eMob ISBN: 978-3-433-60332-1
oBook ISBN: 978-3-433-60329-1

Typesetting: Thomson Digital, Noida, India
Printing and Binding: Betz-druck GmbH, Darmstadt, Germany

Printed in the Federal Republic of Germany.
Printed on acid-free paper

Contents

Editorial

The “Concrete Yearbook” is a very important source of information for engineers involved in design, analysis, planning and production of concrete structures. It is published on a yearly basis and offers chapters devoted to various subjects with high actuality. Any chapter gives extended information based on the latest state of the art, written by renowned experts in the areas considered. The subjects change every year and may return in later years for an updated treatment. This publication strategy guarantees, that not only the most recent knowledge is involved in the presentation of topics, but that the choice of the topics itself meets the demand of actuality as well.

For decades already the themes chosen are treated in such a way, that on the one hand the reader is informed about the backgrounds and on the other hand gets acquainted with practical experience, methods and rules to bring this knowledge into practice. For practicing engineers, this is an optimum combination. Engineering practice requires knowledge of rules and recommendations, as well as understanding of the theories or assumptions behind them, in order to find adequate solutions for the wide scope of problems of daily or special nature.

During the history of the “Concrete Yearbook” an interesting development was noted. In the early editions themes of interest were chosen on an incidental basis. Meanwhile, however, the building industry has gone through a remarkable development. Where in the past predominantly matters concerning structural safety and serviceability were in the centre of attention, nowadays an increasing awareness develops due to our responsibility with regard to society in a broader sense. This is reflected e.g. by the wish to avoid problems related to limited durability of structures. Expensive repair of structures has been, and unfortunately still is, necessary because of insufficient awareness of deterioration processes of concrete and reinforcing steel in the past. Therefore structural design should focus now on realizing structures with sufficient reliability and serviceability for a specified period of time, without substantial maintenance costs. Moreover we are confronted with a heritage of older structures that should be assessed with regard to their suitability to safely carry the often increased loads applied to them today. Here several aspects of structural engineering have to be considered in an interrelated way, like risk, functionality, serviceability, deterioration processes, strengthening techniques, monitoring, dismantlement, adaptability and recycling of structures and structural materials, and the introduction of modern high performance materials. Also the significance of sustainability is recognized. This added to the awareness that design should not focus only on individual structures and their service life, but as well on their function in a wider context, with regard to harmony with their environment, acceptance by society, the responsible use of resources, low energy consumption and economy. Moreover the construction processes should become cleaner, with less environmental nuisance and pollution.

The editors of the “Concrete Yearbook” have clearly recognized those and other trends and offer now a selection of coherent subjects which resort under a common “umbrella” of a broader societal development of high relevance. In order to be able to cope with the corresponding challenges the reader is informed about progress in technology, theoretical methods, new findings of research, new ideas on design and execution, development in production, assessment and conservation strategies. By the actual selection of topics and the way those are treated, the "Concrete Yearbook" offers a splendid opportunity to get and stay aware of the development of technical knowledge, practical experience and concepts in the field of design of concrete structures on an international level.

Prof. Dr. Ir. Dr.-Ing. h.c. *Joost Walraven*, TU Delft
Honorary president of the international concrete federation *fib*

1 Introduction

The wind energy industry in Germany has an excellent global standing when it comes to the development and construction of wind turbines. Germany currently represents the world's largest market for wind energy. So far, more than 21 000 wind turbines with a total output of approx. 25 000 MW have been installed across the country. And at the moment that figure is growing by approx. 2000 MW every year [1]. Developments in land-based installations are moving in the direction of more powerful turbines with more than 3 MW per installation and towers exceeding 140 m in height.[1)]

However, the number of lucrative sites on land (onshore) is dwindling. Therefore, it is planned to construct wind turbines at sea (offshore) in the coming years. The plans provide for offshore wind farms in the North Sea and Baltic Sea and are intended to increase substantially the proportion of renewable energies in electricity generation. The target for the medium-term is installations in the North Sea and Baltic Sea with a total output amounting to some 3000 MW. By 2030 it is hoped that offshore wind turbines with a total output of about 20 000 to 25 000 MW will have been built [2].

Figure 1.1 shows the results of a study carried out by DEWI, the German Wind Energy Institute. It shows the annual installed wind energy output for each year since 1990 plus the forecast up to the year 2030. According to the study, the decline in onshore installations should be compensated for by the anticipated development in offshore

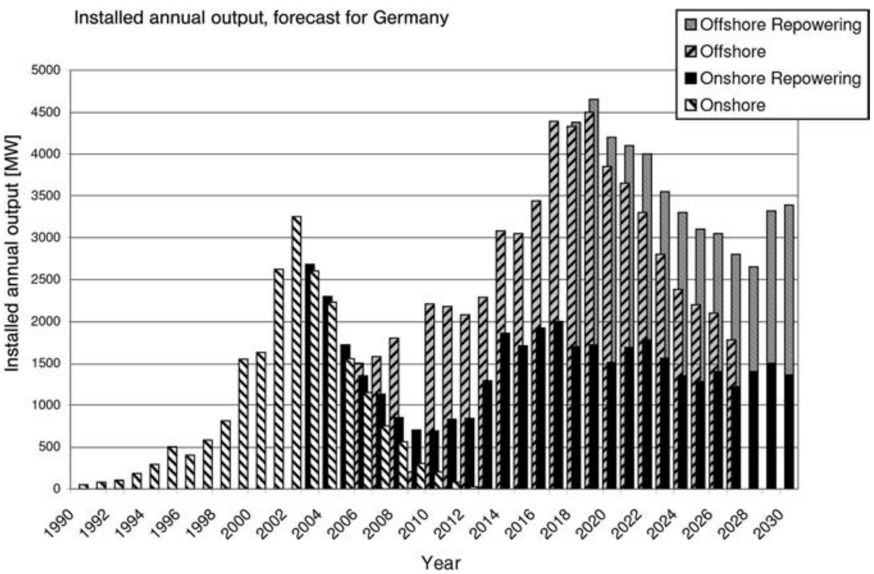

Fig. 1.1 Installed wind energy output per year in Germany [3]

1) Source: Bundesverband der Windenergie e.V. (www.wind-energie.de).

Concrete Structures for Wind Turbines. First edition. Jürgen Grünberg, Joachim Göhlmann.

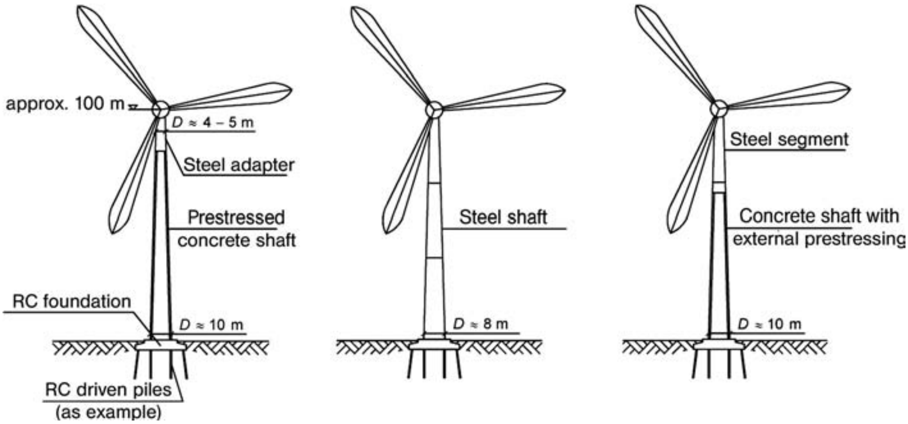

Fig. 1.2 Typical onshore tower designs for wind turbines

wind farms and by the repowering of land-based installations, leading to a doubling in the annual installed output by the year 2020.

The towers supporting onshore wind turbines are mainly of steel or prestressed concrete with internal or external prestressing. Steel lattice masts are also used in isolated instances. The prestressed concrete towers make use of both *in situ* and precast concrete. In recent years, the use of hybrid towers, consisting of a prestressed concrete shaft and a steel top section, has proved to be a very economical solution, especially for wind turbines in the multi-megawatt category. The choice of a suitable tower design is governed by the conditions at the site (fabrication, transport, erection, etc.). Figure 1.2 illustrates typical towers for onshore wind turbines.

Both shallow and deep foundations can be used for onshore wind turbines. Soil improvement measures can be employed to upgrade subsoil properties to those required for shallow foundations [4, 5]. Driven piles of steel or concrete with appropriate toe forms are frequently used as deep foundations.

So far, about 25 wind farms have been approved for construction off the German coast in the North Sea and Baltic Sea within the 12-mile zone and the exclusive economic zone (EEZ) for water depths of up to 45 m. But the better wind conditions at sea call for a greater technical input for the loadbearing structure and the fabrication and erection of the wind turbines [6]. Besides the depth of the water, the choice of a suitable offshore structure is especially dependent on the wave and current conditions plus the subsoil beneath the seabed. Concrete structures in the form of gravity bases are economic propositions for nearshore sites and for greater depths of water, see [7]. Such foundations are built in a dock, for example, then floated out to their final position and sunk. Resolved designs with individual members made from prestressed high-strength concrete are also feasible. An overview of the offshore foundation concepts currently under discussion can be found in Section 5.

The ongoing development of ever more powerful wind turbines plus additional requirements for the design and construction of their offshore foundation structures exceeds the actual experience gained so far in the various disciplines concerned. Wind turbines represent structures subjected to highly dynamic loading patterns. The load cycles of onshore installations can reach $N = 10^9$, but those of offshore installations can be exposed to further load cycles of up to $N = 10^8$ due to the sea conditions. Therefore, for the design of loadbearing structures, fatigue effects – and not just maximum loads – are extremely important. This can lead, in particular, to multi-axial stress states arising in the connections and joints of concrete and hybrid structures (see Sections 3.6 and 4.9), which have considerable effects on the fatigue strength and so far have not been addressed in the applicable design codes.

On the whole, there is still a great need for further research in the various disciplines involved in the planning, design and construction of wind turbines. It was for this reason that the Centre for Wind Energy Research *ForWind* (www.forwind.de) was set up at the Carl von Ossietzky University of Oldenburg and the Leibniz University of Hannover in 2003, thus enabling engineers from different disciplines to work together on research into wind energy. Supported by the Lower Saxony Ministry of Science and Culture, the objective of the centre is to pool research activities. Construction technology research into offshore wind turbines began at the University of Hannover as long ago as 2000 in the shape of the *GIGAWIND* (www.gigawind.de) joint project sponsored by the Federal Ministry for the Environment, Nature Conservation and Nuclear Safety. These research activities are divided into three areas: actions due to wind and waves, design of loadbearing structures (including foundations) and environmental technology aspects. *GIGAWIND alpha ventus* is a project associated with the *RAVE* (***R**esearch at **A**lpha **V**entus*) research initiative and therefore has access to the extensive programme of measurements carried out at the Alpha Ventus test site, Germany's first offshore wind farm. At European level, the University of Hannover participates in the *European Academy of Wind Energy* (www.eawe.eu). The objective here is to promote research and development and to train PhD students in the field of wind energy in various European countries.

The basic concepts for the planning, design, analysis and construction of tower structures, focusing on wind turbines especially, will be explored in the next chapters.

Many aspects of these basic concepts also apply to the structural and constructional requirements of other tower-type structures, for example

– telecommunications towers
– radar towers and lighthouses in shipping lanes
– antenna support structures and masts for mobile telephone networks
– chimneys

For more information on these structures please refer to *Beton-Kalender 2006 Teil 1*, pp. 103–223 [8].

2 Actions on wind turbines

2.1 Permanent actions

In addition to the typical dead loads of the plant (rotor and nacelle) and the structure (tower and foundation), there are also other loads that are classed as permanent actions: for example the loads of items fitted inside the tower (cables, intermediate platforms, etc.), and those due to further electrical equipment, for example transformers, ventilation systems.

And when it comes to offshore wind turbines there are yet further dead loads to be considered such as external platforms, boat moorings or cathodic corrosion protection.

For the dynamic analysis in particular, the masses of the individual items and components must be known and taken into account accurately in the design.

2.2 Turbine operation (rotor and nacelle)

The actions due to the operation of the turbine are determined by means of numerical simulations (see also Section 4.9.1). In addition to various wind load models, with the superposition of wave action effects where applicable, such simulations must also take into account particular operating situations, for example starting and stopping procedures.

The load case combinations to be investigated are laid down in the relevant codes and guidelines, for example the DIBt guideline for onshore wind turbines [9], see Section 4.5.3, and DIN EN 61400-3 for offshore wind turbines [10]. Load combinations are also defined in the guidelines published by a number of certification bodies, for example the *GL Guideline* [11], see Section 4.6.4.

Note: The *GL Guideline* for offshore wind turbines [11] is based on *Rules and Guidelines, IV Industrial Services – 1 Guideline for the Certification of Wind Turbines* dating from 2003/04, which in July 2010 was republished in a revised edition.

2.3 Wind loads

2.3.1 Wind loads for onshore wind turbines

According to DIN 1055-4 [12], the environmental conditions in Germany (including the German Bight) can be divided into four wind zones (Figure 2.1).

The reference values (v_{ref}; q_{ref}) in the table are valid for

– averaging over a period of 10 min,
– a 0.02 probability of being exceeded in one year,
– a height of 10 m above ground level,
– flat, open terrain, which corresponds to terrain category II in DIN 1055-4 annex B.

Concrete Structures for Wind Turbines. First edition. Jürgen Grünberg, Joachim Göhlmann.

Wind zone	v_{ref}	q_{ref}
WZ 1	22.5 m/s	0.32 kN m^2
WZ 2	25.0 m/s	0.39 kN m^2
WZ 3	27.5 m/s	0.47 kN m^2
WZ 4	30.0 m/s	0.56 kN m^2

Fig. 2.1 Wind zones to DIN 1055-4 [12]

The relationship between reference values for wind speed v_{ref} and dynamic pressure q_{ref} is given by the following equation:

$$q_{ref}\,[\mathrm{kPa}] = \frac{(v_{ref}\,[\mathrm{m/s}])^2}{1600}$$

When designing towers, only the reference dynamic pressures for terrain categories II (inland) or I (wind zone 4 directly on the coast) should be assumed. Less onerous terrain categories (III and higher) can be ruled out because the effects of the various ground roughnesses decrease as the height of the structure increases.

Therefore, the combined profiles given in DIN 1055-4 [12] for structures up to 50 m in height should not be used either (see also *Beton-Kalender 2006* [8]).

Prior to the introduction of DIN 1055-4 [12], the wind loads for tower-type structures were calculated according to DIN 1056 [13] or annex A of DIN 4131 [14] or annex A of DIN 4228 [15]. *Beton-Kalender 2006* [8] compares the wind loads according to the old standards and DIN 1055-4 [12].

2.3.1.1 Wind loads according to the DIBt guideline

According to DIN 1055-4, the following basic parameters apply (see Figure 2.2 and Table 2.1):

- 50-year return wind v_{m50} (z)
- 50-year return gust v_{e50} (z)

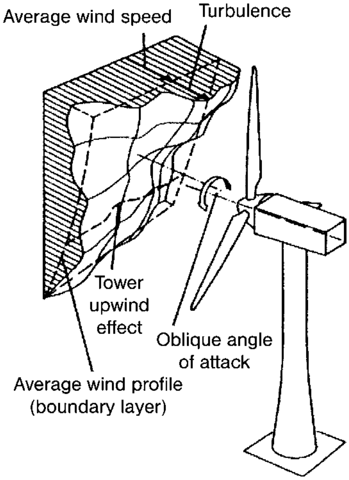

Fig. 2.2 Angle of attack for the rotor of a wind turbine

Table 2.1 Wind conditions for onshore wind turbines in terrain category II according to [12]

Basic parameters according to DIN 1055-4 [12][a)]					Unit	Remarks
Wind zone	WZ 1	WZ 2	WZ 3	WZ 4		
v_{m50} (= v_{ref})[b)]	22.5	25.0	27.5	30.0	m/s	50-year return wind, 10-min average
$v_{e50} = 2.1^{0.5} \cdot v_{m50}$	32.6	36.2	39.9	43.5	m/s	50-year return wind, 2–4 s gust
$v_{m1} = 0.8 \cdot v_{m50}$	18.0	20.0	22.0	24.0	m/s	1-year return wind, 10-min average
$v_{e1} = 0.8 \cdot v_{e50}$	26.1	29.0	31.9	34.8	m/s	1-year return wind, 2–4 s gust
Additional parameters according to DIBt guideline [9] for dynamic analyses						
$V_{ave} = 0.18 \cdot v_{m50}\,(h) = 0.18 \cdot v_{ref} \cdot (h/10)^{0.16}$					m/s	Annual average wind speed at hub height h [m]
$I_{15,A} = 0.18$					—	Average turbulence intensity, class A, for $V_{hub} = 15$ m/s
$a_A = 2$					—	Slope parameter for turbulence characteristics

a) z = 10 m above ground level, terrain category II, site altitude ≤ sea level + 800 m
b) According to [16], V_{ref} (capital V) denotes the wind speed of the 50-year return wind at hub height h.

– 1-year return wind v_{m1} (z)
– 1-year return gust V_{e1} (z)

Additional parameters (DIBt guideline [9]):

– Annual average wind speed v_{ave}
– Average turbulence intensity I_{15}
– Verification of the wind turbine for compliance with the turbulence intensity of turbulence category A according to [16].

2.3.1.2 Checking the susceptibility to vibration

According to DIN 1055-4 [12] Section 10, the wind forces acting on structures not susceptible to vibration are based on the *peak dynamic pressure*, which is averaged over a gust duration of 2–4 s (Table 2.2).

According to DIN 1055-4 [12] 6.2 (2), the wind loads for structures acting as cantilevers may be determined according to the simplified method for structures not susceptible to vibration (see below) provided the following condition is satisfied:

$$\frac{x_s}{h} \le \frac{\delta}{\left(\sqrt{\frac{h_{ref}}{h} \cdot \frac{h+b}{b}} + 0.125 \cdot \sqrt{\frac{h}{h_{ref}}}\right)^2} \quad \text{with} \quad h_{ref} = 25\,\text{m}$$

where

x_s displacement of top of structure under dead load assumed to act in the direction of the wind [m]
δ logarithmic damping decrement according to annex F
b width of structure [m]
h height of structure [m].

Table 2.2 Peak dynamic pressure (to DIN 1055-4 [12] Table B.2)

$q_B(z_j) = \mathbf{c} \cdot q_{ref} \cdot (z_j/10)^{\mathbf{d}} \quad (\text{or} \quad \mathbf{c}_{min} \cdot q_{ref} \quad \text{for } z_j < z_{min})$

Terrain category	I	II	III	IV
Factor **c**	2.6	2.1	1.6	1.3
Exponent **d**	0.19	0.24	0.31	0.40
z_{min}	2.00	4.00	8.00	16.00
$\mathbf{c}_{min}$	1.9	1.7	1.5	1.3

2.3.1.3 Example of application

Prestressed concrete wind turbine structure, hub height 130 m (see Section 5.2):

$$\frac{\delta}{\left(\sqrt{\frac{h_{ref}}{h}\cdot\frac{h+b}{b}}+0.125\cdot\sqrt{\frac{h}{h_{ref}}}\right)^2}=$$

$$\frac{0.04}{\left(\sqrt{\frac{25}{129.7}\cdot\frac{129.7+5.6}{5.6}}+0.125\cdot\sqrt{\frac{129.7}{25}}\right)^2}=\frac{0.04}{\left(\sqrt{4.66}+0.125\cdot\sqrt{5.19}\right)^2}=0.0067$$

$$x_s/h = y_{36}/(z_{36}-z_1) = 4.274/(130.174-0.500) = 0.0330 > 0.0067$$

The tower is therefore susceptible to vibration.

According to [9] 8.3.1, the vibration effect of the tower in the direction of the wind caused by the gustiness of the wind for a wind turbine in the "non-operational" condition (see Section 4.5.2) must be taken into account by way of an equivalent static load, which according to [9] Section B.3 or DIN 1055-4 [12] annex C may be calculated as follows:

Resultant equivalent static wind load in structure segment j ([12] C.2)

$$F_{Wj} = G\cdot c_{fj}\cdot q_m(z_j).A_j$$

where

G	gust response factor to DIN1055-4 [12] C.3
c_{fj}	aerodynamic force coefficient for segment i to DIN 1055-4 [12] 12.6 or 12.7
q_m (z_j)	average dynamic pressure at location z_j
z_j	average height of segment j above ground level
A_j	reference area of segment j

Average dynamic pressure (10-min average) ([12] C.2 (3))

$$q_m(z_j)=\frac{\rho}{2}\cdot\left[v_m(z_j)\right]^2 \quad \text{or} \quad q_m[\text{kPa}]=\frac{(v_m[\text{m/s}])^2}{1600}$$

ρ density of air: $\rho = 1.25\,\text{kg/m}^3$
v_m average wind speed (Table 2.3)

Table 2.3 Average wind speed (to DIN 1055-4 [12] Table B.2).

$\mathbf{v}_m(z_j) = \mathbf{a}\cdot\mathbf{v}_{ref}\cdot(z_j/10)^{\mathbf{b}}$ (or $\mathbf{a}_{min}\cdot\mathbf{v}_{ref}$ for $z_j < z_{min}$)

Terrain category	I	II	III	IV
Factor **a**	1.18	1.00	0.77	0.56
Exponent **b**	0.12	0.16	0.22	0.30
z_{min}	2.00	4.00	8.00	16.00
$\mathbf{a}_{min}$	0.97	0.86	0.73	0.64

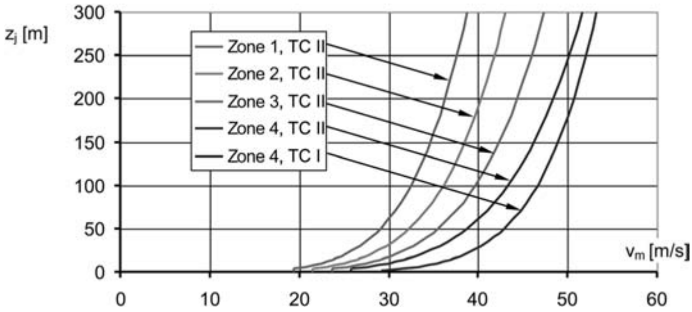

Fig. 2.3 Average wind speeds for various wind zones

Figure 2.3 shows the associated wind speed profiles.

The *gust response factor* (G) is related to the average dynamic pressure q_m. DIN 1055-4 [12] C.3 (1) contains the following formula:

$$G = 1 + 2 \cdot g \cdot I_v(z_e) \cdot \sqrt{Q_0^2 + R_x^2}$$

where

I_v (z_e) turbulence intensity at effective height z_e (Table 2.4)
z_e reference height (see DIN 1055-4 [12] Figure C.1) [m] ($z_e = 0.6 \cdot h$ applies for towers of height h)
g peak factor
Q_0 quasi-static component (basic gust component) of gust response
R_x resonance component of response as a result of gust response

These parameters are explained below.

Figure 2.4 shows the associated turbulence intensity profiles.

Table 2.4 Turbulence intensity (to DIN 1055-4 [12] Table B.2)

$I_v(z_e) = \mathbf{e} \cdot (z_e/10)^{\mathbf{f}}$ $\left(\text{or} \quad I_{v,max} \quad \text{for } z_e < z_{min}\right)$				
Terrain category	I	II	III	IV
Factor **e**	0.14	0.19	0.28	0.43
Exponent **f**	−0.12	−0.16	−0.22	−0.30
z_{min}	2.00	4.00	8.00	16.00
$I_{v,max}$	0.20	0.22	0.29	0.37

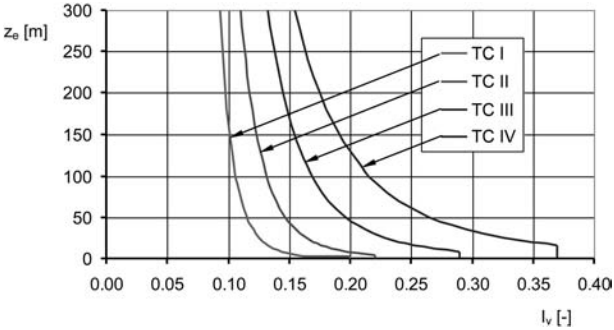

Fig. 2.4 Turbulence intensities for various terrain categories

Peak factor (Figure 2.5) according to DIN 1055-4 [12] C.3 (2):

$$g = \sqrt{2 \cdot \ln(\nu_E \cdot t)} + \frac{0.6}{\sqrt{2 \cdot \ln(\nu_E \cdot t)}}$$

where

t averaging period for reference wind speed v_{ref}: $t = 600\,s$ (= 10 min)

Expected value for frequency of gust response to DIN 1055-4 [12] C.3 (3):

$$\nu_E = \sqrt{\frac{\nu_{E,0}^2 \cdot Q_0^2 + n_{1,x}^2 \cdot R_x^2}{Q_0^2 + R_x^2}}$$

where

$n_{1,x}$ first natural frequency [Hz] of structure vibration in direction of wind (x direction)

$\nu_{E,0}$ expected value of frequency [Hz] of gust response of structure assuming a quasi-static structural behaviour:

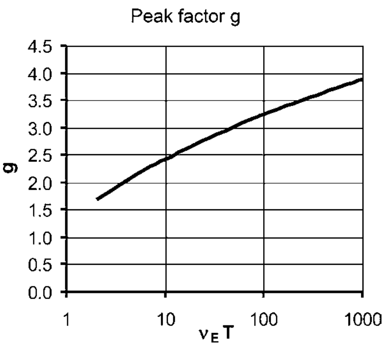

Fig. 2.5 Peak factor

Table 2.5 Integral length L_i (z) of turbulence (to DIN 1055-4 [12] C.3 (4))

$L_i(z) = 300 \cdot (z/300)^{\varepsilon}$ (L_i, z in m) for $z_{min} \leq z \leq 300$ m
$L_i(z) = 300 \cdot (z_{min}/300)^{\varepsilon}$ (L_i, z_{min} in m) for $z \leq z_{min}$

Terrain category	I	II	III	IV
Exponent ε	0.13	0.26	0.37	0.46
z_{min}	2.00	4.00	8.00	16.00

$$\nu_{E,0} = \frac{v_m(z_e)}{L_i(z_e)} \cdot \frac{1}{1.11 \cdot S^{0.615}}$$

where

$$S = 0.46 \cdot \frac{b + h}{L_i(z_e)} + 10.58 \cdot \frac{\sqrt{b \cdot h}}{L_i(z_e)}$$

b, h width, height of structure to DIN 1055-4 [12] Figure C.1
v_m (z_e) average wind speed at effective height $z = z_e$ (see above) to DIN 1055-4 [12] Table B.2 (see above)
L_i (z_e) integral length of longitudinal component of turbulence in direction of average wind for $z = z_e$ (Table 2.5)

Basic gust component Q_0, squared ([12] C.3 (5))

$$Q_0^2 = \frac{1}{1 + 0.9 \cdot \left(\frac{b + h}{L_i(z_e)}\right)^{0.63}}$$

Resonance response component R_x, squared ([12] C.3 (6))

$$R_x^2 = \frac{\pi^2}{2 \cdot \delta} \cdot R_N \cdot R_h \cdot R_b$$

where

δ logarithmic damping decrement for vibrations in wind direction to DIN 1055-4 [12] annex F

Dimensionless spectral density function R_N ([12] C.3 (7))

$$R_N = \frac{6.8 \cdot N_{1,x}}{(1 + 10.2 \cdot N_{1,x})^{5/3}}$$

where

$$N_{1,x} = \frac{n_{1,x} \cdot L_i(z_e)}{v_m(z_e)}$$

Aerodynamic transfer functions R_h and R_b ([12] C.3 (8))

These are specified for the fundamental vibration mode with identical sign (deformation in the same direction) and are calculated, starting from R_L, as follows:

$$R_L = \frac{1}{\eta} - \frac{1}{2 \cdot \eta^2} \cdot \left(1 - e^{-2 \cdot \eta}\right) \quad \text{for} > 0$$
$$R_L = 1 \qquad \text{for} = 0$$

where

$$R_h = R_L \quad \text{with} \quad \eta_h = \frac{4.6 \cdot N_{1,x} \cdot h}{L_i(z_e)}$$

$$R_b = R_L \quad \text{with} \quad \eta_b = \frac{4.6 \cdot N_{1,x} \cdot b}{L_i(z_e)}$$

Logarithmic damping decrement δ ([12] F.5)

Estimate of the logarithmic damping decrement for the fundamental flexural vibration mode to DIN 1055-4 [12] F.5 (1):

$$\delta = \delta_s + \delta_a + \delta_d$$

Structural damping δ_s see Table 2.6.

Aerodynamic damping ([12] F.5 (3))

$$\delta_a = \frac{\rho \cdot b \cdot c_f}{2 \cdot n_{1,x} \cdot m_{1,x}} \cdot v_m(z_e)$$

where

ρ density of air: $\rho = 1.25\,\text{kg/m}^3$

Table 2.6 Structural damping (to DIN 1055-4 [12] F.5 (2))
$\delta_s = a_1 \cdot n_1 + b_1 \geq \delta_{min}$
where
n_1 = fundamental flexural vibration frequency [Hz].
Parameters a_1, b_1, δ_{min} to 1055-4 [12] Table F.2 (extract)

Type of structure	a_1	b_1	δ_{min}
Reinforced concrete towers	0.050	0	0.025
Masonry/concrete chimneys	0.075	0	0.030

b width of structure exposed to the wind [m]
c_f average aerodynamic force coefficient in direction of wind
v_m (z_e) average wind speed at effective height $z = z_e$ (see above)
$m_{1,x}$ equivalent mass for fundamental vibration in direction of wind [kg/m]:

$$m_{1,x} = \frac{\int_0^L m(s) \cdot [\Phi_1(s)]^2 \cdot ds}{\int_0^L [\Phi_1(s)]^2 \cdot ds} \cong \frac{\sum_j m_j \cdot \Delta z_j \cdot \Phi_{1,j}^2}{\sum_j \Delta z_j \cdot \Phi_{1,j}^2} = \frac{\sum_j M_j \cdot \Phi_{1,j}^2}{\sum_j \Delta z_j \cdot \Phi_{1,j}^2}$$

(see DIN 1055-4 [12] F.4)

m (s) mass per unit length at location of coordinate s
Φ_1 (s) fundamental flexural vibration mode (see DIN 1055-4 [12] F.3):

$$\Phi_1(s) = \left(\frac{s}{L}\right)^\zeta \quad \text{or} \quad \Phi_1(z) = \left(\frac{z}{h}\right)^\zeta$$

where $\zeta = 2$ for towers and masts

s; z coordinate s on longitudinal axis of structure or structural member, or height coordinate z
L; h span L, or height h of structure or structural member
$n_{1,x}$ natural frequency for fundamental vibration in direction of wind [Hz] (see above)

Additional damping decrement δ_d ([12] F.5 (4))

Where special measures are provided for increasing the damping (e.g. vibration dampers), δ_d is to be calculated with the help of suitable theoretical or experimental methods.

Aerodynamic force coefficient for towers with a cylindrical cross-section ([12] 12.7.1 (1)):

$$c_{fj} = c_{f0,j} \cdot \psi_\lambda$$

where

$c_{f0,j}$ basic force coefficient for segment j to DIN 1055-4 [12] Figure 19 associated with Table 11 (see Figure 2.6 associated with Table 2.7)
ψ_λ slenderness reduction factor to DIN 1055-4 [12] Figure 26 (see Figure 2.7)

Reynolds number ([12] 12.7.1 (2)):

$$Re = \frac{v \cdot b}{\nu}$$

where $v[m/s] = \sqrt{2 \cdot q/\rho} = 40 \cdot \sqrt{q[kPa]}$

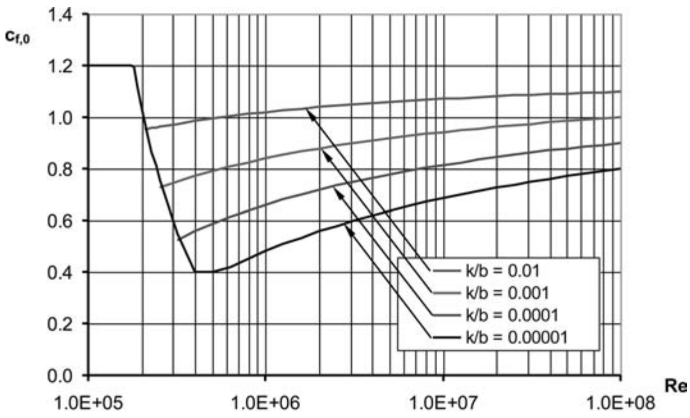

Fig. 2.6 Basic force coefficients for cylinders, see DIN 1055-4 [12] Figure 19

Table 2.7 Equivalent roughnesses (to DIN 1055-4 [12] Table 11)

	Masonry	Smooth concrete	Rough concrete	Timber	Steel	Steel including bolt-heads etc.
k [mm]	4	2	10	2	0.5	1

q peak dynamic pressure to 1055-4 [12] Table B.2, that is *without taking into account the dynamic effect of the wind*:

$$q = q_B(z_j) = \mathbf{c} \cdot q_{ref} \cdot (z_j/10)^{\mathbf{d}} \quad \left(\text{or} \quad \mathbf{c}_{min} \cdot q_{ref} \quad \text{for } z_j < z_{min}\right)$$

ρ density of air: $\rho = 1.25\,\mathrm{kg/m^3}$
b diameter of cylinder [m]
ν kinematic viscosity: $\nu = 15 \cdot 10^{-6}\ \mathrm{m^2/s}$

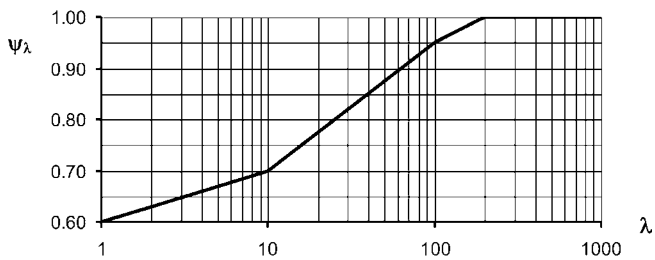

Fig. 2.7 Slenderness reduction factor ψ_λ to DIN 1055-4 [12] Figure 26, for a solidity ratio $\varphi = 1.00$

Effective slenderness λ for cylinders with segment length L and outside diameter b to DIN 1055-4 [12] Table 16:

$$\lambda = \mathrm{Min.}(0.7 \cdot L/b;\ 70) \quad \text{for} \quad L \geq 50\,\mathrm{m}$$
$$\lambda = \mathrm{Min.}(L/b;\ 70) \quad \text{for} \quad L \leq 15\,\mathrm{m}$$

Intermediate values may be obtained by linear interpolation.

Reference area of segment "j" considered (to DIN 1055-4 [12] 12.7.1. (5)):

$$A_j = L_j \cdot b_j$$

Calculation of aerodynamic force coefficient ([12] 12.7.1)

Example: prestressed concrete wind turbine structure, hub height 130 m (see Section 5.2)

	Symbol	Reference to DIN 1055-4 [12]	Value
Height of tower (segment) = reference height	$h = z_e$ [m]	12.7.1 (6)	129.674
Width of tower (segment)	b [m]		5.60
Reference wind speed	v_{ref} [m/s]	WZ 2	25.0
Reference dynamic pressure	q_{ref} [kPa]	WZ 2	0.39
Factor	c	Table B.2	2.10
Exponent	d	Table B.2	0.24
Peak dynamic pressure	$q_B\ (z_e)$ [kPa]	Table B.2	1.52
Equivalent wind speed	$v\ (z_e)$ [m/s]	$= 40 \cdot q_B^{0.5}$	49.27
Kinematic viscosity	ν [m²/s]		1.5E-05
Reynolds number	Re	Eq. (31)	1.8E + 07
Equivalent roughness	k [mm]	Table 11	10
Relative roughness	k/b		0.00179
Basic force coefficient	$c_{f,0}$	Figure 19	0.991
Slenderness	λ	Table 16	16.21
Reduction factor	ψ_λ	Figure 26	0.752
Force coefficient for tower shaft	$\mathbf{c_f}$	Eq. (30)	**0.75**

Determining the equivalent mass [12] annex F

Example: prestressed concrete wind turbine structure, hub height 130 m (see Section 5.2)

Node	z_j [m]	Δz_j [m]	G_j [kN]	Φ_j	$G_j \cdot \Phi_j^2$ [kN]	$\Delta z_j \cdot \Phi_j^2$ [m]
36	130.174	0.148	1120.00	1.0000	1120.00	0.1480
35	129.878	2.163	2330.00	0.9954	2308.80	2.1433
34	125.848	2.015	21.30	0.9344	18.60	1.7593
34	125.848	1.312	51.33	0.9344	44.82	1.1455
33	123.224	1.312	52.49	0.8957	42.11	1.0525
33	123.224	1.275	32.00	0.8957	25.67	1.0229
32	120.674	1.275	32.72	0.8588	24.13	0.9405
32	120.674	0.750	311.02	0.8588	229.41	0.5532
31	119.174	1.250	518.36	0.8375	363.62	0.8768
30	118.174	2.087	301.19	0.8235	204.24	1.4152
29	115.000	3.787	546.53	0.7797	332.22	2.3020
28	110.600	4.400	634.99	0.7209	330.00	2.2866
27	106.200	4.400	634.99	0.6644	280.32	1.9424
26	101.800	4.400	634.99	0.6103	236.48	1.6386
25	97.400	3.625	523.15	0.5584	163.12	1.1303
24	94.550	1.425	205.65	0.5260	56.91	0.3943
24	94.550	0.525	174.42	0.5260	48.26	0.1453
23	93.500	0.775	257.47	0.5144	68.12	0.2050
22	93.000	2.450	445.94	0.5088	115.46	0.6343
21	88.600	4.400	800.87	0.4616	170.63	0.9374
20	84.200	4.400	800.87	0.4166	139.01	0.7637
19	79.800	4.400	800.87	0.3740	112.01	0.6154
18	75.400	4.400	800.87	0.3336	89.14	0.4897
17	71.000	4.400	800.87	0.2956	69.97	0.3844
16	66.600	4.400	800.87	0.2598	54.07	0.2971
15	62.200	4.400	816.42	0.2264	41.84	0.2255

Node	z_j [m]	Δz_j [m]	G_j [kN]	Φ_j	$G_j \cdot \Phi_j^2$ [kN]	$\Delta z_j \cdot \Phi_j^2$ [m]
14	57.800	4.400	847.52	0.1953	32.31	0.1677
13	53.400	4.400	878.62	0.1664	24.33	0.1219
12	49.000	4.400	909.73	0.1399	17.80	0.0861
11	44.600	4.400	940.83	0.1157	12.58	0.0589
10	40.200	4.400	971.93	0.0937	8.54	0.0387
9	35.800	4.400	1018.58	0.0741	5.59	0.0242
8	31.400	4.400	1065.24	0.0568	3.43	0.0142
7	27.000	4.400	1142.99	0.0418	1.99	0.0077
6	22.600	4.400	1236.30	0.0290	1.04	0.0037
5	18.200	4.400	1329.60	0.0186	0.46	0.0015
4	13.800	4.400	1438.46	0.0105	0.16	0.0005
3	9.400	4.400	1457.68	0.0047	0.03	0.0001
2	5.000	4.450	1495.87	0.0012	0.00	0.0000
1	0.500	2.250	827.02	0.0000	0.00	0.0000
Total		h = 129.674	G = 30 010.57		G′ = 6797.25	h′ = 25.9745
				$m = 10^3 \cdot G'/h'/9.81 =$		**26.676 t/m**

The following sample calculation compares the results according to DIN 1055-4 [12] with those of the DIBt guideline [9] which arise as a result of the different approaches.

Calculation of gust response factor

Example: prestressed concrete wind turbine structure, hub height 130 m (see Section 5.2)

	Symbol	Reference	DIN 1055-4 annex C	DIBt guideline
Height of tower	h [m]		129.674	129.674
Width of tower	b [m]		5.60	5.60
Reference height	$z_e = 0.6 \cdot h$ [m]	Figure C.1	77.804	77.804
Reference wind speed	v_{ref} [m/s]	Zone 2	25.0	

	Symbol	Reference	DIN 1055-4 annex C	DIBt guideline
Average wind speed	v_m (z_e) [m/s]	Table B.2	34.71	34.71
Factor	a	Table B.2	1.00	
Exponent	b	Table B.2	0.16	
Turbulence intensity	I_v (z_e)	Table B.2	0.1368	0.1368
Factor	e	Table B.2	0.19	0.19
Exponent	f	Table B.2	−0.16	−0.16
Integral length	L_i (z_e) [m]	(C.9)	211	$L_i = 200$
Exponent	ε	Table C.1	0.26	
Natural frequency of fundamental vibration (see Section 4.3.2)	$n_{1,x}$ $[s^{-1}]$	(F.1)	0.289	0.289
Structural damping	δ_s	(F.8)	0.0250	
Parameter	a_1	Table F.2	0.050	
Minimum value	δ_{min}	Table F.2	0.0250	
Equivalent mass	m_1 [kg/m]	Table	26.676	
Density of air	ρ $[kg/m^3]$		1.25	
Average aerodynamic force coefficient	c_f	Table	0.75	
Aerodynamic damping	δ_a	(F.9)	0.0117	
Logarithmic damping decrement	δ	(F.7)	0.0367	0.0367
Squared basic gust component	Q_0^2	(C.10)	0.595	0.579
Transformed natural frequency	$N_{1,x}$ [−]	(C.13)	1.761	1.667
Spectral density function of wind speed	R_N	(C.12)	0.089	0.092
Aerodynamic transfer function (height)	R_h	(C.15)	0.181	0.181
	η_h	(C.15)	4.973	4.973

	Symbol	Reference	DIN 1055-4 annex C	DIBt guideline
Aerodynamic transfer function (width)	R_b	(C.16)	0.871	
	η_b	(C.16)	0.21	
Squared resonance response component of gust response	R_x^2	(C.11)	1.879	2.227
Coefficient	S	(C.8)	1.644	
Frequency of gust response – quasi-static	$\nu_{E,0}$ [s^{-1}]	(C.7)	0.109	
Expected value of frequency of gust response	ν_E [s^{-1}]	(C.6)	0.258	0.258
Peak factor	g	(C.5)	3.364	3.364
Gust response factor	**G**	(C.4)	**2.448**	2.542

Dynamic pressures taking into account the gust response

a) Evaluation according to DIN 1055-4 [12]:

$$q_j = G \cdot q_{m,j}$$

where

$q_{m,j}$ average dynamic pressure in segment j (q_m (z_j))
G gust response factor to DIN 1055-4 [12]:

$$G = 1 + 2 \cdot g \cdot I_v(z_e) \cdot \sqrt{Q_0^2 + R_x^2}$$

b) Simplified calculation to DIN 1056 [13]:

$$q_j = \varphi_B \cdot q_{B,j}$$

where

$q_{B,j}$ dynamic pressure taking into account the gust response in segment j (q_B (z_j))
φ_B gust response factor to DIN 1056 [13][1]:

$$\varphi_B = [\mathrm{Max.}(1.05 - h/1000;\ 1.0)] \cdot \left[1 + (0.042 \cdot T_1 - 0.0019 \cdot T_1^2) \cdot \delta^{-0.63}\right]$$

with logarithmic damping decrement $\delta = 0.10$ (reinforced concrete in cracked state or at the ultimate limit state)

1) Wind turbine example (5.2): $\varphi_B = 1.0 \cdot [1 + (0.042 \cdot 3.46 - 0.0019 \cdot 3.46^2)/0.10^{0.63}] = 1.523$ ($< G = 2.448$).

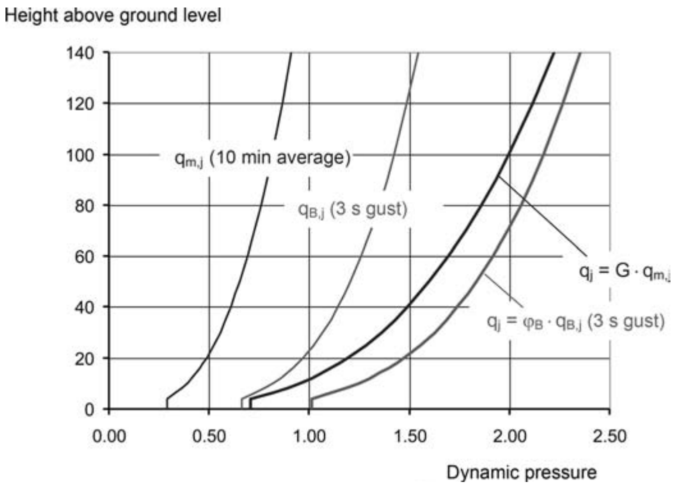

Fig. 2.8 Comparison of dynamic pressures taking into account the gust response according to DIN 1055-4 [12] and DIN 1056 [13]

The simplified calculation is on the safe side for the example shown in Figure 2.8.

2.3.2 Wind loads for offshore wind turbines

2.3.2.1 Classification of wind turbines

The definition of a *wind turbine class* is practical for designing the machinery (rotor – *topsides structure*) of an offshore wind turbine [11].

The values for the wind speed and turbulence intensity parameters should represent the characteristics of numerous different locations, the aim being to determine clearly defined levels of robustness (Table 2.8).

The design of the tower and foundation (*support structure*) for an offshore wind turbine must be based on the representative environmental conditions – including the sea conditions – at the respective location.

The *design working life* of an offshore wind turbine should be at least 20 years.

A rotor (*turbine*) designed according to one of the wind turbine classes given in Table 2.8 can withstand environmental conditions in which the 10-min average of the *extreme wind speed* for a 50-year return period is not greater than the given *reference wind speed* (V_{ref}) *at hub height*.

The *average wind speed* (V_{ave}) is the statistical mean of the momentary wind speed values averaged over a certain period – ranging from a few seconds to several years. In [11] V_{ave} is the *annual average wind speed* over many years. This value is used in the Weibull or Rayleigh functions for the wind speed distributions.

Table 2.8 Wind conditions for offshore wind turbines to [11] Table 4.2.1

Wind turbine class	I	II	III	S	Remarks
V_{ref} [m/s]	50	42.5	37.5	site-specific	50-year return wind 10-min average
V_{ave} [m/s]	10	8.5	7.5		Annual average wind speed

Category	A	B	C	S	Remarks
Turbulence intensity	higher	moderate	lower	site-specific	
$I_{15,A}$ [−]	0.18	0.16	0.145		characteristic turbulence intensity for $V_{hub} = 15$ m/s
a [−]	2	3	3		slope parameter for turbulence characteristics

2.3.2.2 Determining the wind conditions (wind climate)

The following basic parameters for the wind actions must be determined for the draft design and the location [11] 4.2.2.2:

– Reference wind speed V_{ref}
– Annual average wind speed V_{ave}
– Wind speed distribution
– Wind direction distribution (wind rose)
– Turbulence intensity I_{15} for $V_{hub} = 15$ m/s (V_{hub} is the 10-min average of wind speed at hub height)
– Wind shear.

The averaging time used in [11] for the *reference wind speed* (V_{ref}) is 10 minutes (see Table 2.8). The wind conditions (wind climate) may be determined from measurements taken at the location provided the measurement period is at least six months. The effects of seasonal fluctuations must be taken into account where these have a substantial effect on the wind climate.

Here, I_{15} is the characteristic value of the *turbulence intensity* ($I_{15(k)}$). It is calculated by adding the measured standard deviation to the measured mean value ($I_{15(m)}$) of the turbulence intensity. If the standard deviation has not been calculated from measurements, then the characteristic turbulence intensity for $V_{hub} = 15$ m/s may be calculated as follows:

$$I_{15(k)} \cong 1.2 \cdot I_{15(m)}$$

The value $I_{15(k)}$ should be determined from measured data when wind speeds exceed 10 m/s. In agreement with GL Wind (Germanischer Lloyd WindEnergie GmbH), the relevant characteristic values of the wind climate may be determined by numerical methods as an alternative.

2.3.2.3 Normal wind conditions

Wind speed distribution
The local distribution of the 10-min average of the wind speed at hub height (V_{hub}) is significant for the design of an offshore wind turbine because this determines the frequency of occurrence of individual load components.

A Weibull distribution (P_W) must be derived from *in situ* measurements verified by long-term measurements in the immediate vicinity:

$$P_W(V \leq V_{hub}) = 1 - \exp\left[-(V_{hub}/C)^k\right]$$

where

C scale parameter [m/s]
k shape parameter (k = 2 for designs in a standard wind turbine class)

When k = 2, the Weibull distribution produces a Rayleigh distribution which can be used for calculating the wind loads to [11] (Figure 2.9):

$$P_R(V \leq V_{hub}) = 1 - \exp\left(-\pi/4 \cdot (V_{hub}/V_{ave})^2\right)$$

From this we get the probability density for the wind speeds:

$$f(V_{hub}) = \pi/2 \cdot (V_{hub}/V_{ave}) \cdot \exp\left[-\pi/4 \cdot (V_{hub}/V_{ave})^2\right]$$

Normal wind profile model (NWP)
The following power law equation should be assumed for the wind profile V(z):

$$V(z) = V_{hub} \cdot (z/z_{hub})^{\alpha}$$

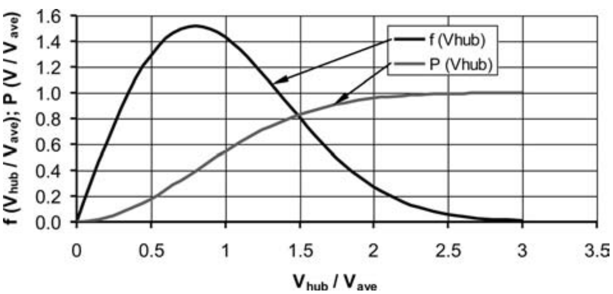

Fig. 2.9 Rayleigh distribution (function P and density f) for wind speeds

where

$V(z)$ wind speed at height z
z height above still water level
z_{hub} height of hub above still water level
α exponent

This wind profile is used to define the average wind shear force on the area swept by the rotor. This model is based on neutral atmospheric stability. Taking a constant surface roughness length of 0.002 m, then $\alpha = 0.14$.

Normal turbulence model (NTM)
The turbulence of the wind is represented by the energy that is transported by turbulence eddies and for which a spectral distribution is assumed. The following parameters are among those that characterise the natural turbulence of the wind over a relatively short period in which the spectrum remains unchanged:

– Average value of wind speed
– Turbulence intensity
– Integral length

The values of the turbulence intensity are defined for the height of the hub. The spectral energy densities of the random wind speed vector field must satisfy the following requirements for the wind turbine classes of Table 2.8:

a) The characteristic value of the standard deviation of the longitudinal wind speed at hub height (z_{hub}) is assumed to be as follows:

$$\sigma_L[\mathrm{m/s}] = I_{15} \cdot (15\,\mathrm{m/s} + a \cdot V_{hub})/(a + 1))$$

This standard deviation is assumed to be invariant over the height. Values for I_{15} and a can be found in Table 2.8. Figure 2.10 shows the standard deviation σ_L and the

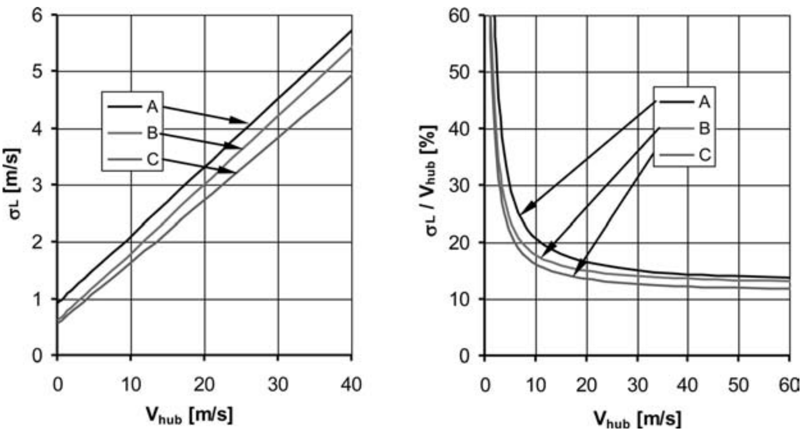

Fig. 2.10 Standard deviation of wind speed and turbulence intensity

turbulence intensity σ_L/V_{hub} (coefficient of variation) for the standard wind turbine classes.

b) The spectral energy density (S_L) of the longitudinal turbulence component must approach the following format asymptotically for very high frequencies:

$$S_L(f)\left[m^2/s^2\right] = 0.05 \cdot \sigma_L^2 \cdot (\Lambda_L/V_{hub})^{-2/3} \cdot f^{-5/3}$$

where

Λ_L turbulence scale parameter, defined as the wavelength at which the dimensionless spectral energy density of the longitudinal turbulence component $(f \cdot S_l\ (f)/\sigma_L^2)$ is 0.05 [m]

f frequency [s^{-1}]

The turbulence scale parameter is to be taken as follows:

$$\Lambda_L = \begin{cases} 0.7 \cdot z_{hub} & \text{for} \quad z_{hub} < 60\,m \\ 42\,m & \text{for} \quad z_{hub} \geq 60\,m \end{cases}$$

Every load simulation with the *normal turbulence model (NTM)* must be carried out for a period of 10 minutes at least. Furthermore, a series of further general requirements must be taken into account for load calculations, see [11] 4.2.2.3.3 (7).

2.3.2.4 Extreme wind conditions

Extreme wind conditions are assumed in order to determine extreme wind loads on offshore wind turbines. These conditions include peak wind speeds during storms and sudden changes to wind speed or direction. The extreme wind conditions also include the possible effects of turbulence, with the exception of the extreme wind speed model (EWM).

Extreme wind speed model (EWM)

The EWM must be based on *in situ* studies. Alternatively, the following data may be used.

The EWM can be either a steady or a turbulent wind model. The basic parameters are the reference wind speed V_{ref} (10-min average of extreme wind speed with a 50-year return period) and a certain standard deviation σ_L. The wind loads are described by applying power law equations over the height:

a) Steady extreme wind model:

$$V_{e,50}(z) = 1.25 \cdot V_{ref} \cdot (z/z_{hub})^{0.14}$$

$$V_{e,1}(z) = 0.8 \cdot V_{e,50}(z)$$

$$V_{red,50}(z) = 1.1 \cdot V_{ref} \cdot (z/z_{hub})^{0.14}$$

$$V_{red,1}(z) = 0.8 \cdot V_{red,50}(z)$$

where

$V_{e,N}$ (z) expected extreme wind speed (N = 50 or N = 1), *averaged over 3 s*
$V_{red,N}$ (z) reduced extreme wind speed (N = 50 or N = 1), *averaged over 60 s*

b) Turbulent extreme wind model:

$$V_{50}(z) = V_{ref} \cdot (z/z_{hub})^{0.14}$$

$$V_1(z) = 0.8 \cdot V_{50}(z)$$

$$\sigma_L = 0.12 \cdot V_{hub}$$

where

V_N (z) expected extreme wind speed (N = 50 or N = 1), *averaged over 10 min*
σ_L standard deviation for taking into account turbulence intensity

The index N stands for the return period (N = 50 years or N = 1 year).
Various general requirements must be considered for load calculations, see [11] 4.2.2.4.1 (7).
Extreme wind speeds can be converted from the 10-min average to other averaging periods using the values given in Table 2.9.

Extreme operating gust (EOG)
The gust speed V_{gustN} at hub height, with a return period of N years, is calculated as follows for standard wind turbine classes:

$$V_{gust,N} = \beta \cdot \frac{\sigma_L}{1 + 0.1 \cdot D/\Lambda_L}$$

where $\sigma_L[m/s] = I_{15} \cdot (15\,m/s + a \cdot V_{hub})/(a + 1))$ (as for the NTM)

Λ_L turbulence scale parameter, calculated as follows:

$$\Lambda_L = \begin{cases} 0.7 \cdot z_{hub} & \text{for } z_{hub} < 30\,m \\ 21\,m & \text{for } z_{hub} \geq 30\,m \end{cases}$$

D rotor diameter
β coefficient: $\beta = 4.8$ for N = 1 $\beta = 6.4$ for N = 50

The change in wind speed over time for a return period of N years is determined using the following equation:

Table 2.9 Conversion factors for wind speeds based on the 10-min average

Averaging period	1 h	*10 min*	1 min	5 s	3 s
Factor	0.91	*1.00*	1.10	1.21	1.25

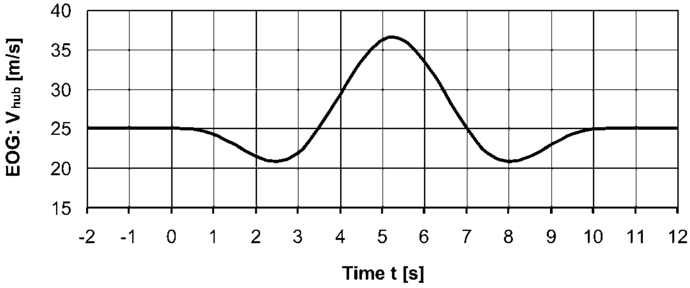

Fig. 2.11 Change in an extreme operating gust over time ($N = 1$, turbulence category A, $D = 42$ m, $z_{hub} = 30$ m, $V_{hub} = 25$ m/s)

$$V(z,t) = \begin{cases} V(z) - 0.37 \cdot V_{gust,N} \cdot \sin\left(\frac{3 \cdot \pi \cdot t}{T}\right) \cdot \left(1 - \cos\left(\frac{2 \cdot \pi \cdot t}{T}\right)\right) & \text{for } 0 \le t \le T \\ V(z) & \text{for } t < 0 \text{ and } t > T \end{cases}$$

where $V(z) = V_{hub} \cdot (z/z_{hub})^{\alpha}$ (NWP, see above)

T period: $T = 10.5$ s for $N = 1$ $T = 14.0$ s for $N = 50$
t time

Figure 2.11 shows an example of how an extreme operating gust changes over time.

Extreme wind direction change (EDC)
The magnitude of the extreme wind direction change θ_{eN} for a return period of N years should be calculated as follows (see Figure 2.12):

$$\theta_{e,N} = \pm\beta \cdot \arctan\left(\frac{\sigma_L}{V_{hub} \cdot (1 + 0.1 \cdot D/\Lambda_L)}\right) \quad \le 180°$$

where

$\sigma_L[m/s] = I_{15} \cdot (15\,m/s + a \cdot V_{hub})/(a + 1))$ (as for the NTM)

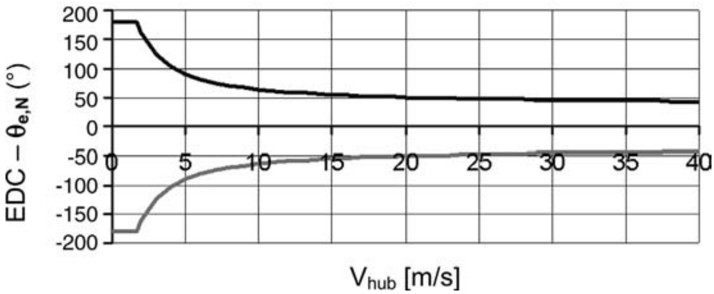

Fig. 2.12 Example of the magnitude of the extreme wind direction change

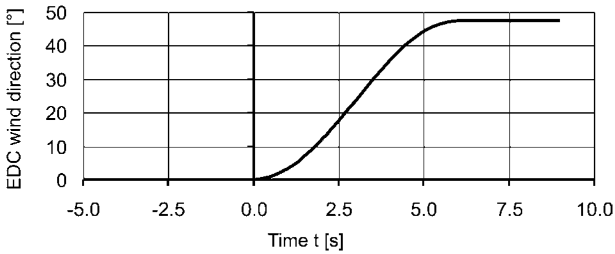

Fig. 2.13 How an extreme wind direction change varies over time (N = 50, turbulence category A, D = 42 m, z_{hub} = 30 m, V_{hub} = 25 m/s)

$$\Lambda_L = \begin{cases} 0.7 \cdot z_{hub} & \text{for } z_{hub} < 30\,\text{m} \\ 21\,\text{m} & \text{for } z_{hub} \geq 30\,\text{m} \end{cases} \quad \text{(as for the EOG)}$$

D and β again as for the EOG

The way the extreme wind direction change θ_N (t) varies over time for a return period of N years should be calculated as follows:

$$\theta_N(t) = \begin{cases} 0 & \text{for} \quad t < 0 \\ 0.5 \cdot \theta_{e,N} \cdot (1 - \cos(\pi \cdot t/T)) & \text{for} \quad 0 \leq t \leq T \\ \theta_{e,N} & \text{for} \quad t > T \end{cases}$$

Here, T = 6 s is the duration of the chronological progression of the extreme change in wind direction. The sign should be chosen in such a way that the loading gives the most unfavourable progression. Afterwards, a constant wind direction is assumed. Figure 2.13 shows an example of an extreme wind direction change.

Extreme coherent gust (ECG)

An extreme coherent gust with a magnitude of V_{cg} = 15 m/s should be assumed when designing for standard wind turbine classes. The change in the wind speed over time is defined as follows (see Figure 2.14):

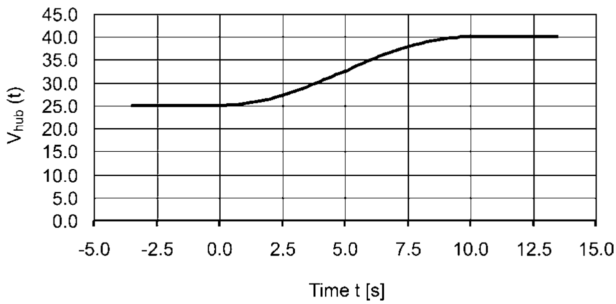

Fig. 2.14 Rise of an extreme coherent gust (V_{hub} = 25 m/s)

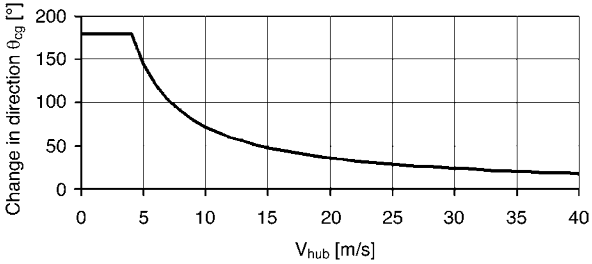

Fig. 2.15 Magnitude of wind direction change for ECD

$$V(z,t) = \begin{cases} V(z) & \text{for} \quad t < 0 \\ V(z) + 0.5 \cdot V_{cg} \cdot (1 - \cos(\pi \cdot t/T)) & \text{for} \quad 0 \leq t \leq T \\ V(z) + V_{cg} & \text{for} \quad t > T \end{cases}$$

where

$$V(z) = V_{hub} \cdot (z/z_{hub})^{\alpha} \quad \text{(NWP, see above)}$$

and

$$T = 10\,\text{s} \quad \text{gust rise time}$$

Extreme coherent gust with wind direction change (ECD)
In this situation we assume, as with the ECG, that the rise in the wind speed takes place simultaneously with a change in direction (θ_{cg}), which is described as follows (see Figure 2.15):

$$\theta_{cg}(V_{hub}) = \begin{cases} 180° & \text{for } V_{hub} < 4\,\text{m/s} \\ 720°/V_{hub}[\text{m/s}] & \text{for } 4\,\text{m/s} \leq V_{hub} \leq V_{ref} \end{cases}$$

The resulting simultaneous change in direction is as follows (see Figure 2.16):

$$\theta(t) = \begin{cases} 0 & \text{for} \quad t < 0 \\ \pm 0.5 \cdot \theta_{cg} \cdot (1 - \cos(\pi \cdot t/T)) & \text{for} \quad 0 \leq t \leq T \\ \pm \theta_{cg} & \text{for} \quad t > T \end{cases}$$

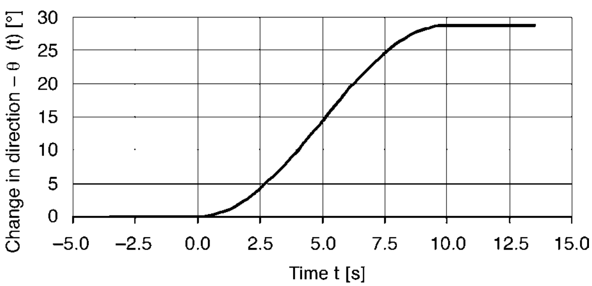

Fig. 2.16 Simultaneous chronological progression of wind direction change for ECD

where

$T = 10$ s gust rise time (ECG, see above)

Extreme wind shear (EWS)
The extreme wind shears with a return period of 50 years are to be considered in the following wind speed progressions:

– For a vertical wind shear varying over time:

$$V(z,t) = \begin{cases} V_{hub} \cdot \left(\frac{z}{z_{hub}}\right)^{\alpha} + \frac{z - z_{hub}}{D} \cdot \left(2.5 + 0.2 \cdot \beta \cdot \sigma_L \cdot \left(\frac{D}{\Lambda_L}\right)^{1/4}\right) \cdot \left(1 - \cos\left(\frac{2 \cdot \pi \cdot t}{T}\right)\right) \\ \qquad \text{for} \quad 0 \le t \le T \\ V_{hub} \cdot \left(\frac{z}{z_{hub}}\right)^{\alpha} \quad \text{for} \quad t < 0 \quad \text{and} \quad t > T \end{cases}$$

– For a horizontal wind shear varying over time:

$$V(y,z,t) = \begin{cases} V_{hub} \cdot \left(\frac{z}{z_{hub}}\right)^{\alpha} + \frac{y}{D} \cdot \left(2.5 + 0.2 \cdot \beta \cdot \sigma_L \cdot \left(\frac{D}{\Lambda_L}\right)^{1/4}\right) \cdot \left(1 - \cos\left(\frac{2 \cdot \pi \cdot t}{T}\right)\right) \\ \qquad \text{for } 0 \le t \le T \\ V_{hub} \cdot \left(\frac{z}{z_{hub}}\right)^{\alpha} \quad \text{for } t < 0 \text{ and } t > T \end{cases}$$

where

$\sigma_L[\text{m/s}] = I_{15} \cdot (15\,\text{m/s} + a \cdot V_{hub})/(a + 1))$ (as for the NTM)

$\alpha = 0.2 \quad \beta = 6.4 \quad T = 12\,\text{s} \quad D = \text{rotor diameter}$

$$\Lambda_L = \begin{cases} 0.7 \cdot z_{hub} & \text{for} \quad z_{hub} < 30\,\text{m} \\ 21\,\text{m} & \text{for} \quad z_{hub} \ge 30\,\text{m} \end{cases} \quad \text{(as for the EOG)}$$

The two extreme wind shears are to be considered independently of each other and therefore are not applied simultaneously. As an example, Figure 2.17 compares the maximum and minimum extreme vertical wind shears. Figure 2.18 is a diagram showing how the wind speeds change over time.

2.3.2.5 Wind farm influence

Offshore wind parks usually comprise multiple wind turbines (up to 200). Wind field perturbations in the wakes of rotors must be considered in the loading assumptions, both with respect to shielding and the reciprocal influences and superpositions. For more information please see [11] 4.2.2.5.

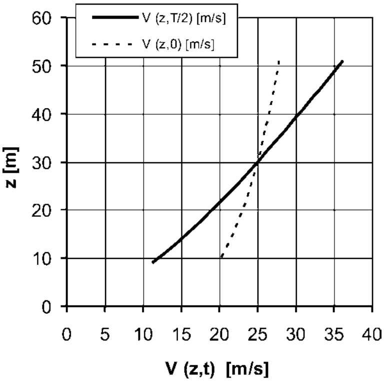

Fig. 2.17 Maximum and minimum extreme wind shears ($t = 0$ and $t = T/2$) ($N = 50$, category A, $z_{hub} = 30$ m, $V_{hub} = 25$ m/s, $D = 42$ m)

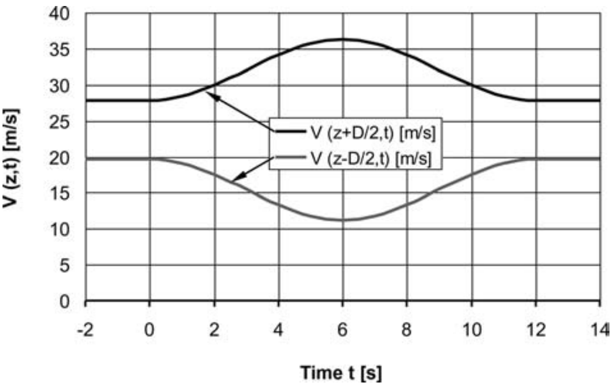

Fig. 2.18 Change in wind speeds over time at low point ($z = z_{hub} - D/2$) and high point ($z = z_{hub} + D/2$) of area swept by rotor

2.4 Height of sea level

The highest sea level with a return period of 50 years should be assumed for the draft design. The effects of tides and storm tides as well as seasonal fluctuations must be considered. In a conservative approach, the highest seawater level (HSWL) is the depth of water at the highest astronomical tide (HAT) plus the increase in level due to a storm tide (see [11] Appendix 4.A.7).

Accordingly, the lowest seawater level that should be assumed is the level with a return period of 50 years. Again, the effects of tides and storm tides as well as seasonal fluctuations must be taken into account. In a conservative approach, the lowest seawater level (LSWL) is the depth of water at the lowest astronomical tide (LAT) minus the decrease in level as a result of a storm ebb.

Table 2.10 Wave elevation coefficient δ

$d/(g \cdot T_D^2)$	$H_D/(g \cdot T_D^2)$					
	0.02	0.01	0.005	0.001	0.0005	0.0001
≥ 0.20	0.60	0.55	0.50	0.50	0.50	0.50
0.02	—	0.68	0.58	0.52	0.50	0.50
0.002	—	—	—	0.87	0.80	0.68

H_D design wave height (= $H_{max,50}$, see Section 2.5.8)
T_D design wave period (see Section 2.5.8)
d depth of water

The highest wave elevation above still water level (HSWL, MSL or LSWL) is specified in [11] as follows:

$$x^* = \delta \cdot H_D$$

where

δ wave elevation coefficient (see Table 2.10)

Intermediate values may be obtained by linear interpolation provided the waves do not break ($H_D < 0.7 \cdot d$).

Estimates of the water depths must be based on measurements carried out at the site. The levels of tides and storm tides must be derived from statistics based on long-term measurements and numerical models.

2.5 Hydrodynamic environmental conditions

The foundations of offshore wind turbines are exposed to the sea state and the currents in addition to the aforementioned actions. The principles for calculating the hydrodynamic actions plus their interaction with the foundation anchored to the seabed are briefly outlined below. In doing so, reference is made to the classic work by Kokkinowrachos, *Hydrodynamik der Seebauwerke* [17], which is recommended for a more in-depth study of the material and the answers to specific questions. Further textbooks for a more thorough introduction to the theory of water waves are given in [18].

2.5.1 Sea currents

The velocity potential of a sea current is mostly determined from the superposition of the tidal current ($U_{c,sub}$) and the wind-generated current ($U_{c,wind}$) plus, if applicable, a current induced by waves, especially breaking waves (U_{surf}) [11].

Tidal current
A power law equation is used for the velocity depending on the depth:

$$U_{c,sub}(z) = U_{c,sub} \cdot \left(\frac{d+z}{d}\right)^{1/7}$$

where

$U_{c,sub}$ velocity of tidal current at still water level ($z = 0$)

Essentially reliable measurements are available for the tidal currents of various sea areas.

Wind-generated current
A linear function is used for the velocity depending on the depth:

$$U_{c,wind}(z) = \begin{cases} U_{c,wind} \cdot \left(\frac{d_0+z}{d_0}\right) & \text{for} \quad -d_0 \leq z \leq 0 \\ 0 & \text{for} \quad z < -d_0 \end{cases}$$

$$d_0 = 20\,\mathrm{m}$$

$$U_{c,wind} = 0.015 \cdot u_{10\,m,1\,h}$$

where

$U_{c,wind}$ velocity of wind-generated current at still water level ($z = 0$)
$u_{10\,m,1\,h}$ wind speed at height of 10 m above still water level, averaged over 1 h

Figure 2.19 shows an example of the superposition of a wind-generated current and a tidal current.

Wave-generated current
Surf-generated currents must be considered when an offshore wind turbine is to be erected in the vicinity of a surf zone. The surf-generated current can be estimated with the help of numerical models, for example the Boussinesq model. A simplification for

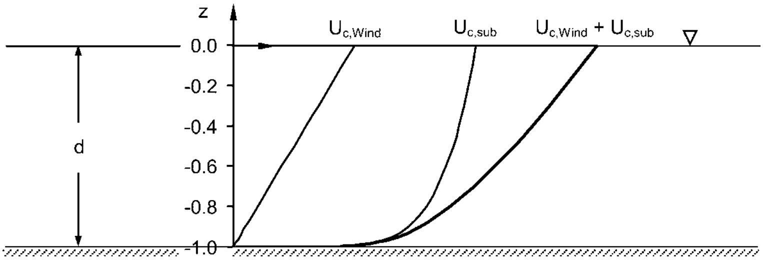

Fig. 2.19 Velocity profiles for a sea current (wind-generated, tidal and total)

coastal currents parallel with the line of the coast is to estimate the design velocity (U_{surf}) in the surf zone as follows:

$$U_{surf} = 2 \cdot s \cdot \sqrt{g \cdot H_B}$$

where

H_B height of breaking wave
s slope of seabed near the shore

We can choose the same power law equation for the vertical profile of the wave-generated current as for the tidal current.

Superposition of currents
The flow velocity resulting from all three components generally has to be combined with the sea state. For simplicity and to remain on the safe side, they are assumed to act in the same direction:

$$U_c(z) = U_{c,sub} \cdot \left(\frac{d+z}{d}\right)^{1/7} + \text{Max.}\left\{U_{c,wind} \cdot \left(\frac{d_0+z}{d_o}\right); 0\right\} + U_{c,surf} \cdot \left(\frac{d+z}{d}\right)^{1/7}$$

Depending on the location, further types of current, such as the velocity constant over the depth due to a permanent current, may need to be added into the equation.

2.5.2 Natural sea state

The term "natural sea state" is understood to be the totality of the observed wave events. This irregular mechanism can only be described with the help of the theory of stochastic processes.

The mathematical concept can be considerably simplified if we are allowed to assume that an observed stochastic process is stationary and ergodic. A process is stationary when the statistical means (moments) of the random variables are time-invariant. A process is ergodic when the generation of means from sampling (ensemble) can be replaced by a temporal averaging from a representative ensemble function, that is from the evaluation of a time series.

The natural sea state may be considered to be approximately stationary for short periods of time. Within the range of validity of this assumption, the sea state can be described as the result of the superposition of an infinite number of low-steepness harmonic waves with various directions, heights, periods and phase positions.

The central limit theorem of statistics can be used to verify that this superposition model leads to a random variable that exhibits a normal (or Gaussian) distribution. Consequently, individual short-term sea states are described by a Gaussian process that is stationary and ergodic. Every sea state, that is the associated Gaussian process, is described unambiguously in the frequency domain by the sea state spectrum, which specifies the distribution of the energy of the sea state by means of frequency and direction of movement.

2.5.3 Harmonic primary wave

The harmonic primary wave (Airy wave) is a solution to the linear, or linearised, boundary value problem for the propagating *gravity wave*, that is for a wave whose restoring force is the force of gravity. This solution is linked with the fundamental assumption of an infinitesimal amplitude, or rather steepness (= wave height/wavelength). The profile of a long-crested (smooth) harmonic primary wave that propagates in the direction of the x axis over a constant depth of water (d) can be described by the following formulation (Figure 2.20):

$$\zeta(x,t) = \frac{H}{2} \cdot \cos(k \cdot x - \omega \cdot t)$$

where

H	wave height
$k = 2 \cdot \pi/\lambda$	wavenumber
λ	wavelength
$\omega = 2 \cdot \pi/T$	angular frequency
T	wave period

The flow field of the primary wave can be unambiguously described by the velocity potential Φ (x, z, t), which is

$$\Phi(x,z,t) = \frac{H}{2} \cdot \frac{g}{\omega} \cdot \frac{\cosh[k \cdot (z + d)]}{\cosh(k \cdot d)} \cdot \sin(k \cdot x - \omega \cdot t)$$

for the wave profile ζ (x, t).

The most important feature of the Airy wave is the existence of a dispersion, that is the angular frequency's dependence on the wavelength or wavenumber, coupled with the gravitational acceleration (g) as an indication of the gravity wave. The dispersion equation is usually written in the following form:

$$\omega^2 = g \cdot k \cdot \tanh(k \cdot d)$$

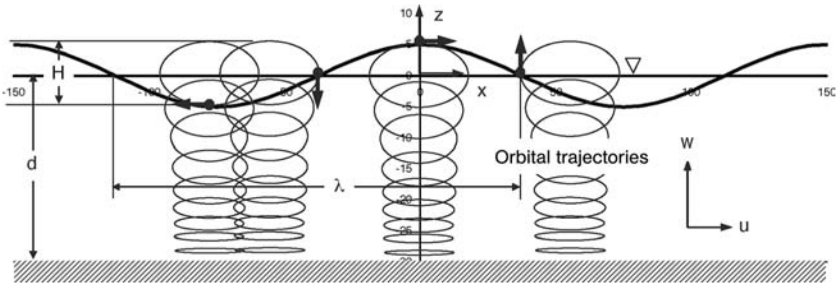

Fig. 2.20 Harmonic primary wave (H = 10.0 m, d = 30 m, λ = 150 m)

Rearranging gives us the phase velocity of the primary wave:

$$c = \frac{\lambda}{T} = \frac{\omega}{k} = \sqrt{\frac{g}{k} \cdot \tanh(k \cdot d)}$$

Consequently, a harmonic primary wave in water with a limited depth can be unambiguously defined by one of the groups of three values [H, λ, d] or [H, T, d]. The approximation tanh $(k \cdot d) \approx 1$ is valid for $d > \lambda/2$, that is $k \cdot d > \pi$. Therefore, for deep water we get

$$\omega^2 = g \cdot k \quad \text{and} \quad c = \frac{\lambda}{T} = \frac{\omega}{k} = \sqrt{\frac{g}{k}} = \sqrt{\frac{g \cdot \lambda}{2 \cdot \pi}}$$

or

$$\lambda = \frac{g \cdot T^2}{2 \cdot \pi} \quad \text{and} \quad c = \frac{\lambda}{T} = \frac{g \cdot T}{2 \cdot \pi}$$

as well.

The Airy wave in deep water is unambiguously defined by one of the pairs of values [H, λ] or [H, T].

For longer waves in very shallow water, that is $d \ll \lambda$ or $k \cdot d \to 0$, the approximation tanh $(k \cdot d) \approx k \cdot d$ gives us

$$c = \sqrt{g \cdot d}$$

that is the phase velocity only depends on the depth of water and no longer on the wavelength.

All the variables of the wave field can be derived from the velocity potential of the primary wave. Taking into account the dispersion equation, we get the following for the components of the velocity field in the wave:

$$u = \frac{\partial \Phi(x, z, t)}{\partial x} = \omega \cdot \frac{H}{2} \cdot \frac{\cosh[k \cdot (z + d)]}{\sinh(k \cdot d)} \cdot \cos(k \cdot x - \omega \cdot t)$$

$$w = \frac{\partial \Phi(x, z, t)}{\partial z} = \omega \cdot \frac{H}{2} \cdot \frac{\sinh[k \cdot (z + d)]}{\sinh(k \cdot d)} \cdot \sin(k \cdot x - \omega \cdot t)$$

Using these velocity components it is easy to show that the water particles pursue closed orbital trajectories during the motion of the wave (Figure 2.20: ellipses in a limited depth of water which gradually change to circles in deep water). There is no transportation of mass; the Airy wave transports energy only.

When calculating the acceleration field in the Airy wave, only the local component of the substantial acceleration is taken into account because assuming a low wave steepness means that the convective acceleration is negligible with respect to the local acceleration. The following then applies:

$$\dot{u} = \frac{\partial u}{\partial t} = \frac{\partial^2 \Phi}{\partial x \, \partial t} = \omega^2 \cdot \frac{H}{2} \cdot \frac{\cosh[k \cdot (z+d)]}{\sinh(k \cdot d)} \cdot \sin(k \cdot x - \omega \cdot t)$$

$$\dot{w} = \frac{\partial w}{\partial t} = \frac{\partial^2 \Phi(x,z,t)}{\partial z \, \partial t} = -\omega^2 \cdot \frac{H}{2} \cdot \frac{\sinh[k \cdot (z+d)]}{\sinh(k \cdot d)} \cdot \cos(k \cdot x - \omega \cdot t)$$

The pressure field in the Airy wave is obtained from the linearised Bernoulli equation for unsteady flows:

$$p + \rho \cdot \frac{\partial \Phi}{\partial t} + \rho \cdot g \cdot z = p_0 \quad \rightarrow \quad \Delta p = p - p_0 = -\rho \cdot g \cdot z - \rho \cdot \frac{\partial \Phi}{\partial t}$$

Accordingly, the difference between this and atmospheric pressure (p_0) consists of a hydrostatic ($-\rho \cdot g \cdot z$) and a hydrodynamic (unsteady) component:

$$p_{inst} = -\rho \cdot \frac{\partial \Phi}{\partial t}$$

Substituting the equation for the velocity potential in this relationship gives us

$$p_{inst} = -\rho \cdot \frac{\partial \Phi(x,z,t)}{\partial t} = \rho \cdot g \cdot \frac{H}{2} \cdot \frac{\cosh[k \cdot (z+d)]}{\cosh(k \cdot d)} \cdot \cos(k \cdot x - \omega \cdot t)$$

Easy to recognise here is the fact that the dynamic pressure is proportional to the wave profile and subsides with the depth ordinate ($z < 0$):

$$p_{inst} = \rho \cdot g \cdot \zeta(x,t) \cdot \frac{\cosh[k \cdot (z+d)]}{\cosh(k \cdot d)}$$

When designing marine structures it is often important to consider the processes involved with the superposition of a current (e.g. tidal or river current) and a primary wave. This results in a change to the wavelength and the wave height. Some important physical relationships can be derived from the simplest case of a situation in deep water.

Let U_C be the flow velocity ($U_C > 0$ in the direction of wave propagation) and index 0 indicate the undisturbed waves. Using a fixed system of coordinates, the condition that the frequency remains constant upon superposition then gives us the following for the change in wavelength from λ_0 to λ:

$$\frac{\lambda}{\lambda_0} = \frac{k_0}{k} = \frac{(1+\chi)^2}{4}$$

where

$$\chi = \sqrt{1 + 4 \cdot \frac{U_C}{c_0}} \quad \text{and} \quad c_0 = \frac{g \cdot T}{2 \cdot \pi}$$

We obtain

$$\omega^2 = g \cdot k_0 = g \cdot k \cdot \frac{(1+\chi)^2}{4} \quad \text{and} \quad c = \frac{\lambda}{T} = \sqrt{\frac{g \cdot \lambda}{2 \cdot \pi}} = c_0 \cdot \frac{1+\chi}{2}$$

for the modified dispersion equation and the phase velocity.

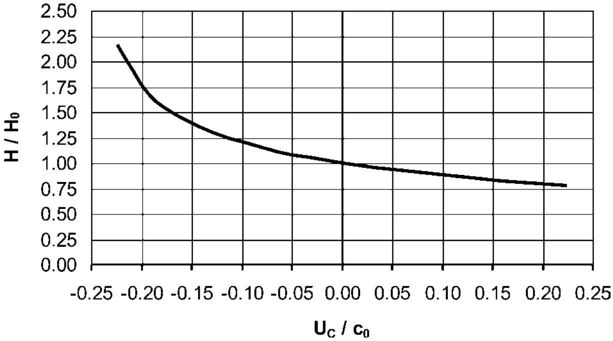

Fig. 2.21 Superposition of primary wave and uniform flow

The change in the wave height can be calculated with the help of the law of conservation of energy and the above relationships as follows:

$$H/H_0 = \sqrt{2/[\chi \cdot (1+\chi)]}$$

We can see from these equations that a current flowing in the direction of the wave ($U_C > 0$) causes the wavelength and the phase velocity to increase and the wave to flatten out. We get the opposite effects when the current flows in the opposite direction to the wave (Figure 2.21); U_C/c_0 must be greater than -0.25 in this case. However, this limiting value is not reached because the wave breaks first!

2.5.4 Waves of finite steepness

The use of the harmonic primary wave, that is linear wave theory, is only justified for the range of *infinitesimal* wave steepness, which in practical terms means $H/\lambda < 1/50$. When designing nearshore structures in particular, we have to describe waves with a *finite* steepness in a finite depth of water. To do this we need solutions to the non-linear problem of the propagating gravity wave. As an explicit and complete solution to the corresponding boundary value problems is impossible, we limit ourselves to approximate solutions of various orders.

The most important solutions to the non-linear wave problem are:

- Stokes waves,
- the elliptical (cnoidal) wave, and
- the solitary wave.

For an identical wave height, the wave crests of Stokes and elliptical waves are steeper than those of Airy waves, the wave troughs flatter. The particle trajectories are no longer closed, which means that transportation of mass takes place.

Stokes' wave theory makes use of formulations in the form of power series for the profile and the velocity potential. So Stokes' third-order theory for deep water gives us the following wave profile (see also Figure 2.22):

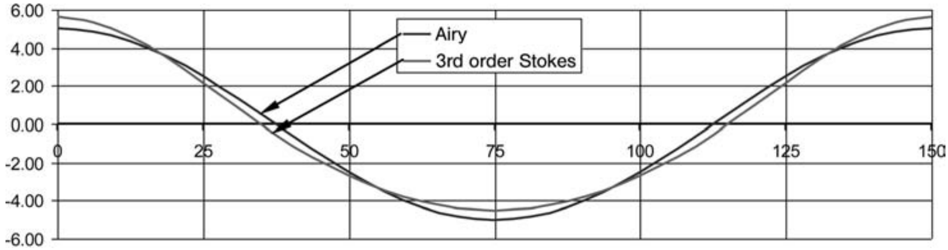

Fig. 2.22 Wave profiles – *Airy* and third-order *Stokes* ($H = 10\,m$, $d = 30\,m$, $\lambda = 150\,m$)

$$\zeta(x,t) = \frac{H}{2} \cdot \left\{ \cos(k \cdot x - \omega \cdot t) + \frac{1}{2} \cdot \frac{\pi \cdot H}{\lambda} \cdot \cos[2 \cdot (k \cdot x - \omega \cdot t)] + \frac{3}{8} \cdot \left(\frac{\pi \cdot H}{\lambda}\right)^2 \cdot \cos[3 \cdot (k \cdot x - \omega \cdot t)] \right\}$$

This expression includes the influence of the finite wave steepness, the maximum value of which for deep water is $(H/\lambda)_{max} = 1/7$.

With *Stokes waves* it is important to note that – as with all waves of finite steepness – the substantial acceleration (Du/dt) must be calculated and – as with the Airy wave – not just its local component ($\partial u/\partial t$):

$$\frac{Du}{dt} = \frac{\partial u}{\partial t} + u \cdot \frac{\partial u}{\partial x} + w \cdot \frac{\partial u}{\partial z}$$

Another non-linear theory with practical significance is the *stream function wave theory* of Dean [19], which covers a wide range of applications. The boundary conditions at the free water surface are completely satisfied by this theory but only partly by Stokes waves [18].

Elliptical waves are used in areas of shallow water where Stokes waves become inaccurate. As a global estimate, this is the case when $d/\lambda \leq 0.1$.

The Stokes and elliptical waves, which are oscillatory, are joined by the *solitary wave* for the surf zone. This purely translational wave consists of a single infinitely long wave crest that lies entirely above the still water level and whose two flanks slope asymptotically towards this. The profile of the solitary wave is defined as

$$\zeta(x,t) = H \cdot \left\{ \cosh^2\left[\sqrt{\frac{3 \cdot H}{4 \cdot d^3}} \cdot (x - c \cdot t)\right] \right\}^{-1}$$

with the phase velocity

$$c = \sqrt{g \cdot d \cdot \left(1 + \frac{H}{d}\right)}$$

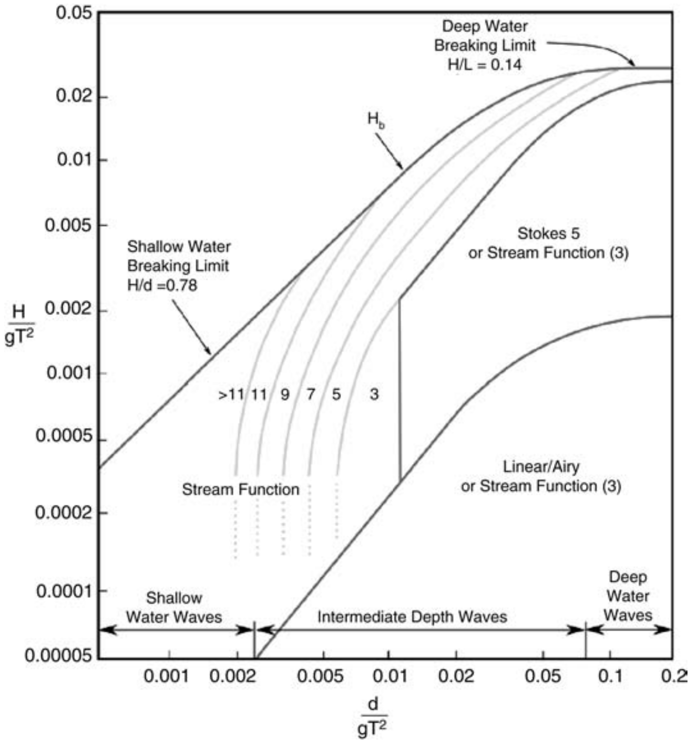

Fig. 2.23 Wave theory selection diagram ([11] 4.G.1)

To conclude this section it should be mentioned that a transition from the deterministic to a statistical concept is not readily possible for waves of finite steepness because the superposition principle does not apply to non-linear wave theories. Figure 2.23 illustrates the validity ranges of the numerical wave theories.

2.5.5 Statistical description of the sea state

A three-part approach is mostly used for describing the sea state [20]:

1. The displacement of the surface of the water at a location is measured over time and classified into solitary waves with an associated period (T_i) and height (H_i) using methods such as the zero-crossing method, for instance (stage 1 – *time series*).
2. To reduce the amount of data, all the waves of one set of measurements are analysed statistically and reduced to significant parameters or spectral functions (e.g. *Pierson-Moskowitz* or *JONSWAP spectrums*) (stage 2 – *short-term statistics*).
3. If we consider the variability of the sea state parameters over longer periods of time, then we arrive at the *sea state climate* (stage 3 – *long-term statistics*), which is mostly presented in the form of a *scatter diagram* or *distribution functions*.

2.5.6 Short-term statistics for the sea state

By assuming that individual *short-term sea states* are of a steady-state nature over periods of approx. 3 h, it has been possible to develop so-called *sea state spectra* for the stochastic description of the sea state [21]. The sea state function ζ (t), that is the corresponding Gaussian process, arising according to the model of the superposition of primary waves can be presented as follows for a long-crested sea state (see also [11]):

$$\zeta(t) = \int_0^\infty \sqrt{2 \cdot S_\zeta(\omega) \cdot d\omega} \cdot \cos[\omega \cdot t - \varepsilon(\omega)]$$

where $S_\zeta(\omega)$ is the *sea state spectrum* and $\varepsilon(\omega)$ a phase angle that, as a random number with the same probability, takes on all the values in the range from 0 to $2 \cdot \pi$. This equation is not a Riemann integral, but rather the mathematical interpretation of the fact that an infinite number of primary waves with amplitudes $\sqrt{2 \cdot S_\zeta(\omega) \cdot d\omega}$ and random phases $\varepsilon(\omega)$ are superposed.

It is expedient and in no way a constraint to agree that the function ζ (t) be measured from the mean value. The normal distribution density is then

$$f(\zeta) = \frac{1}{\sqrt{2 \cdot \pi} \cdot \sigma_\zeta} \cdot \exp\left(-\frac{\zeta^2}{2 \cdot \sigma_\zeta^2}\right) = \frac{1}{\sqrt{2 \cdot \pi \cdot m_0}} \cdot \exp\left(-\frac{\zeta^2}{2 \cdot m_0}\right)$$

where

$$\sigma_\zeta^2 = m_0 = \int_0^\infty S_\zeta(\omega) \cdot d\omega$$

and m_0 is the variance of the distribution, which is equal to the area beneath the spectrum (moment of zero order). All the derivations of the time function ζ (t) likewise exhibit normal distributions:

$$f(\dot{\zeta}) = \frac{1}{\sqrt{2 \cdot \pi \cdot m_2}} \cdot \exp\left(-\frac{\dot{\zeta}^2}{2 \cdot m_2}\right)$$

$$f(\ddot{\zeta}) = \frac{1}{\sqrt{2 \cdot \pi \cdot m_4}} \cdot \exp\left(-\frac{\dot{\zeta}^2}{2 \cdot m_4}\right)$$

where

$$m_\nu = \int_0^\infty \omega^\nu \cdot S_\zeta(\omega) \cdot d\omega$$

and m_ν is the moment of νth order for the area beneath the spectrum.

When representing the short-crested sea state it is assumed that the direction of propagation of the primary waves is scattered over a range of $\pm\pi/2$ about the mean principal direction of propagation of the sea state (roughly the wind direction). In a fixed system of coordinates the short-crested sea state can be represented as follows:

$$\zeta(x, y, t) = \int_0^\infty \int_{\mu_H-\pi/2}^{\mu_H+\pi/2} \sqrt{2 \cdot S_\zeta(\omega, \mu) \cdot d\mu \cdot d\omega} \cdot \cos[k \cdot (x \cdot \cos\mu + y \cdot \sin\mu) - \omega \cdot t - \varepsilon(\omega, \mu)]$$

where μ_H is the principal direction of propagation of the sea state and $S_\zeta(\omega,\mu)$ the direction spectrum.

The following applies for the variance of the short-crested sea state:

$$\sigma_\zeta^2(\mu_H) = m_0(\mu_H) = \int_0^\infty \int_{\mu_H-\pi/2}^{\mu_H+\pi/2} S_\zeta(\omega, \mu) \cdot d\mu \cdot d\omega$$

Statements regarding the distribution and frequency of certain values during a steady-state sea condition, for example maxima or zero crossings of a given level, have a certain practical significance. The nature of such distributions depends on the magnitude of the dimensionless width parameter ε, which is a measure of the width of the sea state spectrum:

$$\varepsilon = \left(1 - \frac{m_2^2}{m_0 \cdot m_4}\right)^{0.5}$$

where m_0, m_2 and m_4 are zero-, second- and fourth-order moments respectively for the area beneath the spectrum. Taking the limit values $\varepsilon = 1$ (very wide spectrum) and $\varepsilon = 0$ (very narrow spectrum), we get a normal or a *Rayleigh distribution* respectively for the maximum values of the long-crested sea state. The following applies for the distribution densities:

$$f(\zeta_M) = \frac{1}{\sqrt{2 \cdot \pi \cdot m_0}} \cdot \exp\left(-\frac{\zeta_M^2}{2 \cdot m_0}\right) \quad \text{for} \quad \varepsilon = 1$$

$$f(\zeta_M) = \frac{\zeta_M}{m_0} \cdot \exp\left(-\frac{\zeta_M^2}{2 \cdot m_0}\right) \quad \text{for} \quad \varepsilon = 0$$

These days we work almost exclusively approximately using a Rayleigh distribution for the maxima although the sea state spectra are not narrow. Assuming a Rayleigh distribution for the maxima results in the height of the wave being overestimated. We get the following distribution density from f (ζ_M):

$$f(H) = \frac{H}{4 \cdot m_0} \cdot \exp\left(-\frac{H^2}{8 \cdot m_0}\right)$$

We can use these equations to calculate the probabilities with which the maximum value of the sea state function ζ_M or the wave height H exceeds or does not exceed certain values. The following applies for the distribution function:

$$F(\zeta_M) = P\left(\zeta_M \leq \zeta_M^*\right) = 1 - \exp\left(-\frac{\zeta_M^{*2}}{2 \cdot m_0}\right) \quad \text{and} \quad P\left(\zeta_M > \zeta_M^*\right) = \exp\left(-\frac{\zeta_M^{*2}}{2 \cdot m_0}\right)$$

or

$$F(H^*) = P(H \leq H^*) = 1 - \exp\left(-\frac{H^{*2}}{8 \cdot m_0}\right) \quad \text{and} \quad P(H > H^*) = \exp\left(-\frac{H^{*2}}{8 \cdot m_0}\right)$$

The *significant wave height* was introduced to characterise the irregular sea state for practical engineering applications. By presuming a Rayleigh distribution for the sea state it

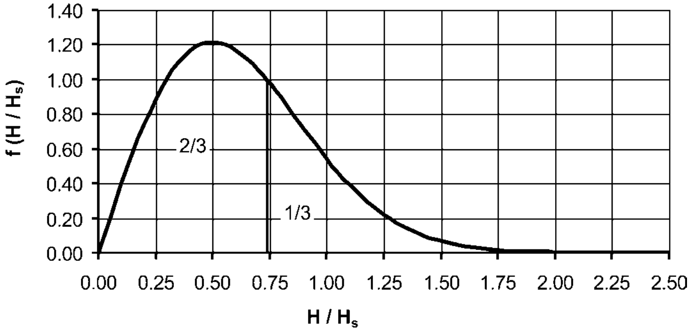

Fig. 2.24 Rayleigh distribution for wave heights; significant wave height

is assumed that the significant wave height H_s can be determined by the wave height $H_{1/3}$ in the time domain, that is by the mean value of the 1/3-highest waves (centroid of area, see Figure 2.24). The following applies:

$$\zeta_{M_S} = \zeta_{M_{1/3}} = 2 \cdot \sqrt{m_0} \quad \text{and} \quad H_S = H_{1/3} = 4 \cdot \sqrt{m_0}$$

Also interesting in connection with the maxima statistics is the determination of the average maxima per unit of time, that is the frequency of the maxima, or its inverse, the average period of the maxima:

$$f_m = \frac{1}{2 \cdot \pi} \cdot \sqrt{\frac{m_4}{m_2}} \quad \text{and} \quad T_m = 2 \cdot \pi \cdot \sqrt{\frac{m_2}{m_4}}$$

Yet another aspect of interest for practical situations is the frequency of, or rather the time intervals between, the zero points ($\zeta_k = 0$) in the same direction (*zero-upcrossing/down-crossing period*):

$$f_0 = \frac{1}{2 \cdot \pi} \cdot \sqrt{\frac{m_2}{m_0}} \quad \text{and} \quad T_0 = 2 \cdot \pi \cdot \sqrt{\frac{m_0}{m_2}}$$

The average period is also often used: $\bar{T} = 2 \cdot \pi \cdot \dfrac{m_0}{m_1}$

The choice of a function for the sea state spectrum is important for the application of the statistical concept. The general form of the sea state spectrum, as Bretschneider shows with the help of similarity mechanism observations, is

$$S_\zeta(\omega) = \alpha \cdot \omega^{-5} \cdot \exp\left(-\beta \cdot \omega^{-4}\right)$$

The *Pierson-Moskowitz spectrum* is frequently recommended in deep water for a so-called *fully developed sea*, that is when assuming a steady-state wind speed U and an unlimited fetch [22]:

$$S_\zeta(\omega) = 8.1 \cdot 10^{-3} \cdot g^2 \cdot \omega^{-5} \cdot \exp\left(-0.74 \cdot g^4 \cdot U^{-4} \cdot \omega^{-4}\right)$$

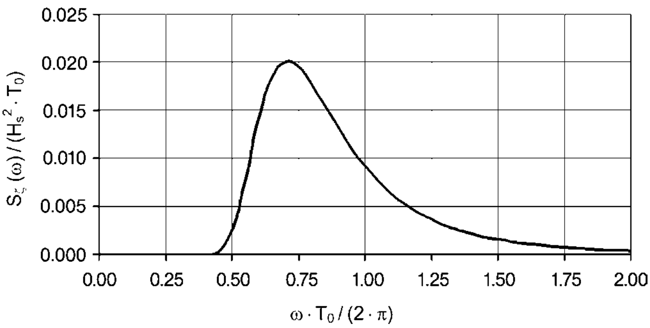

Fig. 2.25 Modified Pierson-Moskowitz spectrum

Comparing the coefficients results in

$$\alpha = 8.1 \cdot 10^{-3} \cdot g^2 \quad \text{and} \quad \beta = 0.74 \cdot g^4 \cdot U^{-4}$$

The following two-parameter (biased) spectrum is mainly used in practice:

$$S_\zeta(\omega) = 124 \cdot H_s^2 \cdot T_0^{-4} \cdot \omega^{-5} \cdot \exp\left(-496 \cdot T_0^{-4} \cdot \omega^{-4}\right)$$

This format is known as the *modified Pierson-Moskowitz spectrum* and is often used in its dimensionless form (Figure 2.25):

$$\begin{aligned} \frac{S_\zeta(\omega)}{H_s^2 \cdot T_0} &= \frac{1}{8 \cdot \pi^2} \cdot \left(\frac{\omega \cdot T_0}{2 \cdot \pi}\right)^{-5} \cdot \exp\left[-\frac{1}{\pi} \cdot \left(\frac{\omega \cdot T_0}{2 \cdot \pi}\right)^{-4}\right] \\ &= 124 \cdot (\omega \cdot T_0)^{-5} \cdot \exp\left[-496 \cdot (\omega \cdot T_0)^{-4}\right] \end{aligned}$$

It can be used to describe both fully developed and developing sea states, that is old and young sea states. One of the pairs of values $[H_s; T_0]$ or $[H_s; \bar{T}]$ is needed for the unambiguous short-term description of a developing long-crested sea state. A third parameter, the direction angle μ_H, is needed as well for short-crested sea states.

The designer is recommended to use the *JONSWAP spectrum* for sea areas with limited *fetch*, or rather developing sea states (see Figure 2.26). This spectrum is based on comprehensive measurements carried out off the German North Sea coast [23]. It is suitable for shallower water and extreme sea state relationships and is mostly written in the following form (see also [11]):

$$S_\zeta(\omega) = \alpha \cdot g^2 \cdot \omega^{-5} \cdot \exp\left[-\frac{5}{4} \cdot \left(\frac{\omega}{\omega_p}\right)^{-4}\right] \cdot \gamma^{\exp\left[-\frac{(\omega-\omega_p)^2}{2 \cdot \sigma^2 \cdot \omega_p^2}\right]}$$

where $\sigma = \begin{cases} \sigma_a & \text{for} \quad \omega \leq \omega_p \\ \sigma_b & \text{for} \quad \omega > \omega_p \end{cases}$

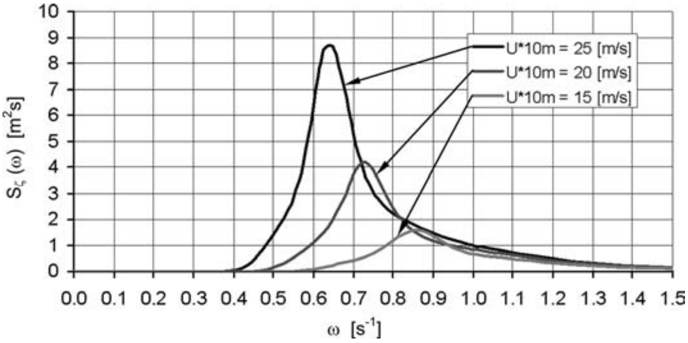

Fig. 2.26 JONSWAP spectra for three wind speeds

The five parameters (α, ω_p, γ, σ_a, σ_b) are defined as follows:

α The so-called Phillips "constant", which has a fixed value of 0.0081 in the *Pierson-Moskowitz spectrum* but in the *JONSWAP spectrum* depends on the significant wave height (H_s) and therefore *fetch* and *time*.

ω_p The angular frequency of the maximum of the spectrum (*peak frequency*) ($\omega_p = 2 \cdot \pi / T_p$, with the peak period T_p, where $T_p = 1.296 \cdot \bar{T} = 1.408 \cdot T_0$).

γ Shape parameter for the enlargement factor with respect to the Pierson-Moskowitz spectrum.

σ_a Characteristic dimension for the width of the spectrum to the *left* of the maximum (usually $\sigma_a = 0.07$).

σ_b Characteristic dimension for the width of the spectrum to the *right* of the maximum (usually $\sigma_b = 0.09$).

The following formats are specified in [11] for parameters α and γ:

$$\alpha = \frac{5}{16} \cdot \frac{H_s^2 \cdot \omega_p^4}{g^2} \cdot C(\gamma)$$

$$C(\gamma) = (1 - 0.287 \cdot \ln\gamma)$$

$$\gamma = \begin{cases} 5 & \text{for} \quad T_p/\sqrt{H_s} < 3.6 \\ \exp\left(5.75 - 1.15 \cdot T_p/\sqrt{H_s}\right) & \text{for} \quad 3.6 \le T_p/\sqrt{H_s} \le 5 \\ 1 & \text{for} \quad T_p/\sqrt{H_s} > 5 \end{cases}$$

Here, C (γ) is a normalising factor included to guarantee that the same significant wave height is used for the JONSWAP spectrum as for the Pierson-Moskowitz spectrum.

When no measurement data from the site is available for the preliminary planning or when the offshore wind turbine is to be designed to a standard wind turbine class (see Table 2.8), the formulations according to [11] Appendix 4.E can be used. The influences of *time* and *fetch* (x) can be taken into account using dimensionless notation as follows:

$$\theta = g \cdot \text{time}/u$$

$$\xi = g \cdot x/u^2$$

where

u wind speed at 10 m above the surface of the water, averaged over 1 h ($u = V_{1h}$, see Table 2.9)

The dimensionless peak frequency can be calculated as follows:

$$\nu = \frac{\omega_p}{2 \cdot \pi} \cdot \frac{u}{g} = \text{Max.}\left(0.16; \quad 2.84 \cdot \xi^{-0.3}; \quad 16.8 \cdot \theta^{-3/7}\right)$$

From this it follows that the *peak period* (T_p) is

$$T_p = \frac{1}{\nu} \cdot \frac{u}{g}$$

The following format can be used for the significant *wave height* (H_s):

$$H_{s,JONSWAP,wind} = 0.0094 \cdot \nu^{-5/3} \cdot \frac{u^2}{g}$$

Three JONSWAP spectra for various wind speeds are plotted in Figure 2.26.

The constant parameters are the fetch (x = 600 km), the time (=12 h) and the characteristic dimensions for the width of the spectrum ($\sigma_a = 0.07$ and $\sigma_b = 0.09$).

Table 2.11 lists the associated parameters.

The TMA spectrum is a modified form of the JONSWAP spectrum and depends on the depth of water. It can be used for the wind-generated sea state in a finite depth of water:

$$S_{\zeta,TMA}(\omega) = S_{\zeta,JONSWAP}(\omega) \cdot \Phi_k(\omega_d) \quad \text{and} \quad \omega_d = \omega \cdot \sqrt{\frac{d}{g}}$$

Table 2.11 JONSWAP spectra for three wind speeds

$U^*_{10\,m}$ [m/s]	α	γ	ω_p [s^{-1}]	f_p [s^{-1}]	T_p [s]	m_0 [m^2]	σ [m]	H_s [m]
25	0.012429	2.734	0.638	0.102	9.9	2.03	1.42	5.7
20	0.012020	2.533	0.725	0.115	8.7	1.14	1.07	4.3
15	0.011505	2.292	0.854	0.136	7.4	0.54	0.74	2.9

with the following transformation factor Φ_k:

$$\Phi_k(\omega_d) = \begin{cases} 0.5 \cdot \omega_d^2 & \text{for} \quad \omega_d \leq 1 \\ 1 - 0.5 \cdot (2 - \omega_d)^2 & \text{for} \quad 1 < \omega_d < 2 \\ 1 & \text{for} \quad \omega_d \geq 2 \end{cases}$$

The result of using this approach is that deep-water conditions may be assumed for $\omega_d \geq 2$, that is for $d \geq g \cdot T^{2/}\pi^2$.

2.5.7 Long-term statistics for the sea state

The long-term behaviour of the sea state can be described by means of wave distribution diagrams (scatter diagrams) which give the frequency of individual short-term sea states. Figure 2.27 shows an example of a scatter diagram for the North Sea.

The significant wave height is denoted by H_s (or $H_{1/3}$), the wave period by T_z (or T_0); H_i or H_j specify the total of the relative frequencies of the *sea states* (duration generally $T_{s0} = 3$ h [24]) of the respective class T_z or H_s. The time-related probability density for the respective class is represented by f_i and f_j [23].

However, results from numerical studies can also be used, for example those developed for the German Bight by Zielke *et al.* [18]. Such simulation computations can be used to draw up, for example, wave distribution diagrams for any locations in the area under investigation [6].

The evaluation of sea state data has shown that the *long-term statistics* for large extreme values H_s can be described with the help of a *Gumbel distribution*:

$$F_{extr}(H_s) = \exp\{-\exp[-a \cdot (H_s - u)]\}$$

It is possible to calculate the following *distribution parameters* from the standard deviation $\sigma_{H,extr}$ (from the long-term statistics, e.g. Figure 2.27) and the modal value u:

$$a = \frac{\pi}{\sqrt{6}} \cdot \frac{1}{\sigma_{H,extr}} = \frac{1.28255}{\sigma_{H,extr}} \quad \text{and} \quad m_{H,extr} = u + \frac{\gamma}{a} = u + \frac{0.577216}{a}$$

H_s class i [m]	T_z class j [s] <4	4..5	5..6	6..7	7..8	8..9	9..10	10..11	11..12	H_i	f_i
0..1	19	86	94	41	10	2				251	288
1..2	3	49	121	99	40	10	2			322	324
2..3	1	17	63	73	40	13	3	1		210	198
3..4		6	27	39	26	10	3	1		111	100
4..5		2	11	19	14	6	2	1		55	48
5..6		1	4	9	7	4	1			26	22
6..7			2	4	4	2	1			13	11
7..8			1	2	2	1	1			7	6
8..9				1	1	1				3	2
9..10				1	1					2	2
H_j	23	160	321	287	144	49	13	3	0	1000	1000
f_j	38	208	341	257	112	33	8	2	0	1000	

Fig. 2.27 Scatter diagram for the open North Sea (after [21])

Gumbel distributions can also be used for other environmental actions, for example wind or snow, and so employing such distributions is a great advantage for sea state actions, primarily with respect to the combinations of actions that are to be applied and the definition of partial safety and combination factors. Characteristic of this distribution is the constancy of the standard deviation $\sigma_{H,extr}$ irrespective of the reference period considered.

A wave distribution diagram (e.g. Figure 2.27) is always valid for a defined period of observation (reference period T_1). It is therefore necessary to convert this to the design working life (reference period T_N) of the structure at the planning stage. The maximum values in the reference period $T_N = N \cdot T_1$ can be obtained through exponentiation [25]:

$$\begin{aligned} F_{extr,N}\left(H_{s,N}\right) = \left[F_{extr,1}(H_s)\right]^N &= [\exp(-\exp(-a \cdot (H_s - u_1)))]^N \\ &= \exp[N \cdot (-\exp(-a \cdot (H_s - u_1)))] \\ &= \exp(-\exp(-a \cdot (H_s - u_1) + \mathrm{In}(N))) \\ &= \exp\left(-\exp\left(-a \cdot \left(H_{s,N} - u_N\right)\right)\right) \end{aligned}$$

This means that the Gumbel distributions develop through a displacement of ln(N)/a on the H_s axis. Accordingly, the modal value u_1, or rather the mean value $m_{H,1}$, is also displaced with respect to the initial distribution. On the other hand, the value of the standard deviation $\sigma_{H,extr}$ does not change. We therefore get

$$u_N = u_1 + \frac{\ln(N)}{a} = u_1 + \ln(N) \cdot \frac{\sqrt{6}}{\pi} \cdot \sigma_{H,extr} \quad \text{and} \quad m_{H,N} = m_{H,1} + \frac{\ln(N)}{a}$$

for the maximum values.

The statistical evaluation of the long-term wave distribution using the example of Figure 2.27 with the help of a linear regression analysis leads to Figure 2.28.

The regression line has the following form:

$$y = b + m \cdot H_s = a \cdot (H_s - u) = -\ln(-\ln(F_{extr}(H_s)))$$

$$a = m = 0.7963\ \mathrm{m}^{-1}$$

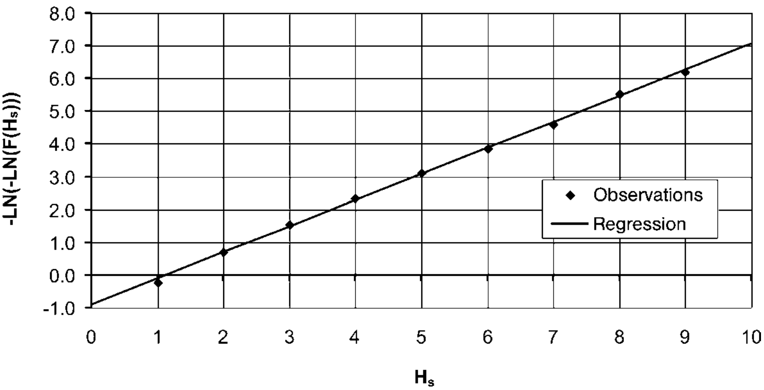

Fig. 2.28 Regression analysis based on a Gumbel distribution

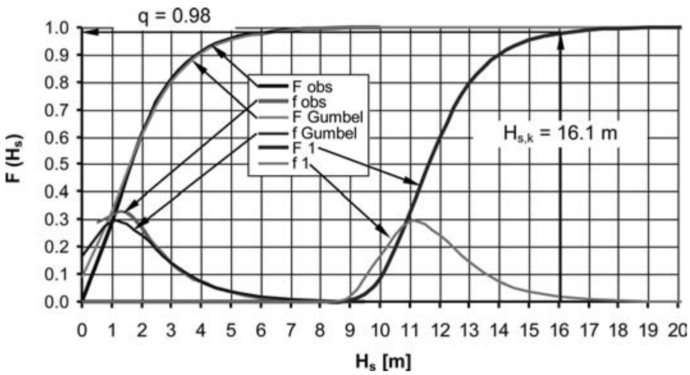

Fig. 2.29 Comparison of the observed and Gumbel-adapted distribution functions and densities plus the 1-year extreme values

and

$$u = -b/a = +0.9039/0.7963 = 1.1351\,\mathrm{m}$$

From this it follows that the standard deviation for the long-term wave distribution is

$$\sigma_{H,extr} = \frac{\pi}{\sqrt{6}} \cdot \frac{1}{a} = \frac{1.28255}{0.79628} = 1.61\,\mathrm{m}$$

The observed data ("obs") and the associated Gumbel values for the distribution function and density are plotted in Figure 2.29. As we assume that the observed quasi-steady sea states (H_s) are related to $T_{s0} = 3\,\mathrm{h}$, they were supplemented by the values for 1 year displaced by "$\ln(N_i)/a$". The following applies here [24, 11]:

$$N_i = 8760\,\mathrm{h/a}/3\,\mathrm{h} = 2920$$

We can see from Figure 2.29 that the observed data agrees very well with the Gumbel distribution in the relevant range of high values. The 98% quantile value related to one year is generally used as the characteristic value:

$$u_1 = u_{3h} + \ln(N)/a = 1.1351 + \ln(2.920)/0.7963 = 11.16\,\mathrm{m}$$

$$H_{s;1;0.98} = H_{s,k} = F^{-1}_{extr,1}(0.98) = u_1 - \frac{1}{a} \cdot \mathrm{In}(-\mathrm{In}(0.98)) = 11.16 + \frac{3.902}{0.7963} = 16.06\,\mathrm{m}$$

Extrapolating for longer reference periods – 5 years for extreme wave loads according to [24] or 50 years for the design working life of an offshore structure – is only permissible when the observed sea state data for extreme values is available for longer periods of time – at least 5 or 20 years. It should be remembered in this context that wind-generated waves depend on the climatic conditions of the seasons, especially the frequency of severe storms [17]. However, assuming that the observed 1-year extreme values correspond to the Gumbel distribution computed above, then the result is the Gumbel distributions for the 5- and 50-year extreme values shown in Figure 2.30.

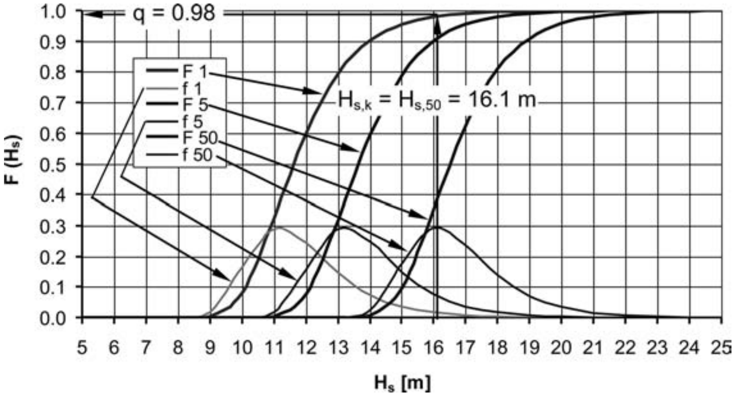

Fig. 2.30 Comparison of the 1-, 5- und 50-year extreme values

2.5.8 Extreme sea state values

Statistics-based statements regarding the extreme values of wave heights within a finite sample are important for the design of marine structures. If we consider the sample to be the chronological sequence of wave heights H_1, H_2, . . . , H_n determined within a certain period Ts, then these values exhibit a *Rayleigh distribution* for the *short-term* (see Section 2.5.6, Figure 2.24) or a *Weibull distribution*, or even a *Gumbel distribution*, for the *long-term* [24].

Putting the H_i values in order of their magnitude gives us the sample (H_1, H_2, . . . , H_n) with $H_1 < H_2 < \ldots < H_n$. Whereas the same distribution, that is the statistical population (e.g. Rayleigh), applies to all values prior to organising them, the ordered values obey various laws depending on their position within the order. Particularly interesting here is the extreme value distribution f (H_n), that is the distribution of the maximum value of all maxima. By way of a simplification, it may be assumed that the individual maxima are statistically independent of each other.

The probability that the *solitary* wave height H_i does not exceed a given limit value H^* can be expressed as follows:

$$P(H_i \leq H^*) = F(H^*)$$

The probability that *all* n maxima H_i do not exceed the value H_n^* can then be formulated thus:

$$P_{extr}\left[\mathrm{Max}(H_1, H_2, \ldots, H_n) = H_n \leq H_n^*\right] = F_{extr}\left(H_n^*\right) = \left[F\left(H_n^*\right)\right]^n$$

Differentiation gives us the probability density:

$$f_{extr}\left(H_n^*\right) = n \cdot \left[F\left(H_n^*\right)\right]^{n-1} \cdot f\left(H_n^*\right)$$

If the statistical population of the wave heights of a short-term sea state exhibits a Rayleigh distribution, then the extreme value distribution (expressed in dimensionless form) is

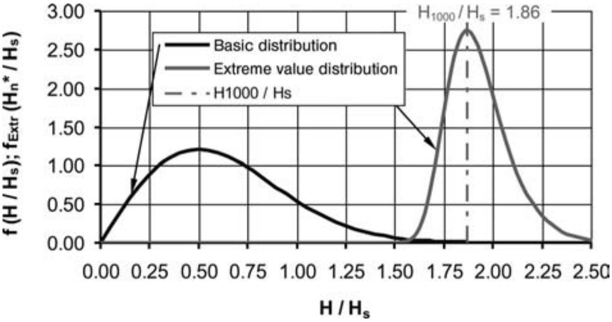

Fig. 2.31 Calculating the design extreme value from the short-term statistics

$$F_{extr}\left(\frac{H_n}{H_s}\right) = \left\{1 - \exp\left[-2 \cdot \left(\frac{H_n}{H_s}\right)^2\right]\right\}^n \quad \text{and}$$

$$f_{extr}\left(\frac{H_n}{H_s}\right) = n \cdot \left\{1 - \exp\left[-2 \cdot \left(\frac{H_n}{H_s}\right)^2\right]\right\}^{n-1} \cdot 4 \cdot \frac{H_n}{H_s} \cdot \exp\left[-2 \cdot \left(\frac{H_n}{H_s}\right)^2\right]$$

An approximate modal value for n is given by

$$\widehat{H}_n/H_s = \sqrt{\ln(n)/2}$$

Figure 2.31 shows an example of the basic distribution of the wave heights (Rayleigh) as well as the extreme value distribution for a sample of size $n = 1000$. The H_{1000} value is interpreted as the most likely extreme value within a 3 h storm (*short-term statistics!*). It amounts to

$$\widehat{H}_{n=1000} = \sqrt{\ln(n)/2} \cdot H_s = 1.86 \cdot H_s$$

Using the example of Figures 2.29 and 2.30 ($H_{s,k} = H_{s,50}$ from the *long-term statistics*) results in a characteristic value for the maximum wave height amounting to

$$H_{max,k} = H_{max,50} = 1.86 \cdot H_{s,50} = 1.86 \cdot 16.06 = 29.9\,m$$

The water depth should be used to check whether the *breaking criterion* has been exceeded!

Very high wave height values often have to be considered in connection with detailed design tasks. The form of the extreme value distribution depends not on the central area of the basic distribution, but more on the way it converges to 1 for high values of H^* (rare end of basic distribution).

The extreme value distribution for large samples ($n > 1000$) is frequently approximated with *Davenport's formula* (for details see [17]). The Davenport extreme value distributions are practically identical with the corresponding Rayleigh distributions raised to the power of n. *Asymptotic extreme value distributions* such as the *Gumbel distribution* (see Section 2.5.7) represent another

approximation for very large values of n.
Ref. [11] contains the following values for the *design wave*:[2)]

– Characteristic value of *design wave period*:

$$11.1 \cdot \sqrt{H_{s,50}/g} \leq T_D \leq 14.3 \cdot \sqrt{H_{s,50}/g} \quad \leq 25\,s$$

where $H_{s,50}$ is the significant wave height for a 50-year return period

– Characteristic value of *design wave height*:

$$H_D = H_{max,50} = H_{s,50} \cdot \sqrt{0.5 \cdot \ln(T_{ref}/T_D)}$$

where T_{ref} is the 3 h reference period ($= 3 \cdot 60 \cdot 60 = 10\,800\,s$)

The distribution function (*Weibull* or *Gumbel*) can be used as an alternative. The smaller value governs.

Accordingly, the value for the aforementioned example is

$$11.1 \cdot \sqrt{16.06/9.81} = 11.1 \cdot 1.28 = 14.2\,s \leq T_D \leq 14.3 \cdot 1.28 = 18.3\,s \quad \leq 25\,s$$

$$\frac{T_{ref}}{T_D|_{mean}} = \frac{10\,800}{(14.2 + 18.3)/2} = 665$$

$$H_D = \widehat{H}^{n=665} = H_{s,50} \cdot \sqrt{\ln(665)/2} = 16.06 \cdot 1.80 = 29.0\,m$$

2.5.9 Breaking waves

The height of breaking waves depends on the depth of water and the slope of the seabed. Basically, it is not necessary to consider any wave heights higher than those of breaking waves (see [11] 4.2.3.1.5).

In a limited depth of water, the wave kinematics can change considerably with respect to the deep-water conditions. Wave crests are much higher and shorter than wave troughs, and the wave profile is asymmetric in such a way that the front flank of the wave crest is steeper than its rear flank. In addition, the distribution function for the wave heights no longer corresponds to a Rayleigh distribution.

In shallow water (index "sh") the empirical limit to the wave height (H_{lim}) is

$$H_{lim,sh} \leq 0.78 \cdot d$$

where d is the local depth of water.

However, waves can break in deep water (index "dp") as well, with a theoretical steepness of 1/7 related to the wavelength (λ):

$$H_{lim,dp} \leq 1/7 \cdot \lambda$$

[2)] The "*design*" *values* are *characteristic values* in the context of the safety concept!

In simplified form, the height of the breaking wave (H_B) can be assumed to be as follows:

$$H_B = \frac{b}{\frac{1}{d} + \frac{a}{g \cdot T^2}}$$

where

$a = 44 \cdot [1 - \exp(-19\ s)]$
$b = 1.6/[1 + \exp(-19\ s)]$

s slope of seabed, $s = \tan\beta$
d depth of water
T wave period

Three types of breaking wave are possible: spilling, plunging and surging. The boundaries between these types depend on the wave height in deep water (H_0), the height of the breaking wave (H_B) and the undisturbed wavelength (λ_0). For more details see [11] 4.2.3.1.5.

2.6 Hydrodynamic analysis

2.6.1 General

The following considerations are valid for the actions of the sea state on a structure permanently anchored to the seabed. Movements, however, can arise from vibrations due to the excitation of the structure, and such vibrations are very important for the design of offshore wind turbines.

The hydrodynamic problem is simplest when we can consider the behaviour of the structure in the sea state as linear. Assuming a linear or linearised structural behaviour means that the structure's response to the natural sea state is obtained through the superposition of the responses to its individual components (primary waves). When carrying out a calculation in the frequency domain, we presume that a Gaussian process can be unambiguously described by its spectrum. This applies to both the Gaussian process for the excitation (sea state) and to that for the response. There is a simple relationship between these spectra which is valid for component i:

$$S_i(\omega) = [Y_i(\omega)]^2 \cdot S_\zeta(\omega)$$

where

$S_i(\omega)$ spectrum of structural response
$Y_i(\omega)$ transfer function
$S_\zeta(\omega)$ spectrum of sea state excitation

The transfer function is defined as the ratio between the amplitudes of the response and the excitation, with its square being able to be considered as the transfer function of the energy.

The type and size of the arrangement of the structure relative to the wave parameters have a decisive influence on the mechanism of the sea state actions. Inertia, drag and diffraction forces occur in this context.

- Inertia and drag effects are critical for structures that are slender in hydrodynamic terms and have structural member dimensions (D) that are small in relation to the wavelength (λ) ($D/\lambda \leq 1/5$, for example jackets, tripods, monopiles). Their action effects are therefore considered semi-empirically (see Section 2.6.2).
- The inertia and diffraction effects dominate in the case of structures that are compact in hydrodynamic terms ($D/\lambda > 1/5$, for example gravity bases). Their action effects can be calculated really quite accurately using potential theory with approximations based on diffraction theory (see Sections 2.6.3, 2.6.4, 2.6.5 and 2.6.7).
- *Non-linear effects*, for example viscosity-related drag forces, wave forces of a higher order, loads due to waves with a finite steepness or large deformations, may not be neglected when it is necessary to consider sea state actions that exhibit a strong non-linear dependence on the wave height (see Section 2.6.6).

Depending on the structure to be designed, the design sea state can either be entered as a *characteristic solitary wave* (deterministic method), considered as a characteristic wave time series, from which a time series of loads on the structure is generated (stochastic method), or be incorporated as a total distribution in order to determine the probabilities of failure for various limit states (probabilistic method).

Deterministic design methods are generally favoured in practice [26], and these will be dealt with below.

2.6.2 Morison formula

Wave loads on narrow bodies are mostly calculated with the help of the *Morison formula*. Let us consider a rigid vertical cylinder in a harmonic primary wave (Figure 2.32). The wave force per unit length of the cylinder is then expressed as the sum of an inertia force and an unsteady drag force (index I: inertia; D: drag):

$$\frac{dF_x(t)}{dz} = \frac{dF_{Ix}(t)}{dz} + \frac{dF_{Dx}(t)}{dz} = c_M \cdot \rho \cdot \frac{\pi \cdot D^2}{4} \cdot \frac{\partial u(t)}{\partial t} + c_D \cdot \frac{1}{2} \cdot \rho \cdot D \cdot |u(t)| \cdot u(t)$$

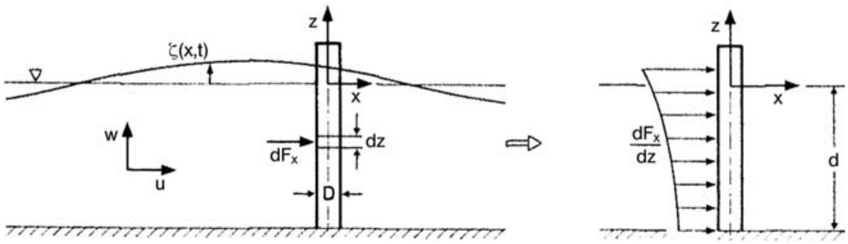

Fig. 2.32 Wave forces on a pile, notation [17]

where

ρ density of water (= 1.0 t/m^3)
u horizontal (orbital) velocity in primary wave
D diameter of vertical cylinder
c_M inertia coefficient
c_D drag coefficient

The wave theories are only defined as far as the still water level ($z = 0$). Stretching methods, for example "Wheeler stretching", are used to modify the particle kinematics to account for the momentary displacement of the surface of the water (under the wave crest and above still water level, see Figure 2.32):

$$z_s = (z - \zeta)/(1 + \zeta/d)$$

The total force on the cylinder is given by integrating over its height:

$$F_x(t) = \int_{z=-d}^{z=\zeta(t)} \frac{dF_x(t)}{dz} \cdot dz$$

Considering just the local ($\partial u/\partial t$) instead of the substantial acceleration (Du/dt) is permissible here because the convective acceleration is negligible with respect to the local acceleration for the *Airy wave* investigated initially. In the case of waves of low steepness (H/λ) and a large relative depth of water (d/λ) or with a low H/d [= $(H/\lambda)/(d/\lambda)$] ratio, the still water level ($z = 0$) is taken to be the upper bound of the integral. Using the notation $|u| \cdot u$ ($= u^2 \cdot \text{sign}\, u$) guarantees that the change in direction of the velocity component is taken into account. The coefficient c_D contains both the form drag and the friction resistance.

The inertia force acting on the body is the sum of:

– the *pressure gradient force* caused by the undisturbed wave field ($= \rho \cdot V \cdot \partial u/\partial t$; V: *displacement*), and
– the *acceleration drag* ($= a_{xx} \cdot \partial u/\partial t = c_a \cdot \rho \cdot V \cdot \partial u/\partial t$; $c_a = a_{xx}/(\rho \cdot V)$: *hydrodynamic mass coefficient*).

The following applies for the inertia force acting:

$$F_{Ix} = \rho \cdot V \cdot \frac{\partial u}{\partial t} + c_a \cdot \rho \cdot V \cdot \frac{\partial u}{\partial t} = (1 + c_a) \cdot \rho \cdot V \cdot \frac{\partial u}{\partial t} = c_M \cdot \rho \cdot V \cdot \frac{\partial u}{\partial t}$$

where $c_M = 1 + c_a$

The $\rho \cdot V \cdot \partial u/\partial t$ component is the *Froude-Kryloff force*. Applying the equation for F_{Ix} to a cylinder element of length "dz", that is for $dV = (\pi^2 \cdot D^2/4) \cdot dz$, gives us the first term in the Morison formula from the following force:

$$dF_{Ix} = c_M \cdot \rho \cdot \frac{\pi \cdot D^2}{4} \cdot dz \cdot \frac{\partial u}{\partial t}$$

The Morison formula is widely used these days for calculating the hydrodynamic loads on marine structures with slender cylindrical members (e.g. piles, monopiles, jackets, legs of gravity structures, pipelines, risers, cables, etc.). However, the evaluation of a large number of measurements has revealed that the Morison formula in the above form can only be used when its c_M and c_D coefficients are neither constants nor variables that are independent of each other. It can be shown that the coefficients depend not only on the roughness of the surface of the body but also on two dimensionless parameters. The latter are defined as follows for a cylinder of diameter D acted upon by a primary wave:

– Reynolds number: $Re(z) = \dfrac{\bar{u}(z) \cdot D}{\nu}$
– Keulegan-Carpenter number: $N_{KC}(z) = \dfrac{\bar{u}(z) \cdot T}{D}$

where

$\bar{u}(z)$ amplitude of orbital velocity at height z
T period
ν kinematic viscosity ($1.3 \cdot 10^{-6}$ m²/s at +10 °C [27])

Applying the Morison formula in practice requires special care when it comes to specifying the c_M and c_D coefficients. For further details of this topic please refer to [17].

Tables 2.12 and 2.13 can be used for practical applications. The critical parameters are the Keulegan-Carpenter number at the still water level ($z = 0$) and the description of the properties of the surface of the structural member instead of the Reynolds number.

Table 2.12 Inertia coefficients c_M for the Morison formula (after [24])

c_M	Surface finish of structural member	
N_{KC} ($z = 0$)	smooth	rough
$2 \leq N_{Kc} \leq 6$	2.0	2.0
$6 < N_{KC} < 30$	linear interpolation	
$N_{KC} \geq 30$	1.65	1.2

Table 2.13 Drag coefficients c_D for the Morison formula (after [24])

c_D	Surface finish of structural member	
N_{KC} ($z = 0$) a)	smooth	rough
$2 \leq N_{Kc} \leq 6$	0.65	1.05
$6 < N_{KC} < 13$	linear interpolation	
$N_{KC} = 13$	0.85	1.50
$13 < N_{KC} < 30$	linear interpolation	
$N_{KC} \geq 30$	0.65	1.05

a) The drag term may be neglected when $N_{KC} < 2$.

The following relationships apply for a primary wave (see also Section 2.5.3):

$$\zeta(x, t) = \frac{H}{2} \cdot \cos(k \cdot x - \omega \cdot t)$$

$$u = \frac{\partial \Phi(x, z, t)}{\partial x} = \omega \cdot \frac{H}{2} \cdot \frac{\cosh\left[k \cdot (z + d)\right]}{\sinh(k \cdot d)} \cdot \cos(k \cdot x - \omega \cdot t)$$

$$\dot{u} = \frac{\partial u}{\partial t} = \frac{\partial^2 \Phi}{\partial x \partial t} = \omega^2 \cdot \frac{H}{2} \cdot \frac{\cosh\left[k \cdot (z + d)\right]}{\sinh(k \cdot d)} \cdot \sin(k \cdot x - \omega \cdot t)$$

Substituting in the Morison formula results in

$$\frac{dF_x(t)}{dz} = \frac{dF_{Ix}(t)}{dz} + \frac{dF_{Dx}(t)}{dz} = c_M \cdot \rho \cdot \frac{\pi \cdot D^2}{4} \cdot \omega^2 \cdot \frac{H}{2} \cdot \frac{\cosh\left[k \cdot (z + d)\right]}{\sinh(k \cdot d)} \cdot \sin(k \cdot x - \omega \cdot t)$$
$$+ c_D \cdot \frac{1}{2} \cdot \rho \cdot D \cdot \left\{\omega \cdot \frac{H}{2} \cdot \frac{\cosh\left[k \cdot (z + d)\right]}{\sinh(k \cdot d)}\right\}^2 \cdot \cos(k \cdot x - \omega \cdot t) \cdot |\cos(k \cdot x - \omega \cdot t)|$$

If we are dealing with a cylinder diameter that is narrow in hydrodynamic terms, that is the diameter of the cylinder is relatively small in relation to the wavelength, then the orbital velocity and acceleration hardly change over the width of the cylinder. Using the values in the position of the cylinder axis ($x = 0$) is then permissible. Therefore, for $x = 0$ it follows that

$$\frac{dF_x(t)}{dz} = \frac{dF_{Ix}(t)}{dz} + \frac{dF_{Dx}(t)}{dz} = -c_M \cdot \rho \cdot \frac{\pi \cdot D^2}{4} \cdot \omega^2 \cdot \frac{H}{2} \cdot \frac{\cosh[k \cdot (z + d)]}{\sinh(k \cdot d)} \cdot \sin(\omega \cdot t)$$
$$+ c_D \cdot \frac{1}{2} \cdot \rho \cdot D \cdot \left\{\omega \cdot \frac{H}{2} \cdot \frac{\cosh[k \cdot (z + d)]}{\sinh(k \cdot d)}\right\}^2 \cdot \cos(\omega \cdot t) \cdot |\cos(\omega \cdot t)|$$

Example of application:

Parameters: $H = 10\,m$, $\lambda = 150\,m$, $D = 2.0\,m$, $d = 30\ m$

$$k = 2 \cdot \pi/\lambda = 2 \cdot \pi/150 = 0.0419\,m^{-1}$$

It follows from the dispersion equation that

$$\omega = [g \cdot k \cdot \tanh(k \cdot d)]^{0.5} = [9.81 \cdot 0.0419 \cdot \tanh(0.0419 \cdot 30)]^{0.5} = 0.591\ s^{-1}$$

$$T = 2 \cdot \pi/\omega = 2 \cdot \pi/0.591 = 10.63\ s$$

$$u(x = 0; z = 0; t = 0) = 0.591 \cdot \frac{10}{2} \cdot \frac{\cosh\left[0.0419 \cdot (0 + 30)\right]}{\sinh(0.0419 \cdot 30)} \cdot 1.0 = 3.48\ m/s$$

$$Re(z = 0) = \bar{u}(z = 0) \cdot D/\nu = 3.48 \cdot 2.0/\left(1.3 \cdot 10^{-6}\right) = 5.35 \cdot 10^6$$

$$N_{KC}(z = 0) = \bar{u}(z = 0) \cdot T/D = 3.48 \cdot 10.63/2.0 = 18.5\ (< 30)$$

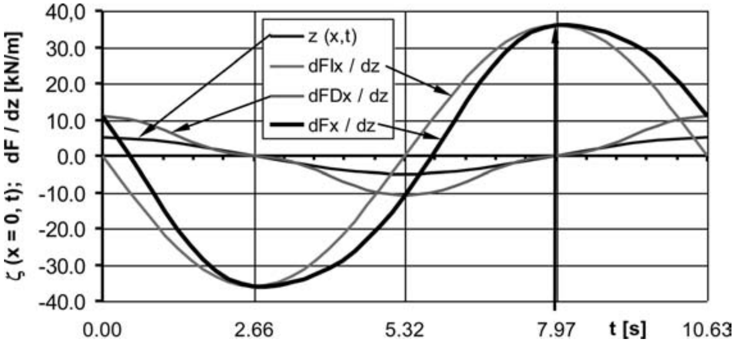

Fig. 2.33 Primary wave with hydrodynamic forces on a vertical cylinder (x = 0) at the still water level (z = 0)

According to Tables 2.12 and 2.13 (assuming a structural member with a smooth surface), it follows that

$$c_M = 1.82 \quad \text{and} \quad c_D = 0.77$$

Figure 2.33 shows the plots of the hydrodynamic forces dF_x (x = 0, z = 0, t)/dz and their components, the inertia force dF_{Ix} (0, 0, t) and the drag force dF_{Dx} (0, 0, t)/dz, with respect to the wave contour ζ (x = 0, t).

Figure 2.34 shows the course of the hydrodynamic force dF_x (x = 0, z, t)/dz over the height of the vertical cylinder, from z = 0 to z = −30 m (seabed), during the phase t = 7.97 s (φ = −90°); the maximum resultant effect is shown here. In this example only the inertia forces are relevant in this phase.

Placing the amplitudes of the drag force and the inertia force in relationship with one another gives us

$$R = \left| \frac{\left(\frac{dF_{Dx}(t)}{dz} \right)_0}{\left(\frac{dF_{Ix}(t)}{dz} \right)_0} \right|_{z=0} = \frac{1}{\pi} \cdot \frac{c_D}{c_M} \cdot \frac{H}{D} \cdot \frac{\cosh(k \cdot d)}{\sinh(k \cdot d)} \sim \frac{c_D}{c_M} \cdot \frac{H/\lambda}{D/\lambda}$$

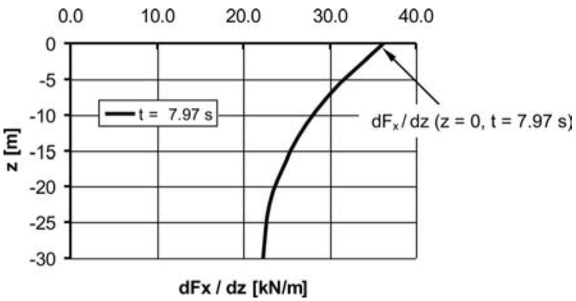

Fig. 2.34 Hydrodynamic force acting on a vertical cylinder

We can see from this that with constant coefficients c_D and c_M, the drag force for large D/λ values or a small wave steepness H/λ or also a small H/D ratio is small compared with the inertia force.

The extent to which the wave force depends on the D/λ ratio can be calculated by solving the *diffraction problem*. The result according to the *diffraction theory of MacCamy and Fuchs* [29] allows us to derive the following rules for vertical cylinders (see Sections 2.6.2, 2.6.5 and Figure 2.42):

- The Morison formula applies to bodies that are narrow (slender) in hydrodynamic terms ($D/\lambda < 1/5$).
- Potential theory can be expected to supply reliable results for large-volume, compact structures ($D/\lambda > 1/5$). This situation corresponds to $N_{KC} < 2$, see above [24]. The orbital velocity at the still water level u ($z = 0$) gives us the Keulegan-Carpenter number:

$$N_{KC}(z) = \frac{\bar{u}(z=0) \cdot T}{D} = \omega \cdot \frac{H}{2} \cdot \frac{\cosh[k \cdot d]}{\sinh(k \cdot d)} \cdot \frac{T}{D} = \pi \cdot \frac{H}{D} \cdot \frac{1}{\tanh(k \cdot d)}$$

For $N_{KC} < 2$ it follows that

$$\frac{H}{D} < \frac{2}{\pi} \cdot \tanh(k \cdot d) \approx 0.5$$

In principle, the Morison formula may be used to calculate the forces caused by waves of finite steepness as well. In such cases the substantial acceleration (Du/dt) should be used instead of the local acceleration ($\partial u/\partial t$), and the integration of the resulting actions should be carried out over the momentarily wetted surface of the structural component.

In many cases the Morison formula must be applied to cylindrical structural members inclined at an angle. To do this, a vectorial formulation of the Morison formula is necessary:

$$\vec{f} = c_M \cdot \rho \cdot \frac{\pi \cdot D^2}{4} \cdot \dot{\vec{v}}_N + c_D \cdot \frac{1}{2} \cdot \rho \cdot D \cdot \left|\vec{v}_N\right| \cdot \vec{v}_N$$

where $\vec{f}$ is the force vector, $\vec{v}_N$ the velocity vector and $\dot{\vec{v}}_N$ the acceleration vector, all perpendicular to the axis of the structural member. The following relationships apply [30]:

$$\vec{v}_N = \vec{e} \times \left(\vec{v} \times \vec{e}\right) \quad \text{and} \quad \dot{\vec{v}}_N = \vec{e} \times \left(\dot{\vec{v}} \times \vec{e}\right)$$

where

$\vec{v} = \{u_x; u_y; w\}$ orbital velocity vector
$\dot{\vec{v}} = \{\dot{u}_x; \dot{u}_y; \dot{w}\}$ orbital acceleration vector (Figure 2.35)
$\vec{e} = \{e_x; e_y; e_z\}$ unit vector in direction of member axis (Figure 2.35)

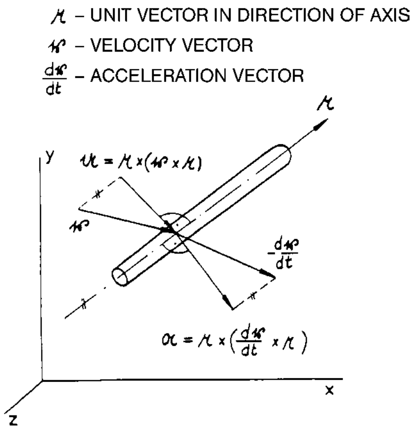

Fig. 2.35 Vectors for the bar element [30]

The evaluation of the above vector products for the case of a planar flow field ($u_x = u$; $u_y = 0$; w) – at coordinates {x, z} – results in (in component notation):

$$\begin{aligned}
v_{N,x} &= u - e_x \cdot (e_x \cdot u + e_z \cdot w); \quad & \dot{v}_{N,x} &= \dot{u} - e_x \cdot (e_x \cdot \dot{u} \cdot e_z \cdot \dot{w}) \\
v_{N,y} &= -e_y \cdot (e_x \cdot u + e_z \cdot w); \quad & \dot{v}_{N,y} &= -e_y \cdot (e_x \cdot \dot{u} + e_z \cdot \dot{w}) \\
v_{N,z} &= w - e_z \cdot (e_x \cdot u + e_z \cdot w); \quad & \dot{v}_{N,z} &= \dot{w} - e_z \cdot (e_x \cdot \dot{u} + e_z \cdot \dot{w})
\end{aligned}$$

One important issue is ascertaining the statistical distribution of the force acting on a cylindrical component during the natural sea state. Assuming that the sea state function ζ (t) is described by a Gaussian process with the following variance:

$$\sigma_\zeta^2 = m_0 = \int_0^\infty S_\zeta(\omega) \cdot d\omega$$

then the velocity u and the acceleration $\dot{u}$ are also described by Gaussian processes. For details of this see [17].

2.6.3 Potential theory method – linear motion behaviour

The velocity potential of the flow field caused by the presence of a body can be formulated as follows:

$$\Phi(x, y, z, t) = \Phi_0(x, y, z, t) + \Phi_S(x, y, z, t)$$

where

Φ_0 undisturbed primary wave potential
Φ_S perturbation potential

Within the scope of a linear or linearised calculation of the hydrodynamic forces for a floating body, it is possible to split the perturbation potential into *diffraction* and *radiation* problems:

$$\Phi_S(x, y, z, t) = \Phi_{diff}(x, y, z, t) + \sum_{j=1}^{6} \dot{s}_{j0} \cdot \Phi_j(x, y, z, t)$$

where

Φ_{diff} perturbation potential for the flow around the body held in the primary wave
Φ_j potential of the flow field that results from the enforced motion of the body in direction “j” with velocity amplitude “1” in the originally smooth water
$\dot{s}_{j0}$ complex amplitude of velocity of body motion in direction j (j = 1, 2, 3: translations; j = 4, 5, 6: rotations)

The superposition of the radiation and these solutions to the boundary value problems of the diffraction leads to a solution for the floating body according to potential theory.

Only the *diffraction problem* has to be solved for *offshore structures* permanently anchored to the seabed. The total potential describing the interaction between wave and structure is therefore expressed as follows:

$$\Phi(x, y, z, t) = \Phi_0(x, y, z, t) + \Phi_{diff}(x, y, z, t)$$

Both potentials are defined between still water level (z = 0) and seabed (z = −d). The perturbation potential oscillates harmonically with the frequency of the incident wave ($\omega = 2 \cdot \pi \cdot f$). Therefore, it follows that

$$\Phi_{diff}(x, y, z, t) = \varphi_{diff}(x, y, z) \cdot e^{-i \cdot \omega \cdot t}$$

where

φ_{diff} (x, y, z) steady-state part of perturbation potential

The perturbation potential must always satisfy the *Laplace differential equation*:

$$\Delta\Phi_{diff}(x, y, z, t) = 0 \quad \text{or} \quad \Delta\varphi_{diff}(x, y, z, t) = 0$$

Furthermore, it must satisfy the following boundary conditions:

– the combined linearised boundary condition at the surface of the water

$$\frac{\partial^2 \Phi_{diff}}{\partial t^2} + g \cdot \frac{\partial \Phi_{diff}}{\partial z} = 0 \quad \text{or} \quad -\omega^2 \cdot \varphi_{diff} + g \cdot \frac{\partial \Phi_{diff}}{\partial z} = 0$$

– and the kinematic boundary condition at the seabed

$$\frac{\partial \Phi_{diff}}{\partial z} = 0 \quad \text{or} \quad \frac{\partial \varphi_{diff}}{\partial z} = 0$$

Note:

The Laplace differential equation and the boundary conditions given above are satisfied in accordance with the definition by the potential of the undisturbed primary wave (Φ_0, see Section 2.5.3).

In addition, the perturbation potential must satisfy the Sommerfeld general radiation condition:

$$\lim_{r\to\infty} \sqrt{r} \cdot \left(\frac{\partial \varphi_{diff}}{\partial r} - \frac{\omega^2}{g} \cdot \varphi_{diff} \right) = 0 \quad \text{where} \quad r = \sqrt{x^2 + y^2 + z^2}$$

The kinematic boundary condition must be satisfied for the body held in the wave, that is the velocity component normal to the surface of the body must disappear with respect to the total potential ($\Phi_0 + \Phi_{diff}$):

$$\left.\frac{\partial \Phi}{\partial n}\right|_{S_0} = \left.\frac{\partial (\Phi_0 + \Phi_{diff})}{\partial n}\right|_{S_0} = 0 \quad \text{or} \quad \left.\frac{\partial \varphi}{\partial n}\right|_{S_0} = \left.\frac{\partial (\varphi_0 + \varphi_{diff})}{\partial n}\right|_{S_0} = 0$$

It follows from this that

$$\left.\frac{\partial \Phi_{diff}}{\partial n}\right|_{S_0} = -\left.\frac{\partial \Phi_0}{\partial n}\right|_{S_0} \quad \text{or} \quad \left.\frac{\partial \varphi_{diff}}{\partial n}\right|_{S_0} = -\left.\frac{\partial \varphi_0}{\partial n}\right|_{S_0}$$

Here, S_0 is the wetted surface at rest, and n is the exterior normal of S_0 acting towards the fluid.

2.6.4 Integral equation method (singularity method)

The integral equation method is based on the principle that the flow around fixed bodies is described by choosing a suitable distribution of pulsating singularities. The perturbation potential φ_{diff} required for the diffraction problem can be expressed as

$$\varphi_{diff}(x, y, z) = \frac{1}{4 \cdot \pi} \cdot \iint_{S_0} Q(\xi, \eta, \zeta) \cdot G(x, y, z, \xi, \eta, \zeta) \cdot dS$$

for the three-dimensional case. In this integral equation, Q describes the *singularity density* at point $\{\xi, \eta, \zeta\}$ on the surface of the body (S_0) and the Green (or influence) function G describes how the potential of a pulsating *unit source* at that point affects the point being considered $\{x, y, z\}$. The reader is referred to [17] for details of the analytical description.

According to potential theory, the kinematic boundary condition at the surface of the body is

$$\frac{\partial \varphi_0}{\partial n} = -\frac{\partial \varphi_{diff}}{\partial n} = \frac{1}{2} \cdot Q(x, y, z) - \frac{1}{4 \cdot \pi} \cdot \iint_{S_0} Q(\xi, \eta, \zeta) \cdot \frac{\partial G(x, y, z, \xi, \eta, \zeta)}{\partial n} \cdot dS$$

$$\varphi_S(x,y,z) = \sum_{j=1}^{N} Q_j(\xi_j,\eta_j,\zeta_j)\,\frac{1}{4\pi}\iint_{\Delta S_j} G(x,y,z,\xi_j,\eta_j,\zeta_j)\,dS$$

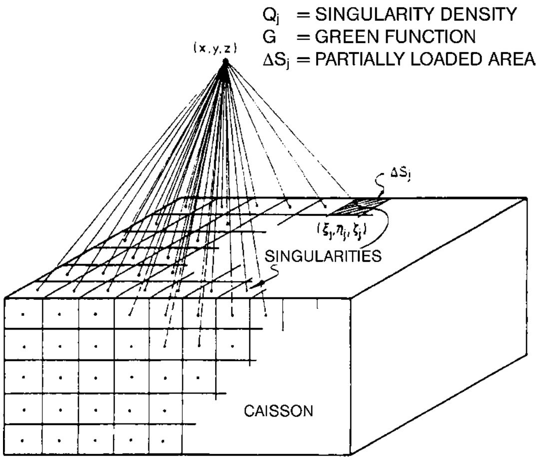

Fig. 2.36 Singularity distribution for a compact structure [30]

We therefore have a Fredholm integral equation of the second kind for determining the singularity density Q (ξ, η, ζ) required. A closed solution to this equation is impossible because the kernel $\partial G/\partial n$ is very complex.

A numerical treatment requires us to divide the wetted surface of the body into a finite number (N) of *partially loaded areas* (ΔS_j) with singularities placed at their centroids having a constant *singularity density* (Q_j), see Figure 2.36.

The undisturbed wave potential (Φ_0) can be described with the linear approach of *Airy*, but also with a non-linear approach, for example fifth-order Stokes. The perturbation potential is basically described by a linear approach because satisfying the non-linear surface condition is extremely difficult. Consequently, the total potential can satisfy only the linearised boundary condition at the surface of the water [30].

The above integral equation can therefore be transformed into a set of linear equations with the following form:

$$Q_i + \sum_j a_{ij} \cdot Q_j = 2 \cdot h_i \qquad (i, j = 1, 2, \ldots, N)$$

where

$$a_{ij} = -\frac{1}{2\cdot\pi}\cdot\iint_{\Delta S_j} \frac{\partial G\left(x_i, y_i, z_i, \xi_j, \eta_j, \zeta_j\right)}{\partial n}\cdot dS_j \quad \text{and} \quad h_i = \left.\frac{\partial \varphi_0}{\partial n}\right|_{\Delta S_i}$$

and $\{x_i, y_i, z_i\}$ is the position of the centroid of element "i". A coefficient a_{ij} describes the velocity at the centroid $\{x_i, y_i, z_i\}$ of element "i" perpendicular to its surface. This velocity is induced by a unit source uniformly distributed over element "j".

If the coefficient matrix $\{a_{ij}\}$ and the vector on the right $\{h_i\}$ are known, then we can obtain the unknown singularity densities $Q_j = Q\ (\xi_j, \eta_j, \zeta_j)$ as solutions to the set of linear equations. Further, the perturbation potential required (φ_{diff} or φ_S) is a linear combination (Figure 2.36). Powerful commercial computer programs are available for the numerical analysis.

The load of a compact structure consists of the hydrodynamic pressure acting on the *wetted surface of the body* and resulting from the *Bernoulli equation* [30], see also Section 2.6.6:

$$p_i = -\frac{\rho}{2} \cdot \left[\left(\frac{\partial \Phi_i}{\partial x} \right)^2 + \left(\frac{\partial \Phi_i}{\partial y} \right)^2 + \left(\frac{\partial \Phi_i}{\partial z} \right)^2 \right] - \rho \cdot \frac{\partial \Phi_i}{\partial t} - \rho \cdot g \cdot z$$

In this equation the first term is the *velocity pressure* (p_v), the second term the *unsteady pressure* (p_{inst}), the third term the *hydrostatic pressure* (p_{stat}) and Φ_i the total potential at point $\{x_i, y_i, z_i\}$ on the surface of the body:

$$\Phi_i = \Phi_0(x_i, y_i, z_i, t) + \varphi_{diff}(x_i, y_i, z_i) \cdot e^{-i \cdot \omega \cdot t}$$

The velocity field results from the gradient of the total potential to which the *steady flow velocity* has been added:

$$\vec{v} = \nabla[\Phi_0(x, y, z, t) + \Phi_{diff}(x, y, z, t)] + \vec{v}_C(x, y, z) = \vec{v}_0 + \vec{v}_{diff} + \vec{v}_C$$

The acceleration field follows from differentiation with respect to time:

$$\dot{\vec{v}} = \frac{\partial \vec{v}}{\partial t} = \dot{\vec{v}}_0 + \dot{\vec{v}}_{diff}$$

Again, owing to the linear approach for the perturbation potential, only the local component of the substantial acceleration is considered here.

Where a structure consists of a compact foundation and a more slender substructure (monotower) that does not have to be analysed according to diffraction theory, then the hydrodynamic loads can be obtained from a combination of the *singularity method* and the *Morison formula* ([31] and Figure 2.37).

The total potential (Φ) contains not only the (generally) non-linear formulation (Φ_0) for the incident wave but also the perturbation potential (Φ_{diff}). This approach enables the influence of the foundation on the substructure ("blockage effect") to be taken into account.

The combined linearised boundary condition at the surface of the water means that the velocity potential is defined only as far as the still water level. However, the wetted surface of the structure in the wave and the surface bounded by the still water level are

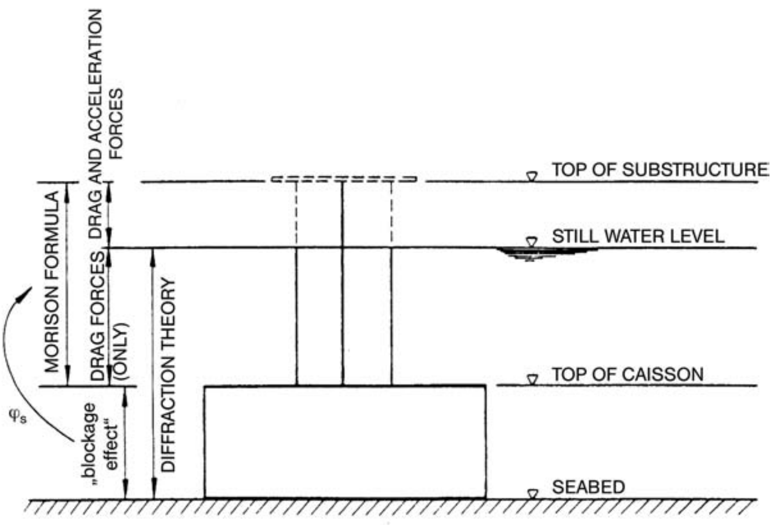

Fig. 2.37 Hydrodynamic analysis of a monotower on a compact foundation [30]

considerably different from each other. Therefore, the loading equations should be modified as follows (Figure 2.37):

- In order to obtain the pressure distribution over the entire structure for a subsequent analysis in a finite element model, diffraction theory is applied to both the compact foundation and also the monotower, but only as far as the still water level.
- At the same time, the Morison formula is applied to the monotower. The inertia forces between the still water level and the top edge of the foundation are, however, suppressed because these forces correspond to the distribution of the unsteady pressure (p_{inst}) determined from diffraction theory.
- In order to calculate the remaining drag forces appropriately, we apply not only the potential of the incident wave (Φ_0) and the steady flow velocity (v_C) but also the perturbation potential (Φ_{diff} – "blockage effect") ensuing from the foundation.
- However, the perturbation potential ensuing from the monotower must be suppressed because it supplies diffraction effects that falsify the drag forces. (If we require the drag forces on the foundation as well, the total perturbation potential must be suppressed.)
- The drag forces below the still water level are distributed with a cosine form over the circumference of the monotower. In doing so, a cylindrical or conical form is assumed for the structure.
- The drag forces related to the axis of the structure must be assigned to the hydrodynamic pressure acting on the surface. Corresponding bar elements and partially loaded areas are therefore defined (Figure 2.38).
- Only the Morison formula is used above the still water level (Figure 2.37). The drag and inertia forces acting in this area are determined because they can make an appreciable contribution to the resulting forces and moments at foundation level. The stability of the entire structure depends on these forces and moments.

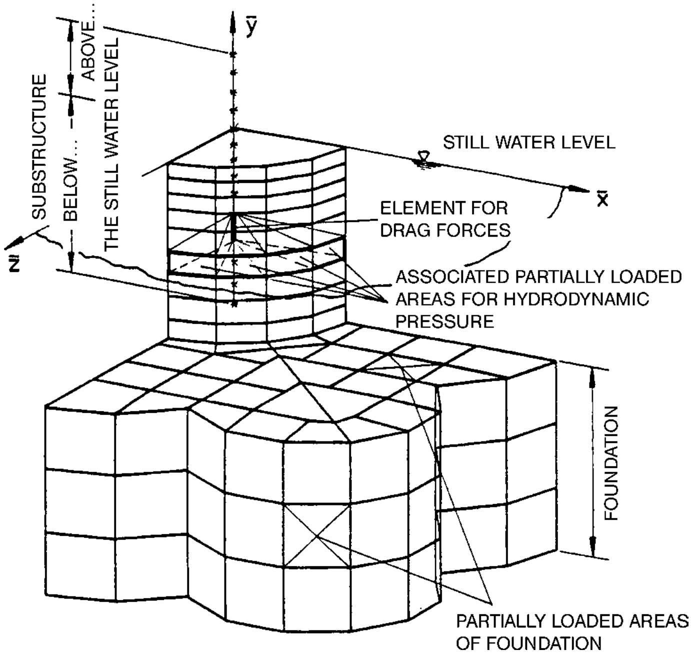

Fig. 2.38 Allocation of bar elements and partially loaded areas [30]

- Owing to the combined linearised boundary condition at the surface of the water, the hydrodynamic pressure – on both the positive pressure and the negative pressure side of the structure – is defined exactly as far as the still water level. In reality the wave contour represents the upper boundary for the wetted surface and for the hydrodynamic pressure and so the resulting differential pressures are roughly triangular (Figure 2.39). As the wave contour changes over time, every interval must be considered separately.
- The part of the hydrodynamic pressure (velocity pressure) dependent on the square of the velocity vector is obtained by including the second-order terms of the Bernoulli equation in the calculations (Figure 2.40). Flow velocities tangential to the surface of the structural member generate negative pressures which, for example, lead to a drop in the wave contour as it flows around the monotower.

2.6.5 Vertical cylinders (MacCamy and Fuchs)

The large-volume vertical cylinder has a special significance as a solitary structure and also as a component of marine structures. It has therefore been thoroughly investigated in the past, theoretically and experimentally. MacCamy and Fuchs devised one important analytical method for ascertaining the diffraction of a primary wave around a large-diameter vertical cylinder erected on the seabed [29].

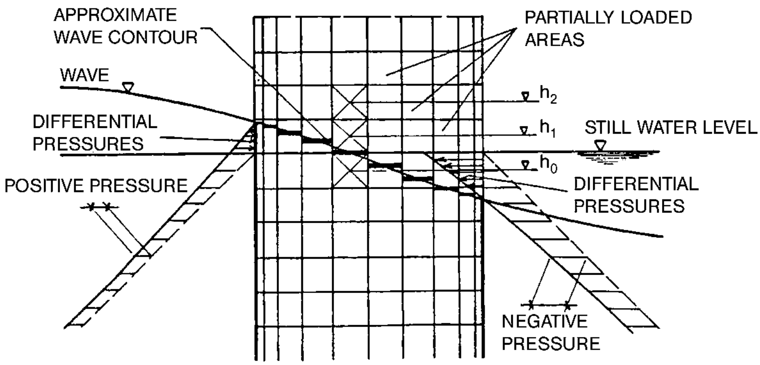

Fig. 2.39 Differential pressures in the region of the surface of the water [30]

The starting point is given by the wave profile and the *velocity potential of the undisturbed primary wave* in Cartesian coordinates (z = 0 at seabed, Figure 2.41) and in complex notation:

$$\zeta_0(x,t) = \frac{H}{2} \cdot e^{i \cdot (k \cdot x - \omega \cdot t)}$$

$$\Phi_0(x,z,t) = -i \cdot \frac{H}{2} \cdot \frac{g}{\omega} \cdot \frac{\cosh(k \cdot z)}{\cosh(k \cdot d)} \cdot e^{i \cdot (k \cdot x - \omega \cdot t)}$$

It is expedient to formulate the boundary value problem in terms of cylindrical coordinates. Following transformation, the result is (Figure 2.41)

$$\zeta_0(r,\theta,t) = \frac{H}{2} \cdot \left[\sum_{m=0}^{\infty} \varepsilon_m \cdot i^m \cdot J_m(k \cdot r) \cdot \cos(m \cdot \theta)\right] \cdot e^{-i \cdot \omega \cdot t}$$

$$\Phi_0(r,\theta,z,t) = -\frac{g \cdot H}{2 \cdot \omega} \cdot \frac{\cosh(k \cdot z)}{\cosh(k \cdot d)} \cdot \left[\sum_{m=0}^{\infty} \varepsilon_m \cdot i^{m+1} \cdot J_m(k \cdot r) \cdot \cos(m \cdot \theta)\right] \cdot e^{-i \cdot \omega \cdot t}$$

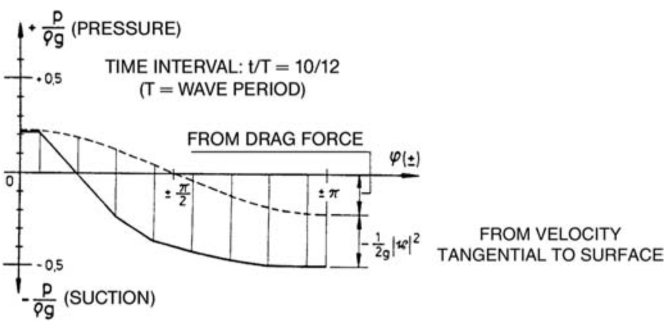

Fig. 2.40 Pressure distribution around circumference of cylinder (second-order terms) [30]

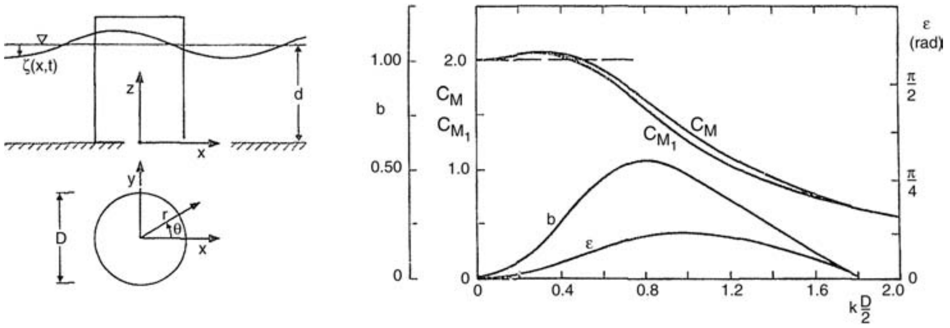

Fig. 2.41 Vertical cylinder erected on the seabed; coefficients c_M, c_{M1}, b and phase angle ε after MacCamy and Fuchs [17]

where J_m is the Bessel (cylinder) function of the first kind and mth order [27] and ε_m is the so-called Neumann symbol ($\varepsilon_0 = 1$; $\varepsilon_m = 2$ for $m \geq 1$).

As a solution to the diffraction problem, we get the following for the velocity potential (total potential Φ (r, θ, z, t)):

$$\Phi(r,\theta,z,t) = -\frac{g \cdot H}{2 \cdot \omega} \cdot \frac{\cosh(k \cdot z)}{\cosh(k \cdot d)} \cdot e^{-i \cdot \omega \cdot t} \cdot \sum_{m=0}^{\infty} \varepsilon_m \cdot i^{m+1} \cdot \left[J_m(k \cdot r) - \frac{J'_m(k \cdot a)}{H'_m(k \cdot a)} \cdot H_m(k \cdot r) \right] \cdot \cos(m \cdot \theta)$$

where

a radius of cylinder

Here, H_m is the Hankel function of the first kind and mth order [27], and J'_m, H'_m are the derivations of the functions according to their argument.

The following applies for the Hankel function of the first kind and mth order:

$$H_m(k \cdot r) = J_m(k \cdot r) + i \cdot Y_m(k \cdot r)$$

where J_m $(k \cdot r)$, Y_m $(k \cdot r)$ are Bessel functions of the first and second kind.

All the variables of the flow field can be determined from the velocity potential. In real notation, the force per unit height of the cylinder is

$$\frac{dF_x(z,t)}{dz} = \rho \cdot \pi \cdot a^2 \cdot c_{M_1} \cdot \left(\frac{\partial u}{\partial t}(z) \right)_0 \cdot \sin(\omega \cdot t - \varepsilon)$$

where

$$c_{M_1} = \frac{4}{\pi \cdot (k \cdot a)^2} \cdot \frac{1}{\sqrt{\left[J_1'(k \cdot a)\right]^2 + \left[Y_1'(k \cdot a)\right]^2}}$$

$$\varepsilon = \arctan\left[\frac{J_1'(k \cdot a)}{Y_1'(k \cdot a)}\right]$$

$$\left(\frac{\partial u}{\partial t}(z)\right)_0 = \omega^2 \cdot \frac{H}{2} \cdot \frac{\cosh(k \cdot z)}{\sinh(k \cdot d)}$$

and $(\partial u/\partial t)_0$ is the amplitude of the acceleration of the undisturbed primary wave.

The force per unit height can be transformed into the following form:

$$\frac{dF_x(z,t)}{dz} = c_M \cdot \rho \cdot \pi \cdot a^2 \cdot \frac{\partial u}{\partial t}(z,t)\bigg|_{x=0} + b \cdot \rho \cdot \pi \cdot a^2 \cdot \omega \cdot u(z,t)|_{x=0}$$

where

$$c_M = c_{M_1} \cdot \cos\varepsilon = \frac{4}{\pi \cdot (k \cdot a)^2} \cdot \frac{Y_1'(k \cdot a)}{\sqrt{\left[J_1'(k \cdot a)\right]^2 + \left[Y_1'(k \cdot a)\right]^2}}$$

$$b = c_{M_1} \cdot \sin\varepsilon = \frac{4}{\pi \cdot (k \cdot a)^2} \cdot \frac{J_1'(k \cdot a)}{\sqrt{\left[J_1'(k \cdot a)\right]^2 + \left[Y_1'(k \cdot a)\right]^2}}$$

$$u(z,t)|_{x=0} = \omega^2 \cdot \frac{H}{2} \cdot \frac{\cosh(k \cdot z)}{\sinh(k \cdot d)} \cdot \cos(\omega \cdot t)$$

$$\frac{\partial u}{\partial t}(z,t)\bigg|_{x=0} = -\omega^2 \cdot \frac{H}{2} \cdot \frac{\cosh(k \cdot z)}{\sinh(k \cdot d)} \cdot \sin(\omega \cdot t)$$

Here, $u|_{x=0}$ and $(\partial u/\partial t)|_{x=0}$ are the amplitudes of the velocity and acceleration of the undisturbed primary wave on the axis of the cylinder ($x = 0$).

This format expresses the wave force resulting from diffraction theory in a similar way to the Morison formula (*modified Morison formula*).

The dependency of the variables c_{M1}, c_M, b and ε on the dimensionless parameter $(k \cdot a)$ is plotted in Figure 2.41. This parameter expresses the diameter/wavelength ratio in physical terms:

$$k \cdot a = \frac{2 \cdot \pi \cdot a}{\lambda} = \frac{\pi \cdot D}{\lambda}$$

Using the above format, the wave force can be considered as the sum of two components. The first of these is proportional to the acceleration and the second is proportional to the velocity of the undisturbed primary wave (inertia and potential damping).

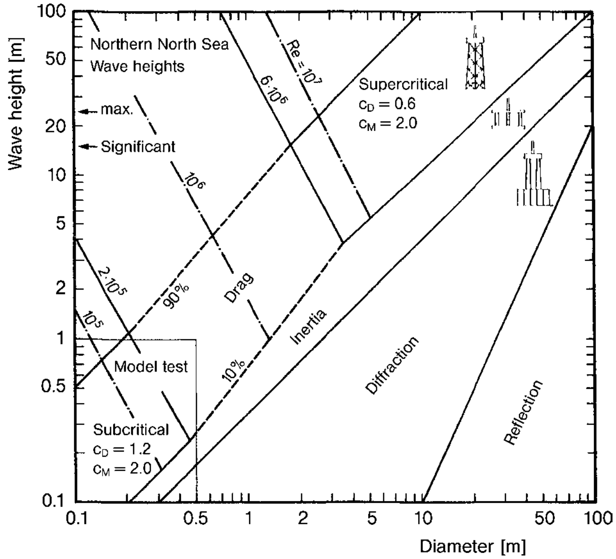

Fig. 2.42 Relative significance of the various types of force [17]

Particularly interesting is the limit value of the inertia coefficient c_M or c_{M1} for $k \cdot a \to 0$. We can see from Figure 2.41 that for $k \cdot a \leq 0.6$, that is for $D/\lambda \leq 1/5$, according to potential theory, $c_M = c_{M1} = 2.0$, that is $c_a = 1.0$, may be used in the calculations for a good approximation! This result is identical with the assumption of a hydrodynamic mass equal to the displaced mass of water, as is the case for an infinitely long cylinder in an accelerated fluid unconfined in all directions.

Diffraction effects can therefore be ignored in the range $D/\lambda \leq 1/5$. As on the other hand in a real fluid the viscosity-related effects prevail in this range, c_M depends on factors that were dealt with in Section 2.6.2.

Diffraction effects have to be considered for $D/\lambda > 1/5$, which for the cylinder considered here are covered analytically by the coefficients c_{M1}, c_M and b. As D/λ grows, so the drag effects become less significant, which means that the potential theory calculation results in a good approximation for large-volume, compact structures. The $D/\lambda = 1/5$ limit is also the basis for the Morison formula evaluation shown in Figure 2.42.

For further information and examples please see [17].

2.6.6 Higher-order potential theory

Non-linearities in the behaviour of a marine structure or its components can, for example, be caused by:

- viscosity-related unsteady drag forces,
- finite deformations,

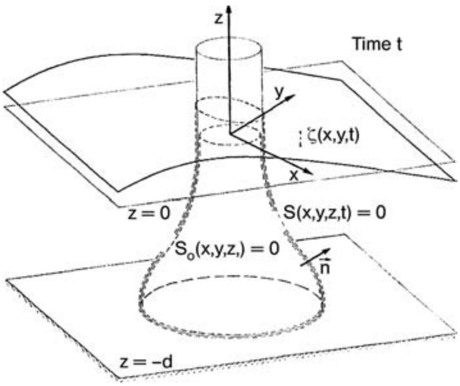

Fig. 2.43 Definitions for the non-linear potential theory problem

– non-linear restoring forces,
– hydrodynamic impacts (slamming),
– movements of fluids in partially filled spaces (sloshing),
– and so on.

A brief introduction to the non-linear potential theory problem of the interaction between wave and structure is given below.

If the exciting wave can no longer be represented with good approximation according to *Airy*, then higher-order potential theory solutions must be used to ascertain the interaction between structure and wave. A number of the fundamental assumptions of linear theory are no longer permissible in such a non-linear concept. This will be illustrated here by formulating the non-linear boundary value problem using the example of a structure erected on the seabed (Figure 2.43).

The wetted surfaces for still water (S_0) and in the wave field (S) at time t are described by

$$S_0(x, y, z, t) = 0 \quad \text{and} \quad S(x, y, z, t) = 0$$

The surface of the water outside the structure is taken as

$$\zeta = \zeta(x, y, t)$$

The Laplace differential equation has to be satisfied throughout the entire flow field:

$$\Delta\Phi = 0$$

The result is the following boundary conditions:

a) The kinematic boundary condition on the seabed

$$\frac{\partial\Phi}{\partial z} = 0$$

for $z = -d$

b) The kinematic boundary condition at the surface of the structure

$$\frac{\partial \Phi}{\partial n} = 0$$

for $\quad S(x, y, z, t) = 0$

c) The *dynamic* boundary condition at the surface of the water (Bernoulli)

$$\rho \cdot \frac{\partial \Phi}{\partial t} + \frac{\rho}{2} \cdot \left[\underline{\left(\frac{\partial \Phi}{\partial x}\right)^2} + \underline{\left(\frac{\partial \Phi}{\partial y}\right)^2} + \underline{\left(\frac{\partial \Phi}{\partial z}\right)^2} \right] + \rho \cdot g \cdot \zeta = 0$$

for $\quad \zeta = \zeta(x, y, t)$

d) The *kinematic* boundary condition at the surface of the water

$$\frac{\partial \Phi}{\partial z} = \frac{\partial \zeta}{\partial t} + \underline{\frac{\partial \zeta}{\partial x} \cdot \frac{\partial \Phi}{\partial x}} + \underline{\frac{\partial \zeta}{\partial y} \cdot \frac{\partial \Phi}{\partial y}}$$

for $\quad \zeta = \zeta(x, y, t)$

e) The radiation condition

$$\lim_{r \to \infty} \sqrt{r} \cdot \left(\frac{\partial \Phi}{\partial r} - i \cdot \frac{\omega^2}{g} \cdot \Phi \right) = 0$$

In linear theory the underlined higher-order terms may be neglected provided the dynamic field may be considered as an (infinitesimally) small disturbance of the steady state. In this case it is permissible to satisfy the kinematic and dynamic boundary conditions at still water level ($z = 0$) and not at the wave profile ($z = \zeta$). From this we get the combined linearised boundary condition at the surface of the water (see Section 2.6.3):

$$\frac{\partial^2 \Phi}{\partial t^2} + g \cdot \frac{\partial \Phi}{\partial z} = 0$$

In non-linear theory we have to describe the pressures on the wetted surface (S) at time t. The surface is bounded by the unknown wave surface ζ (x, y, t). We solve this problem by developing the partial derivations of the potential function at the still water level ($z = 0$) in Taylor series. That results in the approximate solutions of the first, second, . . . , nth order.

For example, the second-order boundary value problem gives us the pressure field from the Bernoulli equation – as was already used in 2.6.4:

$$p_i = -\frac{\rho}{2} \cdot \left[\left(\frac{\partial \Phi_i}{\partial x}\right)^2 + \left(\frac{\partial \Phi_i}{\partial y}\right)^2 + \left(\frac{\partial \Phi_i}{\partial z}\right)^2 \right] - \rho \cdot \frac{\partial \Phi_i}{\partial t} - \rho \cdot g \cdot z$$

2.6.7 Wave loads on large-volume offshore structures

It is essential to consider the diffraction effects that occur if we are to calculate the hydrodynamic loads on compact, large-volume offshore structures reliably [32].

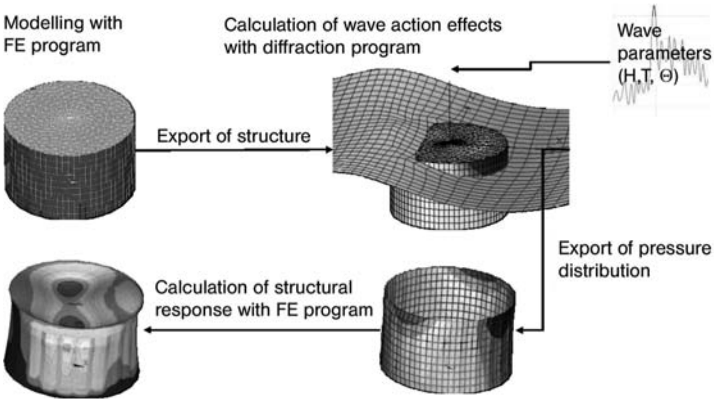

Fig. 2.44 Action affects on a gravity base caused by wave loads [32]

The solution to the diffraction problem is generally based on a potential theory formulation (see Section 2.6.3) and calls for the solution space to be discretised. Suitable numerical methods for this are the boundary element method or the singularity method (see Section 2.6.4). Figure 2.44 shows the interaction between the *hydrodynamic analysis* according to the singularity method and the *structural analysis* according to the finite element method.

Suitable software packages are very expensive because of the numerical complexity. In addition, owing to the boundary conditions that have to be maintained at the structure, it is not possible to separate the mathematical description of the wave kinematics from the actual calculation of the hydrodynamic loading. This leads to a small bandwidth of applicable wave theories.

On the other hand, the wave loads on resolved slender offshore structures (e.g. monopiles, jackets) may be calculated using the empirical *Morison formula* (see Section 2.6.2). Diffraction effects are not included in the Morison approach, that is the wave kinematics and the hydrodynamics are separated from each other. Consequently, in contrast to diffraction theory, the complete range of available wave theories can be used to calculate the wave loads.

Owing to their simpler implementation, programs based on the Morison formula are often less expensive and thus more widely used. Therefore, such programs are frequently employed to obtain rough estimates of the wave loads on large-volume offshore structures. This can lead to inappropriate results because critical diffraction effects are ignored.

The numerical sensitivity analysis of a simple typical structure is ideal for clarifying just how much the results of the Morison formula and diffraction theory differ from each other [32]. Let us consider a simple cylinder (Figure 2.45) that extends from the seabed to the still water level. The relevant application ranges for diffraction theory and

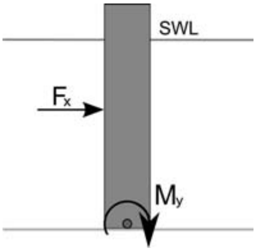

Fig. 2.45 Hydrodynamic forces acting on the cylinder

the Morison formula can be represented by varying the cylinder diameter and the wavelength, or rather the wave period corresponding to this.

The resulting total hydrodynamic forces at the base of the cylinder are calculated using the Morison formula and also with the diffraction formulation of MacCamy and Fuchs (see Section 2.6.5). Linear wave theory and a water depth of 30 m are assumed for both methods. The Morison formula uses the inertia coefficient $c_M = 2.0$ (Table 2.12) and the drag coefficient $c_D = 0.7$ (Table 2.13).

Figures 2.46 and 2.47 show representative results of the sensitivity analysis for wave periods T = 6 s and T = 18 s. The horizontal forces F_x (surge) and pitch moments M_y according to the diffraction approach, related to the Morison formula, are plotted over the diameter/wavelength quotient D/λ.

There is hardly any difference between the results of the two different types of calculation up to the ratio D/λ = 0.2 (see Section 2.6.5). But above this limit ratio the Morison formula severely overestimates the wave forces for smaller wave periods, and hence smaller wavelengths. The error when using the Morison formula remains small for large wave periods (e.g. for a 50-year design wave) and correspondingly large

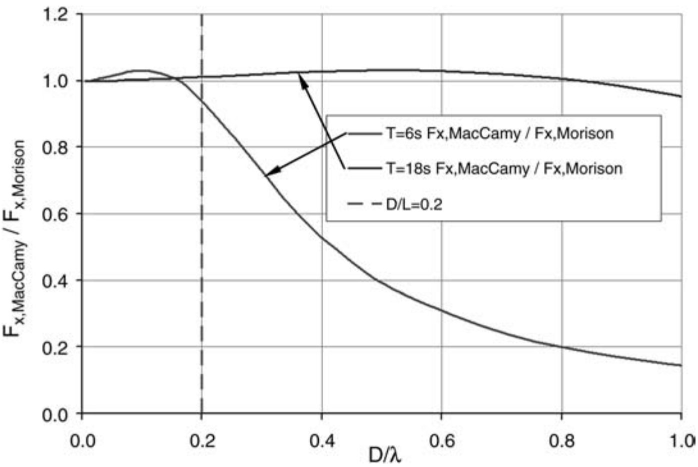

Fig. 2.46 Horizontal forces F_x according to the diffraction approach, related to the Morison formula

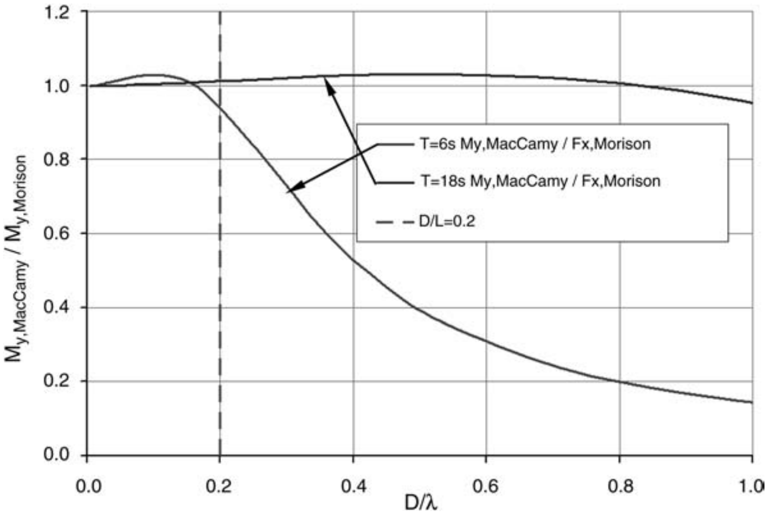

Fig. 2.47 Pitch moments M_y according to the diffraction approach, related to the Morison formula

wavelengths. The lack of the drag force in the diffraction approach is negligible when compared with the resulting total force.

The differences between the results of the two methods of calculation will be illustrated below with the help of a more realistic example [32]. To do this we will investigate a large-volume reinforced concrete offshore foundation structure for a wind turbine with a design typical for the North Sea. Figure 2.48a shows the geometry of the structure (see also Section 5.4.2).

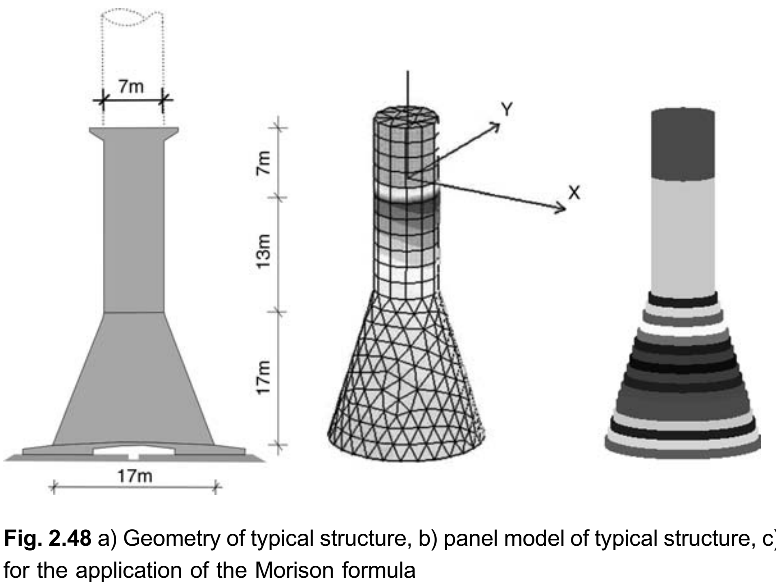

Fig. 2.48 a) Geometry of typical structure, b) panel model of typical structure, c) model of structure for the application of the Morison formula

A 30 m depth of water is assumed. In order to calculate the wave loads, the structure is modelled as a panel model (Figure 2.48b) in a diffraction program based on the boundary element method. As a comparison, the structure is modelled in another program based on the Morison formula (Figure 2.48c). The inertia coefficient $c_M = 2.0$ and drag coefficient $c_D = 0.7$ are used again here.

According to the definition, the empirical Morison formula may only be applied to cylindrical, slender elements. That results in a problem when modelling the conical bottom segment of the structure. The only way of modelling this section is to consider it as a series of short cylindrical segments, each of which has a diameter slightly larger than the previous one.

The individual elements of the Morison model only supply hydrodynamic components normal to the bar axis. Consequently, in contrast to the diffraction panel model, this model cannot be used to calculate vertical forces nor their contribution to the pitch moment M_y. Linear wave theory states that the maxima of the vertical wave force exhibit a 90° phase shift with respect to the maxima of the horizontal force. This and the fact that our typical structure offers very much more horizontal than vertical surface on which forces can act means that the errors in the Morison calculation – due to the fact that the vertical components are ignored when calculating the maximum moment M_y – can be expected to remain small.

The hydrodynamic forces on the structure are calculated using linear wave theory and for various wave periods [32]. The results plotted in Figures 2.49 and 2.50 show the total hydrodynamic forces – again in relation to the values according to the Morison formula – over the wave period T.

The diagrams show that the results obtained using the Morison formula are always larger than those obtained using diffraction theory. The difference is largest for small wave periods. The difference remains more or less constant for the larger wave periods.

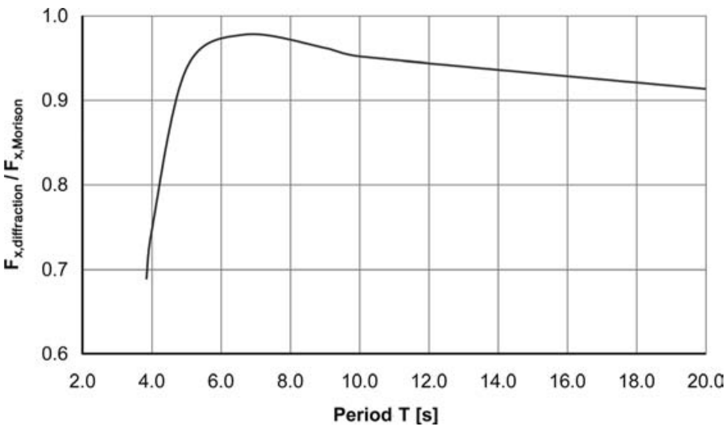

Fig. 2.49 Ratios of horizontal forces over wave period

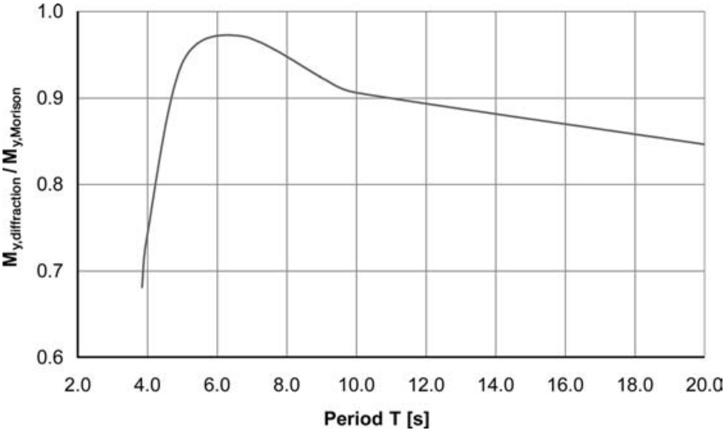

Fig. 2.50 Ratios of pitch moments over wave period

The *sensitivity analysis* carried out on the simple cylinder and the calculation of the hydrodynamic loads on the realistic example show that the differences between the Morison formula and diffraction theory regarding the ensuing wave loads are small for large wave periods and accordingly larger corresponding wavelengths.

It is sufficient to use the Morison formula within the scope of a *preliminary design* or when only a rough estimate is needed of the maximum loads acting on a large-volume compact offshore structure due to a design wave with correspondingly large wavelength. If diffraction effects are ignored, the calculated forces increase and therefore must be considered as being on the safe side. A modified inertia coefficient c_M can be employed to improve the results given by the Morison approach.

At the *fatigue limit state*, environmental influences, for example wind and wave loads, are described by a collective load. The collective wave load contains waves with various wave heights and wave periods, normally represented by extreme value distributions. In such distributions the mean value of the wave period for North Sea conditions lies between 4 and 7 s. Therefore, considering diffraction effects is relevant when checking fatigue. Applying the Morison formula here leads to an accumulation of damage which would exceed the permissible limits. Only diffraction theory supplies reliable results in this case.

The drag force is neglected here but, if necessary, can be calculated in an additional step with the Morison formula (see also Section 2.6.4).

2.7 Thermal actions

According to Section 6.4.5 of the DIBt guideline [9], the following applies:

1. Deformations due to asymmetric solar irradiation are not considered (combination coefficient $\psi_{0,T} \rightarrow 0$ for combinations with wind loads).

2. The temperature gradient in the shaft wall due to differing climatic conditions is

$$\Delta T = \pm 15\,K$$

From this we get a thermal expansion gradient:

$$\varepsilon_T = \pm\alpha_T \cdot \Delta T/2 = \pm 15.10^{-5}/2 = \pm 0.075‰$$

In the absence of specific data, the following *standard environmental conditions* should be assumed for offshore wind turbines (see [11] 4.2.4.1):

- Wind turbines are to be designed for ambient temperatures between −20 and +50 °C. The following uniform temperature change is to be assumed: $\Delta T_N = \pm 35\,K$ in relation to a mean temperature of +15 °C.
- It must be possible to operate the wind turbine at ambient temperatures between −10 and +40 °C.
- Relative humidity of max. 100%
- Unpolluted marine atmosphere
- Intensity of solar irradiation: 1000 W/m^2
- Density of air: 1.225 kg/m^3
- Density of water: 1025 kg/m^3
- Salt content of seawater: 3.5%

The lowest seawater temperature may be assumed to be 0 °C.

Other assumptions will be necessary for locations with extreme changes of temperature (see [11] 4.2.4.2) or ice conditions.

2.8 Sea ice

Erecting wind turbines in areas affected by ice formation or drifting ice requires the effects of these ice conditions to be taken into account by means of the following properties and statistical data (Table 2.14) [24,26,28]:

Table 2.14 Properties of sea ice [24]

Density	900 kg/m^3
Unit weight	8.84 kN/m^3
Modulus of elasticity	2 GPa[a)]
Poisson's ratio	0.33
Friction coefficient – ice-ice	0.1
Dynamic friction coefficient – ice-concrete	0.2
Dynamic friction coefficient – ice-steel	0.1

a) Figure given in [28]: $E_{ice} = 9.5$ to 12.0 GPa

- Form, size, surface finishes and stiffness of the structure
- Size, form and thickness of ice, rate of advance
- Type of ice and ice formation (ice floes, drifting ice, ice ridges/ramparts)
- Temperature and salt content of the ice plus the strength of the ice dependent on this
- Angle of incidence of the ice on the structure
- Mechanical properties of the ice (compressive strength r_u, bending strength r_f)
- Rate of load application

Modelling
The *thickness of the ice* is an important parameter for calculating ice loads and should be specified based on local data (Table 2.15).

Another input in the load calculation can be the *frost index* K, which is defined as the sum of the mean daily temperatures for a particular location on which the mean temperature lies below 0 °C. The frost index K varies from year to year and can be presented as a probability function (Weibull) based on statistically evaluated data [24]. The compressive strength r_u, the bending strength r_f and the thickness of the ice can be expressed as functions of the frost index K.

Ice loads
Lateral ice loads should be determined by *in situ* measurements, model tests at a suitable scale or other recognised theoretical methods. Ice loads for locations on the open sea should be determined depending on the current *characteristic ice thickness* [24].

Loads other than lateral ice loads can also occur, for example:

- Loads due to a rigid covering of ice, including loads due to arching effects (e.g. locations near the coast)
- Dead loads due to ice frozen on the structure
- Ice pressures due to pack ice or an ice dam
- Thermal ice pressure (restraint forces) as a result of thermal actions on a rigid covering of ice

Table 2.15 Measured maximum ice thicknesses as guidance values for design [26]

North Sea	max. h [cm]	Baltic Sea	max. h [cm]
Heligoland	30 to 50	Flensburg Fjord	32 to 40
Wilhelmshaven	40	Eckernförde Bay	50
Büsum	45	Kiel Fjord	55
Meldorf (harbour)	60	Bay of Lübeck	50
Wittdün harbour	60	Bay of Wismar	60
		Rostock-Warnemünde	40
		Stralsund – Palmer Ort	65

Table 2.16 Compressive strength of sea ice [24]

Return period [years]	Compressive strength of ice $\sigma_{0,k}$ [MPa]; Designations simplified after [26]	
	Southern North Sea, Skagerrak, Kattegat	Western and southern Baltic Sea
5	1.0	1.0
10	1.5	1.5
50	1.6	1.9
100	1.7	2.1

Lateral ice loads should be assumed to act in the same direction as the wind loads. Either the high or low water level, with the necessary return period, should be assumed in combination with ice loads. The combination with the most unfavourable effects governs.

The *characteristic compressive strength* of ice $\sigma_{0,k}$ depends on the ambient conditions at the location, for example the local salt content of the seawater. Table 2.16 lists reference values.

According to [26], the *horizontal ice load for a compression failure* due to drifting ice acting *on vertical piles*, irrespective of their cross-sectional form, is calculated as follows:

$$F_{0,k} = 0.36 \cdot s_{0,k} \cdot d^{0.5} \cdot h^{1.1} \quad [\mathrm{kN}]$$

where

d width of single pile [cm]
h thickness of ice [cm]

Tests have shown that the compressive strength of the ice reaches its maximum value at the specific rate of expansion $\dot{\varepsilon} = 0.003\,s^{-1}$, which is the value used here. If the case of the start of the ice movement for firmly attached ice has to be considered, then according to [26], other loading assumptions apply.

The *characteristic local ice pressure* acting on the surface of a structural member due to incident drifting ice should be taken as follows [24]:

$$\sigma_{local,k} = \sigma_{0,k} \cdot \sqrt{1 + 5 \cdot \frac{t_k^2}{A_{local}}}$$

where

$\sigma_{0,k}$ characteristic compressive strength of ice (s. Table 2.16)
t_k characteristic thickness of ice
A_{local} area on which the ice load acts

Table 2.17 Bending strength of sea ice [24]

Return period [years]	Bending strength of ice $\sigma_{B,k}$ [MPa]; Designations simplified after [26]	
	Southern North Sea, Skagerrak, Kattegat	Western and southern Baltic Sea
5	—	0.25
10	—	0.39
50	0.50	0.50
100	—	0.53

The *characteristic bending strength* of ice $\sigma_{B,k}$ governs for ice loads acting on the inclined surfaces of structural members (Table 2.17).

In the case of *raking piles*, ice floes can be broken up by shearing or bending earlier than the crushing of the ice. According to [26], the *horizontal ice load* due to drifting ice acting on *raking piles*, irrespective of their cross-sectional form, is calculated as follows:

a) For a shear failure

$$F_{s,k} = c_{fs} \cdot \tau_{,k} \cdot k \cdot \tan\beta \cdot d \cdot h \quad [\mathrm{kN}]$$

b) For a bending failure

$$F_{b,k} = c_{fb} \cdot \sigma_{B,k} \cdot \tan\beta \cdot d \cdot h \quad [\mathrm{kN}]$$

where

c_{fs} shape factor for shear failure after [26]
τ_k characteristic shear strength [MPa]
k contact coefficient, generally $k = 0.75$
c_{fb} shape factor for bending failure after [26]
$\sigma_{B,k}$ characteristic flexural tensile strength [MPa]
β angle of inclination of pile from the horizontal (compression failure governs when $\beta > 80°$, see above)
d width of single pile [cm]
h thickness of ice [cm]

The smaller ice load governs in each case. This is usually flexural tensile failure because the shape factors are about one power of 10 smaller than those for shear failure.

According to [28], the compressive strength $\sigma_{0,k}$, shear strength τ_k and flexural tensile strength $\sigma_{B,k}$ of sea ice are related as follows:

$$\tau_k \cong \sigma_{0,k}/6$$

$$\sigma_{B,k} \cong \sigma_{0,k}/3$$

(compare Tables 2.16 and 2.17)

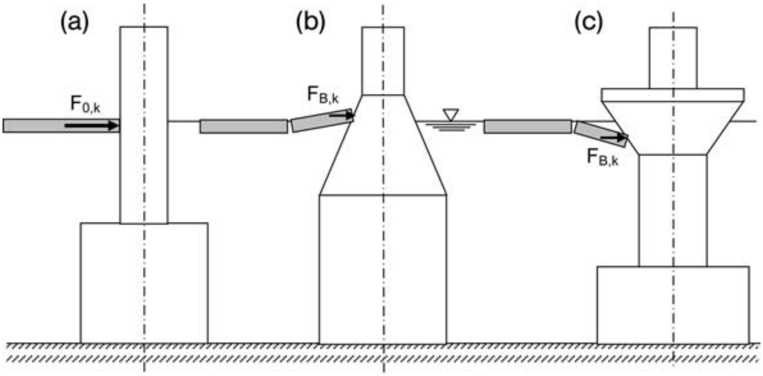

Fig. 2.51 Ice load scenarios for offshore structures: a) vertical surface, b) ice cone, c) inverted ice cone

According to [26][3)], the ice loads on large structures can be calculated as follows:

a) For compression failure (in front of vertical surfaces):

$$F_{0,k} = 10 \cdot k \cdot \sigma_{0,k} \cdot h \quad [\mathrm{kN/m}]$$

b) For bending failure (in front of inclined surfaces)

$$F_{B,k} = 1.0 \cdot k \cdot \sigma_{B,k} \cdot h \cdot \tan\beta \quad [\mathrm{kN/m}]$$

where

- k contact coefficient, generally $k = 0.33$
- $\sigma_{0,k}$ characteristic compressive strength [MPa]
- $\sigma_{B,k}$ characteristic flexural tensile strength [MPa]
- h thickness of ice [cm]
- β angle of inclination of loaded area from the horizontal (compression failure governs when $\beta > 80°$)

Figure 2.51 shows the various scenarios connected with the incidence of ice on an offshore structure.

The ice loads due to flexural tensile failure are lower than those as a result of compressive failure and so the designer is recommended to include inclined surfaces (ice cones) in the splash zones of foundations, especially compact foundations.

Ice loads on inclined surfaces of structural members (e.g. foundations with a conical form in the splash zone) may be calculated with the help of *Ralston's formula* (see [24] Appendix L):

a) The following applies for horizontal components:

$$R_H = [A_1 \cdot r_f \cdot t^2 + A_2 \cdot \gamma_w \cdot t \cdot b^2 + A_3 \cdot \gamma_w \cdot t \cdot (b^2 - b_T^2)] \cdot A_4$$

[3)] Owing to a printing error, the reader is advised to consult the 1996 edition of the EAU!

b) The following applies for vertical components:

$$R_V = B_1 \cdot R_H + B_2 \cdot \gamma_w \cdot t \cdot (b_2 - b_T^2)$$

where

r_f bending strength of ice (see Table 2.17 for characteristic values $\sigma_{B,k}$)
γ_w specific weight of seawater
t thickness of ice
b diameter of cone at the waterline
b_T diameter of top edge of cone

There are dimensionless coefficients A_1, A_2, A_3, A_4, B_1 and B_2 that depend on the friction coefficient μ between the surface of the cone and the ice and the angle of inclination α[4)] of the cone with respect to the horizontal (see [24] Appendix L). The formulations are valid for angles exceeding approx. $\alpha = 65°$.

For an optimum ice cone design, its maximum angle should be selected such that the design ice load is not greater than the design wave load. "Inverted" ice cones force the incident drifting ice beneath the water. The underside of such a cone should lie underwater by a distance at least equal to the thickness of the ice (for design low water!).

For further regulations see [24] and Germanischer Lloyd: *Guideline for the Construction of Fixed Offshore Installations in Ice-Infested Waters.*

2.9 Icing-up of structural members

An ice covering 30 mm thick should be assumed on all sides of non-rotating components of offshore wind turbines, with an ice density of 900 kg/m^3 (see [11] 4.2.4.4). A thicker covering of ice should be assumed when spray from the sea is expected as well. An ice thickness of 100 mm is to be assumed in the absence of specific data.

A mass distribution should be assumed for the build-up of ice on rotating rotor blades. This distribution should increase linearly from zero at the hub to a value μ_E at half the blade length and then remain constant from there to the tip of the blade (Figure 2.52). See [24] 6.4.6 and [11] 4.2.4.4 for details of μ_E.

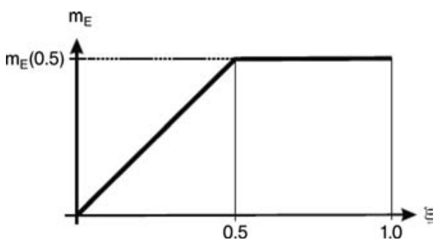

Fig. 2.52 Ice accumulation on rotor blades of wind turbines in operation [24]

4) Inclination α [24] and angle of inclination β [26] are equivalent.

3 Non-linear material behaviour

3.1 General

DIN 1045-1 [33] 8.6 stipulates that the equilibrium state of loadbearing structures with bar-type members or walls subjected to axial compression – and in particular the equilibrium state of these members themselves – has to be verified taking into account the effects of member deformations when such deformations reduce the load-carrying capacity by more than 10%. This situation should generally be assumed for slender towers.

The equilibrium state with respect to the deformed loadbearing structure is verified by calculating the internal forces according to *second-order theory*, that is by using a *geometric non-linear analysis*. The deformations of the loadbearing structure or the structural members subjected to axial compression increase disproportionately as the load increases and so the ultimate limit state is especially critical. The ultimate load decreases in comparison to a calculation based on first-order theory, or stability problems occur, depending on the flexibility of the loadbearing structure or the slenderness of the member being investigated, see [34].

Deformation analyses at the ultimate limit state must take into account the non-linear material behaviour of reinforced concrete, that is

- the formation of cracks in the tension zones of the member cross-sections,
- the non-linear stress-strain curve for the concrete (Figure 3.1),
- the non-linear stress-strain curve for the reinforcing steel (Figure 3.2) and, if applicable,
- the non-linear stress-strain curve for the prestressing steel (Figure 3.4).

A *geometric* and *physical non-linear analysis* of the internal forces is therefore necessary. Such an analysis requires an iterative procedure because the changes in stiffness associated with the load increases have to be recalculated again and again. That is only possible with the help of computer programs.

Such calculations are very involved and so the *model column method* may be used when verifying compression members with square, rectangular or circular cross-sections that fall within the range of applicability given in DIN 1045-1 [33] 8.6.5. The model column method converts the calculations according to second-order theory into a cross-sectional design based on the strains ε_{yd} upon yielding of the longitudinal reinforcement [34].

The deformed loadbearing structure is still just in equilibrium at the yield condition. However, this limit state, which can be derived from the stress-strain curves of Section 3.2, is not reached in a slender tower because:

- either a stability failure occurs first in the deformation calculation, or
- the load-carrying capacity of the cross-section determined according to Section 3.5 becomes critical.

Concrete Structures for Wind Turbines. First edition. Jürgen Grünberg, Joachim Göhlmann.

In both cases the actual deformations remain smaller than those of the yield condition.

A non-linear calculation of the internal forces according to second-order theory is therefore unavoidable if we are to achieve a realistic and hence also economic design of the tower shaft. *Bending moment-curvature relationships* can be used as a basis for this (see Section 3.3).

3.2 Material laws for reinforced and prestressed concrete

Deformation calculations according to second-order theory (see Section 3.1) may be based on short-term action effects when the wind loads govern. The following stress-strain curves may be assumed in this situation.

3.2.1 Non-linear stress-strain curve for concrete

We generally use the mean values of the cylinder compressive strength of the concrete ($f_{cm} = f_{ck} + 8$ [MPa]) when calculating the deformations (Figure 3.1). Deformation calculations according to second-order theory require the theoretical mean values of the material strengths according to DIN 1045-1 [33] 8.5.1 (4) when using non-linear methods to determine the internal forces (Table 3.1), that is:

$$f_c = f_{cR} = 0.85 \cdot \alpha \cdot f_{ck} \quad \text{and} \quad E_{cR} = E_{c0m} = 9500 \cdot (f_{ck} + 8)^{1/3} \text{ }^{1)}$$

A uniform partial safety factor ($\gamma_R = 1.30$ or $\gamma_{RA} = 1.10$) should be used for the design value of the ultimate resistance. Alternatively, DIN 1045-1 [33] 8.6.1 (7) does permit

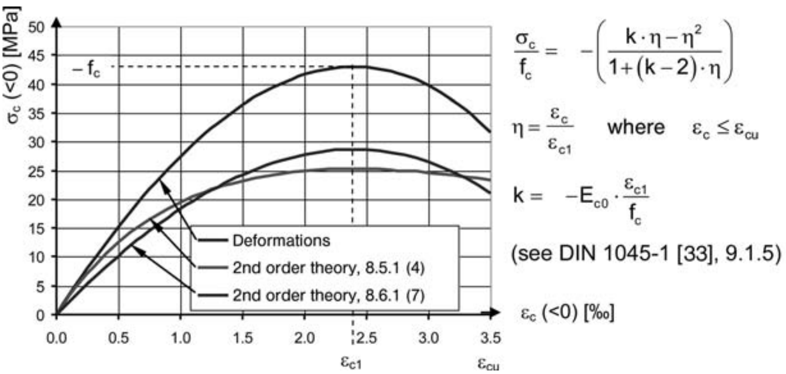

Fig. 3.1 Stress-strain curve for concrete for use in deformation calculations

1) Other values for the elastic modulus of concrete were specified in [36]. The following applies for the secant moduli: E_{cm} [MPa] $= 22\,000 \cdot (f_{cm}/10)^{0.3}$. The following applies for the tangent moduli: $E_{c0m} = 1.05 \cdot E_{cm}$.

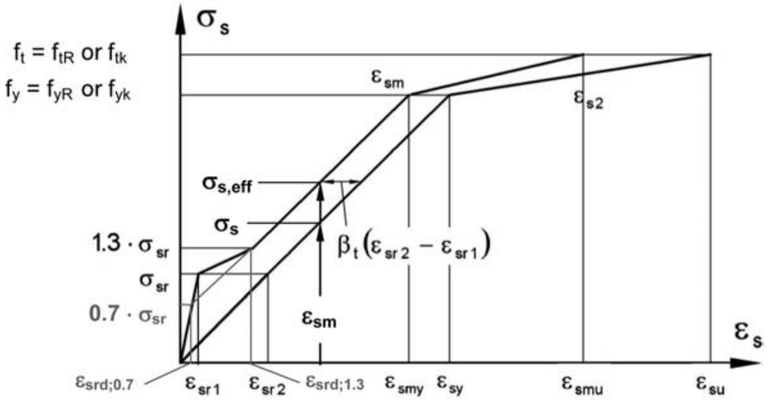

Fig. 3.2 Stress-strain curve for steel reinforcement for use in deformation calculations, including tension stiffening (see [35] 8.5.1)

the use of the mean values of the material properties divided by the partial safety factor ($\gamma_C = 1.50$ or $\gamma_{CA} = 1.30$) (Table 3.1):

$$f_c = \frac{f_{cm}}{\gamma_C} = \frac{f_{ck} + 8[\text{MPa}]}{\gamma_C} \quad \text{and} \quad E_{c0} = \frac{E_{c0m}}{\gamma_C} \quad \left(\text{or} \quad E_c = \frac{E_{cm}}{\gamma_C}\right)$$

In the latter case, however, the design values of the material strengths (e.g. $\alpha \cdot f_{ck}/\gamma_C$) have to be used for determining the ultimate load-carrying capacity at the critical cross-section.

3.2.2 Non-linear stress-strain curve for reinforcing steel

Figure 3.2 applies to reinforcement in tension. The bilinear stress-strain curve of DIN 1045-1 [33] 9.2 applies to reinforcement in compression.

According to Figure 3.2, the unfavourable tension stiffening effect can be taken into account for the redistribution of the internal forces in statically indeterminate structures. However, when calculating the internal forces according to second-order

Table 3.1 Comparison of both approaches for normal-strength concretes (see also Figure 3.1)

DIN 1045-1	Concrete	C 12/15	C 16/20	C 20/25	C 25/30	C 30/37	C 35/45	C 40/50	C 45/55	C 50/60
8.5.1 (4)	f_{cR} [MPa] =	8.67	11.56	14.45	18.06	21.68	25.29	28.90	32.51	36.13
	E_{cR} [MPa] =	25 787	27 403	28 848	30 472	31 939	33 282	34 525	35 685	36 773
	k =	5.354	4.504	4.192	3.711	3.389	3.159	2.987	2.799	2.647
8.6.1 (7)	f_c[MPa] =	*13.33*	*16.00*	*18.67*	*22.00*	*25.33*	*28.67*	*32.00*	*35.33*	*38.67*
	E_{c0}[MPa] =	*17 191*	*18 268*	*19 232*	*20 314*	*21 293*	*22 188*	*23 017*	*23 790*	*24 516*
	k =	*2.321*	*2.169*	*2.164*	*2.031*	*1.933*	*1.858*	*1.798*	*1.717*	*1.648*

theory, tension stiffening brings about a decrease in the deformations and hence an increase in the ultimate resistance. Therefore, the partial safety factor $\gamma_C = 1.50$ should be used for the load-carrying capacity of the concrete. Consequently, we get the following equations for the effective stress in the steel $\sigma_{s,eff}$ and the effective stiffness modulus $E_{s,eff}$:

a) Uncracked ($0 < \varepsilon_s \leq \varepsilon_{srd;0.7}$):
In this case the appearance of the first crack should be assumed to coincide with reaching the design value of the concrete tensile strength f_{ctd}:

$$f_{ctd} = \frac{f_{ctk;0.05}}{\gamma_C} = \frac{0.7 \cdot f_{ctm}}{\gamma_C}; \quad \varepsilon_{srd;0.7} = \frac{f_{ctk;0.05}}{E_{c0m}} = \frac{0.7 \cdot f_{ctm}}{E_{c0m}}$$

$$\sigma_{s,eff} = \underbrace{E_s \cdot \frac{1 + \alpha_{Ed} \cdot \rho_s}{\alpha_{Ed} \cdot \rho_s}}_{E_{s,eff}} \cdot \varepsilon_s \leq \sigma_{s,eff;0.7} = \frac{0.7 \cdot f_{ctm}}{\gamma_C} \cdot \frac{1 + \alpha_{Ed} \cdot \rho_s}{\rho_s} = \frac{0.7 \cdot \sigma_{sr}}{\gamma_C}$$

$$\text{with} \quad \rho_s = \frac{A_s}{A_c}, \quad \alpha_{Ed} = \gamma_C \cdot \frac{E_s}{E_{c0m}} \quad \text{and} \quad \sigma_{sr} = f_{ctm} \cdot \frac{1 + \alpha_{Ed} \cdot \rho_s}{\rho_s}$$

b) Formation of cracks ($\varepsilon_{srd;0.7} < \varepsilon_s \leq \varepsilon_{srd;1.3}$):

$$\sigma_{s,eff;1,3} = \frac{1.3 \cdot \sigma_{sr}}{\gamma_C}; \quad \varepsilon_{srd;1.3} = \frac{f_{ctm}}{E_{c0m}} \cdot \frac{1.3 \cdot (1 + \alpha_{Ed} \cdot \rho_s) - \beta_t}{\alpha_{Ed} \cdot \rho_s}$$

The value of $\varepsilon_{srd;1.3}$ results from considering the stabilised cracking (c).

$$E_{s,eff} = \frac{\sigma_{s,eff;1.3} - \sigma_{s,eff;0.7}}{\varepsilon_{srd;1.3} - \varepsilon_{srd;0.7}} = \frac{0.6 \cdot E_s \cdot (1 + \alpha_{Ed} \cdot \rho_s)}{1.3 + 0.6 \cdot \alpha_{Ed} \cdot \rho_s - \beta_t}$$

c) Stabilized cracking ($\varepsilon_{srd;1.3} < \varepsilon_s \leq \varepsilon_{smy}$):
In this case the tension stiffening, similarly to DIN 1045-1 [33] 8.6.1 (7), should be based on the reduced mean value of the concrete tensile strength f_{ctm}/γ_C:

$$\varepsilon_{sm} = \varepsilon_{s2} - \beta_t \cdot (\varepsilon_{sr2d} - \varepsilon_{sr1d}) = \varepsilon_{s2} - \beta_t \cdot \left(\frac{\sigma_{sr}}{\gamma_C \cdot E_s} - \frac{f_{ctm}}{E_{c0m}}\right) = \varepsilon_{s2} - \frac{f_{ctm}}{E_s} \cdot \frac{\beta_t}{\gamma_C \cdot \rho_s}$$

where

β_t coefficient for taking into account the influence of the duration of loading or a repeated loading on the mean strain according to DAfStb No. 525, 8.5.1 [35] ($\beta_t = 0.40$ for a single short-term loading)

$$\sigma_s = E_s \cdot \varepsilon_{sm} = \sigma_{s,eff} - \beta_t \cdot \left(\frac{\sigma_{sr}}{\gamma_C} - \alpha_{Ed} \cdot \frac{f_{ctm}}{\gamma_C}\right) = \sigma_{s,eff} - f_{ctm} \cdot \frac{\beta_t}{\gamma_C \cdot \rho_s}$$

$$\sigma_{s,eff} = \sigma_s + f_{ctm} \cdot \frac{\beta_t}{\gamma_C \cdot \rho_s}$$

The $\sigma_{s,eff} - \varepsilon_s$ and $\sigma_s - \varepsilon_s$ curves are parallel and therefore $E_{s,eff} = E_s$.
We have the following situation when crack formation is complete:

$$\frac{1.3 \cdot \sigma_{sr}}{\gamma_C} = E_s \cdot \varepsilon_{srd;1.3} + f_{ctm} \cdot \frac{\beta_t}{\gamma_C \cdot \rho_s}; \quad \varepsilon_{srd;1.3} = \frac{f_{ctm}}{E_{c0m}} \cdot \frac{1.3 \cdot (1 + \alpha_{Ed} \cdot \rho_s) - \beta_t}{\alpha_{Ed} \cdot \rho_s}$$

The characteristic value for the yield point f_{yk} is reached for

$$\varepsilon_{smy} = \frac{f_{yk}}{E_s} - \frac{f_{ctm}}{E_{c0m}} \cdot \frac{\beta_t}{\alpha_{Ed} \cdot \rho_s} = \frac{f_{yk}}{E_s} - \frac{f_{ctm}}{E_s} \cdot \frac{\beta_t}{\gamma_C \cdot \rho_s}$$

d) Yielding of the steel ($\varepsilon_s > \varepsilon_{smy}$):
Without taking into account strain hardening, the result is $\sigma_{s,eff} = f_{yk}$.

Tension stiffening is very much dependent on the stress σ_{sr} leading to the appearance of the first crack. The tension stiffening effect of the concrete between the cracks therefore increases as the percentage of reinforcement decreases (Figure 3.3).

A section is said to be under-reinforced when the steel reinforcement reaches its yield point before the tensile strength of the concrete is exceeded. Such a minimal percentage of steel reinforcement should be avoided because the reinforcement would fail suddenly upon the appearance of the first crack. In a similar way to DIN 1045-1 [33] 13.1.1 (1), the following condition must be complied with in order to guarantee ductile behaviour of a structural member:

$$\sigma_{sr} = \frac{f_{ctm}}{\rho_s} \cdot (1 + \alpha_{Ed} \cdot \rho_s) < f_{yk}$$

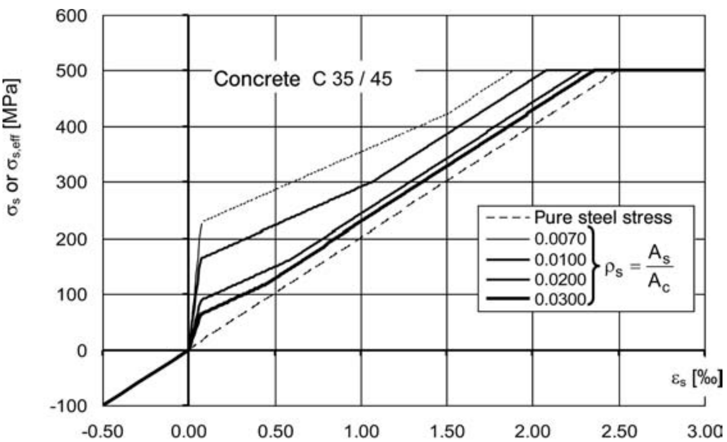

Fig. 3.3 Tension stiffening effect for different reinforcement percentages

where

f_{ctm} mean value of concrete tensile strength to DIN 1045-1 [33] Tables 9 or 10.
f_{yk} characteristic value of yield point of steel reinforcement

$$\alpha_{Ed} = \frac{E_s}{E_{c0}} = \gamma_C \cdot \frac{E_s}{E_{c0m}}$$

where

E_{c0m} see DIN 1045-1 [33] Tables 9 or 10[2)]

From this we get the minimum reinforcement (see Table 3.2):

$$\rho_s > \frac{f_{ctm}}{f_{yk} - \alpha_{Ed} \cdot f_{ctm}}$$

3.2.3 Non-linear stress-strain curve for prestressing steel

We generally assume an idealised bilinear curve (see Figure 3.4).

According to [36], the maximum strain in the prestressing steel at the ultimate limit state is

$$\varepsilon_{pud} = \varepsilon_p^{(0)} + 25‰ \leq 0.9 \cdot \varepsilon_{puk}$$

Provided the upper limit ($0.9 \cdot \varepsilon_{puk}$) does not govern, the reinforcing steel can be used up to the design value of its maximum strain ($\varepsilon_{sud} = 25‰$) in the case of pretensioning or post-tensioning (Figure 3.5).

Table 3.2 Minimum percentage of reinforcement for ductile behaviour of structural member

Concrete	f_{ck} [MPa]	f_{ctm} [MPa]	E_{c0m} [GPa]	α_{Ed}	min ρ_s [%]
C 12/15	12	1.57	25.8	11.63	0.33
C 16/20	16	1.90	27.4	10.95	0.40
C 20/25	20	2.21	28.8	10.42	0.46
C 25/30	25	2.56	30.5	9.84	0.54
C 30/37	30	2.90	31.9	9.40	0.61
C 35/45	35	3.21	33.3	9.01	0.68
C 40/50	40	3.51	34.5	8.70	0.75
C 45/55	45	3.80	35.7	8.40	0.81
C 50/60	50	4.07	36.8	8.15	0.87

2) According to [36], other values apply for the tangent moduli (see above).

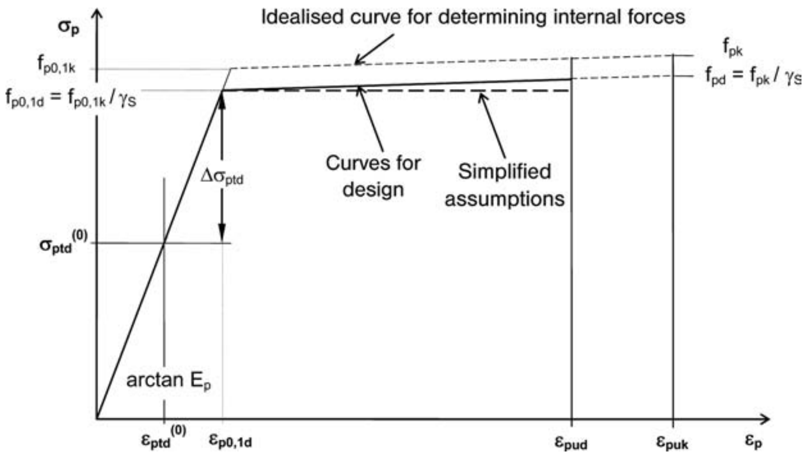

Fig. 3.4 Stress-strain curve for prestressing steel for calculating internal forces and for detailed design (without tension stiffening)

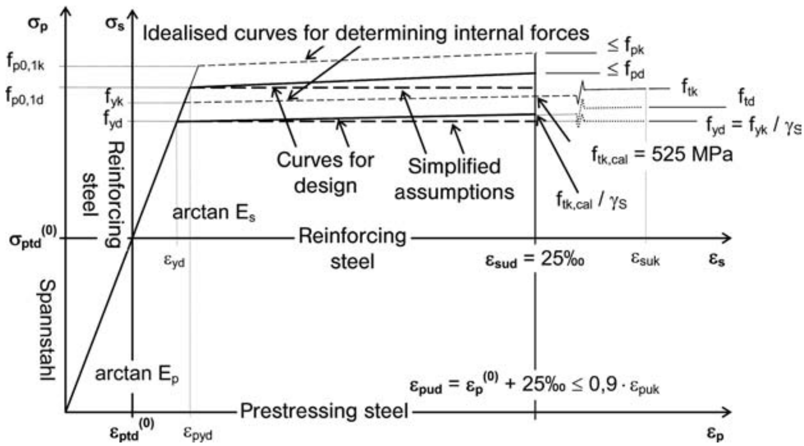

Fig. 3.5 “Collaboration” between the stress-strain curves for prestressing and reinforcing steel for use in detailed design

3.3 Bending moment-curvature relationships

3.3.1 Reinforced concrete cross-sections in general

The following conditions apply for analyses according to second-order theory:

- The member cross-sections remain plane up until failure (Bernoulli hypothesis).
- The strains remain within the limits given in DIN 1045-1 [33], that is $\varepsilon_s \leq 25‰$, $\varepsilon_c \geq -3.5‰$; failure of the cross-section is equivalent to one of these strains being reached.
- The stress-strain curves for the physical non-linear behaviour according to Section 3.2 are assumed.

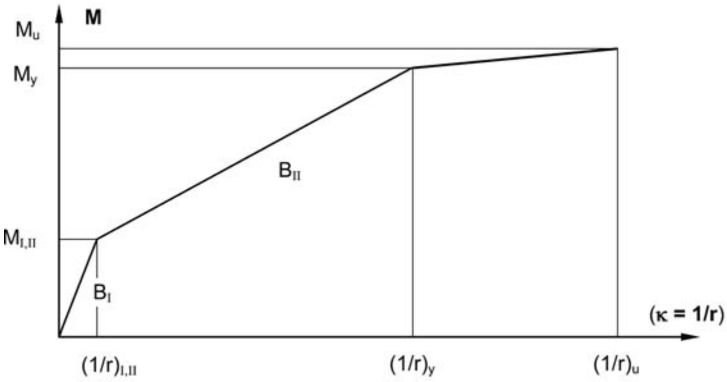

where

B_I, B_{II} bending stiffness in uncracked state (I)($= E_{cm} \cdot I_{c,I}$) or cracked state (II) ($= dM/d(1/r)$)

$M_{I,II}$ bending moment at transition from uncracked (I) to cracked state (II)(= *cracking moment*)

M_y moment at yielding of steel reinforcement

M_u moment at failure of steel reinforcement or concrete

$(1/r)_{I,II}$ curvature associated with $M_{I,II}$ ($= M_{I,II}/B_I$)

Fig. 3.6 Bending moment-curvature relationship (rectangular reinforced concrete cross-section) to DIN 1045-1 [33] 8.5.2

From this it follows that a *bending moment-curvature relationship* for a rectangular cross-section is approximately *trilinear* (see Figure 3.6).

In order to be able to use this relationship in the calculations, it is sufficient to determine the positions of the kinks, that is the transition from the uncracked (I) to the cracked (II) state, the onset of yield in the flexural tension reinforcement and the failure condition.

Furthermore, the quantitative progression of the bending moment-curvature curve (M-κ curve) depends on the *magnitude of the axial force* N_{Ed}. A change in N_{Ed} therefore changes the shape of the M-κ curve (see Section 3.3.3).

3.3.2 Prestressed concrete cross-sections in general

The character of the bending moment-curvature relationship is different for *prestressed concrete cross-sections*. One difference is that the prestressing acts like an external compressive force. This force generally acts eccentrically in the case of beams (see Figure 3.7), but concentrically in towers (see Figure 3.9). The *cracking moment* ($M_{I,II}$) therefore increases, in the case of eccentric prestressing also helped by the *precambering* ($\kappa_0 = (1/r)_0$).

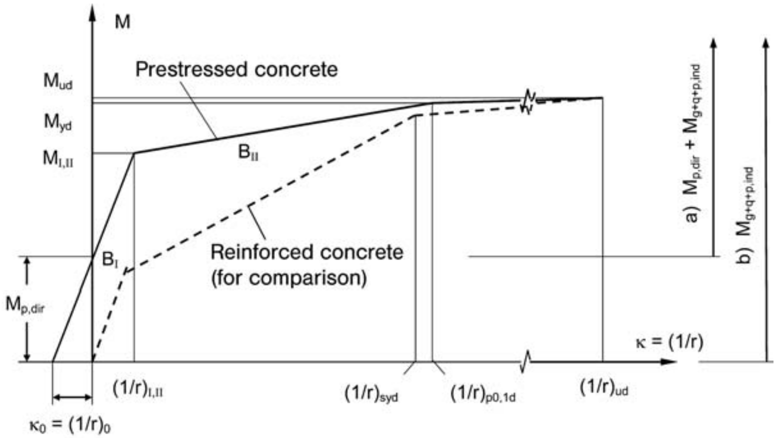

Note: Ordinate (a) indicates the bending moment (including the primary effects of prestressing) acting on the reinforced concrete cross-section, whereas ordinate (b) specifies the bending moment acting on the total cross-section (including prestress ing steel).

Fig. 3.7 Bending moment-curvature relationship for rectangular prestressed concrete cross-sections (simplified)

The progression of the M-κ relationship after exceeding $M_{I,II}$ differs according to the type of prestress:

– *Pretensioned and grouted post-tensioned tendons*: The M-κ relationship in the cracked state (II) is generally flatter than for the non-prestressed reinforced concrete cross-section, depending on the cross-sectional area of the prestressing steel. The prestressing steel contributes to carrying the external action effects up until the 0.1% proportionality limit is reached ($f_{p0.1}$; $(1/r)_{p0.1}$). Its reserves of loadbearing capacity depend on the effective prestress $\sigma_P^{(0)}$ at the ultimate limit state taking into account all losses of prestress at the point in time being considered ($t_0 \leq t < \infty$), see Figures 3.4 and 3.5:

$$\Delta\sigma_{ptd} = f_{p0.1d} - \sigma_{ptd}^{(0)} = f_{p0.1k}/\gamma_S - \gamma_P \cdot \sigma_{Pmt}^{(0)}$$

– *Internal* or *external unbonded tendons*: The cross-section of the prestressing steel only contributes to carrying the external action effects via the internal statically indeterminate coupling with the reinforced concrete cross-section. If this is neglected, the cross-section behaves like a reinforced concrete cross-section with an additional eccentric or concentric compressive force.

3.3.3 Annular reinforced concrete cross-sections

Figure 3.8 shows the strain condition in an annular reinforced concrete cross-section.

Converting the cylindrical coordinates into Cartesian coordinates:

$$\begin{aligned} y_{wj} &= r_w \cdot \cos\alpha_j \\ z_{wj} &= r_w \cdot \sin\alpha_j \end{aligned}$$

with the indices w = i (inner edge), si (inner reinforcement), m (centre-line of wall), sa (outer reinforcement) and a (outer edge)

The individual pairs of values $M_z = M\ (\kappa_z)$ are determined iteratively as follows:

a) Start values for iteration step k = 1:
Specify a curvature κ_z for which the bending moment M_z is to be found.
Specify the normal force action effect N_x.
Calculate the start value of the concentric strain (i.e. compressive strain):

$$\varepsilon_{xk} = \frac{N_x}{E_{c0} \cdot A_c + E_s \cdot A_s} = \frac{N_x}{E_{c0} \cdot \left(r_a^2 - r_i^2\right) \cdot \pi + E_s \cdot \left(a_{si} \cdot r_{si} + a_{sa} \cdot r_{sa}\right) \cdot 2 \cdot \pi}$$

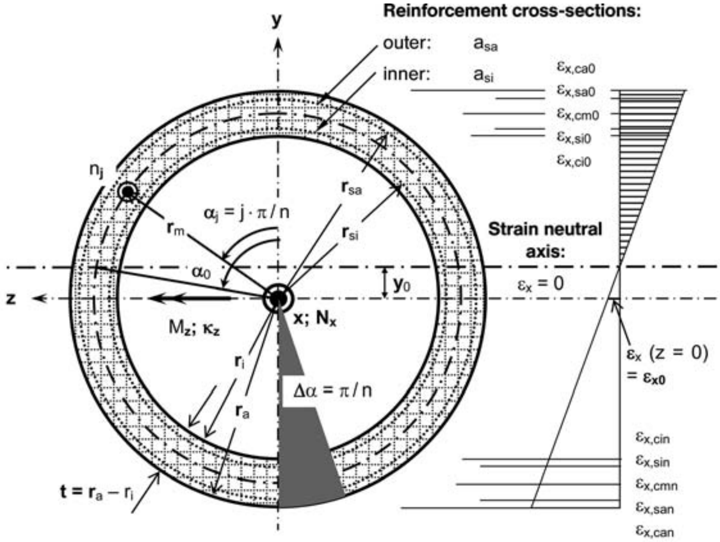

<u>Legend</u>

Maximum compressive strains ($\alpha = 0°$)		Maximum tensile strains ($\alpha = 180°$)	
$\varepsilon_{x,ca0}$	at outer edge ($y = +r_a$)	$\varepsilon_{x,cin}$	at inner edge ($y = -r_i$)
$\varepsilon_{x,sa0}$	at position of outer reinforcement ($y = +r_{sa}$)	$\varepsilon_{x,sin}$	at position of inner reinforcement ($y = -r_{si}$)
$\varepsilon_{x,cm0}$	on centre-line of wall ($y = +r_m$)	$\varepsilon_{x,cmn}$	on centre-line of wall ($y = -r_m$)
$\varepsilon_{x,si0}$	at position of inner reinforcement ($y = +r_{si}$)	$\varepsilon_{x,san}$	at position of outer reinforcement ($y = -r_{sa}$)
$\varepsilon_{x,ci0}$	at inner edge ($y = +r_i$)	$\varepsilon_{x,can}$	at outer edge ($y = -r_s$)

Fig. 3.8 Geometry of and strains in an annular reinforced concrete cross-section

b) Action effects on the concrete
Strains:

$$\begin{aligned}
\varepsilon_{x,cij} &= \varepsilon_{xk} - \kappa_z \cdot y_{ij} = \varepsilon_{xk} - \kappa_z \cdot r_i \cdot \cos\alpha_j \\
\varepsilon_{x,cmj} &= \varepsilon_{xk} - \kappa_z \cdot y_{mj} = \varepsilon_{xk} - \kappa_z \cdot r_m \cdot \cos\alpha_j \\
\varepsilon_{x,caj} &= \varepsilon_{xk} - \kappa_z \cdot y_{aj} = \varepsilon_{xk} - \kappa_z \cdot r_a \cdot \cos\alpha_j \\
\alpha_j &= j \cdot \Delta\alpha = j \cdot \pi/n; j = 0 \ldots n
\end{aligned}$$

Material law for determining internal forces to DIN 1045-1 [33]:

$$\frac{\sigma_c}{f_c} = \text{Min.}\left[0; \quad \frac{k \cdot \eta - \eta^2}{1 + (k-2) \cdot \eta}\right] \quad \text{(for details see section 3.2.1)}$$

This only takes into account the compressive stresses in the cross-section; tensile stresses in the concrete are taken into account through the tension stiffening of the reinforcing steel ($\sigma_{s,eff}$).
Integration of the stresses over the thickness of the cross-section:

$$\begin{aligned}
n_{cj} &= \frac{\pi}{n} \cdot \left(\sigma_{x,cij} \cdot r_i + 4 \cdot \sigma_{x,cmj} \cdot r_m + \sigma_{x,caj} \cdot r_a\right) \cdot \frac{t}{6}; \quad j = 0 \ldots n \\
m_{cj} &= \frac{\pi}{n} \cdot \left(\sigma_{x,cij} \cdot r_i \cdot y_{ij} + 4 \cdot \sigma_{x,cmj} \cdot r_m \cdot y_{mj} + \sigma_{x,caj} \cdot r_a \cdot y_{aj}\right) \cdot \frac{t}{6}; \quad j = 0 \ldots n
\end{aligned}$$

c) Action effects on the reinforcement
Strains:

$$\begin{aligned}
\varepsilon_{x,sij} &= \varepsilon_{x0} - \kappa_z \cdot y_{ij} = \varepsilon_{x0} - \kappa_z \cdot r_{si} \cdot \cos\alpha_j \\
\varepsilon_{x,saj} &= \varepsilon_{x0} - \kappa_z \cdot y_{aj} = \varepsilon_{x0} - \kappa_z \cdot r_{sa} \cdot \cos\alpha_j \\
\alpha_j &= j \times \pi/n
\end{aligned}$$

Material law for determining internal forces to DIN 1045-1:

$$\sigma_s = \text{Min.}\left[E_s \cdot \varepsilon_s; \quad \sigma_{s,eff}; \quad f_y\right]; \quad f_y = f_{ym}/\gamma_S \approx f_{yk} \quad \text{(for details see section 3.2.2)}$$

Note: As the deformations no longer converge once the yield point (f_y) has been exceeded, strain hardening is not considered.

Integration of the stresses over the thickness of the cross-section:

$$\begin{aligned}
n_{sj} &= \sigma_{x,sij} \cdot a_{si} + \sigma_{x,saj} \cdot a_{sa} \\
m_{sj} &= \sigma_{x,sij} \cdot a_{si} \cdot y_{sij} + \sigma_{x,saj} \cdot a_{sa} \cdot y_{saj} \\
j &= 0 \ldots n
\end{aligned}$$

d) Action effects on the total cross-section
Summary of the “differential” action effects:

$$\begin{aligned}
n_j &= n_{cj} + n_{sj}; \quad j = 0 \ldots n \\
m_j &= m_{cj} + m_{sj}; \quad j = 0 \ldots n
\end{aligned}$$

Integration over the circumference of the annular cross-section:

$$N_{x,k+1} = \frac{1}{3} \cdot \sum_{1}^{n/2} \left(n_{2\cdot j-2} + 4 \cdot n_{2\cdot j-1} + n_{2\cdot j} \right)$$

$$M_{z,k+1} = \frac{1}{3} \cdot \sum_{1}^{n/2} \left(m_{2\cdot j-2} + 4 \cdot m_{2\cdot j-1} + m_{2\cdot j} \right)$$

e) Calculation of the new (improved) value for concentric strain:

$$\varepsilon_{x,k+1} = \varepsilon_{x,k} + \frac{\varepsilon_{x,k} - \varepsilon_{x,k-1}}{N_{x,k} - N_{x,k-1}} \cdot \left(\mathbf{N}_x - N_{x,k} \right) \qquad \left(\varepsilon_{x,0} = 0; N_{x,0} = 0 \text{ applies for } k = 1 \right)$$

Once $N_{x,k} \cong N_x$, it is no longer necessary to continue the calculation. Otherwise, the iteration process must be continued with $k \rightarrow k + 1$ from step (b).

Figure 3.9 shows typical bending moment-curvature relationships for an annular cross-section determined with the iteration procedure described above.

The following parameters were selected for this:

Concrete: C 35/45
Reinforcing steel: BSt 500
Outside diameter: $r_a = 2.50\,m$
Inside diameter: $r_i = 2.00\,m$
Percentage of longitudinal reinforcement (alternative): $\rho_s = 0.006/0.03$
Normal forces (alternative): $N_x = 0/-50$ MN

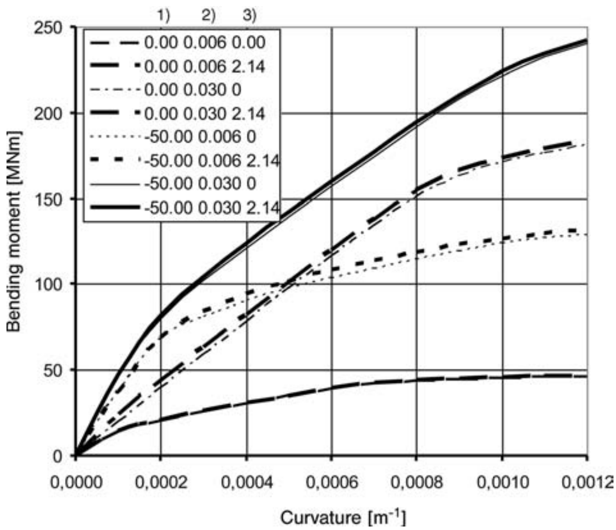

Fig. 3.9 Bending moment-curvature relationships for an annular cross-section subjected to different normal forces

The M-κ curves are shown alternately with and without tension stiffening.
The values in the legend are: 1) normal force N_x, 2) percentage of reinforcement ρ_s, 3) design value for tensile strength f_{ctd}.
The value $f_{ctd} = 0$ means that tension stiffening was ignored.

In contrast to the rectangular cross-section, the result is continuously curved M-κ curves – without the distinctive kinks upon reaching the decompression state or the yield point of the reinforcement. The reasons for this are the annular form of the cross-section and the reinforcement uniformly distributed around the circumference.

Tension stiffening has a relatively stronger effect with a lower percentage of reinforcement ρ_s and a lower normal force N_x (see Figure 3.3). It may certainly be neglected with high percentages of reinforcement yet still remain on the safe side, see DIN 1045-1 [33] 8.6.1 (8).

3.4 Deformations and bending moments according to second-order theory

For a given bending moment diagram M_z (x), it is possible to determine the associated course of the curvatures $\kappa_z (x) = \kappa (M_z (x))$ along the bar axis. This is done with the help of the M-κ curves, which depend on the associated normal forces (see *Beton-Kalender 2006* [8] for an example of an application).

The yield condition described in Section 3.1, which is based on the model column method[3)] according to DIN 1045-1 [33], is not reached when calculating the deformations of a slender tower with the help of second-order theory because the member already becomes unstable at an earlier stage due to the increasing deformation as the bending stiffness decreases. Therefore, the portions of the M-κ curves beyond the yield point of the reinforcement are irrelevant for practical applications.

Integrating twice while taking into account the boundary conditions enables us to calculate the rotations φ_z (x) and the deflection f_y (x) from the curvatures κ_z (x). It is worth carrying out a numerical integration according to the trapezoidal rule or Simpson's rule, paying special attention to discontinuities, for example at abrupt changes in cross-section or for sudden changes of loading.

The final bending moments according to second-order theory are determined iteratively. The starting point is the bending moment diagram according to first-order theory – or possibly the bending moments according to second-order theory based on an estimated deflection curve.

The convergence criterion is satisfying the equilibrium conditions. This calculation can generally be carried out easily by hand by comparing the loads acting on the deformed structure (deflection curve) and the support reactions.

[3)] The *model column method* is equivalent to the *method based on nominal curvature* acc. to DIN EN 1992-1-1 [23] 5.8.8.

The bending moments according to second-order theory at the base of a concrete chimney can be estimated with the following approximation [13]:

$$M_{Ed}^{II} = M_{Ed}^{I} \cdot \left(1 + 0.9 \cdot \alpha^2\right)$$

where

$$\alpha^2 = \frac{N \cdot h_F^2}{E_{cm} \cdot I_c}$$

E_{cm} mean value of the secant modulus of the concrete
I_c mean value of the second moments of area of the shaft cross-sections
h_F total height of deformed structure
N vertical load at base of tower (chimney)

This approximation can generally be used as a guide for reinforced concrete towers as well.

3.5 Design of cross-section for ultimate limit state

The member cross-sections have to be designed for the internal forces that were determined according to second-order theory with the reduced mean values of the material properties for short-term action effects ($f_{cR} = (f_{ck} + 8)/\gamma_C$; $f_{yR} = f_{yk}$), but with the design values of the material properties for permanent action effects ($f_{cd} = \alpha \cdot f_{ck}/\gamma_C$; $f_{yd} = f_{yk}/\gamma_S$; see DIN 1045-1 [33] 8.6.1 (7)).

If this results in a reinforcement requirement that is larger than was used for the deformation calculation, then this reinforcement is on the safe side and may be selected for construction. Performing the deformation calculation again with more reinforcement would lead to less deflections and hence to lower bending moments in the deformed system, that is ultimately to less reinforcement being needed as well. An iterative procedure enables the amount of steel reinforcement to be optimised.

3.5.1 Material resistance of concrete

The parabolic-rectangular stress diagram according to DIN 1045-1 [33] is used here, but with the constraint shown in Figure 3.10 for the compressive strain in the concrete in the centre-line of the shaft wall in compression. This corresponds to the stipulation for the design of fully overcompressed flange plates in T-beam cross-sections and also the provision according to [13] applied hitherto. The compressive strain in the concrete $-\varepsilon_{c2m}$ was merely raised to the compressive yield strain ε_{yd}, similarly to concentrically compressed members, so that the reinforcement in compression can be fully utilised.[4)]

However, it is quite acceptable to use this higher value as a limit value for compressive strain in the centre-line of the shaft wall provided, on the one hand, small creep deformations are taken into account and, on the other, we do not forget that stress

[4)] Comparison of the approaches for the material resistances given in DIN 1056 [13] and DIN 1045-1 [33], see *Beton-Kalender 2006* [8].

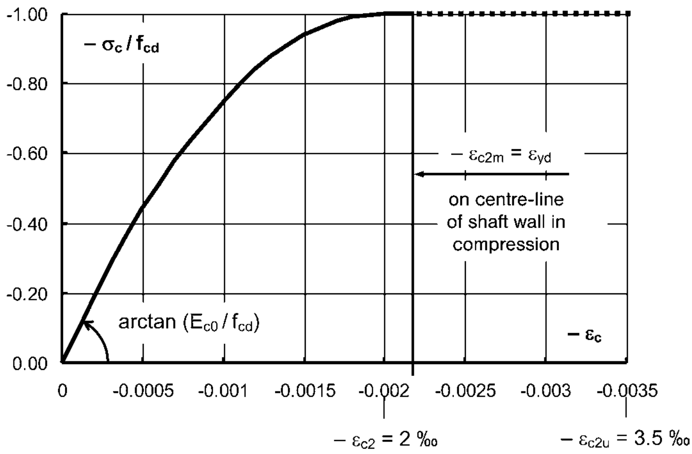

Note:
The values for strains ε_{c2} and ε_{c2u} apply for normal-strength concretes up to C 50/60.

Fig. 3.10 Concrete stress-strain curve for design

redistributions are possible, both to the inner shaft reinforcement and also to the sides of the most highly stressed segment of the shaft.

3.5.2 Material resistance of reinforcement

The bilinear diagram according to DIN 1045-1 [33], valid for tension and compression, is assumed for the *reinforcing steel* (Figure 3.11). Tension stiffening has no effect because tensile stresses in the concrete are not considered during the design.

The *prestressing steel stress-strain curve* for the detailed design also has a bilinear form (see Figure 3.4).

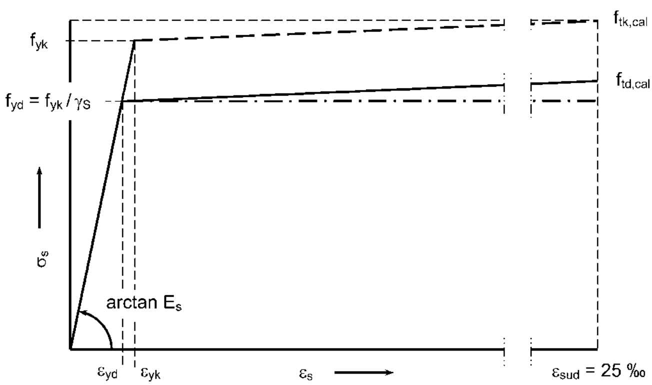

Fig. 3.11 Reinforcing steel stress-strain curve for design

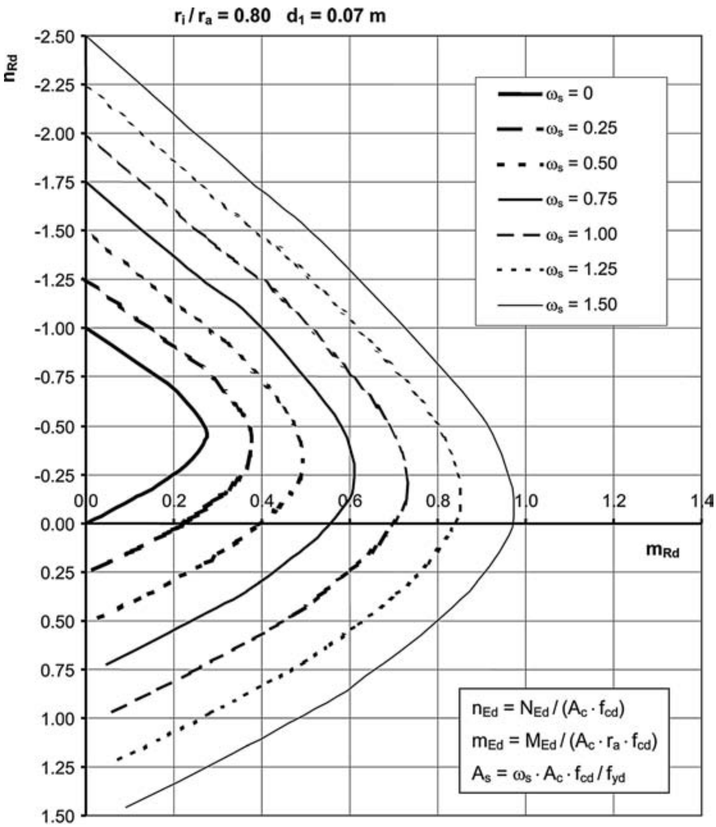

Fig. 3.12 Design chart for an annular cross-section with $r_i/r_a = 0.80$, $d_1 = 0.07$ m; valid for concrete grades C 12/15 to C 50/60

As an example, a design chart for annular cross-sections with the popular radius ratio $r_i/r_a = 0.8$ is given below (Figure 3.12). For further design charts see [8]. These design charts assume that half of the longitudinal reinforcement is positioned near the outer face, half near the inner face, and that every layer of reinforcement is positioned at an axial distance of $d_1 = 0.07$ m from the associated surface. This corresponds to an actual concrete cover amounting to approx. $c_V = 40$ mm for horizontal reinforcement on the outside.

As the input values are dimensionless internal forces, the design charts are valid for all normal-strength concretes (C 12/15 to C 50/60).

3.6 Three-dimensional mechanical models for concrete

Stress states in all three directions occur at many places in plain and reinforced concrete structures, for example in loadbearing zones with abrupt changes of stiffness or at concentrations of force transfers. Such situations are also found in towers and become significant when fatigue limit states can occur, as in the structural members of *wind turbines* (see Section 4.9). Three-dimensional mechanical models for concrete will therefore be looked at below; they are dealt with in more detail in [37,8]. Such models can provide a realistic description of the non-linear material behaviour, the crack formation, or rather the progressive damage, and the potential failure conditions, and can be fed into a numerical analysis with FEM programs.

The literature contains many uniaxial models which can satisfactorily describe non-linear material properties such as strain hardening, softening or crack formation. However, the three-dimensional models available are still unsatisfactory and thus require further development. Their parameters should be chosen in such a way that they can be calibrated with the help of tests.

3.6.1 Failure envelopes and stress invariants

The failure envelopes are frequently described geometrically by the stress invariants I_1, J_2 and J_3, see [38], for instance. Here, I_1 represents the hydrostatic stress state, whereas J_2 and J_3 are expressed by the components of the stress deviator. Formulating with the help of the Haigh-Westergaard coordinates ξ, ρ and θ is expedient. Figure 3.13 shows the intersection curves between the failure envelopes and a principal meridian plane and the deviatoric cross-sections.

The intersection between the failure envelopes and the stress plane $\sigma_{11} - \sigma_{22}$ (biaxial stress) results in a closed curve which can be compared with the results of tests according to Kupfer [39].

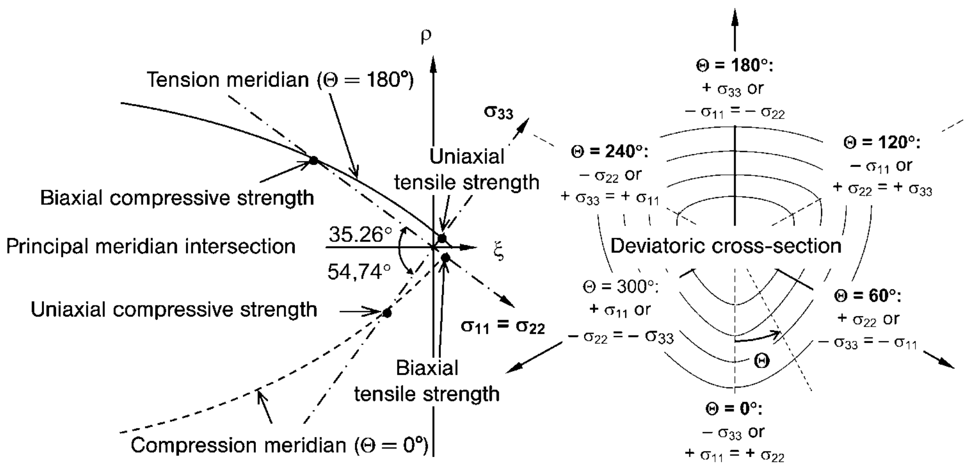

Fig. 3.13 Failure envelopes illustrated by means of Haigh-Westergaard coordinates

3.6.2 Common failure models for concrete

The following one-parameter models are among those described in the literature [40] as the simplest approaches:

- the *Rankine failure theory*,
- the *Tresca yield condition*, and
- the *Von Mises yield condition*.

These models can be used to describe brittle (Rankine) or ductile (Tresca, Von Mises) material behaviour, but not the full complexity of concrete. Therefore, the following two-parameter models [40] are frequently used for concrete (and related mineral materials):

- the *Mohr-Coulomb yield condition*, or
- the *Drucker-Prager yield condition*, which describes a cone whose axis of rotation is the ξ axis:

$$f(\xi, \rho) = \sqrt{6} \cdot \alpha \cdot \xi + \rho - \sqrt{2} \cdot k = 0$$

In order to adapt this yield condition to the biaxial failure condition [39], the angle of the surface of the cone α must be small. Distinguishing between ductile and brittle concrete failures is then only possible if it is postulated that both the Drucker-Prager yield condition and the principal stress criterion of Rankine are satisfied – as is illustrated in Figure 3.14 for biaxial stress.

The three-dimensional edges that result from the intersection between the Drucker-Prager cone and the three Rankine planes cannot be understood in physical terms and represent a problem for the numerical analysis. On the other hand, fracture surfaces evolve continuously when higher-value models are used, for example:

- the *Willam-Warnke three-parameter model*, or
- the *Willam-Warnke five-parameter model* [41].

The *three-parameter model* develops the failure envelope from the Drucker-Prager cone by introducing the tension and compression meridians with different angles and generating the intervening cone surfaces by way of elliptical interpolation. The compression meridians describe stress states $\sigma_{11} < \sigma_{22} = \sigma_{33}$; the tension meridians, on the other hand, describe stress states $\sigma_{11} > \sigma_{22} = \sigma_{33}$. The three free parameters are determined from the uniaxial compressive strength $f_{c,1}$, the uniaxial tensile strength $f_{ct,1}$ and the biaxial compressive strength $f_{c,2}$ [41].

The difference between the *five-parameter* and the *three-parameter models* is that the principal meridians are not assumed to be straight lines, but rather second-order parabolas:

$$f(\xi, \rho, \theta_{INT}) = \frac{\rho}{\sqrt{5} \cdot f_{c,1} \cdot r(\xi, \theta_{INT})} - 1 = 0$$

Compression meridian:

$$r_1(\xi) = a_0 + a_1 \cdot (\xi / f_{c,1}) + a_2 \cdot (\xi / f_{c,1})^2$$

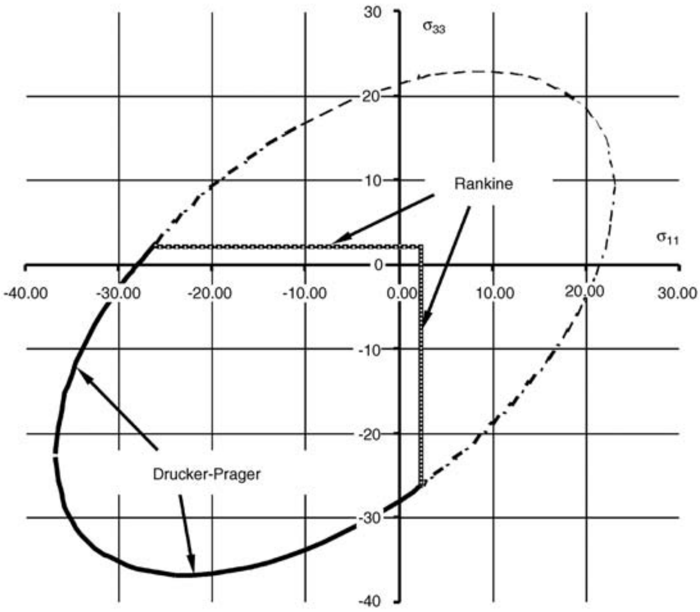

Fig. 3.14 Drucker-Prager or Rankine failure in biaxial stress

Tension meridian:

$$r_2(\xi) = b_0 + b_1 \cdot (\xi/f_{c,1}) + b_2 \cdot (\xi/f_{c,1})^2$$

Convexity condition:

$$r_1/2 < r_2 \leq r(\theta_{INT}) \leq r_1$$

(elliptical interpolation for $-60° \leq \theta_{INT} \leq +60°$)

The principal meridians meet at the apex of the cone and therefore produce two additional free parameters – the "high" tension meridian stress f_Z and the "high" compression meridian stress f_D – in order to determine the coefficients a_0, a_1, a_2 and b_0, b_1, b_2 [41]. See [8] for more details.

Whereas the strength values $f_{c,1}$, $f_{c,2}$ and f_{ct} have to be obtained from tests, the "high" meridian stresses should lie in the region of the largest hydrostatic compression action effect of the structure being investigated. The idea is that the five-parameter model approximates the Von Mises model for these limit states.

3.6.3 Three-phase model

The aim of this model is to formulate a continuously differentiable approach – and hence an approach suitable for numerical analyses – which can be adapted to the test results available with the help of a few physically sensible parameters

[37]. Taking this objective into account, this model should satisfy the following conditions:

1. Fractures occur in zones with principal tensile stresses close to the tensile strength. Rankine's failure hypothesis can be used in these zones ("brittle phase").
2. As the hydrostatic pressure increases, so the failure modes change (hybrid failure behaviour). The failure meridians gradually curve towards the hydrostatic stress axis ("transition phase").
3. Shear failures can be expected at high hydrostatic pressures. They can be described with meridians at a shallow angle to the hydrostatic stress axis ("ductile phase"). The design approach for confined columns according to [42]. can be employed in order to describe the principal meridians mathematically.

This results in a failure surface that is similar to a Rankine failure surface for positive and small negative mean stresses and gradually changes to an elliptically curved failure surface for larger negative mean stresses.

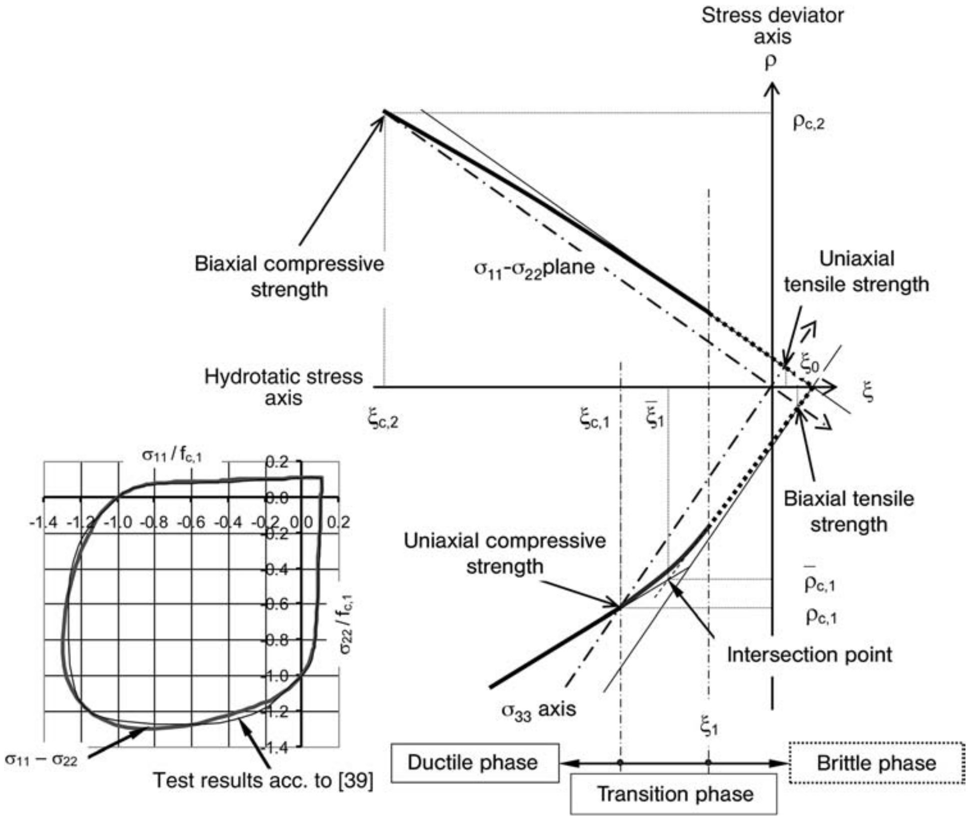

Fig. 3.15 Three-phase model, principal meridian intersection curve, biaxial stress intersection curve

One important aspect here is the tendency to use ever higher concrete strengths for building reinforced concrete towers in the future. The three-phase model is suitable for describing the material behaviour of high-performance concrete (HPC), even ultra-high-performance concrete (UHPC). One subproject in the "Sustainable building with UHPC" programme of the German Research Foundation (DFG) focuses on the uniaxial and multi-axial fatigue behaviour of UHPC.

It is very easy to see in Figure 3.15 how – starting from the brittle phase – the ductility increases with increasing hydrostatic pressure. The figure also shows that the three-phase model allows a very good approximation of the test results according to [39].

3.6.4 Constitutive models

In addition to the failure models, we require constitutive models with which we can describe the deformation behaviour and damage development, elastic and non-elastic behaviour, strain hardening and softening. Constitutive models for concrete are described in various sources, for example [38,43].

As a starting point for further deliberations, the reader is referred to the non-linear–elastic model with isotropic damage described in [8].

4 Loadbearing structures and detailed design

The basic concepts for the analysis of towers according to second-order theory were dealt with in Section 3. This section is intended to provide the reader with an overview of the structural engineering plus special aspects of the design.

4.1 Basis for design

The following publications generally apply to the *structural engineering for onshore wind turbines*:

- DIBt guideline [9]: *Richtlinie für Windenergieanlagen, Einwirkungen und Standsicherheitsnachweise für Turm und Gründung*, March 2004
- DIN EN 61400-1 [16]: Wind turbines – Part 1: Design requirements, August 2007

The *structural engineering for offshore wind turbines* should be based on the following publications when GL certification is required:

- GL Guideline [11]: Germanischer Lloyd WindEnergie GmbH (pub.): *Rules and Guidelines. IV Industrial Services – 2 Guideline for the Certification of Offshore Wind Turbines*, 2005
- DIN EN 61400-3 [10]: Wind turbines – Part 3: Design requirements for offshore wind turbines, January 2010

The *actions* on wind turbines should be based on the following standards and guidelines in particular:

- DIN 1055-100 [44]: Actions on structures – Part 100: Basis of design, safety concept and design rules, March 2001
- DIN EN 1990 [45]: Basis of structural design, October 2002 – with DIN EN 1990/NA 1 [46]: National Annex – Nationally determined parameters, 2010
- DIN 1055-4 [12]: Actions on structures – Part 4: Wind loads, March 2005, 1st amendment, March 2006
- DIN 1055-9 [47]: Actions on structures – Part 9: Accidental actions, August 2003

The *detailed design* of wind turbine support structures in reinforced and prestressed concrete should be based on the following standards and guidelines in particular:

- DIN 1045-1 [33]: Concrete, reinforced and prestressed concrete structures – Part 1: Design and construction, August 2008
- DIN EN 1992-1 [48]: Eurocode 2: Design of concrete structures – Part 1-1: General rules and rules for buildings, 2005 – with DIN EN 1992-1-1/NA [36]: National Annex – Nationally determined parameters, January 2011
- DAfStb No. 525 [35]: Erläuterungen zu DIN 1045-1, 2003 (new ed. 2010)
- DAfStb No. 439 [49]: Ermüdungsfestigkeit von Stahl- und Spannbetonbauteilen mit Erläuterungen zu den Nachweisen gemäß CEB-FIP Model Code 1990
- DIN 1054 [50]: Ground – Verification of the safety of earthworks and foundations, 2005

Concrete Structures for Wind Turbines. First edition. Jürgen Grünberg, Joachim Göhlmann.

4.2 Structural model for tower shaft

A structural model must be devised for the structural calculations. It is easy to see that the primary structure comprises the tower and the foundation, whereas mast extension, antenna platforms and plant floor are secondary structures. The latter items must be analysed separately and their support reactions applied to the primary structure.

The structural analysis of the primary structure at the ultimate limit state requires a numerical model that can be used to ascertain both the geometrical non-linearity (second-order theory) and the physical non-linearity of the material laws (see Section 3.1).

Figure 4.1 shows the elements of the structural model:[1)]

1. Idealisation as a bar structure with nodes at designated levels or regular intervals ($a \approx 1 \cdot \varnothing$ to $2 \cdot \varnothing$)
2. Bar elements with an annular cross-section that varies linearly (see Section 3.3.3)
3. Rotational springs for the elastic support on the subsoil

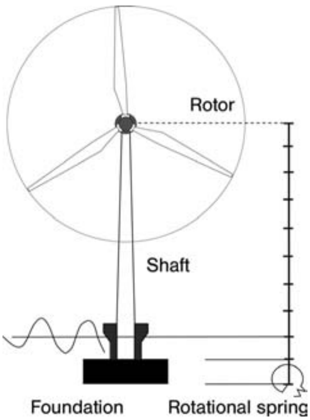

Fig. 4.1 Structural model

4.2.1 Rotation of the foundation

A permanent rotation of the foundation independent of the loading or dependent on the permanent loading is specified as an imperfection. Such non-uniform subsoil deformations must be considered in the case of cohesive soils in particular and are generally specified by a soil mechanics specialist (see also Section 4.7.1). A brief rotation of the foundation φ (essentially due to the wind load) is based on a quasi-elastic subsoil deformation and calculated as follows [51] (Figure 4.2, see also [52]):

$$\varphi = \frac{M_{found}}{c_s \cdot I_{found}}$$

[1)] See *Beton-Kalender 2006* [8].

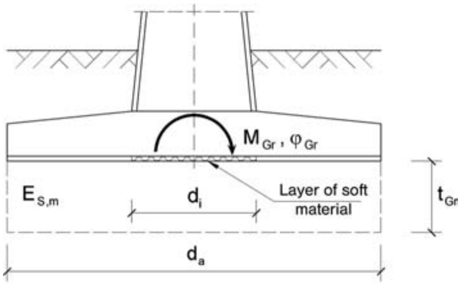

Fig. 4.2 Reaction in the subsoil to the tower loads acting on an annular foundation

where

M_{found}	fixed-end moment at soil/structure interface
c_s	foundation modulus
I_{found}	second moment of area for area of foundation

Only the rotation of the foundation dependent on a short-term increase in the fixed-end moment at the soil/structure interface is significant for the *vibration calculation* (see Section 4.3) and the *calculation of deformations at the serviceability limit state*. According to [53], the foundation modulus for determining the subsoil deformations due to overturning amounts to

$$c_{s,dyn} = \frac{E_{s,dyn}}{f' \cdot \sqrt{A_{found}}} = \frac{E_{s,dyn}}{t_{found}}$$

where

$E_{s,dyn}$	dynamic modulus of compressibility
A_{found}	area of foundation
$f' = 0.25$	shape factor for overturning
$t_{found} = 0.25 \cdot \sqrt{A_{found}}$	effective depth for antisymmetric action effect

Non-elastic rotations of the foundation must be considered as well when *calculating the deformations according to second-order theory at the ultimate limit state* (see Section 4.7.1). In the author's experience, these non-linear effects can be taken into account approximately by assuming the static modulus of compressibility $E_{s,stat}$ instead of the dynamic one.

We get the following ratios depending on the type of soil [53]:

a) Non-cohesive soils: $\approx 2 < E_{s,stat}/E_{s,dyn} < \approx 4$
b) Cohesive soils: $\approx 6 < E_{s,stat}/E_{s,dyn} < \approx 20$

Accordingly, the static foundation modulus is as follows:

$$c_{s,stat} = \frac{E_{s,stat}}{f' \cdot \sqrt{A_{found}}} = \frac{E_{s,stat}}{t_{found}}$$

Taking the above assumptions, the (dynamic or static) rotational spring stiffness c_φ at the soil/structure interface can be calculated as follows:

$$c_\varphi = \frac{\partial M_{found}}{\partial \varphi} = c_s \cdot I_{found} = \frac{E_s \cdot I_{found}}{t_{found}} = \frac{4 \cdot E_s \cdot I_{found}}{\sqrt{A_{found}}}$$

This equation is evaluated below for the customary foundation forms:

a) Square pad foundation (side length a_{found}):

$$t_{found} = 0.25 \cdot a_{found}; \quad c_\varphi = 0.333 \cdot E_s \cdot a_{found}^3$$

b) Circular foundation (diameter d_{found}):

$$t_{found} = 0.25 \cdot (A_{found})^{0.5} = 0.125 \cdot \pi^{0.5} \cdot d_{found} = 0.222 \cdot d_{found}$$

$$c_\varphi = \frac{E_s \cdot I_{found}}{t_{found}} = 0.125 \cdot E_s \cdot \pi^{0.5} \cdot d_{found}^3 = 0.222 \cdot E_s \cdot d_{found}^3$$

c) Annular foundation (outside dia. d_a, inside dia. d_i):

An upper estimate of the effective depth t_{found} is as follows:

$$t_{found} < 0.222 \cdot d_a$$

From this we get a lower estimate for c_φ:

$$c_\varphi = \frac{E_s \cdot I_{found}}{t_{found}} > 0.222 \cdot E_s \cdot \frac{d_a^4 - d_i^4}{d_a}$$

4.2.2 Stability of towers on soft subsoils

A flexible spread foundation beneath a tower can lead to instability but not necessarily to a heave failure (just like an excessively high centre of gravity can cause a floating body to capsize).

The following description is based on [54]. A horizontal load H applied to the top of the tower causes the tower to tilt as a consequence of its elastic support (Figure 4.3).

The deformed structure (second-order theory!) therefore experiences an additional destabilising moment:

$$M_1 = G \cdot h_s \cdot \sin\vartheta \cong G \cdot h_s \cdot \vartheta$$

This together with the moment from the horizontal load

$$M_2 = H \cdot h$$

causes the following reaction beneath the tower foundation:

$$\Delta\sigma = \pm(M_1 + M_2)x/I_{found} = \pm k_s \cdot x \cdot \tan\vartheta \cong \pm k_s \cdot x \cdot \vartheta$$

where

A_{found} area of foundation
I_{found} second moment of area
k_s modulus of subgrade reaction

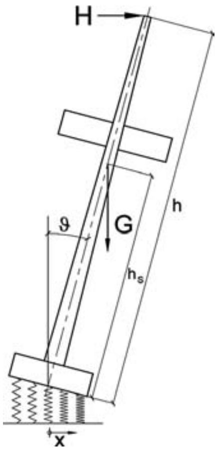

Fig. 4.3 Elastically bedded tower foundation

Substituting for M_1 and M_2 results in the following rearranged equation:

$$H \cdot h = (k_s \cdot I_{found} - G \cdot h_s) \cdot \vartheta$$

In this equation the action effect is on the left, the resistance on the right. A stable condition is only achieved when the expression in the brackets is positive, that is

$$h_s < k_s \cdot I_{found}/G$$

Introducing the settlement due to dead load here, that is $s = G/(k_s \cdot A_{found})$, allows the upper bound of the centroid position to be estimated as follows:

$$h_s < I_{found}/(s \cdot A_{found})$$

The foundation modulus k_s, or the settlement s, should be estimated carefully, that is in the form of the lower bound for concentric long-term action effects on the soil/structure interface. In cases of doubt, a deep foundation should be chosen instead of a flexible spread foundation.

4.3 Investigating vibrations

The structural analysis of a tower begins with an analysis of the vibrations. The methods of classical vibration theory are available for this, which are based on the differential equation for the mass-spring system with a single degree of freedom.

The practical methods that can be used are the modal analysis of the mass-spring system with multiple degrees of freedom or, when only the first eigenmode is required, simplified approaches according to the principle of conservation of energy.

4.3.1 Mass-spring systems with single/multiple degrees of freedom

The model of the mass-spring system with a single degree of freedom can be used to determine the period of oscillation of the fundamental frequency of a wind turbine

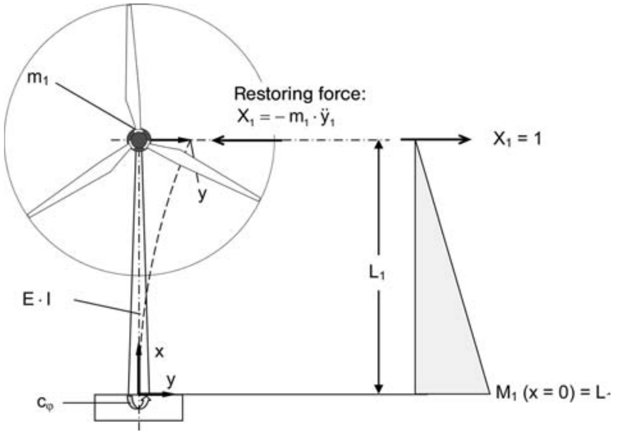

Fig. 4.4 Modelling a tower as a mass-spring system with a single degree of freedom

tower approximately when its mass is mainly concentrated in the nacelle and its centre of gravity can be assumed to be located there, too (Figure 4.4).

The equation of motion for a mass-spring system with a single degree of freedom can be formulated according to D'Alembert's principle as an equilibrium condition:

$$m_1 \cdot \ddot{y}_1 + X_1 = 0$$

The displacement y_1 can be determined with the work theorem:

$$y_1 = X_1 \cdot k_{11}$$

with the following deformation modulus:

$$k_{11} = \int_{x=0}^{x=L_1} \frac{M_1^2}{E \cdot I} \cdot dx + \frac{M_1(x=0)}{c_\varphi} \cdot L_1 = \frac{L_1^3}{3 \cdot E \cdot I} + \frac{L_1^2}{c_\varphi}$$

Substituting the first equation in the second gives us the Euler differential equation for the mass-spring system with a single degree of freedom in the following form:

$$y_1 = -m_1 \cdot \ddot{y}_1 \cdot k_{11}$$

Using the formula for the fundamental mode

$$y_1 = \hat{y}_1 \cdot \sin(\omega \cdot t)$$

results in the equation for determining the damped angular frequency ω:

$$1 = m_1 \cdot \omega^2 \cdot k_{11}$$

From this we get the period of oscillation:

$$T = \frac{2 \cdot \pi}{\omega} = 2 \cdot \pi \cdot \sqrt{m_1 \cdot k_{11}}$$

In order to ascertain the distribution of mass more accurately, we can employ a *modal analysis* to investigate a *mass-spring system with multiple degrees of freedom* and a finite number of discrete individual masses. A model with just a few concentrated masses, provided these are arranged at the associated centres of gravity, suffices to determine the first eigenmode with sufficient accuracy. For details see also [8].

4.3.2 The energy method

Only the first eigenmode (fundamental vibration) is significant for the gust response of a tower. The higher eigenmodes can certainly be very relevant for analysing vortex-induced transverse vibrations. However, owing to the (generally) low critical wind speeds v_{crit}, these do not play a role in heavyweight towers made from reinforced or prestressed concrete.

The eigenmode and natural frequency of the fundamental vibration can be determined for any distribution of mass on the basis of the conservation of energy principle, which states that the sum of potential energy U and kinetic energy W must be constant at every point in time, that is

$$E_0 = U + W = \text{const.}$$

Replacing the unknown eigenmode y (x) by the deflection curve that would result from the horizontal effect of the distributed dead load γ (x) enables us to determine the kinetic energy and potential energy approximately by evaluating the following integrals:

$$U = \int_{x=0}^{x=L} \frac{1}{2} \cdot \gamma(x) \cdot y(x) \cdot dx$$

$$W = \int_{x=0}^{x=L} \frac{\gamma(x)}{2 \cdot g} \cdot [\dot{y}(x)]^2 \cdot dx$$

where $g = $ acceleration due to gravity $= 9.81\ \text{m/s}^2$

These integrals are evaluated with the formula for the fundamental mode

$$y(x) = \hat{y}(x) \cdot \sin(\omega \cdot t)$$

At rest, only the kinetic energy is available at time $t = 0$:

$$E_0 = \int_{x=0}^{x=L} \frac{\gamma(x)}{2 \cdot g} \cdot [\omega \cdot \hat{y}(x)]^2 \cdot dx$$

At maximum deflection, only the potential energy is available at time $t = \pi/(2 \cdot \omega)$:

$$E_0 = \int_{x=0}^{x=L} \frac{1}{2} \cdot \gamma(x) \cdot \hat{y}(x) \cdot dx$$

Equating the two expressions gives us the natural angular frequency of the fundamental mode:

$$\omega^2 = \frac{\int_{x=0}^{x=L} \gamma(x) \cdot \hat{y}(x) \cdot dx}{\int_{x=0}^{x=L} \frac{\gamma(x)}{g} \cdot [\hat{y}(x)]^2 \cdot dx}$$

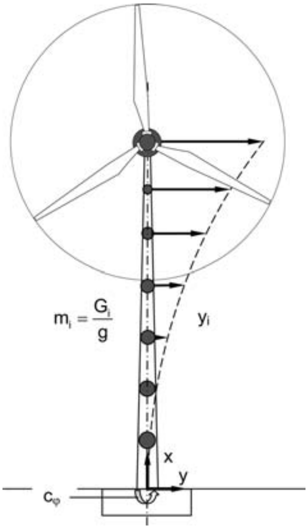

Fig. 4.5 Dynamic model of the structure

Replacing the distributed dead load γ (x) by discrete dead loads G_i acting horizontally, with the associated ordinates of the deflection curve y_i (see Figure 4.5), converts the integrals into summation expressions:

$$\omega^2 = \frac{\sum_i G_i \cdot y_i}{\sum_i \frac{G_i}{g} \cdot y_i^2}$$

4.3.2.1 Practical vibration analysis [8]

The self-weight of the tower itself, the loads of the fitting-out and the quasi-permanent imposed loads are applied to the nodes of the bar structure as individual loads $\mathbf{G_i}$ acting horizontally (see Figure 4.5).

The deflection curve with the ordinates $\mathbf{y_i}$ at the nodes of the bar structure is then calculated. From that we get the period of oscillation of the fundamental frequency:[2)]

$$T = \frac{2 \cdot \pi}{\omega} = 2 \cdot \pi \cdot \sqrt{\frac{\sum_i G_i \cdot y_i^2}{g \cdot \sum_i G_i \cdot y_i}}$$

4.3.2.2 Example of application

Calculating the first period of oscillation T_1

Example: prestressed concrete wind turbine structure, hub height 130 m (see Section 5.2)

2) This equation can also be found in DIN 4131 [14].

	Class	E_{cm} [MPa]	γ [kN/m^3]					c_φ [MNm]
Concrete	C 45/55	32 800	25.0		Rotational spring stiffness			500 000
Structural steel	S 355	210 000	78.5					
Node	height z_j [m]	Δz_j [m]	outside D_j [m]	wall d_j [m]	G_j [kN]	y_j [m]	$G_j \cdot y_j$ [MNm]	$G_j \cdot y_j^2$ [MNm^2]
36	130.174	0.148	4.006		1120.00	4.274	4.786	20.454
35	129.878	2.163	4.006		2330.00	4.258	9.920	42.237
34	125.848	2.015	4.006		21.30	4.041	0.086	0.348
34	125.848	1.312	4.006	0.040	51.33	4.041	0.207	0.838
33	123.224	1.312	4.096	0.040	52.49	3.901	0.205	0.799
33	123.224	1.275	4.096	0.025	32.00	3.901	0.125	0.487
32	120.674	1.275	4.187	0.025	32.72	3.765	0.123	0.464
32	120.674	0.750	5.600	1.200	311.02	3.765	1.171	4.409
31	119.174	1.250	5.600	1.200	518.36	3.686	1.911	7.042
30	118.174	2.087	5.600	0.350	301.19	3.633	1.094	3.975
29	115.000	3.787	5.600	0.350	546.53	3.466	1.894	6.564
28	110.600	4.400	5.600	0.350	634.99	3.235	2.054	6.646
27	106.200	4.400	5.600	0.350	634.99	3.007	1.909	5.742
26	101.800	4.400	5.600	0.350	634.99	2.782	1.767	4.915
25	97.400	3.625	5.600	0.350	523.15	2.561	1.340	3.432
24	94.550	1.425	5.600	0.350	205.65	2.421	0.498	1.205
24	94.550	0.525	5.600	0.900	174.42	2.421	0.422	1.022
23	93.500	0.775	5.600	0.900	257.47	2.370	0.610	1.446
22	93.000	2.450	5.600	0.450	445.94	2.345	1.046	2.453
21	88.600	4.400	5.600	0.450	800.87	2.134	1.709	3.648
20	84.200	4.400	5.600	0.450	800.87	1.929	1.545	2.980
19	79.800	4.400	5.600	0.450	800.87	1.731	1.386	2.399
18	75.400	4.400	5.600	0.450	800.87	1.540	1.234	1.900
17	71.000	4.400	5.600	0.450	800.87	1.359	1.089	1.480
16	66.600	4.400	5.600	0.450	800.87	1.189	0.952	1.132
15	62.200	4.400	5.700	0.450	816.42	1.030	0.841	0.866
14	57.800	4.400	5.900	0.450	847.52	0.883	0.749	0.661
13	53.400	4.400	6.100	0.450	878.62	0.749	0.659	0.494
12	49.000	4.400	6.300	0.450	909.73	0.628	0.571	0.359
11	44.600	4.400	6.500	0.450	940.83	0.519	0.488	0.254
10	40.200	4.400	6.700	0.450	971.93	0.423	0.411	0.174
9	35.800	4.400	7.000	0.450	1018.58	0.338	0.345	0.117
8	31.400	4.400	7.300	0.450	1065.24	0.266	0.283	0.075
7	27.000	4.400	7.800	0.450	1142.99	0.204	0.233	0.048
6	22.600	4.400	8.400	0.450	1236.30	0.152	0.188	0.029
5	18.200	4.400	9.000	0.450	1329.60	0.109	0.145	0.016
4	13.800	4.400	9.700	0.450	1438.46	0.073	0.105	0.008
3	9.400	4.400	10.350	0.425	1457.68	0.043	0.063	0.003
2	5.000	4.450	11.100	0.400	1495.87	0.019	0.029	0.001
1	0.500	2.250	12.100	0.400	827.02	0.000	0.000	0.000
Total		129.674			30 010.57		**44.192**	**131.119**

Fundamental period of oscillation:

$$T_1 = 2\pi \cdot \sqrt{\frac{\sum_i (G_i \cdot y_i^2)}{g \cdot \sum_i (G_i \cdot y_i)}} = 2\pi \cdot \sqrt{\frac{131.119}{9.81 \cdot 44.192}} = \mathbf{3.46\,s}$$

Fundamental natural frequency:

$$f = n_{1,x} = 1/T_1 = 1/3.46 = \mathbf{0.289\,Hz}$$

4.3.3 Natural frequency analysis of loadbearing structure

There should be an adequate safety margin between the natural frequency of the total system, consisting of foundation, tower, nacelle and rotor, and the excitation frequencies. Therefore, the structural engineer should design the tower structure in such a way that the desired natural frequency is reached but at the same time the structural safety is guaranteed.

The excitation frequencies of a wind turbine support structure are (Figure 4.6):[3)]

a) Periodic excitation with 1 × rotational speed (= rotor frequency) = 1P excitation
b) Periodic excitation with 3 × rotational speed from blade passing frequency = 3P excitation
c) Whole-number multiples of the rotor frequency

The ranges of the permissible natural frequencies are shown in the Campbell diagram, in this example for a 5 MW turbine (Figure 4.7).

The closer the tower excitation frequencies are to the range of natural frequencies, the higher are the action effects of the mechanical components and the tower itself.

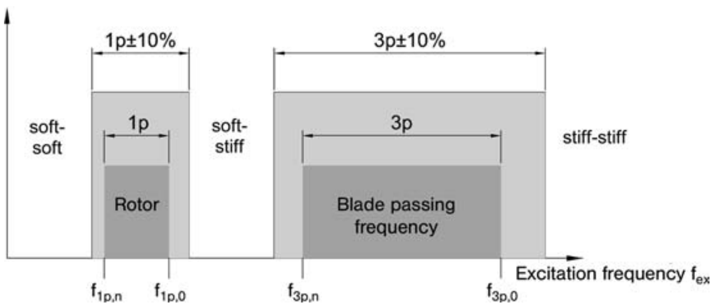

Fig. 4.6 Natural frequency analysis of loadbearing structure

3) Always take into account the design of the wind turbine manufacturer!

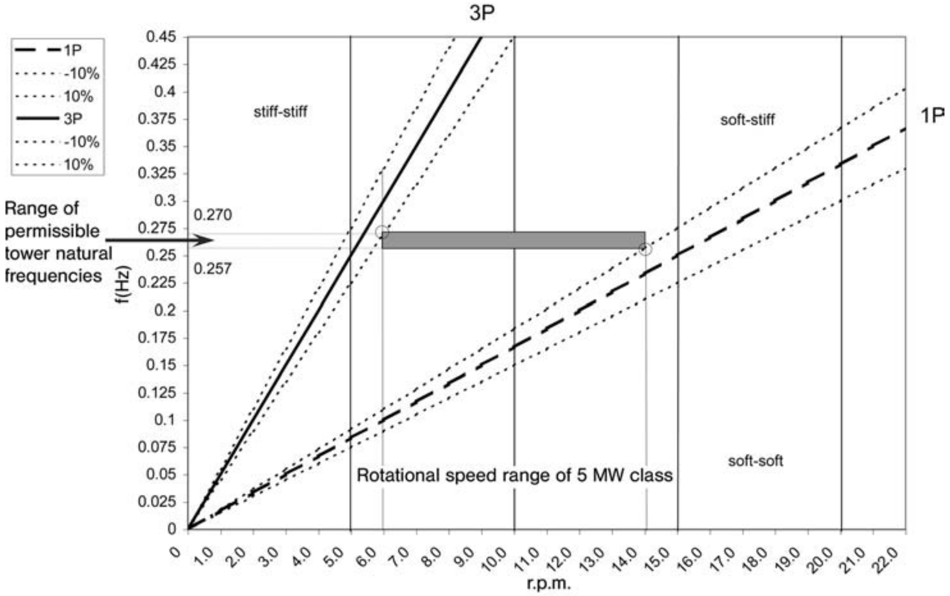

Fig. 4.7 Campbell diagram for a 5 MW turbine

A turbine structure design where the first natural frequency of the total tower[4)] lies below the blade passing frequency (3P) and above the rotor frequency (1P) is designated "soft-stiff".

A turbine structure design where the first natural frequency of the total tower[4)] lies above the blade passing frequency (3P) is designated "stiff-stiff".

Such stiff designs are uneconomic and should be avoided.

Note 1:

The natural frequency in the example taken from Section 5.2 is $f = 0.289$ Hz and therefore within the resonance range of the 3P excitation. If the rotational speed range of the wind turbine is not to be restricted, then the stiffness of the structure must be reduced or the arrangement of the mass modified.

Note 2:

The natural frequency should be calculated using the secant modulus of the concrete E_{cm} according to DIN 1045-1 [33] 9.1.5 and Table 9[5)] because the excitation lies on the level of the frequent actions ($\sigma_c \approx -0.4\ f_c$), see Figure 4.8.

4) Taking into account a 10% safety margin.

5) The higher E_{cm} values according to [36,55] result in a theoretically stiffer structure!

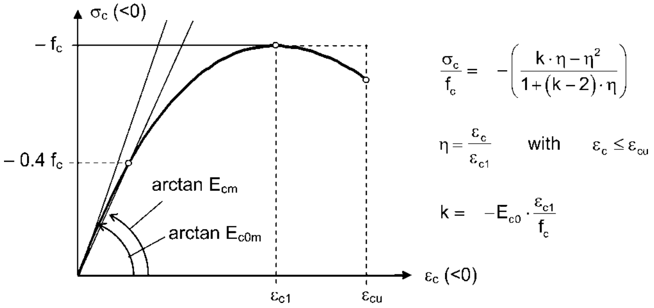

Fig. 4.8 Stress-strain curve for concrete for use in deformation calculations

4.4 Prestressing

Prestressing forces applied by tendons can be considered as *actions* due to the anchorage and change-of-direction forces, or as active internal forces. The resulting internal forces in the composite cross-section disappear in loadbearing structures with statically determinate supports. A *residual stress state* is established between the prestressing force in the steel tendons and the reaction internal forces in the concrete cross-section (Figure 4.9).

The prestressing introduces an eccentric compressive force $N_{cp}^{(0)}$, with the following associated bending moment $M_{cp}^{(0)}$:

$$N_{cp}^{(0)} = -P^{(0)} \qquad M_{cp}^{(0)} = -P^{(0)} \cdot z_{ip}$$

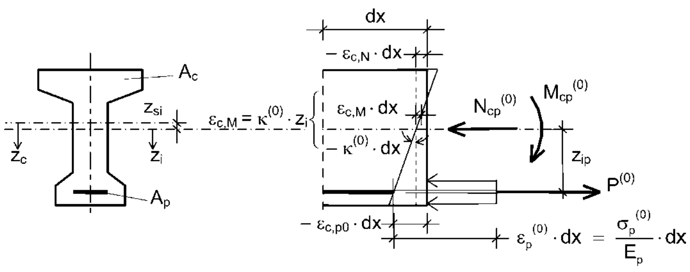

Fig. 4.9 Residual stress state for prestressing

Alternatively, the prestressing can be regarded as a *strain state* (prestrain $\varepsilon_p^{(0)}$ with corresponding precamber $\kappa^{(0)}$). The prestrain $\varepsilon_p^{(0)}$ is then taken into account in the resistance of the cross-section and is related to the *prestressing bed condition*. The prestressing bed condition is the stress and strain state in the prestressing steel corresponding to the stress-free concrete cross-section, and indeed for any point in time t taking into account time-dependent deformations of the prestressing steel and the concrete, see DIN 1045-1 [33] 8.7.1 (3):

$$\varepsilon_p^{(0)} = \frac{P^{(0)}}{E_p \cdot A_p} \qquad \kappa^{(0)} = \left(\frac{1}{r}\right)_0 = \frac{M_{cp}^{(0)}}{E_c \cdot I_i}$$

Owing to the random directions of the horizontal actions (wind loads), towers are always prestressed concentrically. Therefore, in principle, the residual stress state for prestressing acts on the reinforced concrete like an external normal force. However, the prestressing forces for pretensioning with and without bonded tendons should be taken into account differently in the structural analysis (see Section 4.7).

4.4.1.1 Prestressing with grouted post-tensioned tendons

Towers constructed from prefabricated segments generally employ *grouted post-tensioned tendons*. As the deformed loadbearing structure does not experience any second-order internal forces as a result of prestressing, the prior deformations here, $\varepsilon_p^{(0)}$ and $\kappa^{(0)}$, should be taken into account on the resistance side. Considering the prestressing force as an action means that both the compressive forces in the concrete and the tensile forces in the prestressing steel must be applied to the deformed loadbearing structure!

4.4.1.2 External prestressing with unbonded tendons

Cast-in-place concrete towers are frequently constructed with *external prestressing*, that is with *unbonded tendons*. Therefore, the prestressing forces must be applied as external actions, that is as change-of-direction and anchorage forces (Figure 4.10). Another aspect that must be considered with external prestressing is that the anchorage forces of the tendons act tangentially to the deformed structure, that is with restoring horizontal components.

The eccentricities of the prestressing tendons also have to be considered in the deformed loadbearing structure. If the prestressing tendons are exposed over the

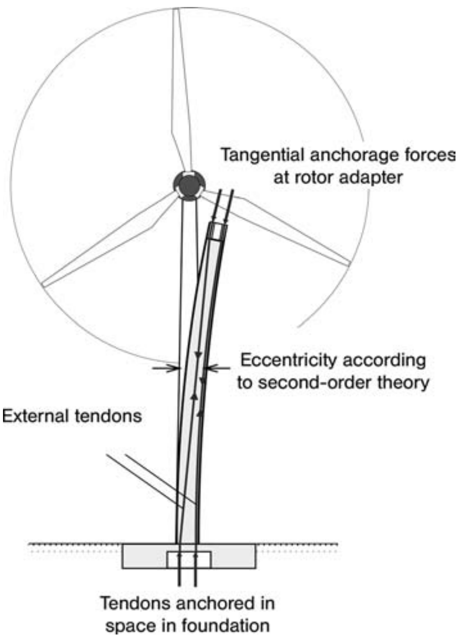

Fig. 4.10 Deformed tower with external prestressing [56]

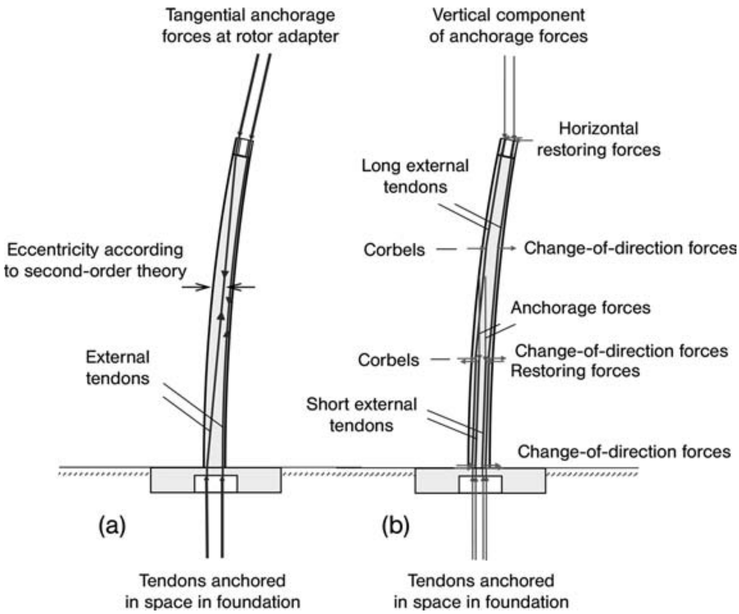

Fig. 4.11 a) Actions of exposed external prestressing tendons, b) actions of corbel-guided staged tendons

full height of the tower (for examples see [8]), then the tendons on the windward side coincide with the chord, whereas those on the leeward side touch the inside of the tower shaft (see Figures 4.10 and 4.11a).

The positioning of the tendons can be improved, however, by building corbels on the inside of the tower shaft in such a way that the tendons follow a polygonal line in the deformed loadbearing structure without touching the inside of the tower shaft. This results in restoring forces and second-order change-of-direction forces with associated friction forces, for which the corbels must be designed (see Figure 4.11b).

Comparing Figure 4.11a and b it is easy to see that when the prestressing tendons are guided over corbels, which are positioned at the third-points at least, the prestressing force does not have to be applied to the action side. Instead it is sufficient – as with grouted post-tensioned tendons – to consider the action of the concentric prestress as an axial compressive force in the concrete cross-section on the resistance side, for example in the bending moment-curvature relationships M (κ), see Section 3.3.3.

4.5 Design of onshore wind turbine support structures

4.5.1 Total dynamic analysis

The following points characterise the total dynamic analysis of a wind turbine support structure:

– The dynamic simulation is carried out in the time domain and on the basis of elastic theory.

– In doing so, the composite structure consisting of foundation, tower and wind turbine is considered in the three-dimensional turbulent wind field.
– Owing to the linear-elastic simulation, the dynamic actions are verified with the partial safety factor $\gamma_F = 1.00$.
– On the other hand, the verification of the cross-sections is carried out with partial safety factors $\gamma_F \geq 1.00$ depending on the design load case group according to [9].
– At the ultimate limit state, the increase in the internal forces as a result of non-linear influences (e.g. second-order theory, cracked state) has to be taken into account (quasi-static calculation with $\gamma_F \geq 1.00$).

Details of the total dynamic analysis are described in Section 4.9.1.1.

4.5.2 Simplified analysis

A simplified analysis may only be carried out when resonance effects play only a minor role, that is with the condition that the first natural frequency deviates by at least 10% from the excitation due to the 1x rotational frequency of the rotor (see Campbell diagram, Figure 4.7). Furthermore, the simplified analysis is characterised by the following points:

– The collective loads resulting from the prior aeroelastic simulation calculations are applied to the machinery/tower interface as actions.
– These and the other actions are considered as *quasi-static actions*, that is given partial safety factors $\gamma_F \geq 1.00$, depending on the design load case group according to [9].
– At the ultimate limit state, the increase in the internal forces as a result of non-linear influences (e.g. second-order theory, cracked state) has to be taken into account.

4.5.2.1 Sensitivity to vibration

Wind turbine towers should generally be classed as sensitive to vibration. In doing so we must distinguish between wind-induced vibrations of the tower in the direction of the wind and transverse to the direction of the wind.

Tower vibrations in the direction of the wind are taken into account as follows:

– Turbine not in operation
  a) Applying the turbulent extreme wind speed model (EWM): internal forces as a result of the average wind speed (10-min mean) are multiplied by the gust response factor G according to DIN 1055-4 [12] annex C (see Section 2.3.1).
  b) Applying the steady extreme wind speed model (if the tower is not vulnerable to vibration) with the internal forces as a result of the gust wind speed (3 s average), but without the gust response factor G.
– Turbine in operation
  The gust response does not need to be considered in this case.

Vortex-induced transverse vibrations are of minor significance in reinforced and prestressed concrete towers and therefore may be ignored in most cases (see also

Section 4.3.2). Their effects are calculated according to DIN 1055-4 [12] annex D if the critical wind speed v_{crit} causes relevant resonance effects.

4.5.2.2 Vibration damping

Resonance effects are minimised by damping measures. The total damping δ is applied according to DIN 1055-4 annex D [12] as follows:

$$\delta = \delta_s + \delta_a$$

where

δ_s logarithmic damping decrement of structural damping
δ_a logarithmic damping decrement of aerodynamic damping

It is possible to use the values of the DIBt guideline [9] as an alternative:

a) Structural damping for concrete towers

$$\delta_s = 0.04$$

b) Aerodynamic damping for concrete towers

$\delta_s = 0.06$ (This includes the influence of the rotor blades!)

The aerodynamic damping δ_a may not be used in connection with action effects due to vortex-induced transverse vibrations!

4.5.3 Design load cases according to DIBt guideline (onshore)

The design load cases are defined in Tables 4.1 and 4.2.

4.5.3.1 Critical design load cases

The design load cases of groups N (normal and extreme), A (accidental) and T (transport and erection) must be investigated separately for *strength and stability failure*. The internal forces must be assessed in a non-linear analysis according to second-order theory (for deformation analysis see Sections 3.4 and 4.7.1). Analyses must be carried out with the most unfavourable of all design load cases for groups N, A and T. DIN 1045-1 [33] must be used when designing reinforced and prestressed concrete structures.

When it comes to checking *fatigue failure*, only those design load case groups designated with F (fatigue) need to be investigated. In doing so, the actions of the individual operating conditions are to be accumulated. Difference from DIN 1045-1 [33]: according to the DIBt guideline [9], the fatigue analysis is to be carried out in line with CEB-FIP Model Code 1990 (DAfStb No. 439 [49]). A detailed analysis of the concrete is unnecessary when the “simplified analysis” of the DIBt guideline [9] is adhered to.

Table 4.1 Design load cases according to DIBt guideline [9] Table 1

Operating conditions (with ref. to section 7.4.x of DIN EN 61400-1:2004[a)])	DLC	Wind condition		Other conditions	DLC group
1. Power production (7.4.1)	1.0[b)]	NTM	$V_{in} \leq V_{hub} \leq V_{out}$	Action effects with a frequency of exceedance $> 10^{-4}$	N
	1.1	NTM	$V_{in} \leq V_{hub} \leq V_{out}$		N
	1.2	NTM	$V_{in} \leq V_{hub} \leq V_{out}$		F
	1.3	ECD	$V_{hub} = V_r$		N
	1.4	NWP	$V_{hub} = V_r$ or V_{out}	External electrical fault	N
	1.5	EOG_1	$V_{hub} = V_r$ or V_{out}	Grid loss	N
	1.6	EOG_{50}	$V_{hub} = V_r$ or V_{out}		N
	1.7	EWS	$V_{hub} = V_r$ or V_{out}		N
	1.8	EDC_{50}	$V_{hub} = V_r$ or V_{out}		N
	1.9	ECG	$V_{hub} = V_r$		N
	1.10[b)]	NWP	$V_{hub} = V_r$	Ice loads	F
	1.11[b)]	NWP	$V_{hub} = V_r$ or V_{out}	Thermal actions	N
	1.12[b)]	NWP	$V_{hub} = V_r$ or V_{out}	Earthquake	A
2. Power production plus fault (7.4.2)	2.1	NWP	$V_{in} \leq V_{hub} \leq V_{out}$	Failure of control system	N
	2.2	NWP	$V_{in} \leq V_{hub} \leq V_{out}$	Failure of control system or prior electrical fault	A
	2.3	NTM	$V_{in} \leq V_{hub} \leq V_{out}$	Failure of control or safety system	F
3. Start-up (7.4.3)	3.1	NWP	$V_{in} \leq V_{hub} \leq V_{out}$		F
	3.2	EOG_1	$V_{hub} = V_{in}$, V_r or V_{out}		N
	3.3	EDC_1	$V_{hub} = V_{in}$, V_r or V_{out}		N
4. Normal shutdown (7.4.4)	4.1	NWP	$V_{in} \leq V_{hub} \leq V_{out}$		F
	4.2	EOG_1	$V_{hub} = V_r$ or V_{out}		N
5. Emergency shutdown (7.4.5)	5.1	NWP	$V_{hub} = V_r$ or V_{out}		N
	5.2[b)]	NWP	$V_{hub} = V_r$ or V_{out}	Earthquake	A
6. Parked (standstill or idling) (7.4.6)	6.0[b)]	NWP	$V_{hub} = V_{m,1}$ (h)[c)]		N
	6.1	EWM	50-year return period[c)]		N
	6.2	EWM	50-year return period[c)]	Grid loss	A
	6.3	EWM	1-year return period[c)]		N
	6.4	NTM	$V_{hub} \leq 0.7 \cdot V_{m,50}$ (h)[c)]		F
	6.5[b)]	EDC_{50}	$V_{hub} = V_{m,50}$ (h)[c)]	Ice loads	A
	6.6[b)]	NWP	$V_{hub} = V_{m,1}$ (h)[c)]	Thermal actions	N
7. Parked after a fault (7.4.7)	7.1	EWM	1-year return period[c)]		A
8. Transport, erection, maintenance and repairs (7.4.8)	8.1	To be specified by the manufacturer			T
	8.2[b)]			Vortex-induced transverse vibrations	F

a) The respective section of DIN EN 61400-1 is also valid for the additional design load cases of the corresponding operating condition.

b) Design load case to be considered in addition to DIN EN 61400-1.

c) Wind conditions to DIN 1055-4.

Table 4.2 Designations for design load cases

DLC	Design load case	DIN EN 61400-1 section
NWP	Normal wind profile model	6.3.1.2
NTM	Normal turbulence model	6.3.1.3
EWM	Extreme wind speed model	6.3.2.1
EOG	Extreme operating gust	6.3.2.2
EDC	Extreme wind direction change	6.3.2.3
ECG	Extreme coherent gust	6.3.2.4
ECD	Extreme coherent gust with change of wind direction	6.3.2.5
EWS	Extreme wind shear	6.3.2.6

Alternatively, the *wind turbulence models* can be handled as follows [9]:

1. Submission of three representative analyses with different realisations of the turbulent wind field (various wind seeds). It must be shown that the moving 3 s average of the wind speed time series satisfies the value required for the 50-year gust/1-year gust once in each of the three simulations at any point in the area swept by the rotor. At the same time, it has to be verified that the statistical parameters of the turbulent wind field satisfy the requirements according to DIN EN 61400-1 [16] for all three time series.
2. Submission of three representative analyses with different realisations of the turbulent wind field (various wind seeds). It must be shown that the moving 3 s average of the wind speed time series satisfies the required value for the 50-year gust/1-year gust in each of the three simulations for at least three points at non-adjacent positions within the area swept by the rotor. It is then unnecessary to verify the statistical properties of the wind speed field according to DIN EN 61400-1 [16].

Note: The three representative simulations should be selected from a larger number of simulations, for example 10, for both alternatives.

4.5.4 Partial safety factors according to DIBt guideline

The partial safety factors given in Table 4.3 should be used for the design load cases according to Section 4.5.3 (see Table 4.1 in conjunction with Table 4.2).

Partial safety factors γ_M for the ultimate resistances of concrete structural components can be found in DIN 1045-1 [33] 5.3.3 (Table 2).

Table 4.3 Partial safety factors γ_F according to DIBt guideline [9], Table 3

Action	Design load case (DLC) group		
	N normal and extreme	A accidental	T transport/ erection
Inertia and gravitational loads			
unfavourable	1.35[a)]	1.10	1.25
favourable	1.00	1.00	1.00
prestress[c)]	1.00	1.00	1.00
Wind loads	1.35[b)]	1.10	1.50
Operational forces	1.35	1.10	1.50
Thermal actions	1.35	—	—
Earthquake	—	1.00	—

[a)] Provided it is verified that the actual unit weights do not deviate by more than 5% from the assumed loads, for example by weighing the machinery of the turbine installation, a partial safety factor of $\gamma_F = 1.10$ may be used.

[b)] The internal forces for the tower and the foundation for DLC 6.1 to Table 4.1 ([9] Table 1) are to be calculated with both $\gamma_F = 1.35$ and $\gamma_F = 1.50$. It is not necessary to consider an oblique angle of attack in the case of $\gamma_F = 1.50$ (angle of attack $\beta = 0$). The most unfavourable combination of internal forces of the two variations governs.

[c)] According to DIN 1045-1 [33] 8.7.5 (3), the following must be taken into account:
If the rise in stress in the prestressing steel is taken into account in the case of unbonded tendons, then its characteristic value $\Delta\sigma_{pk}$ must be determined with the mean values of the material properties. A value of γ_P ($\gamma_{\Delta P}$) = 1.0 applies when calculating the design value $\Delta\sigma_{pd} = \gamma_P\ (\gamma_{\Delta P}) \cdot \Delta\sigma_{pk}$ based on a linear elastic calculation for the internal force. An upper or lower bound must be assumed for γ_P when using a non-linear method to determine the internal forces; the formation of cracks or the opening of joints (prefabricated construction) must be considered here:
$\gamma_{P,sup}\ (\gamma_{\Delta P,sup}) = 1.20\ (1.20)$ and $\gamma_{p,inf}\ (\gamma_{\Delta P,inf}) = 0.83\ (0.80)$
The most unfavourable value is to be used in each case (the values in brackets apply according to [36]).

4.6 Design of offshore wind turbine structures

4.6.1 Control and safety systems

The system concept for an offshore wind turbine includes control and safety systems. The aim of the *control system* is to ensure that the offshore wind turbine is operated safely and optimally, that is efficiently, without malfunctions. The *safety system* has to guarantee that in the event of a malfunction, the offshore wind turbine can be transferred to a *fail-safe* condition [11].

The range of normal operating conditions embraces rotational speeds between the *"minimum" and "maximum" rotor r.p.m.* ($n_1 \leq n \leq n_3$). The *"rated speed"* (n_r) is established at the *"rated wind speed"* (V_r). Once the *"cut-out speed"* (n_4) is reached, the wind turbine is shut down by the control system. Upon reaching the *"activation speed"* (n_A), the safety system must shut down the turbine immediately. The *"maximum overspeed"* (n_{max}) may never be exceeded. Figure 4.12 shows the relationships between the various rotor and wind speeds.

The *"rated power"* (L_r) is the maximum continuous electrical power (effective power) produced at the output terminals of the offshore wind turbine. Reaching the *"overpower"* (L_T) triggers an intervention by the control system. Once the *"activation power"* (L_A) is reached, the wind turbine is shut down immediately by the safety system.

The *"cut-in wind speed"* (V_{in}) is the lowest wind speed at hub height (normal wind speed model, NWP) at which the offshore wind turbine starts to produce power. The *"rated wind speed"* (V_r) is the lowest average wind speed at hub height at which the offshore wind turbine produces its *"rated power"* (L_r). The *"cut-out wind speed"* (V_{out}) is the maximum wind speed at hub height at which the wind turbine must be shut down. The turbine must be shut down immediately if the *"short-term cut-out wind speed"* (V_A) is exceeded only momentarily.

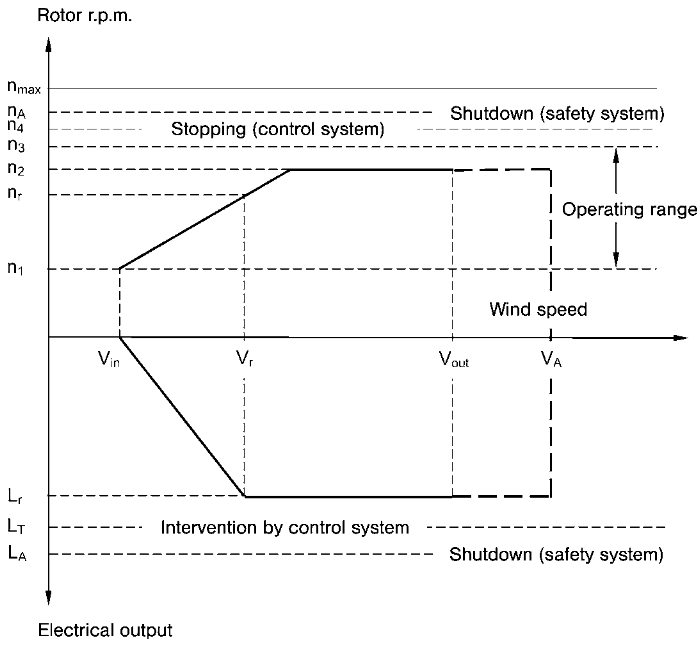

Fig. 4.12 Range of normal operating conditions [11] 2.2.2.5

4.6.2 Design situations and load cases

The load cases relevant to the design must be defined based on the conditions at the site and the design principles as well as the operational and safety concept of the offshore wind turbine [57]. The load cases must include all those cases necessary for verifying the structural integrity of the wind turbine structure. Basically, we distinguish between loads for verifying the structural durability and extreme loads for verifying the general stability (strength, stability, external stability). The structural durability loads must be representative of the operation of the offshore wind turbine over a design working life of at least 20 years. The extreme loads must encompass all events that lead to the highest loads when considering the probability of their simultaneous occurrence, for example “50-year gust”, “50-year wave”, extreme oblique angle of attack for the rotor, ship impact (service vessel), ice pressure, and so on.

After defining and evaluating the design load cases, the loading calculations, taking into account the complete structural dynamics, must be carried out and submitted to the certification body/specialist for checking. The certification body/specialist will check the plausibility of the loading assumptions and the results by comparing them with typical calculations.

The design working life of an offshore wind turbine can be represented by many design situations during the structural design in order to cover the most significant conditions that experience has shown a turbine is exposed to. In principle, the design load cases for determining the structural integrity of an offshore wind turbine structure may be derived from the following combinations [11]:

- Normal design situations with normal external conditions
- Normal design situations with extreme external conditions
- Fault design situations with the appropriate external conditions
- Design situations for transportation, installation and maintenance work with the appropriate external conditions

Normal external conditions refer to a return period of one year, whereas extreme external conditions are generally based on a return period of 50 years. If there is any connection between an extreme external condition and a fault situation, then a realistic combination of the two should be considered as a design load case.

The external conditions are made up of combinations of wind, sea state, ice, current and sea level conditions. Scatter diagrams from the long-term statistics, which reflect wave heights, wave periods and wind speeds (see Section 2.5.7), should be used to analyse the loads due to the interaction of wind and waves. The extreme external conditions (wind, sea state, current, sea ice and sea level) should be combined in such a way that they result in extreme environmental effects on the structure with the specified combined return period (1 year or 50 years).

If no long-term statistical data is available, then one and the same storm event with a 3 h duration can be assumed for the extreme external conditions. Both the average wind speed and the average current velocity plus the significant wave height are extrapolated independently of each other for the same specified return period and then combined with each other. It should be assumed that there is a correlation between average wind speed and significant wave height, but not the short-term extreme values. The extreme wave height and the extreme gust are not considered to act simultaneously. Instead, they are assumed to act with a random distribution [11] (see also Section 4.6.3). The various design load cases for offshore wind turbine structures are dealt with in Section 4.6.4.

4.6.3 Fundamental considerations regarding the safety concept

4.6.3.1 Safety analysis

a) A probabilistic safety analysis with the help of the first-/second-order reliability method (FORM/SORM) can be carried out on the given loadbearing structure when the problem is a non-linear one or is formulated in general terms. More advanced methods, for example simulations, are generally not worthwhile.
The limit state function is defined based on the failure model to be used. Using derivatives with respect to the standard deviations σ_X and the mean values m_X of the basic variables (X) enables the reliability index β to be determined as a measure of the probability of failure P_f. This is then compared with the normative target value according to [44,45] irrespective of the reference period.

b) If linearisation is possible, or the problem itself is a linear one, then the safety analysis can be carried out semi-probabilistically according to [44,45,46] with the help of partial safety factor γ_F or γ_M and combination factor ψ.
The design values of the basic variables (X) derived from the linear limit state equation are used to determine the specified safety elements [44,45,58,25]. These depend on the parameters for the distribution functions (m_X and σ_X) and the weighting factors (α_X). Fixed weighting factors ($\alpha_E = -0.7$ and $\alpha_R = 0.8$) are generally used here in order to separate actions (E) and resistances (R).
If actions with high standard deviations dominate (as is the case for sea state and wind), then $\alpha_E = -1.0$ and $\alpha_R = 0.4$ should be used as fixed weighting factors.

Partial safety factors γ_Q for variable actions (Q) depending on the coefficient of variation ($V_Q = \sigma_Q/m_Q$) are given in Figure 4.13.

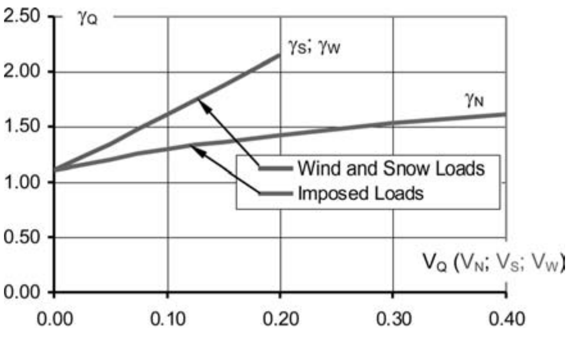

Fig. 4.13 Partial safety factors for variable actions [25]

Figure 4.13 distinguishes between imposed loads and environmental actions:

– For imposed loads, the partial safety factor related to the 95% quantile for a reference period of 50 years is taken as the characteristic value:

$$\gamma_{imp} = \frac{E_{imp,d}}{E_{imp,k;0.95;N=50}}$$

– For environmental actions, on the other hand, it is customary to specify the 98% quantile related to one year as the characteristic value:

$$\gamma_{env} = \frac{E_{env,d}}{E_{env,k;0.98;N=1}} = \frac{E_{env,d}}{E_{env,k;0.364;N=50}}$$

Converting this value to the reference period of 50 years results in the 36.4% quantile ($0.98^{50} = 0.364$). This leads to higher partial safety factors for environmental actions than for imposed loads for the same coefficient of variation!

Furthermore, the combination factors $\psi_{0,i}$ depend on the basic time interval (T_1), that is the period of time during which a constant value for the action may be assumed in the model [58,25]. The number of basic time intervals during the design working life (50 years) is

$$N_1 = \frac{50}{T_1}$$

Values for basic time intervals are specified in [59,60,61].

Combination factors $\psi_{0,i}$ for variable actions (Q) depending on the coefficient of variation ($V_Q = \sigma_Q/m_Q$) and various basic time intervals (N_1) are given in Figure 4.14.

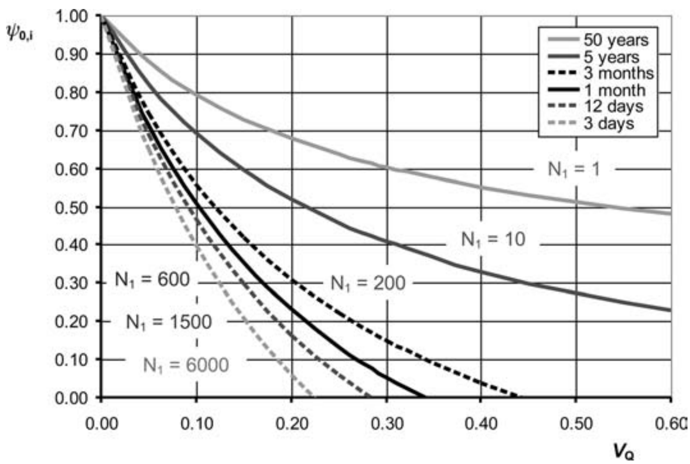

Fig. 4.14 Combination factors for variable actions and various basic time intervals [25]

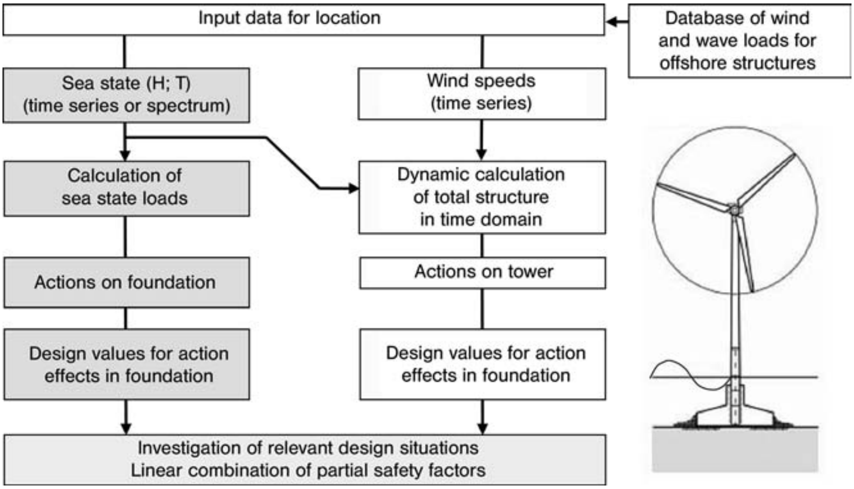

Fig. 4.15 Safety analysis according to normative regulations

4.6.3.2 Combined sea state and wind

According to the applicable normative regulations, the design situations are investigated for the limit states to be verified by combining all independent actions linearly with the help of partial safety factors. The actions due to sea state and wind are determined independently of each other (Figure 4.15).

Using statistically evaluated measurements (e.g. measured at FINO-1) as a basis, an ongoing research project [62] is aiming to determine adapted extreme value distributions and the critical statistical influencing parameters for the actions due to sea state and wind. On the one hand, the aim is to consider the directional dependence, on the other, the correlation between wind and sea state.

A distinction is necessary here (see Section 4.6.2):

– There is a strong correlation between the significant wave height H_s and the dynamic pressure q_{ref} dependent on the 10-min average of the wind speed V_{ref}. A *linear combination* may be considered as a conservative approximation.
– There is only a weak correlation between the maximum wave height (H_{max}) and the peak dynamic pressure q_{gust} averaged over a gust duration of 2–4 s. A non-conservative approximation would be to consider this as *actions not dependent on stochastics*.

This results in the following combination rules (with partial safety factors γ_H and γ_W plus combination factors ψ_W and ψ_H for sea state and wind):

a) $E_1\ (H, q) = \gamma_H \cdot E\ (H_{max}) + \gamma_W \cdot [E\ (q_{ref}) + \psi_W \cdot E\ (q_{gust} - q_{ref})]$
b) $E_2\ (q, H) = \gamma_W \cdot E\ (q_{gust}) + \gamma_H \cdot [E\ (H_s) + \psi_H \cdot E\ (H_{max} - H_s)]$

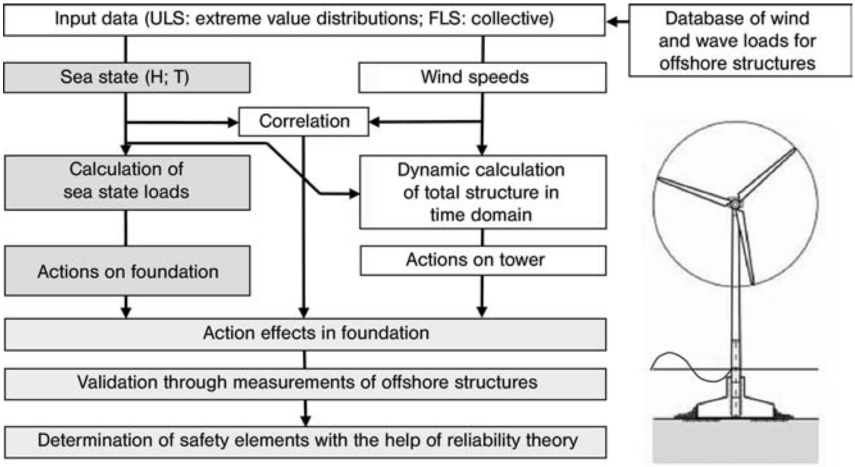

Fig. 4.16 Probability-based safety analysis

The combination factors ψ_W and ψ_H drawn in turn from the provisions of the GL Guideline [11] are approximated in Section 4.6.4 as follows:

a) $\psi_W \cong (q_{red} - q_{ref})/(q_{gust} - q_{ref}) = (1.1^2 - 1)/(1.25^2 - 1) = 0.37 \cong \mathit{0.4}$
b) $\psi_H \cong (H_{red} - H_s)/(H_{max} - H_s) = (1.32 - 1)/(1.86 - 1) = 0.37 \cong \mathit{0.4}$

Furthermore, the correlations between sea state and wind should be ascertained by way of time series analyses taking into account the measurement data available.

Based on this, the structural safety should be evaluated with reliability theory methods (see [25,44,45,58] and Figure 4.16).

4.6.4 Design load cases according to GL guideline

The design load cases are divided into the groups **N** (normal), **E** (extreme), **A** (accidental), **T** (transport and erection) and allocated to the limit states **U** (strength failure) and **F** (fatigue failure), see Table 4.4.

The *significant wave height* ($H_{s,N}$) and the corresponding *extreme value distribution* $F_{extr,3h}$ ($H_{s,N}$), for example Weibull or Gumbel, are determined on the basis of long-term statistics (e.g. scatter diagram, see Section 2.5.7) for sea states of generally 3 h duration, see [11] 4.3.3.2 (2), (4) with 4.2.3.1.4 (2).

Return period N = 50 years:

$$H_{s,50} = F^{-1}_{extr,3h}(1 - 1/N_{SS,50}) \quad \text{where } N_{ss,50} = 50 \cdot 365 \cdot 8 = 146\,000$$

Return period N = 1 year:

$$H_{s,1} = F^{-1}_{extr,3h}(1 - 1/N_{SS,1}) \quad \text{where } N_{ss,1} = 1 \cdot 365 \cdot 8 = 2920$$

Note: Eight sea states each lasting 3 h are possible each day.

Table 4.4 Design load cases to [11] Table 4.3.1

Design situation	DLC	Wind conditions[b)]	Sea state conditions	Other conditions	Limit state	Partial safety factors
1. Power production	1.1	NTM $V_{in} \leq V_{hub} \leq V_{out}$	Irregular sea state: H_s (V) or taken from scatter diagram		U	N
	1.2	NTM $V_{in} \leq V_{hub} \leq V_{out}$	Irregular sea state: H_s (V) or taken from scatter diagram		F	a)
	1.3	ECD $V_{in} \leq V_{hub} \leq V_r$	$H = H_s$ (V)		U	E
	1.4	NWP $V_{in} \leq V_{hub} \leq V_{out}$	$H = H_s$ (V)	External electrical fault	U	N
	1.5	EOG_1 $V_{in} \leq V_{hub} \leq V_{out}$	$H = H_s$ (V)	Grid loss	U	N
	1.6	EOG_{50} $V_{in} \leq V_{hub} \leq V_{out}$	$H = H_s$ (V)		U	E
	1.7	EWS $V_{in} \leq V_{hub} \leq V_{out}$	$H = H_s$ (V)		U	E
	1.8	EDC_{50} $V_{in} \leq V_{hub} \leq V_{out}$	$H = H_s$ (V)		U	E
	1.9	ECD $V_{in} \leq V_{hub} \leq V_r$	$H = H_s$ (V)		U	E
	1.10	NWP $V_{in} \leq V_{hub} \leq V_{out}$	$H = H_s$ (V)	Ice formation on rotor blades	F/U	a)/E
	1.11	Thermal actions, if applicable			U	E
	1.12	Earthquake, if applicable			U	A
	1.13	NWP $V_{hub} = V_r$ or V_{out}	$H = H_s$ (V)	Grid loss	F	a)
	1.14	NWP $V_{hub} = V_r$ or V_{out}		Sea ice	F/U	a)/E
	1.15	NWP $V_{hub} = V_r$ or V_{out}	$H = H_{max,1}$ or H_s (V)		U	N
2. Power production plus fault	2.1	NWP $V_{in} \leq V_{hub} \leq V_{out}$	$H = H_s$ (V)	Fault in control system	U	N
	2.2	NWP $V_{in} \leq V_{hub} \leq V_{out}$	$H = H_s$ (V)	Fault in safety system or prior electrical failure	U	A
	2.3	NTM $V_{in} \leq V_{hub} \leq V_{out}$		Fault in control or safety system	F	a)
3. Start-up	3.1	NWP $V_{in} \leq V_{hub} \leq V_{out}$	$H = H_s$ (V)		F	a)
	3.2	EOG_1 $V_{in} \leq V_{hub} \leq V_{out}$	$H = H_s$ (V)		U	N
	3.3	EDC_1 $V_{in} \leq V_{hub} \leq V_{out}$	$H = H_s$ (V)		U	N
4. Normal shutdown	4.1	NWP $V_{in} \leq V_{hub} \leq V_{out}$	$H = H_s$ (V)		F	a)
	4.2	EOG_1 $V_{in} \leq V_{hub} \leq V_{out}$	$H = H_s$ (V)		U	N
5. Emergency shutdown	5.1	NWP $V_{in} \leq V_{hub} \leq V_{out}$	$H = H_s$ (V)		U	N
6. Parked (standstill or idling)	6.1a	EWM $V_{hub} = V_{ref}$ turbulent wind model	Irregular sea state with $H_{s,50}$	Wind/wave misalignment	U	E

	6.1b	EWM $V_{hub} = V_{e,50}$ steady wind model	$H = H_{red,50}$	Wind/wave misalignment	U	E
	6.1c	EWM $V_{hub} = V_{red,50}$ steady wind model	$H = H_{max,50}$	Wind/wave misalignment	U	E
	6.2a	EWM $V_{hub} = V_{ref}$ turbulent wind model	Irregular sea state with $H_{s,50}$	Grid loss	U	A
	6.2b	EWM $V_{hub} = V_{e,50}$ steady wind model	$H = H_{red,50}$	Grid loss	U	A
	6.3a	EWM $V_{hub} = V_{e,1}$ turbulent wind model	Irregular sea state with $H_{s,50}$	Extremely oblique angle of attack	U	E
	6.3b	EWM $V_{hub} = V_{e,1}$ steady wind model	$H = H_{red,1}$	Extremely oblique angle of attack	U	E
	6.4	NTM $V_{hub} < 0.7 \cdot V_{ref}$	Irregular sea state with H_s (V)		F	$*$)
	6.5	EDC_{50} $V_{hub} = V_{ref}$	$H = H_{red,1}$	Formation of ice on rotor blades and structure	U	E
	6.6	Thermal actions, if applicable			U	E
	6.7	EWM $V_{hub} = V_{red,50}$ Steady wind model	—	50-year sea ice	U	E
7. Parked after a fault	7.1a	EWM $V_{hub} = V_{e,1}$ steady wind model	$H = H_{red,0.1}$		U	A
	7.1b	EWM $V_{hub} = V_{red,1}$ steady wind model	$H = H_{max,1}$		U	A
	7.2	NTM $V_{hub} < 0.7 \cdot V_{ref}$	Irregular sea state with H_s (V)		F	a)
8. Transport, erection, maintenance and repairs	8.1	EOG_1 $V_{hub} = V_T$	$H = H_{s,T}$	To be specified by manufacturer	U	T
	8.2a	EWM $V_{hub} = V_{e,1}$ steady wind model	$H = H_{red}$ (V)	Locked state	U	A
	8.2b	EWM $V_{hub} = V_{red,1}$ steady wind model	$H = H_{max}$ (V)	Locked state	U	A
	8.3			Vortex-induced transverse vibrations	F	a)
	8.4	NTM $V_{hub} < 0.7 \cdot V_{ref}$	Irregular sea state with H_s (V)	No grid over long period	F/U	a)/A
	8.5	NWM $V_{hub} < V_T$	$H = H_{s,T}$	Ship impact	U	A

a) Partial safety factor for the effects of fatigue: $\gamma_{F,fat} = 1.00$ (see [11] 4.3.7.2.2).

b) If a cut-out wind speed (V_{out}) has not been defined, use the reference wind speed (V_{ref}).

Note: The indices 1 and 50 for the EOG and EDC wind conditions denote the 1- and 50-year return periods respectively.

Table 4.5 Wind condition designations in Table 4.4

DLC	Design load case	GL Guideline [11], section
NWP	Normal wind profile model	4.2.2.3.2
NTM	Normal turbulence model	4.2.2.3.3
EWM	Extreme wind speed model	4.2.2.4.1
EOG	Extreme operating gust	4.2.2.4.2
EDC	Extreme direction change	4.2.2.4.3
ECG	Extreme coherent gust	4.2.2.4.4
ECD	Extreme coherent gust with change of wind direction	4.2.2.4.5
EWS	Extreme wind shear	4.2.2.4.6

The similarity between the designations in [9,11] is obvious.

Table 4.6 Wave height designations in Table 4.4

No.	Symbol	Description	GL Guideline [11], section
1	H_s (V)	Significant wave height (H_s) corresponding to 10-min average of wind speed at hub height (V_{hub})	4.3.3.2 (6), (7)
2	H_{red} (V)	Reduced wave height corresponding to V_{hub}	4.3.2.3.1 & 4.3.3.2
3	H_{max}	Maximum wave height corresponding to V_{hub}	4.3.2.3.1 & 4.3.3.2
4	$H_{s,1}$	Significant wave height for 1-year return period	4.2.3.1.4
4	$H_{s,50}$	Significant wave height for 50-year return period	4.2.3.1.4
2	$H_{red,N}$	Reduced wave height for N-year return period	4.3.2.3.1, 4.2.3.1.4
3	$H_{max,1}$	Maximum wave height for 1-year return period	4.3.2.3.1
3	$H_{max,50}$	Significant wave height for 50-year return period	4.3.2.3.1, 4.2.3.1.4
5	H_B	Height of breaking wave[a)]	4.2.3.1.5

[a)] See Section 2.5.9.

4.6.4.1 Commentary to Table 4.4

Power production (DLC 1.1 to 1.15)

In this design situation the offshore wind turbine is in operation and connected to the electricity grid. A conservative combination of the deterministic wind and sea state conditions is required, which means that the phase shifts between wave crest and peak gust are arbitrary and therefore can occur in the most unfavourable combination.

Irregular sea state conditions should be assumed for DLC 1.1 and 1.2. The wind speed intervals within the range to be investigated ($V_{in} \le V = V_{hub} \le V_{out}$) may not be selected as greater than $\Delta V = 2$ m/s. The significant wave height ($H = H_s$ (V)), the peak frequency of the sea state spectrum (T_p) and the direction of movement of every normal sea state together with the associated average wind speed (V_{hub}) should be selected on the basis of the combined long-term distribution of the wind and sea state parameters for the location. During the design work it should be ensured that the fatigue damage to the structure is ascertained for the complete long-term distribution of the wind and sea state parameters (see Section 4.9).

Average wind speeds ($V_{in} \le V_{hub} \le V_{out}$) and the corresponding regular waves with significant wave heights ($H = H_s$ (V)) should be used for DLC 1.3 to 1.13, see [11] 4.3.3.2 (6) and (7).

If no data is available regarding the probabilities of the combined occurrence of wind and sea state or if the wind turbine classes according to Table 2.8 are to be used, then it is possible to use the relationships between the hourly average of the wind speed ($U = U_{10m,1h}$) and the peak frequency of the JONSWAP spectrum as well as the significant wave height (H_s (U)) to [11] appendix 4.E (see Section 2.5.6 and Table 2.11).

Example (equations taken from Section 2.5.6, conversion factor from Table 2.9):

Wind speed at hub height ($z_{hub} = 100$ m) : $V_{hub} = 25\,\mathrm{m/s}$

Corresponding wind speed at 10 m height above sea level:

$$\bar{U}_{10\,\mathrm{m},1\,\mathrm{h}} = 0.91 \cdot V_{hub} \cdot (10/z_{hub})^{0.14} = 0.91 \cdot 25 \cdot (10/100)^{0.14} = 16.48\,\mathrm{m/s}$$

$$\text{Fetch}: \quad x = 600\,\mathrm{km}$$

$$\text{Time}: \quad t = 12\,\mathrm{h}$$

$$\xi = g \cdot x/U^2 = 9.81 \cdot 600\,000/16.48^2 = 21\,672$$

$$\theta = g \cdot \text{time}/U = 9.81 \cdot (12 \cdot 60 \cdot 60)/16.48 = 25\,716$$

$$\nu = \text{Max.}(0.16; 2.84 \cdot \xi^{-0.3}; 16.8 \cdot \theta^{-3/7}) = \text{Max.}(0.16; 0.141; 0.216) = 0.216$$

$$\text{Peak frequency}: \quad T_p = U/(g \cdot \nu) = 16.48/(9.81 \cdot 0.216) = 7.78\,\mathrm{s}$$

Significant wave height:

$$H_{s,JONSWAP} = 0.0094 \cdot \nu^{-5/3} \cdot U^2/g = 0.0094 \cdot 0.216^{-5/3} \cdot 16.48^2/9.81 = 3.35\,\mathrm{m}$$

The average wind speeds ($V_{hub} = (V_r$ or $V_{out})$) and either the corresponding maximum wave heights (H_{max} (V_{hub})) or the maximum 1-year wave height ($H = H_{max,1}$) should be used for DLC 1.15. The larger values govern in each case.

Power production plus fault (DLC 2.1 to 2.3)
Every fault in the control and safety systems or an internal fault in the electrical system that is relevant for the load on the offshore wind turbine structure must be taken into account during power production. In doing so, it may be assumed that faults not dependent on each other do not occur simultaneously.

Average wind speeds and the corresponding significant wave heights should be used for DLC 2.1 and 2.2 (as for DLC 1.3 to 1.13).

Irregular sea states should be assumed for DLC 2.3 (as for DLC 1.1 and 1.2).

Start-up (DLC 3.1 to 3.3)
This design situation embraces all events that lead to loads on the offshore wind turbine structure during the transition from standstill or idling to power production. The average wind speeds and the corresponding significant wave heights should be assumed for this (as for DLC 1.3 to 1.13).

Normal shutdown (DLC 4.1 and 4.2)
This design situation embraces all events that lead to loads on the offshore wind turbine structure during the transition from power production to standby mode (standstill or idling). The average wind speeds and the corresponding significant wave heights should be assumed for this (as for DLC 1.3 to 1.13).

Emergency shutdown (DLC 5.1)
Average wind speeds and the corresponding significant wave heights should be assumed for the case of the manual activation of the emergency-stop switch (as for DLC 1.3 to 1.13).

Parked (standstill or idling, DLC 6.1 to 6.7)
In this situation the rotor of an offshore wind turbine is in standby mode. According to Table 4.4, either the *steady* or the *turbulent wind model* should be used for this design situation (see Section 2.3.2). When applying the turbulent wind model, a *dynamic simulation* should be carried out in combination with a stochastic sea state model. However, when applying the steady wind model in combination with a deterministic design wave, a *quasi-static structural analysis* should be carried out with appropriate corrections for the dynamic response.

The turbulent wind model together with irregular sea states should be used for DLC 6.1a and 6.2a. The significant 50-year wave ($H = H_{s50}$) and the average 50-year wind speed ($V_{hub} = V_{ref}$) should be used here. The average values of H_{s50} and V_{ref} are to be adapted to the duration of the simulation (see Table 2.9).

The steady extreme wind model in combination with the reduced design wave should be used for DLC 6.1b and 6.2b. The extreme 50-year wind speed, the *max. 3 s gust* ($V_{hub} = V_{e,50}$) and the *reduced 50-year wave height* ($H = H_{red,50}$)[6] should be used here, see [11] 4.3.3.2 (15):

$$V_{e,50}(z) = 1.25 \cdot V_{ref} \cdot (z/z_{hub})^{0.14}$$
$$H_{red,50} = 1.32 \cdot H_{s,50} \leq H_B$$

[6] Note: The frequency of occurrence of H_{red} is 3% in deep water.

The steady reduced wind model in combination with the extreme design wave should be used for DLC 6.1c. The *max. 50-year wave height* ($H = H_{max,50}$)[7] during a 3 h storm and the reduced 50-year wind speed, that is the *extreme 1-min wind speed average* ($V_{hub} = V_{red,50}$) are used here, see [11] 4.3.3.2 (15):

$$H_{max,50} \quad = 1.86 \cdot H_{s,50} \leq H_B \quad \text{(see Section 2.5.8)}$$
$$V_{red,50}(z) = 1.1 \cdot V_{ref} \cdot (z/z_{hub})^{0.14}$$

The turbulent wind model together with irregular sea states should be used for DLC 6.3a. The significant 1-year wave ($H = H_{s1}$) and the average 1-year wind speed ($V_{hub} = V_1$) are to be used here. The average values of H_{s1} and V_1 are to be adapted to the duration of the simulation, see Table 2.9.

The steady extreme wind model in combination with the reduced design wave should be used for DLC 6.3b. The extreme 1-year wind speed, the *max. 3 s gust* ($V_{hub} = V_{e,1}$) and the *reduced 1-year wave height* ($H = H_{red,1}$) are to be used here, see [11] 4.3.3.2 (15):

$$V_{e,1}(z) = 0.8 \cdot V_{e,50}$$
$$H_{red,1} \quad = 1.32 \cdot H_{s,0.1} \leq H_B$$

Irregular sea states are to be assumed for DLC 6.4 (as for DLC 1.1 and 1.2). In doing so, the related average wind speed should be limited to $V_{hub} < 0.7 \cdot V_{ref}$.

The average 50-year wind speed ($V_{hub} = V_{ref}$) is to be combined with the reduced 1–year wave height ($H = H_{red,1}$) for DLC 6.5.

The 50-year ice load (see Section 2.8) is to be combined with the reduced 50-year wind speed ($V_{hub} = V_{red,50}$) for DLC 6.7.

Parked after a fault (DLC 7.1 to 7.2)
This design situation takes into account the non-standby state (standstill or idling) in the event of a fault.

The steady extreme wind model in combination with the reduced design wave is to be used for DLC 7.1a (as for DLC 6.3b).

The steady reduced wind model in combination with the extreme design wave is to be used for DLC 7.1b. The *max. 1-year wave height* ($H = H_{max,1}$) during a 3 h storm and the reduced 1-year wind speed, that is the *extreme 1-min average of the wind speed* ($V_{hub} = V_{red,1}$) are to be used here, see [11] 4.3.3.2 (15):

$$H_{max,1} \quad = 1.86 \cdot H_{s,1} \leq H_B$$
$$V_{red,1}(z) = 0.8 \cdot V_{50,red}$$

Irregular sea states are to be assumed for DLC 7.2 (as for DLC 1.1 and 1.2).

The details of these design load cases (including transport, erection, maintenance and repairs) are described in [11] 4.3.3.5.

[7] Note: H_{max} is the maximum value on the basis of 1000 waves in deep water.

4.6.5 Partial safety factors according to GL guideline

At the serviceability limit state the partial safety factors for all actions are $\gamma_F = 1.00$, likewise at the fatigue limit state ([11] 4.3.7.2.2).

4.7 Ultimate limit state

4.7.1 Deformation calculations according to second-order theory

The internal forces for the tower and the foundation of a wind turbine are generally calculated according to the following scheme for the ultimate limit state:

1. Conception of structural model according to Section 4.2 with *imperfections*.
   The following must be taken into account according to DIBt guideline [9] 6.4.1:
   a) Vertical misalignment as a result of fabrication and erection inaccuracies and the influence of asymmetric solar irradiation:

   $$\varphi_a = 5\ \text{mm/m or } 0.005$$

   b) Vertical misalignment as a result of differential settlement of the subsoil:
   A differential settlement between the outer edges of the foundation amounting to 40 mm or a vertical misalignment of the tower amounting to 3 mm/m is a reasonable value that can be assumed for standard calculations. The correctness of this assumption should be confirmed by a soil mechanics specialist in individual cases.
2. Calculation of the internal forces for the tower and the foundation according to second-order theory when the conditions stated in DIN 1045-1 [33] 8.6.1 apply (for details see Section 3.1).
   a) According to [33] 8.6.1 (6), the theoretical mean values are to be used for the material strengths. According to [33] 8.5.1 (4), these amount to[8)]

   Concretes up to C 50/60:
   $$f_{cR} = 0.85 \cdot \alpha \cdot f_{ck} = \alpha \cdot f_{ck}/\gamma_{Cm} = \alpha \cdot f_{ck}/1.20$$
   Concretes grade C 55/67 and higher:
   $$f_{cR} = 0.85 \cdot \alpha \cdot f_{ck}/\gamma'_C = \alpha \cdot f_{ck}/(\gamma_{Cm} \cdot \gamma'_C) = \alpha \cdot f_{ck}/(1.20 \cdot \gamma'_C)$$
   Reinforcing steel:
   $$f_{yR} = 1.1 \cdot f_{yk}$$
   Prestressing steel:
   $$f_{p0.1R} = 1.1 \cdot f_{p0.1k}$$

   The member cross-sections (concrete dimensions, cross-sectional area of reinforcing steel and, if applicable, prestressing steel) are to be designed in advance in such a way that the uniform partial safety factor may not be lower than $\gamma_R = 1.30$ (groups N, E, F and T) or $\gamma_{RA} = 1.10$ (group A) according to [33] 8.5.1 (4) for the design value of the ultimate resistance.

8) According to [36], the additional partial safety factor γ'_C is unnecessary for high-strength concretes.

b) *Alternatively*, the deformations according to [33] 8.6.1 (7) may be determined on the basis of design values. These amount to (see Section 3.2)

Concretes up to C 50/60:
$f_{cR} = f_{cm}/\gamma_C = (f_{ck} + 8\ [MPa])/\gamma_C$
Concrete grade C 55/67 and higher:
$f_{cR} = f_{cm}/(\gamma_C \cdot \gamma'_C) = (f_{ck} + 8[MPa])/(\gamma_C \cdot \gamma'_C)$
Reinforcing steel:
$f_{yR} = f_{yk}$

Prestressing steel:
$f_{p0.1R} = f_{p0.1k}$

Under these conditions, the member cross-sections are to be designed in advance in such a way that the partial safety factors γ_M for the design values of the material strengths are not lower than those of [33] 5.3.3 or according to Table 4.8.

c) If the stress increase in the prestressing steel is taken into account in unbonded tendons, then the characteristic value $\Delta\sigma_{pk}$ for the stress increase in the prestressing steel is determined using the mean values of the material properties. The formation of cracks or opening joints should be considered here (DIN 1045-1 [33] 8.7.5).
Determining the internal forces with the help of a non-linear method requires $\Delta\sigma_{pk}$ to be multiplied by the upper or lower limit for γ_P according to Table 4.3.

3. Owing to the given strength values, the stress-strain curves for concrete and reinforcing steel, including tension stiffening, are used (see Section 3.2), or the bending moment-curvature relationships are developed (see Section 3.3).
4. Determining the critical design load cases from the permanent actions (self-weight of structure and permanent fitting-out loads) plus the variable actions according to Section 4.5.3 or 4.6.4.
According to [44] Equation 4.7, the design value of an action E_d is generally determined from the design values of the actions, the geometric variables and, if necessary, the material properties as follows:

$$E_d = E(F_{d,1}, F_{d,2}, \ldots, a_{d,1}, a_{d,2}, \ldots, X_{d,1}, X_{d,2}, \ldots)$$

In the case of geometric and physical non-linear calculations according to second-order theory, $\vec{a}_d = \{\text{height, cross-section, inclination } \varphi_a\}$ and $\vec{x}_d = \{f_{cR}, f_{yR}, f_{p0.1R}\} = \vec{x}_R$ describe the deformation characteristics of the loadbearing structure dependent on the dimensions of the structure, imperfections and material laws. These are taken into account, for example, with the help of the bending moment-curvature relationships (see Section 3.3).
The following generally applies to onshore wind turbines [9] for group N (normal and extreme), or to offshore wind turbines [11] for groups N (normal), E (extreme) and T (transport/erection):

$$E_d = E\left\{\sum_{j\geq 1}\gamma_{G,j} \cdot G_{k,j};\quad \gamma_P \cdot P_k;\quad \sum_{i\geq 1}\gamma_{Q,i} \cdot Q_{k,i};\quad \vec{a}_d;\quad \vec{x}_R\right\}$$

The extreme wind speed model (EWM) should be combined with a design wave for *design load case 6.1b* (see Table 4.4). If we explicitly consider only the design load cases, then the following applies in particular:

$$E_d = E\left\{\sum_{j\geq 1} \gamma_{G,j} \cdot G_{k,j};\quad 1.00 \cdot P_k;\; 1.35 \cdot \left[Q\left(1.25 \cdot V_{e,50}(z)\right) + Q\left(1.32 \cdot H_{s,50}\right) + Q_{N,k}\right]\right\}$$

where $Q_{N,k}$ stands for the characteristic operational forces.
Accordingly, the following applies for *design load case 6.1c*:

$$E_d = E\left\{\sum_{j\geq 1} \gamma_{G,j} \cdot G_{k,j};\quad 1.00 \cdot P_k;\; 1.35 \cdot \left[Q\left(1.10 \cdot V_{e,50}(z)\right) + Q\left(1.86 \cdot H_{s,50}\right) + Q_{N,k}\right]\right\}$$

The following generally applies for group A (accidental, earthquake):

$$E_{dA} = E\left\{\sum_{j\geq 1} \gamma_{GA,j} \cdot G_{k,j};\quad \gamma_{PA} \cdot P_k;\quad A_d;\quad \sum_{i\geq 1} \gamma_{QA,i} \cdot Q_{k,i};\quad \vec{a}_d;\quad \vec{x}_R\right\}$$

If we explicitly consider only the design load cases, then the following applies for *design load case 6.2b* (see Table 4.4) in particular:

$$E_d = E\left\{\sum_{j\geq 1} \gamma_{GA,j} \cdot G_{k,j}; 1.00 \cdot P_k; A_d; 1.10 \cdot \left[Q\left(1.25 \cdot V_{e,50}(z)\right) + Q\left(1.32 \cdot H_{s,50}\right) + Q_{N,k}\right]\right\}$$

Here, A_d stands not for an action, but for the accidental event “grid loss”.
The partial safety factors to be used are those of Table 4.3 for onshore wind turbines, Table 4.7 for offshore wind turbines. These are $\gamma_{G,sup} = 1.35$ for permanent loads or $\gamma_{GA,sup} = 1.10$ for unfavourable effects and $\gamma_{G,inf} = 1.00$ (onshore) or 0.90 (offshore) for favourable effects.

Table 4.7 Partial safety factors γ_F for actions according to [11] Table 4.3.4

Source of action	Unfavourable actions				Favourable actions
	Design situation (see Table 4.4)				All design situations
	N normal	E extreme	A accidental	T transport/erection	
Inertia and gravitational loads	1.10/1.35[a)]	1.10/1.35[a)]	1.10	1.25	0.90
Other inertia forces	1.20	1.25	1.10	1.30	0.90
Prestressing	–[b)]	–[b)]	–[b)]	–[b)]	–[b)]
Environmental actions	1.20	1.35	1.10	1.50	0.90
Operational forces	1.20	1.35	1.10	1.50	0.90
Thermal actions	—	1.35	—	—	0.90

a) For cases where the masses are not determined by weighing.

b) Partial safety factors for prestressing are to be agreed with GL Wind. However, the conditions according to DIN 1045-1 [33] 8.7.5 (3) are to be taken into account, see Table 4.3.

Table 4.8 Partial safety factors γ_M for ultimate resistances of concrete structural components according to [11] Table 5.4.1

Material	Ultimate limit state		Serviceability limit state
	Failure or stability	Fatigue	
Concrete (γ_C)	1.50[a] (1.20)[b]	1.50	1.00
Fibre-reinforced concrete (γ_C)	1.40[a] (1.20)[b]	1.40	1.00
Reinforcing and prestressing steel (γ_S)	1.15[a]	1.15	1.00

[a] When designing for accidental situations, for example earthquakes, $\gamma_{CA} = 1.30$ may be used for concrete and fibre-reinforced concrete, $\gamma_{SA} = 1.00$ for reinforcing and prestressing steel.

[b] The value in brackets $\gamma_{Cm} = 1.20$ may be used in deformation calculations if the geometric and physical non-linearities are taken into account.
The value $\gamma_{Cm} = 1.20$ may be used for concrete in calculations based on second-order theory, see [11] 5.4.1.4.2 (1). This corresponds to $f_{cR} = \alpha \cdot f_{ck}/\gamma_{Cm} = \alpha \cdot f_{ck}/1.20 = 0.85 \cdot \alpha \cdot f_{ck}$ according to [33] 8.5.1 (4).

5. Performing the deformation calculation according to second-order theory generally requires the help of a computer program.
6. Checking the capacities of the cross-section:
   If the deformation calculation was carried out according to [33] 8.6.1 (6) using the theoretical mean values for the material strengths according to [33] 8.6.1 (4), then the ultimate load-carrying capacities at the critical cross-sections must be verified using the uniform partial safety factor γ_R or γ_{RA} for the design value of the ultimate resistance (see above):

   $$E_d \leq R(f_{cR}; f_{yR}; f_{p0.1R})/\gamma_R \quad \text{or} \quad E_{dA} \leq R(f_{cR}; f_{yR}; f_{p0.1R})/\gamma_{RA}$$

   Performing the deformation analysis according to [33] 8.6.1 (7) as an *alternative* approach means using the following design values for the material strengths and associated partial safety factors γ_M when calculating the ultimate load-carrying capacities at the critical cross-sections:

   Concretes up to C 50/60:
   $f_{cd} = \alpha \cdot f_{ck}/\gamma_C$ or $f_{cdA} = \alpha \cdot f_{ck}/\gamma_{CA}$
   Concrete grade C 55/67 and higher:
   $f_{cd} = \alpha \cdot f_{ck}/(\gamma_C \cdot \gamma'_C)$ or $f_{cdA} = \alpha \cdot f_{ck}/(\gamma_{CA} \cdot \gamma'_C)$
   Reinforcing steel:
   $f_{yd} = f_{yk}/\gamma_S$ or $f_{ydA} = f_{yk}/\gamma_{SA}$

Prestressing steel:

$$f_{p0.1d} = f_{p0.1k}/\gamma_S \text{ or } f_{p0.1dA} = f_{p0.1k}/\gamma_{SA}$$

7. Checking the level of prestress.
The *design value of the 0.1% proportionality limit for the prestressing steel* may not be exceeded if the stability of the loadbearing structure in the deformed state is not to be endangered (see also Section 3.1):

$$\varepsilon_{pd} \leq \varepsilon_{p0.1d} = E_p \cdot f_{p0.1k}/\gamma_S$$

On the other hand, the partial safety factors γ_P according to Table 4.3 also apply for the detailed design.
This results in limited *reserves of stress in the prestressing steel* at the ultimate limit state. With a *favourable effect of the prestress*, this can lead to the prestressing steel not being able to be fully mobilised for flexural tension action effects:

$$\text{For example : St } 1500/1770: \quad \sigma_{pm\,0} = 0.55 \cdot f_{pk} = 973.5\,\text{MPa}$$
$$\sigma_{p,Rd} = 1500/1.15 = 1304\,\text{MPa}$$

Maximum reserves for flexural tension with unbonded tendons:

$$\Delta\sigma_{p0d} \leq \Delta\sigma_{p0k} \cdot \gamma_{P,inf} = (\sigma_{p,Rd} - \sigma_{pm0}) \cdot \gamma_{P,inf} = (1304 - 973.5) \cdot 0.83 = 274\,\text{MPa}$$

However, this flexural tension reserve is irrelevant when the stress increase in the prestressing steel $\Delta\sigma_{ptd}$ at the ultimate limit state has been ignored right from the very start.
The situation is more favourable when using *grouted post-tensioned tendons*; the values in the above example change as follows:
Maximum reserves for flexural tension with grouted post-tensioned tendons:

$$\Delta\sigma_{p0d} \leq \sigma_{p,Rd} - \sigma_{pm0} = 1304 - 973.5 = 330.5\,\text{MPa}$$

This difference in stress can be exploited at the ultimate limit state in order to transfer the bending moments across the joints in a prestressed concrete tower. The goal should be to achieve a flexural tension reserve in the region of the design value of the reinforcing steel. To do this, however, the level of prestress must be reduced as follows:

$$\sigma_{pm\,0} \leq \sigma_{p,Rd} - f_{yd} = 1304 - 435 = 869\,\text{MPa} (= 0.49 \cdot f_{pk})$$

With a favourable effect of the prestress, that is for verifying decompression, a relatively low level of prestress is then available: The realistic assumption of a 25% loss in prestress with concentric prestressing would then result in

$$\sigma_{p\infty k,inf} = 0.90 \cdot \sigma_{pm\infty} = 0.90 \cdot 0.75 \cdot \sigma_{pm\,0} = 0.90 \cdot 0.75 \cdot 869 = 586\,\text{MPa}$$

However, the flexural tension reserve then increases noticeably. In the case of *grouted post-tensioned tendons*, the result is then

$$\Delta\sigma_{p\infty d} \leq \sigma_{p,Rd} - \sigma_{pm\infty} = 1304 - 586 = 718\,\text{MPa} (> f_{yd})$$

The flexural tension reserve – under the condition $\varepsilon_{pd} \leq \varepsilon_{p0.1d}$ (see above) – gives us the following maximum reserve for the *bending moment that can be accommodated* by the cross-sectional area of prestressing steel:

$$\Delta M_{p0d} \leq \Delta\sigma_{p0d} \cdot A_p \cdot r_p/2$$

where

A_p total cross-sectional area of external tendons inside tower
r_p radius of circumcircle of external tendons

All in all, it should be pointed out that with respect to ensuring adequate reserves of flexural tension at the ultimate limit state, it is not a good idea to select an excessively high *level of prestress* for the concentric tendons in the tower.

An example of a calculation for an *antenna support structure* can be found in *Beton-Kalender 2006* [8]. The *tower for a wind turbine* would be analysed in a similar way.

4.7.2 Linear analysis of internal forces

DIN 1045-1 [33] 8.6.1 stipulates that verifying the equilibrium state of loadbearing structures with bar-type members or walls subjected to axial compression (and in particular the equilibrium state of these members themselves taking into account the effects of member deformations) is essential when deformations reduce the load-carrying capacity by more than 10%.

By implication, this means that in all other cases the internal forces at the ultimate limit state may be calculated using a linear analysis (to first-order theory), which in turn means that the internal forces due to the individual independent actions may be combined linearly according to the superposition principle [44].

This requirement is generally satisfied in power production.

The following applies to onshore wind turbines [9] for group N (normal and extreme), or to offshore wind turbines [11] for groups N (normal), E (extreme) and T (transport/erection):

$$E_d = \sum_{j\geq 1} \gamma_{G,j} \cdot E_{Gk,j} + \gamma_P \cdot E_{Pk} + \sum_{i\geq 1} \gamma_{Q,i} \cdot E_{Qk,i}$$

The normal wind profile model (NWP) is combined with a design wave for *design load case 1.15* (see Table 4.4). The following applies in particular for an explicit consideration of the design load cases:

$$E_d = \sum_{j\geq 1} \gamma_{G,j} \cdot E_{Gk,j} + 1.00 \cdot E_{Pk} + 1.20 \cdot \left[E_{Q(V_r \text{ or } V_{out})} + E_{Q\left(H_s(V) \text{ or } H_{max,1}\right)} + Q_{N,k}\right]$$

The following generally applies for group A (accidental, earthquake):

$$E_{dA} = \sum_{j \geq 1} \gamma_{GA,j} \cdot E_{Gk,j} + \gamma_{PA} \cdot E_{Pk} + E_{Ad} + \sum_{i \geq 1} \gamma_{QA,i} \cdot E_{Qk,i}$$

The following applies in particular for an explicit consideration of the design load cases for *design load case 2.2* (system failure, see Table 4.4):

$$E_{dA} = \sum_{j \geq 1} \gamma_{GA,j} \cdot E_{Gk,j} + 1.00 \cdot E_{Pk} + 1.10 \cdot \left[E_{Q(V_{hub})} + E_{Q(H_s(V))} + E_{QN,k}\right]\Big|_{A_d(DLC\ 2.2)}$$

4.7.3 Analysis of stresses in tower shaft

The design values for the internal forces (M_{Ed}, N_{Ed}) are taken from the deformation analysis (see Section 4.7.1). The stresses are calculated on the basis of a linear strain curve according to Section 3.5 with the help of the stress-strain curves (Figures 3.10 and 3.11). The analysis must take into account *openings in the shaft wall* (width B_i, Figure 4.17); Section 4.7.4 deals with the design of such openings.

In contrast to Section 3.3.3, the stresses may be related to the shell middle surface, so the bending stiffness of the shell is excluded. The error associated with this is negligible for thin shells.

The final strains are determined iteratively with the help of the equilibrium conditions between the internal forces and the external internal forces (N_{Ed}, $M_{z,Ed}$):

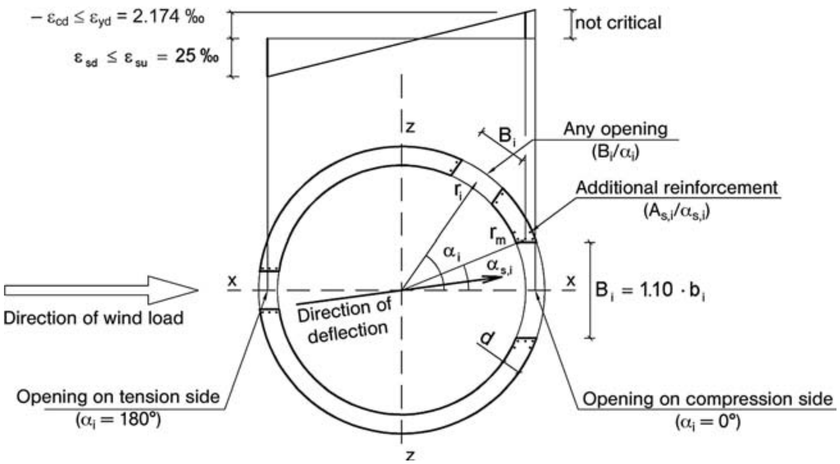

Fig. 4.17 Taking into account openings in the cross-section and additional reinforcing steel

$$\sum_{i(\text{shell})} (\sigma_{ci} + \sigma_{si} + \rho_s) \cdot A_{ci} - \sum_{i(\text{opening})} \sigma_{ci} \cdot B_i \cdot d + \sum_{i(\text{reveal})} \sigma_{si} \cdot A_{si} \overset{!}{=} N_{Ed}$$

$$\sum_{i(\text{shell})} (\sigma_{ci} + \sigma_{si} + \rho_s) \cdot A_{ci} \cdot r_i \cdot \cos\alpha_i - \sum_{i(\text{opening})} \sigma_{ci} \cdot B_i \cdot d \cdot r_i \cdot \cos\alpha_i$$
$$+ \sum_{i(\text{reveal})} \sigma_{si} \cdot A_{si} \cdot r_i \cdot \cos\alpha_i \overset{!}{=} M_{z,Ed}$$

$$\sum_{i(\text{shell})} (\sigma_{ci} + \sigma_{si} + \rho_s) \cdot A_{ci} \cdot r_i \cdot \sin\alpha_i - \sum_{i(\text{opening})} \sigma_{ci} \cdot B_i \cdot d \cdot r_i \cdot \sin\alpha_i$$
$$+ \sum_{i(\text{reveal})} \sigma_{si} \cdot A_{si} \cdot r_i \cdot \sin\alpha_i \overset{!}{=} 0$$

The ultimate limit state can therefore be verified:

$$-\varepsilon_{c2} \le \varepsilon_i \le \varepsilon_{su}$$

A temperature gradient in the shaft wall (see Section 2.7) does not need to be considered during the design either because

$$\varepsilon_{c2} + \varepsilon_T = 2.0‰ + 0.075‰ = 2.075‰ < \varepsilon_{c2u} = 3.5‰$$

Details can be found in [8], which uses a telecommunications tower as an example.

4.7.4 Special characteristics of prefabricated construction

4.7.4.1 Terminology

Prestressed concrete members made up of smaller precast concrete elements are characterised by the fact that the individual elements are assembled in the loadbearing direction and then post-tensioned together.

The joints between the elements are in the form of compression or filled joints, using materials with a cement or polymer binder. Reinforcing steel crossing the joints is not provided. Grouted post-tensioned tendons are installed in the loadbearing direction.

Reinforcing steel is provided in the individual precast concrete elements and they can be prestressed, for example, transverse to the principal loadbearing direction.

Compression joint:

A fine mortar based on cement or a polymer resin (adhesive) which is compressed by post-tensioning the elements together immediately after being applied to the faces of the joint; any excess mortar exudes out of the joint.

Filled joint:

The elements are not post-tensioned together until after the compacted mortar or concrete of the joint has reached a sufficient degree of hardness.

Shear force transfer across fully overcompressed joints:

Eq. (84) from DIN 1045-1 [33] 10.3.6 should be applied here in a suitable form. As the end faces of the elements are generally cast without any profile, $c_j = 0$ may be used

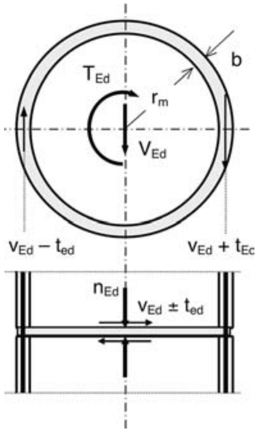

Fig. 4.18 Action effects on fully overcompressed joint between precast concrete elements

(assumption: "very smooth"). Using the coefficient of friction $\mu = 0.5$, it follows that (Figure 4.18)

$$v_{Rd,ct} = \left(c_j \cdot f_{ctd} - \mu \cdot \sigma_{Nd}\right) \cdot b = \frac{-0.5 \cdot N_{Ed}}{2 \cdot \pi \cdot R_m}$$

Action effects in the circumferential direction of the joint:

$$v_{Ed} = \frac{V_{Ed}}{\pi \cdot R_m}; \qquad t_{Ed} = \frac{T_{Ed}}{2 \cdot \pi \cdot R_m^2}$$

Using the format for checking the load-carrying capacity

$$v_{Ed} + t_{Ed} \leq v_{Ed,ct}$$

it follows that

$$V_{Ed} + \frac{T_{Ed}}{2 \cdot R_m} \leq -0.25 \cdot N_{Ed}$$

At the serviceability limit state, joints between elements must be fully overcompressed in the (frequent) design load cases (*decompression limit state*, see Section 4.8.3).

Furthermore, the level of prestress should be chosen in such a way that no decompression occurs even under a fatigue action effect, see Section 4.9.

4.7.4.2 Shear force transfer across opening joints

The shear capacity of opening joints between elements must be determined as follows for *external prestressing*.

Eq. (84) from [33] 10.3.6 should be applied here in a suitable form to the flexural compression zone (Figure 4.19):

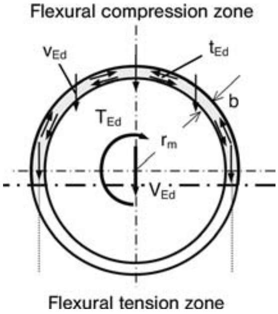

Fig. 4.19 Action effects on opening joint between precast concrete elements

$$v_{Rd,ct} = -\mu \cdot \sigma_{Nd} \cdot b + v_{Rdj,sy} \leq v_{Rdj,max}$$

with the following flexural compressive stress varying over the flexural compression zone:

$$\sigma_{Nd} = \sigma_{cd}(R_m \cdot \cos\varphi) \leq f_{cd}$$

The resultant shear force that can be accommodated via the area of the flexural compression zone is therefore

$$V_{Rd,ct} = -\mu \cdot F_{cd}$$

The loadbearing reserves of the prestressing steel (as a contribution to $v_{Rdj,sy}$) cannot be activated in this simplified structural model.

A Bredt shear flow can no longer be established in the overcompressed partial cross-section and so the torque must be accommodated solely via the St. Venant moment of resistance:

$$t_{Rd(ct)} = -\mu \cdot \sigma_{Nd} \cdot b^2/3$$

or

$$T_{Rd(ct)} = -\mu \cdot F_{cd} \cdot b/3$$

In a similar way to DIN 1045-1 [33] 10.4.2 (5), a quadratic interaction can be assumed for the combined analysis of the load-carrying capacity:

$$\left(\frac{V_{Ed}}{V_{Rd,ct}}\right)^2 + \left(\frac{T_{Ed}}{T_{Rd(ct)}}\right)^2 \leq 1$$

As the St. Venant torsional capacity is low, it can be critical for determining the thickness of the shell required for the tower.

An alternative would be to provide keyed joints (joggle joints) between the precast concrete elements, in a similar way to prestressed precast concrete bridges.

When using *grouted post-tensioned internal tendons*, the shear capacity of opening joints is determined in a similar way to DIN 1045-1 [33] 10.3.6 (13). It should be remembered here that joints at 90° to the system axis function like bending cracks and their faces should therefore be rough or profiled. The *shear force capacities* should therefore be verified according to DIN 1045-1 [33] 10.3.3 and 10.3.4. In doing so, $V_{Rd,ct}$ according to Eq. (70), $V_{Rd,c}$ according to Eq. (74) and $V_{Rd,max}$ according to Eq. (76) should be reduced in the ratio $c_j/0.50$.

If *torsion* is also involved, then the shear capacity in the region of the joint should be checked in a similar way to DIN 1045-1 [33] Eq. (88) as follows (compare analysis of complete overcompression, Figure 4.18):

$$v_{Ed} + t_{Ed} < v_{Rd,F}$$

where

$$v_{Ed} = \frac{V_{Ed}}{\pi \cdot R_m}$$

$$t_{Ed} = \frac{T_{Ed}}{2 \cdot \pi \cdot R_m^2}$$

c_j roughness factor to DIN 1045-1 [33] Table 13
$v_{Rd,F}$ shear capacity in the region of the joint:

a) without the shear reinforcement theoretically required similarly to DIN 1045-1 [33] Eq. (70):

$$v_{Rd,ct,F} = c_j/0.50 \cdot v_{Rd,ct}$$

where

$$v_{Rd,ct} = \left[\frac{0.15}{\gamma_c} \cdot \kappa \cdot \eta_1 \cdot (100 \cdot \rho_L \cdot f_{ck})^{1/3} - 0.12 \cdot \sigma_{cd}\right] \cdot b \geq \left[\eta_1 \frac{\kappa_1}{\gamma_c} \cdot \sqrt{\kappa^3 \cdot f_{ck}} - 0.12 \cdot \sigma_{cd}\right] \cdot b$$

b) with shear reinforcement similar to DIN 1045-1 [33] Eq. (75):

$$v_{Rd,sy,F} = \frac{A_{sw}}{s_w} \cdot f_{yd} \cdot \cot\theta_F$$

$$0.58 \leq \cot\theta_F \leq \frac{1.2 - 1.4 \cdot \sigma_{cd}/f_{cd}}{1 - v_{Rd,c,F}/v_{Ed}}$$

similar to Eq. (73), and

$$v_{Rd,c,F} = c_j \cdot 0.48 \cdot \eta_1 \cdot f_{ck}^{1/3} \cdot (1 + 1.2 \cdot \sigma_{cd}/f_{cd}) \cdot b,$$

similar to Eq. (74), but with c_j according to DIN 1045-1 [33] Table 13.

c) maximum, similar to DIN 1045-1 [33] Eq. (76):

$$v_{Rd,max,F} = c_j/0.50 \cdot v_{Rd,max}$$

where

$$v_{Rd,max} = \frac{\alpha_c \cdot f_{cd}}{\cot\theta + \tan\theta} \cdot b$$

In components with shear reinforcement, $v_{Rd,c}$ and $v_{Rd,max}$ must be reduced at least up to a distance of $L_e = 0.5 \cdot \cot\theta \cdot d$ on both sides of the joint.

Interaction between bending and torsion in the joint between the elements can be taken into account in the bending design by adding a differential tensile force $\Delta N_{Ed,T}$ to the respective design value of the normal force N_{Ed}; the former depends on the associated torsion action effect t_{Ed} – similar to DIN 1045-1 [33] Eq. (92):

$$\Delta N_{Ed,T} = t_{Ed} \cdot u_k \cdot \cot\theta_F$$

4.7.4.3 Detailed design

The capacities of the cross-sections are verified according to DIN 1045-1 [33]; for details see Section 4.7.1. The concrete strength design value, for example for a C 50/60 concrete, is

$$f_{cd} = 0.85 \cdot 50/1.50 = 28.3\,\text{MPa}$$

The partial safety factor for the concrete compressive strength should be increased by 10% because of the possible drop in strength near the joints, see DIN 4227-3 [63]:

$$f_{cd} = 0.85 \cdot 50/1.65 = 25.8\,\text{MPa}$$

4.7.4.4 Transferring prestressing forces

Transverse tensile forces $N_{\varphi,Ed}$ in the circumferential direction occur at the force transfer zones above and below the prestressing points and the spacers (Figure 4.20):

$$N_{\varphi,Ed} \leq 0.10 \cdot F_{p,max}$$

Radial change-of-direction forces h_{Ed} are thus mobilised and these cause bending action effects $m_{s,Ed}$ at the edges of the shell [64]:

$$h_{Ed} = N_{\varphi,Ed}/r_m$$
$$m_{s,Ed} = -h_{Ed} \cdot \frac{r_m}{\kappa} \cdot e^{-\kappa \cdot \frac{s}{r_m}} \cdot \sin\left(\kappa \cdot \frac{s}{r_m}\right)$$

The hoop tension forces $N_{\varphi,Ed}$ can be accommodated by tangential reinforcing steel, the bending disturbances $m_{s,Ed}$ by vertical U-bars.

4.7.4.5 Erecting and prestressing precast concrete elements

The precast concrete elements are bedded on plastic spacers in fresh mortar joints. The tendons are generally prestressed as a whole from their upper ends (Figure 4.21).

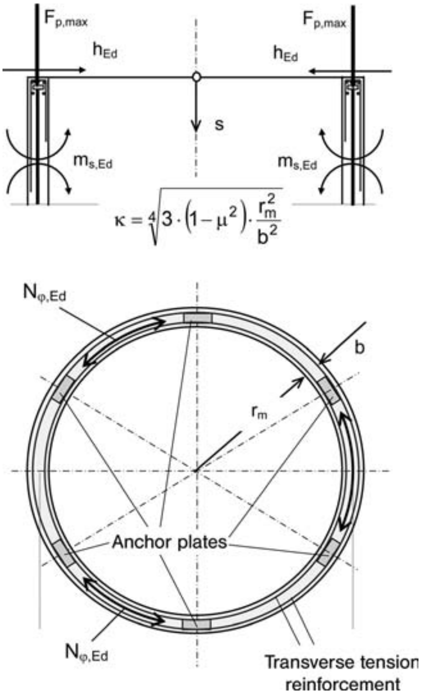

Fig. 4.20 Transferring prestressing forces at joints between precast concrete elements

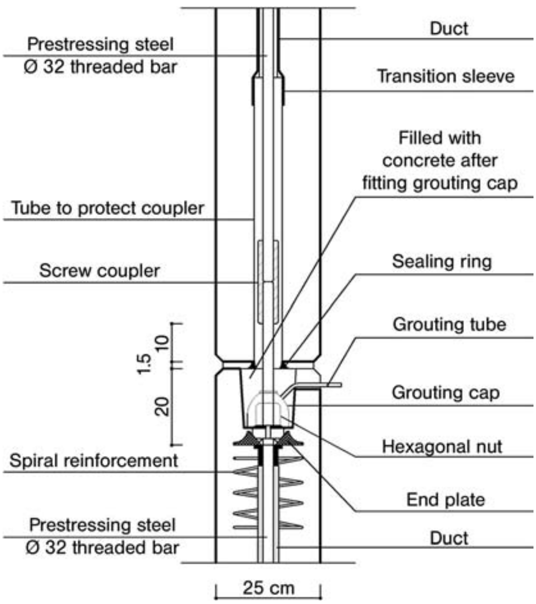

Fig. 4.21 Tendon coupling at a joint between precast concrete segments

Therefore, they should be arranged in such a way that the necessary prestress can be applied for the final condition as well as interim conditions during construction.

Individual tendons can also be prestressed at intermediate points if required for the stability of an interim condition during construction. The tendons are normally connected with screw couplers. The edge distances of the tendon end plates must be very accurately maintained in order to prevent prestressing forces causing spalling at the edges of the shell.

4.7.4.6 Design of openings

Vertical direction
The inclusion of openings means that the heavily loaded concrete is missing as a component of the cross-section in the flexural compression zone (Figure 4.22). Door openings at the base of the tower are particularly critical. Therefore, the widths of openings should be kept as small as possible (e.g. $L_w = 0.72\,m$).

The door reveals require additional reinforcing steel (not prestressing tendons, which would increase the compression!). The centroid axis is displaced because of the opening. The eccentricity moments due to the concentric dead loads and the prestressing increase

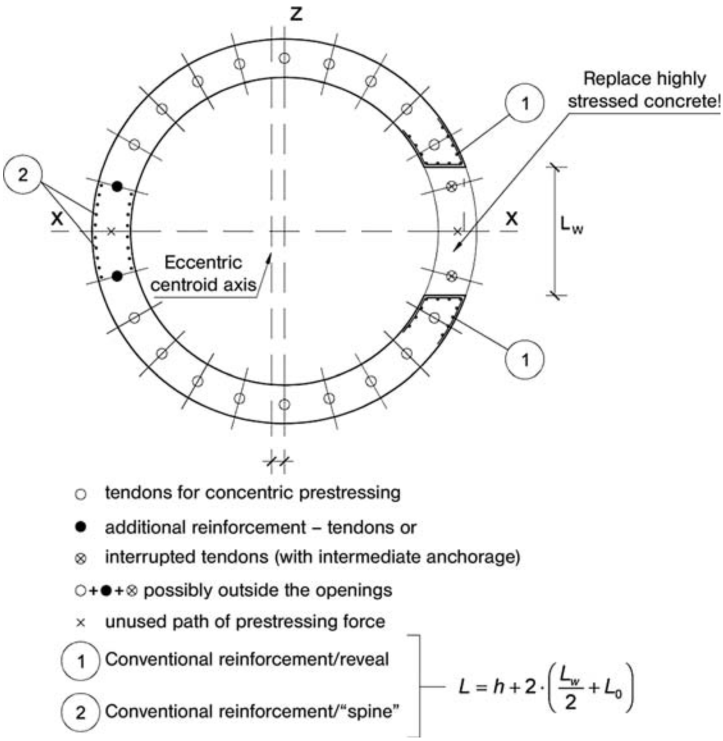

Fig. 4.22 Vertical reinforcement at an opening in the cross-section of a precast concrete element

the compression in the reveals. Interrupting the tendons around the opening and introducing an eccentric “spine tensioning” are therefore recommended.

Horizontal direction (DIN 1056 [13], DAfStb No. 240 [65])
Figure 4.23 gives us the following design equations:

Lintel load to [13] 9.3 for $L_w < 1.4\,\text{m}$ (and smaller than the inner radius):

$$q_{Ed} \leq 2/3 \cdot \left(f_{cd} + \rho_s \cdot f_{yd}\right) \cdot d$$

where

f_{cd} design value of concrete strength
f_{yd} design value of yield point of steel
d wall thickness
ρ_s geometric reinforcement ratio

Tie reinforcement in lintel and threshold:

$$①A_{s,F} = 0.09 \cdot q_{Ed} \cdot 1.15 \cdot L_w \cdot \gamma_S/f_{yk} = 0.12 \cdot q_{Ed} \cdot L_w/f_{yk} \text{ with } \gamma_S = 1.15$$

Support reinforcement in lintel and threshold:

$$②A_{s,F} = 0.21 \cdot q_{Ed} \cdot L_w/f_{yk}$$

Example: $d = 0.40\,\text{m}$, C 30/37, $\rho_s = 1\%$, BSt 500:

$$q_{Ed} = 2/3 \cdot (17.0 + 0.01 \cdot 435) \cdot 0.40 = 5.7\,\text{MN/m} \quad \text{or} \quad 5700\,\text{kN/m}$$

$$A_{s,F} = 0.12 \cdot 5700 \cdot 0.72/50 = 9.8\,\text{cm}^2$$

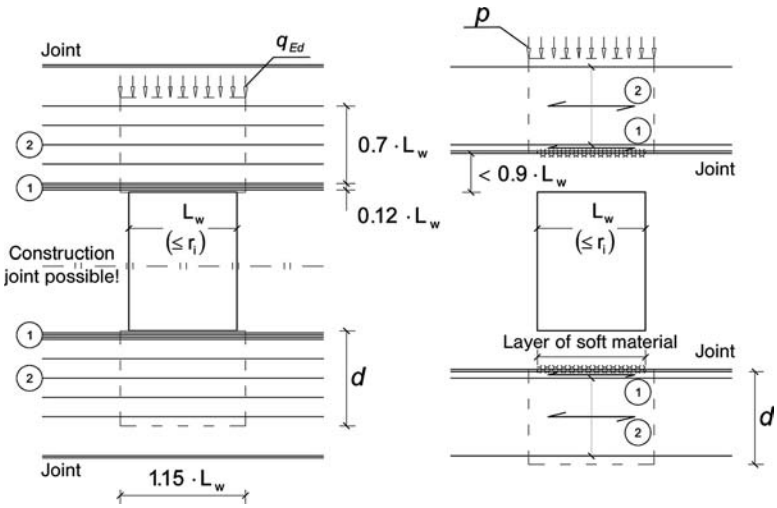

Fig. 4.23 Horizontal reinforcement around an opening in a precast concrete wall

Selected (example): 6 No. ∅ 16

$$A_{s,st} = 0.21 \cdot 5700 \cdot 0.72/50 = 17.2\,\text{cm}^2$$

distributed over a height of $0.7 \cdot 0.72 = 0.50$ m

Selected (example): 2 × 5 No. ∅ 16 ($s_w = 10\,\text{cm}$)

4.8 Analysis of serviceability limit state

4.8.1 Action effects in tower shaft due to external actions

4.8.1.1 Limiting the deformations

The deformations must be limited to suit the usage requirements. In cases with particular requirements, the angular rotations of the rotor hub of a wind turbine must be limited for the operating condition, likewise the associated stress level.

4.8.1.2 Limiting the stresses

The compressive stresses in the concrete must be limited as follows:

– for the rare DLC 1.6: $\sigma_c \leq 0.60 \cdot f_{ck}$
– for the quasi-permanent DLC 1.0: $\sigma_c \leq 0.45 \cdot f_{ck}$

4.8.1.3 Limiting crack widths and decompression limit state

Limiting the crack widths should be carried out according to Table 4.9 for the stabilised cracking state.

Table 4.9 Requirements for limiting crack width and decompression

Type of construction	Design load case[a)] for verifying . . .		Theoretical crack width
	decompression	crack width limitation	
Reinforced concrete and prestressed concrete with unbonded tendons	—	quasi-permanent DLC 1.0	0.20 mm
Prestressed concrete with bonded tendons	quasi-permanent DLC 1.0	frequent DLC 1.5 and DLC 1.11	

[a)] The value $P_{k,inf} = r_{inf} \cdot P_{m,t}$ may be used as a characteristic value for prestressing, where $r_{inf} = 0.95$ for prestressing with unbonded tendons and $r_{inf} = 0.90$ for prestressing with bonded tendons [33,36].

The tensile stresses in the vertical reinforcing steel should be calculated for the cracked state for the critical design load case, that is quasi-permanent or frequent, in order to determine either the maximum diameter of the reinforcing bars d_s or their maximum spacing according to [33]. A minimum amount of reinforcement for controlling crack widths is unnecessary because the tower shaft is a statically determinate component without restraint stresses.

Similarly to DIN 1045-1 [33] 13.1.1 (1), the following minimum reinforcement is required to guarantee ductile behaviour of the member (see Section 3.2 and Table 3.2):

$$\rho_s > \frac{f_{ctm}}{f_{yk} - \alpha_{Ed} \cdot f_{ctm}}$$

where

f_{ctm}	mean value of concrete tensile strength according to [33] Tables 9 or 10
f_{yk}	characteristic value of yield point of reinforcing steel
$\alpha_{Ed} = \gamma_C \cdot E_s/E_{c0m}$	see Section 3.2

Table 4.9 replaces Tables 18 and 19 of DIN 1045-1 [33].

4.8.2 Restraint stresses acting on shaft wall

The temperature gradient between the exterior air and the inside of the tower give rise to a bending restraint in both the vertical and circumferential directions.

According to DIN 1045-1 [33] 11.2.2, we get the following minimum percentage of reinforcement for guaranteeing limited crack widths under bending restraint stresses:

$$\rho_s = 0.2 \cdot \frac{\sigma_{c,\Delta T}}{\sigma_s} \leq 0.2 \cdot \frac{f_{ctm}}{\sigma_s} \quad \text{related to the total wall thickness}$$

where $\sigma_{c,\Delta T} = \alpha_{T,c} \cdot E_{c0m} \cdot \Delta T/2$ and $\Delta T = \pm\, 15\,K$ according to [9].

Here, $\boldsymbol{\sigma_s}$ is the permissible steel stress in the minimum reinforcement immediately following the appearance of the first crack, depending on the theoretical crack width w_k (see Section 4.8.1) and the limiting diameter d_s^* (see DIN 1045-1, Table 20 [33]).

From this we get, for example, for C 20/25 concrete:

$$\sigma_{c,\Delta T} = \pm 10^{-5} \cdot 28\,800 \cdot 15/2 = \pm 2.16\,\text{MPa} < f_{ctm} = 2.21\,\text{MPa}$$

According to this, the minimum reinforcement for limiting the crack widths according to DIN 1045-1 [33] 11.2.2 already governs for concrete grades C 20/25 and higher.

Further, assuming $w_k = 0.20\,\text{mm}$ and $d_s = 12\,\text{mm}$, then

$$d_s^* = d_s \cdot \frac{f_{ct0}}{f_{ctm}} = 12 \cdot \frac{3.0}{2.21} = 16.3\,\text{mm}$$

$$\sigma_s = 214\,\text{MPa}$$

according to DIN 1045-1 Table 20 [33]

$$\rho_s = 0.2 \cdot \frac{2.21}{214} = 0.21\%$$

4.8.3 Special aspects of construction with precast concrete elements

Compared with prestressed *in situ* concrete, higher demands are placed on the overstressed joints because outside the zones directly affected by the tendons it is not possible to verify the crack width limitation at the joints.

No tensile stresses are permissible in the load case "$G_k + P_{m\infty} + 0.4 \cdot Q_{k,W}$" according to DIN 4228 [15] 6.3 (*decompression limit state*). Similarly, according to DIN 4227-3 [63], the following applies for this case:

$$\sigma_{c,Gk} + 0.9 \cdot \sigma_{cpm\infty} + 0.4 \cdot \sigma_{c,QkW} \leq -1.0\,\text{MPa}$$

According to [63] 7.1, the *crack formation limit state* must be investigated for the characteristic load combination (= normal load according to [15]). It is not necessary to verify the crack width at the joints provided

$$\sigma_{c,Gk} + 0.9 \cdot \sigma_{cpm\infty} + 1.0 \cdot \sigma_{c,QkW} \leq -2.0\,\text{MPa}$$

In this case it is to be expected that the tendons, including their ducts, remain overcompressed for a temperature gradient in the wall amounting to $\Delta T = 15\,\text{K}$.

Figure 4.24 shows the effect of a temperature gradient over the wall thickness.

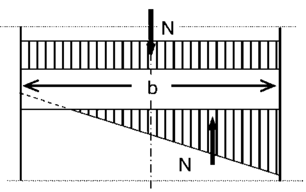

Fig. 4.24 Restraint stresses as a result of a temperature gradient

$$\text{Example : C } 50/60 \quad E_{cm} = 36800\,\text{MPa}$$

$$\sigma_{c,\Delta T} = \pm 15/2 \cdot 36\,800 \cdot 10^{-5} = \pm 2.8\,\text{MPa}$$

$$\sigma_{c,n} \leq -2.0\,\text{MPa}$$

$$N = \sigma_{c,n} \cdot b \cong x \cdot (2 \cdot \sigma_{c,\Delta T}/b) \cdot x/2$$

$$(x/b) = (\sigma_{c,n}/\sigma_{c,\Delta T})^{0.5} = (2.0/2.8)^{0.5} = 0.84$$

Otherwise, Equation (2) in [63] results in the *joint crack width* in the vicinity of tendons being effectively limited to $w_k \leq 0.04\,mm$:

$$d_p \leq \frac{r}{\Delta\sigma_p^2} \cdot 10^4 \quad \text{with r} = 10 \text{ according to [19] Table 2 for ribbed bars.}$$

According to DIN 1045-1 [33], the *limiting diameter* d_s^* for a given crack width $w_{k,cal}$ is

$$d_s^* = 6 \cdot w_{k,cal} \cdot \frac{E_s \cdot f_{ct,eff}}{\sigma_{sII}^2}$$

Using the bond coefficient $\xi = 0.7$ for a ribbed prestressing tendon, the reference value for the concrete tensile strength $f_{ct0} = 3.0$ MPa and $E_s = 200\,000$ MPa, we obtain

$$d_p^* = 6 \cdot w_{k,cal} \cdot \frac{E_s \cdot \xi \cdot f_{ct,eff}}{\Delta\sigma_p^2} = 252 \cdot 10^4 \cdot \frac{w_{k,cal}}{\Delta\sigma_p^2} \cdot \frac{f_{ct,eff}}{f_{ct0}}$$

Comparing the coefficients of the formats for d_p and d_p^* on the basis of $f_{ct,eff} = f_{ct0}$ results in the crack width required:

$$w_{k,cal} \leq \frac{r = 10}{252} = 0.04\,\text{mm}$$

4.9 Fatigue limit state

In prestressed concrete loadbearing structures, fatigue analyses must be carried out for the concrete, reinforcing steel and prestressing steel (and its anchorages). These analyses may be performed according to the stipulations of the DIBt Guideline [9] in line with the method of analysis given in Model Code 90 [66].

The level of prestress should be chosen in such a way that no decompression occurs under fatigue loads. This approach enables the stress ranges in the prestressing steel to be limited and prevents cracking of the cross-section, which could lead to damage!

The following equation should be used instead of the quasi-permanent design load case:

$$\sigma_{c,Ed} = \sigma_{c,Gk} + r_{inf} \cdot \sigma_{c,pm\infty} + \psi_{1,W} \cdot \left[\sigma_{c,Wk} + \sigma_{c,Hs(Wk)}\right] + \psi_{2,\Delta T} \cdot \sigma_{c,\Delta Tk} \leq 0$$

where

- $\sigma_{c,Gk}$ stress in concrete under permanent actions
- $\sigma_{c,pm\infty}$ prestress taking into account the loss of prestress over time at time $t \to \infty$, with the scatter factor r_{inf} according to DIN 1045-1 [33] 8.7.4 (2)
- $\sigma_{c,Wk}$ stress in concrete under characteristic wind loads (see Sections 4.5.3 or 4.6.4), with the combination factor $\psi_{1,W} = 0.5$ for frequent wind loads
- $\sigma_{c,Hs(Wk)}$ stress in concrete under the action effect resulting from characteristic sea state loads for characteristic wind loads with the significant wave height H_s $(V(W_k))$, see Sections 2.5.6 and 4.6.4
- $\sigma_{c,\Delta Tk}$ stress in concrete under characteristic thermal actions, with the combination factor $\psi_{2,\Delta T} = 0.5$ for quasi-permanent action effects (according to DIN Special Report 101)

Note: The maximum values of the wind loads under the EWM wind conditions (see Section 2.3.2) should be used as the characteristic wind loads.

4.9.1 Fatigue-inducing actions on wind turbine support structures

4.9.1.1 Actions due to wind and turbine operation

Numerical simulations are performed in order to determine the extreme and operating loads relevant for a wind turbine structure. The representative environmental relationships used in these calculations are based on DIN 1055-4 and are regulated in the DIBt guideline [9] or DIN EN 61400-1 [16] and DIN EN 61400-3 [10] (see Section 2.3). Besides the steady inflow of the wind, the aerodynamic model also has to take into account the turbulence and gust characteristics of the wind plus sudden changes in the wind direction, and so on. The dynamic response behaviour of the total system – consisting of wind turbine, tower and foundation – to the resultant loading plus the influences imposed by the control and regulation of the wind turbine, for example rotor r.p.m., generator r.p.m., blade pitch angle, also have to be included in the calculations [67], see also [68,69].

The numerical simulation does not cover the entire design working life of a wind turbine because that would require an excessive amount of calculation. Instead, individual periods are considered which, for example, include the design load cases given in Table 4.1 or 4.4. Those design load cases include normal turbine operation, gusts, oblique angle of attack, starting and stopping procedures, grid loss, plus combinations of these (see Section 2.3.2). The design load cases specified depending on the operating conditions are divided into groups N (normal and extreme), A (accidental), F (fatigue) und T (transport/erection) (see Sections 4.5.3 and 4.6.4).

The loading time series thus obtained are combined using statistical methods and taking into account the probability of occurrence of the individual events.

A time series for the design working life required can therefore be compiled for every internal force component. In doing so, the time series must be determined for all the design cross-sections of the support structure [70]. Figure 4.25 shows the course of a numerical load simulation.

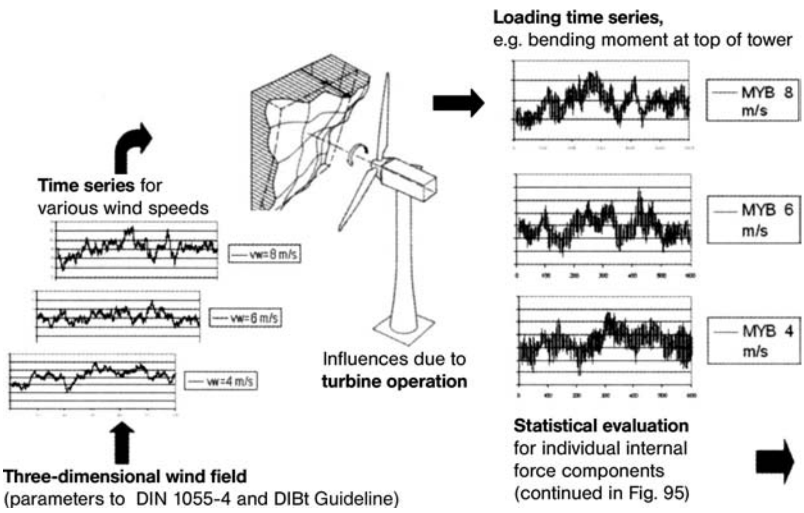

Fig. 4.25 Schematic presentation of a load simulation (after [70])

Rainflow classification of internal forces over time and compilation of **Markov matrices**

Amplitude [kN]	Mean value [kN]	No. of load cycles [-]
10	−5	12508
10	0	12359
10	5	56248
10	10	684289
10	15	25361
12.5	−10	95625
12.5	−5	41588
12.5	0	51236
12.5	5	357851
12.5	10	25948
12.5	15	3215
15	−5	58753
etc.		

Approximation with the distribution of the average wind speeds over the entire design working life

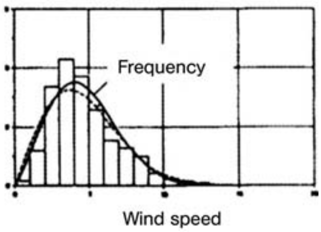

Fig. 4.26 Classification of internal forces [70]

A *total dynamic design* of the support structure with the time series determined is only carried out in exceptional circumstances because of the huge effort required. Normally, a simplified calculation is performed, which involves evaluating the simulated load cycles at the individual design cross-sections using a suitable counting method (e.g. rainflow counting) and classifying them according to mean values and stress ranges. The collective loads obtained in this way are combined together with the associated number of load cycles, for example in Markov matrices, and extrapolated to the design working life of the wind turbine (see Figure 4.26). The chronological relationship between the different action effects is lost while doing this, which means that there may be an unfavourable superposition of individual internal forces that do not occur simultaneously within one collective load [67].

In a total dynamic analysis, which should be carried out on the combined structure consisting of foundation, tower, wind turbine and three-dimensional wind field, the design internal forces may be determined with a partial safety factor $\gamma_F = 1.00$. If on the other hand in a simplified calculation, collective loads from the aeroelastic simulation are applied to the turbine/tower interface, then the collective loads must be multiplied by the partial safety factors depending on the design load case groups of Tables 4.3 or 4.7.

Strength and stability analyses with the most unfavourable of all design load cases must be carried out for groups N, (E,) A and T at the ultimate limit state. On the other hand, the analyses for fatigue failure are carried out with the design load cases for group F.

Analysing the limits to stresses and crack widths and decompression (see above) for the serviceability limit state calls for the use of the design load cases to Tables 4.1 or 4.4. These cases correspond to DIN 1045-1 [33] depending on the analyses of the rare, frequent or quasi-permanent design load cases that have to be performed. For details see [9].

4.9.1.2 Actions due to waves and sea state

The design of support structures for offshore wind turbines must include, in particular, the dynamic excitation due to wave loads (see Sections 2.4 and 2.5). Both the extreme wave loads and the fatigue loads due to the sea state are critical for the design. Offshore structures can be subjected to more than 10^8 wave load cycles over a design working life of 20 years.

Up to 10^9 load cycles for wind loads alone can be expected over the same period [23]. The sea state is customarily described on the basis of short- and long-term statistics. The methods used for this are described in detail in Section 2.5.

4.9.2 Fatigue analyses according to DIBt wind turbine guideline

4.9.2.1 Simplified analyses for concrete

According to [9], a more accurate analysis of the concrete for repeated compressive loads is unnecessary in wind turbine support structures with $N_{nom} \leq 2 \cdot 10^9$ load cycles provided the condition according to Equation 4.1 is adhered to:

$$S_{cd,max} \leq 0.40 + 0.46 \cdot S_{cd,min} \tag{4.1}$$

Here, $S_{cd,min}$ and $S_{cd,max}$ denote the minimum and maximum effective concrete compressive stress respectively due to the design load cases of Tables 4.1 or 4.4, group F, to be investigated. They are calculated using Equations 4.2 and 4.3:

$$S_{cd,min} = \gamma_{sd} \cdot \sigma_{c,min} \cdot \eta_c / f_{cd,fat} \tag{4.2}$$

$$S_{cd,max} = \gamma_{sd} \cdot \sigma_{c,max} \cdot \eta_c / f_{cd,fat} \tag{4.3}$$

where

$\gamma_{Sd} = 1.10$	partial safety factor for modelling inaccuracies in the stress calculation
$\sigma_{c,max}$	max. concrete compressive stress
$\sigma_{c,min}$	min. concrete compressive stress at the same point at which $\sigma_{c,max}$ occurs, calculated for the lower value of the action (use $\sigma_{c,min} = 0$ for tensile stresses)
η_c	factor for taking into account the non-uniform distribution of the concrete compressive stresses according to Equation 4.4 ($\eta_c = 1.0$ may be used for simplicity)

The maximum concrete compressive stress at the extreme fibres may be reduced by the factor η_c according to Equation 4.4 in the case of eccentric fatigue loads. This takes into account the way the redistribution of stresses within the cross-section has a positive influence on the resultant fatigue strength.

Therefore, the S-N curves derived from the uniaxial fatigue tests can be used when determining the number of fatigue cycles to failure, also in the case of eccentric action effects.

$$\eta_c = \frac{1}{1.5 - 0.5 \cdot \frac{|\sigma_{c1}|}{|\sigma_{c2}|}} \tag{4.4}$$

Figure 4.27 shows the stress distribution for calculating η_c according to Model Code 90 [66]. Figure 4.28 shows this distribution transferred to a tower cross-section.

The reason for limiting the distance from the outer edge to $x \leq 300\,\text{mm} \leq t$ ($t =$ shaft wall thickness) in Model Code 90 [66] is given in [49], which states that stress redistributions are to be especially expected in structural cross-sections with a low

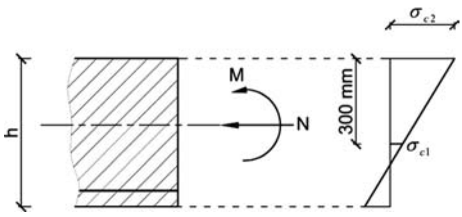

Fig. 4.27 Stresses for calculating η_c according to Model Code 90 [66]

depth. To what extent stress redistributions take place in thicker cross-sections has not yet been investigated. The limit laid down in Model Code 90 is therefore to be regarded as an estimate based on engineering experience.

The design value for the fatigue strength of the concrete $f_{cd,fat}$ subjected to compression loads is determined as follows:

$$f_{cd,fat} = 0.85 \cdot \beta_{cc}(t) \cdot f_{ck} \cdot (1 - f_{ck}/250)/\gamma_c \tag{4.5}$$

where

$\beta_{cc}(t)$ coefficient for taking into account the increase in the concrete strength over time. (In the simplified analysis according to Equation 4.1 this should be $\beta_{cc}(t) = 1.0$ provided the first cyclic load takes place when the concrete is $\geq$ 28 days old; but if the first cyclic load takes place earlier, then the factor $\beta_{cc}(t) < 1.0$ has to be determined and taken into account in the analysis.)
f_{ck} characteristic cylinder compressive strength
γ_c partial safety factor for concrete

The factor of 0.85 in Equation 4.5 takes into account how the permanent load component affects the concrete compressive strength and the difference between

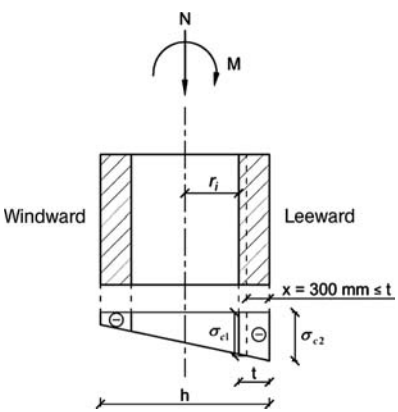

Fig. 4.28 Stresses in the tower shaft for calculating η_c

the loading frequencies of laboratory tests and those of real structures. The fatigue strengths determined experimentally in laboratory tests lead to larger values than the fatigue strengths of actual structures because of the higher loading frequency. In addition, as the strength increases, so the increasingly brittle failure behaviour of the concrete is taken into account by the factor $(1 - f_{ck}/250)$ in Equation 4.5.

As for the short-term strength according to [33], the partial safety factor is taken as $\gamma_c = 1.50$ (or according to [11], see also Section 4.6.5, Table 4.8).

As the actions are taken into account by employing collective loads that already include the maximum values of the actions, the partial safety factor for the actions according to Model Code 90 [66] is $\gamma_{f,fat} = 1.00$.

The following must always be investigated in a simplified analysis (Figure 4.29):

- stress range ΔS_{cd} with $S_{cd,min}$
- maximum stress range max ΔS_{cd}
- stress range ΔS_{cd} with $S_{cd,max}$
- stress range ΔS_{cd} with $S_{cd,m}$

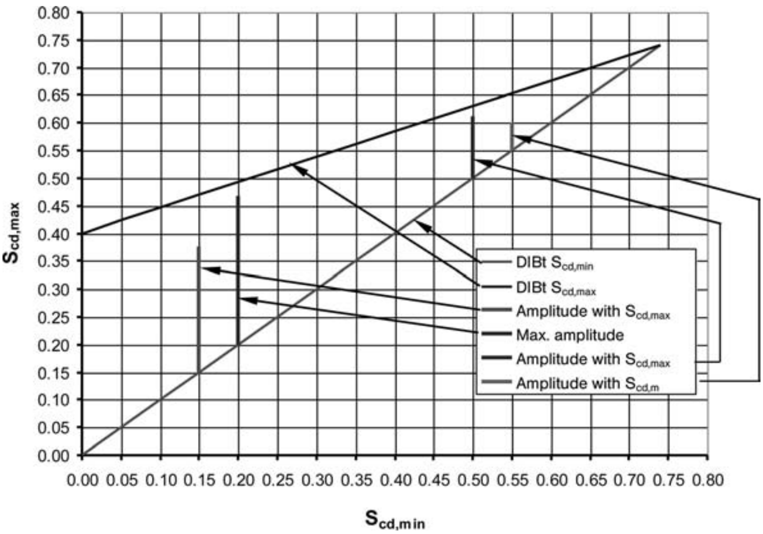

Fig. 4.29 Goodman diagram for concrete subjected to a repeated compressive load

4.9.2.2 Direct analysis according to DIBt guideline

If the conditions for the simplified analysis are not satisfied, the fatigue analysis can be carried out on the basis of the total loading spectrum according to Model Code 90 [66]. The fatigue analysis is based on a model for calculating damage according to Palmgren and Miner [49]. As already outlined in Section 4.9.1.1, the basic idea here is that every cyclic action effect causes damage in the structural component and that this damage accumulates linearly until a critical level is reached. At that point it is presumed that the structural component fails. The assumption here is that the sequence of the action effects has no influence on the damage development.

The analysis therefore uses Equation 4.6 to show that the damage D^{P-M} to the structural component as a result of a repeated action effect does not exceed the damage limit D_{lim}:

$$D^{P-M} = \sum_{i=1}^{j} \frac{N_i}{N_{fi}} \leq D_{lim} \tag{4.6}$$

where

N_i No. of fatigue cycles of loading block i, for example from Markov matrices
N_{fi} No. of fatigue cycles to failure from the S-N curve for concrete (see Figure 4.30)

The limit value for damage according to [9] is $D_{lim} = 1.0$ and corresponds to the stipulations in Model Code 90. Refs. [33] and [66] do not contain details of fatigue analyses in seawater.

Ref. [71] specifies the limit value for offshore structures depending on the options available for maintenance and repairs. A damage value of $D_{lim} \leq 0.33$ must always be assumed for harsh North Sea conditions. The value specified for splash zones is $D_{lim} = 0.5$, the value for areas above these is $D_{lim} = 1.0$. The damage analysis in [71] is also based on the linear damage approach of Palmgren-Miner.

Model Code 90 [66] specifies S-N curves for uniaxial compressive loads and also for tensile or reversed loads; there is no information regarding the fatigue strength of submerged concrete. Instead, the reader is referred to [71], for instance. The relevant publications do not cover how multi-axial stress states influence the resultant fatigue strength.

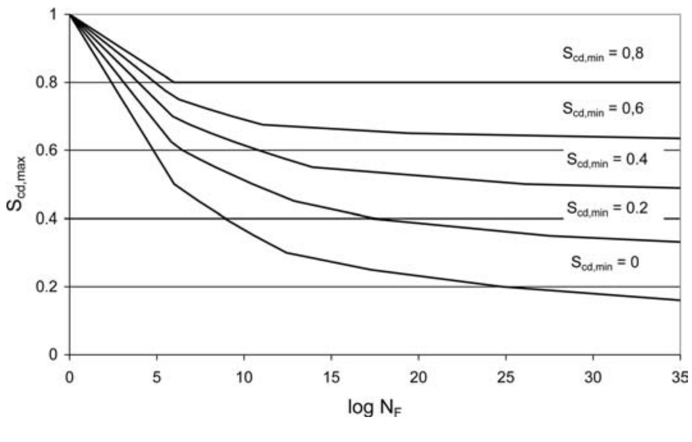

Fig. 4.30 S-N curves for concrete subjected to a repeated compressive load according to Model Code 90 [66]

The S-N curves for repeated compressive loads are as follows:

When $0 < S_{cd,min} < 0.8$, then

$$\log N_1 = (12 + 16 \cdot S_{cd,min} + 8 \cdot S^2_{cd,min}) \cdot (1 - S_{cd,max}) \tag{4.7}$$

$$\log N_2 = 0.2 \cdot \log N_1 \cdot (\log N_1 - 1) \tag{4.8}$$

$$\log N_3 = \log N_2 \cdot (0.3 - 3 \cdot S_{cd,min}/8)/\Delta S \tag{4.9}$$

The critical numbers of fatigue cycles log N are defined according to Equations 4.10 to 4.13:

$$\begin{aligned}&\text{If } \log N_1 \leq 6, \text{then}\\ &\log N = \log N_1\end{aligned} \tag{4.10}$$

$$\begin{aligned}&\text{If } \log N_1 > 6 \text{ and } \Delta S \geq 0.3 - 3 \cdot S_{cd,min}/8, \text{then}\\ &\log N = \log N_2\end{aligned} \tag{4.11}$$

$$\begin{aligned}&\text{If } \log N_1 > 6 \text{ and } \Delta S < 0.3 - 3 \cdot S_{cd,min}/8, \text{then}\\ &\log N = \log N_3\end{aligned} \tag{4.12}$$

$$\begin{aligned}&\text{with } S_{cd,min} \text{ and } S_{cd,max} \text{ according to Eqs.(4.2) and (4.3).}\\ &\Delta S = S_{cd,max} - S_{cd,min}\end{aligned} \tag{4.13}$$

Equation 4.14 applies for the S-N curve for plain concrete subjected to a repeated tensile load:

$$\log N = 12 \cdot (1 - S_{td,max}) \tag{4.14}$$

$$\begin{aligned}&\text{where} \quad S_{td,max} = \gamma_{sd} \cdot \sigma_{ct,max}/f_{ctd,fat}\\ &\text{and} \quad f_{ctd,fat} = f_{ctk;\,0.05}/g_c\end{aligned} \tag{4.15}$$

Figure 4.31 shows the S-N curve for a repeated tensile load.

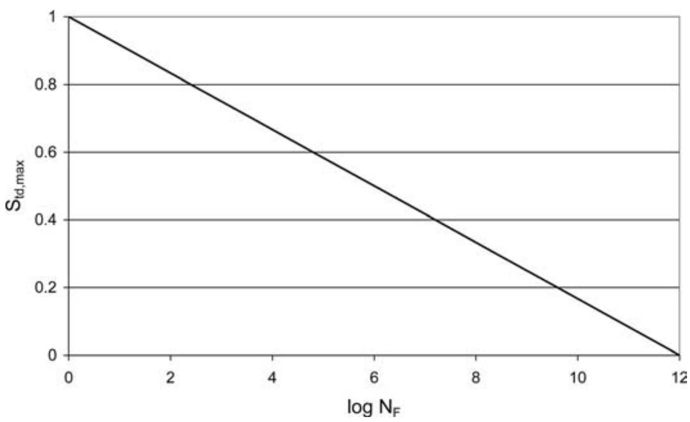

Fig. 4.31 S-N curve for concrete subjected to a repeated tensile load according to Model Code 90 [66]

According to [49], the conditions for both a repeated compressive load and a repeated tensile load should be satisfied for reversed loads.

Here, the minimum stress for a repeated tensile load is

$$\sigma_{ct,min} = 0 \tag{4.16}$$

and that for a repeated compressive load is

$$\sigma_{cd,min} = 0 \tag{4.17}$$

The reader is referred to the information given in [33] and Model Code 90 [66] for the analysis of the fatigue capacity in connection with cyclic shear forces. Commentaries can be found in, for example, [49,72].

4.9.3 Multi-stage fatigue loads

Support structures for wind turbines are subjected to high numbers of load cycles with different stress ranges and maximum stresses. Up until now the influence of such multi-stage fatigue loads on the fatigue behaviour of concrete could only be determined indirectly by exploiting the numbers of fatigue cycles to failure on the basis of a linear accumulation hypothesis. It is therefore not possible to obtain details about the ongoing development of stiffness, or rather damage, during the predicted design working life of a loadbearing structure. However, in order to be able to ascertain the true fatigue process with more accuracy, such information is critical for designs, for example prestressed concrete towers, in which changing stiffness relationships lead to redistributions of stress. In particular, knowledge about the actual distribution of stiffness as a result of fatigue is indispensable for numerical analyses of the structural behaviour of a design if we are to obtain realistic calculations.

Based on an energy approach to the fatigue process, Pfanner [73] devised a mechanical damage model for fatigue loads with a constant stress range.

Further studies can be found in [74], which deals with to what extent Pfanner's energy-based damage model [73] can be extended to multi-stage fatigue loads. The reader is referred to [74] for the damage development in concrete subjected to multi-stage fatigue loads and the evaluation of the linear accumulation hypothesis.

4.9.4 Numbers of fatigue cycles to failure for multi-axial fatigue loads

4.9.4.1 Procedure

The regulations currently applicable do not contain details of how to calculate the numbers of fatigue cycles to failure for multi-axial fatigue loads. Some tests for determining the number of fatigue cycles to failure for selected loading relationships can be found in the literature.

Ref. [74] introduces a new approach for ascertaining the numbers of fatigue cycles to failure for multi-axial fatigue loads; this is summarised below. It is based on a change in the failure envelopes of the concrete when subjected to multi-axial fatigue loads. According to the method, the volume enclosed by the failure envelope decreases as the number of fatigue cycles increases.

This phenomenon can be illustrated using the example of the uniaxial fatigue strength. As the number of fatigue cycles increases, so the uniaxial fatigue strength decreases. What this means for the failure envelope is that at the points of the uniaxial compressive strength, both the value on the hydrostatic axis and the distance ρ increase over the course of the fatigue loading (see Figure 4.33). If these changes are known for significant loading conditions and an increasing number of fatigue cycles, then the modified form of the failure envelope can be described mechanically. It therefore becomes possible to calculate the fatigue strengths for other loading relationships depending on the numbers of fatigue cycles.

Introducing damage variables

The failure model of [41], introduced in Section 3.6.2, is used for the mechanical description of the multi-axial concrete strength. The model describes the shape of the failure envelope with the help of five parameters. Knowledge about the changes to the five parameters depending on the numbers of fatigue cycles enables the multi-axial fatigue strength to be determined by way of the changes to the failure envelope.

In order to describe the changes to the principal meridian for fatigue loads, the damage variable κ_c^{fat} is introduced for the compression meridians and the damage variable κ_t^{fat} for the tension meridians. These damage variables enable the decrease in strength under fatigue loads to be described with the damage model of [41]. For simplicity we shall assume that the fatigue behaviour along the principal meridians can be determined approximately by one damage variable for each case.

Boundary conditions for principal meridians subjected to fatigue loads

The curvatures of the principal meridians are described by Equation 4.18 for the tension meridian and Equation 4.19 for the compression meridian. Furthermore, compliance with convexity conditions according to [41] is essential. The resulting boundary conditions for formulating the principal meridians for fatigue loads are described in Section 3.6.2 and listed in Table 4.10 together with the damage variables introduced.

Parameters for principal meridian equations

By including the parameters for fatigue loads, the parabolic equations for the principal meridians according to [41] (see Section 3.6.2) can continue to be used. These parameters can be determined by taking into account the boundary conditions given in Table 4.10.

The parameters of the parabolic equation for the tension meridian are in accordance with Equation 4.18:

$$a_0 = \frac{2}{\sqrt{3}} \cdot \alpha_{c2} \cdot a_1 - \frac{4}{3} \cdot \left(\kappa_t^{fat} \cdot \alpha_{c2}\right)^2 \cdot a_2 + \sqrt{\frac{2}{15}} \cdot \kappa_t^{fat} \cdot \alpha_{c,2} \tag{4.18}$$

$$a_1 = \frac{1}{\sqrt{3}} \cdot \kappa_t^{fat} \cdot \left(2 \cdot \alpha_{c2} - \alpha_{ct,1}\right) \cdot a_2 + \sqrt{\frac{6}{15}} \cdot \frac{\left(\alpha_{ct,1} - \alpha_{c,2}\right)}{\left(2 \cdot \alpha_{c2} + \alpha_{ct,1}\right)}$$

$$a_2 = \frac{\sqrt{\frac{6}{15}} \cdot \left(\alpha_{ct,1} - \alpha_{c,2}\right) \cdot \alpha_c - \sqrt{\frac{6}{5}} \cdot \alpha_{ct,1} \cdot \alpha_{c2} + \frac{1}{\sqrt{5}} \cdot \delta_Z \cdot \left(2 \cdot \alpha_{c2} + \alpha_{ct,1}\right)}{\left(2 \cdot \alpha_{c2} + \alpha_{ct,1}\right) \cdot \left(\alpha_c^2 - \frac{2}{\sqrt{3}} \cdot \alpha_{c2} \cdot \alpha_c + \frac{1}{\sqrt{3}} \cdot \alpha_{ct,1} \cdot \alpha_c - \frac{2}{3} \cdot \alpha_{ct,1} \cdot \alpha_{c2}\right) \cdot \kappa_t^{fat}}$$

where $\alpha_0 = \dfrac{-a_1 - \sqrt{a_1^2 - 4 \cdot a_0 \cdot a_2}}{2 \cdot a_2 \cdot \kappa_c^{fat}}$

Table 4.10 Boundary conditions for principal meridian equations

Boundary condition	$\xi/f_{c,1}$	$\rho/f_{c,1}$	θ_{INT}	$r(\xi/f_{c1}, \theta_{INT})$
$\sigma_{11} = \kappa_t^{fat} \cdot f_{ct,1}$	$\frac{1}{\sqrt{3}} \cdot \kappa_t^{fat} \cdot \alpha_{ct,1}$	$\sqrt{\frac{2}{3}} \cdot \kappa_t^{fat} \cdot \alpha_{ct,1}$	$0°$	$r_1\left(\frac{1}{\sqrt{3}} \cdot \kappa_t^{fat} \cdot \alpha_{ct,1}\right)$
$\sigma_{11} = \sigma_{22} = -\kappa_t^{fat} \cdot f_{c,2}$	$-\frac{2}{\sqrt{3}} \cdot \kappa_t^{fat} \cdot \alpha_{c,2}$	$\sqrt{\frac{2}{3}} \cdot \kappa_t^{fat} \cdot \alpha_{c,2}$	$0°$	$r_1\left(-\frac{2}{\sqrt{3}} \cdot \kappa_t^{fat} \cdot \alpha_{c,2}\right)$
—	$-\kappa_t^{fat} \cdot \alpha_c$	$\kappa_t^{fat} \cdot \delta_Z$	$0°$	$r_1\left(-\kappa_t^{fat} \cdot \alpha_c\right)$
$\sigma_{11} = -\kappa_c^{fat} \cdot f_{c,1} \leq$	$-\frac{1}{\sqrt{3}} \cdot \kappa_c^{fat}$	$\sqrt{\frac{2}{3}} \cdot \kappa_c^{fat}$	$60°$	$r_2\left(-\frac{1}{\sqrt{3}} \cdot \kappa_c^{fat}\right)$
—	$-\kappa_c^{fat} \cdot \alpha_c$	$\kappa_c^{fat} \cdot \delta_D$	$60°$	$r_2\left(-\kappa_c^{fat} \cdot \alpha_c\right)$
—	$\kappa_c^{fat} \cdot \alpha_0$	0	$60°$	$r_2\left(\kappa_c^{fat} \cdot \alpha_0\right)$

The parameters of the parabolic equation for the compression meridian are in accordance with Equation 4.19:

$$b_0 = -\kappa_c^{fat} \cdot \alpha_0 \cdot b_1 - \left(\kappa_c^{fat} \cdot \alpha_0\right)^2 \cdot b_2 \tag{4.19}$$

$$b_1 = \kappa_c^{fat} \cdot \left(\frac{1}{\sqrt{3}} - \alpha_0\right) \cdot b_2 - \sqrt{\frac{2}{15}} \cdot \frac{1}{\left(\frac{1}{\sqrt{3}} + \alpha_0\right)}$$

$$b_2 = \frac{\frac{1}{\sqrt{5}} \cdot \left(\alpha_0 + \frac{1}{\sqrt{3}}\right) \cdot \delta_D - \sqrt{\frac{2}{15}} \cdot (\alpha_0 + \alpha_c)}{(\alpha_0 + \alpha_c) \cdot \left(\alpha_c - \frac{1}{\sqrt{3}}\right) \cdot \left(\alpha_0 + \frac{1}{\sqrt{3}}\right) \cdot \kappa_c^{fat}}$$

The damage variables introduced now have to be determined depending on the numbers of fatigue cycles in order to describe the failure envelope of the concrete when subjected to fatigue loads.

4.9.4.2 Derivation of damage variables κ_c^{fat} and κ_t^{fat}

The damage variables are derived from the qualitative S-N curves for uniaxial and multi-axial fatigue loads because these describe the decrease in the concrete strength as the number of fatigue cycles increases for various loading situations.

Determining the damage variable κ_c^{fat}, which is intended to describe the changes to the compression meridian for fatigue loads, requires the S-N curve for a uniaxial repeated compressive load. On the other hand, the description of the damage parameter κ_t^{fat} for the tension meridian is based on the strength development for a biaxial repeated compressive load.

The equations for the S-N curves given in Model Code 90 are used for the mathematical description of both damage parameters (see Section 4.9.2.2). Whereas Model Code 90 specifies equations for the S-N curves for uniaxial repeated compressive loads with different minimum stresses, the S-N curve for uniaxial repeated tensile loads is only defined for an effective minimum stress of $S_{cd,min} = 0$. This is a straight line, see Equation 4.14 and Figure 4.31. Up to the point log N = 6, the line coincides with that for a uniaxial repeated compressive load. Model Code 90 contains no information about biaxial fatigue loads. This missing information is therefore derived from the test results given in [75].

The damage parameters are therefore presented for the stress states at the fatigue limit state. However, the lines are not dependent on the design condition and so the damage parameters are not indexed.

Approach for damage variable κ_t^{fat} in low-cycle range

As the S-N curves for biaxial repeated compressive loads from the studies of [75] show, these curves up to a transition range from log N = 10^3 to log N = 10^4 are comparable, in qualitative terms, with those for uniaxial repeated compressive loads. Going beyond this transition range, that is into the high-cycle range, the S-N curves for biaxial repeated compressive loads diverge noticeably from those for uniaxial repeated compressive loads. Therefore, on the whole there is no straight line as for the uniaxial repeated tensile load. After the aforementioned transition range, the S-N curves for biaxial repeated compressive loads lie between the S-N curves for uniaxial repeated tensile and compressive loads.

Looking at the course of the damage variable κ_t^{fat} for biaxial repeated compressive loads, we can assume that it coincides with the S-N curves for uniaxial repeated compressive loads in the low-cycle range and lies between the S-N curves for uniaxial repeated tensile and compressive loads in the high-cycle range.

Therefore, in order to describe the damage variables, the equations of Model Code 90 [66] for uniaxial repeated tensile loads are modified in such a way that they can be used to describe the fatigue behaviour for biaxial repeated compressive loads. Although Model Code 90 contains only one S-N curve for $S_{cd,min} = 0$, ref. [76] and others specify that the curves for uniaxial repeated tensile loads related to the uniaxial strength down to a minimum stress of $S_{cd,min} = 0.6$ correspond to those for uniaxial repeated compressive loads and the same equations may be used. The course of the uniaxial repeated compressive load is used for numbers of fatigue cycles $<$ log N = 6.

Approach for damage variable κ_t^{fat} in high-cycle range

In the high-cycle range, the curve for numbers of fatigue cycles $\geq$ log N = 6 is chosen such that it lies between the uniaxial repeated tensile and compressive loads. The criterion specified is that the course of the tension meridian for $S_{cd,min} = 0$ at log N = 12 leads to a failure envelope that just still satisfies the convexity conditions of the failure model of [41]. This means that the tension meridian is embrittled so severely under fatigue loads that the strength reached under biaxial repeated compressive loads for log N = 12 lies noticeably below the uniaxial compressive fatigue strength. A biaxial compressive load increases the strength. However, not only is this effect lost at very high load cycles, there is also a significant reduction in the strength, something that was already indicated by the test results of [75]. For the fatigue loads relevant in practice, for example for wind turbines with a number of fatigue cycles $\log N \leq 9$, this approach retains the effect of an increase in strength for biaxial repeated compressive loads.

At the same time, this approach also leads to isotropic fatigue behaviour up to a number of fatigue cycles $\log N = 6$ because the same results can be presumed for the damage variables on the compression and tension meridians.

The convexity condition of the Willam-Warnke model [41] results in the S-N curve for uniaxial repeated tensile loads with an effective minimum stress $S_{cd,min} = 0$ having to be changed in such a way that the curve intersects the abscissa not at $\log N = 12$, but rather later, at $\log N = 15$. This difference of $\Delta \log N = 3$ is used for all minimum stresses with $S_{cd,min} \neq 0$.

The choice of $\Delta \log N$ can influence the course of the damage in the high-cycle range. For example, a higher value of $\Delta \log N = 6.95$ leads to the biaxial compressive fatigue strength corresponding exactly to the fatigue strength as for uniaxial repeated compressive loads for $S_{cd,min} = 0$ in the failure model of [41] at $\log N = 12$, and the convexity condition is still clearly satisfied. Consequently, validating the damage development on the tension meridian requires tests involving biaxial repeated compressive loads, with numbers of fatigue cycles to failure $> \log N = 6$ and the ability to derive the development of the damage variable κ_t^{fat} in the high-cycle range.

Figure 4.32 shows the resulting courses of the damage variables κ_c^{fat} and κ_t^{fat} for the boundary conditions specified here.

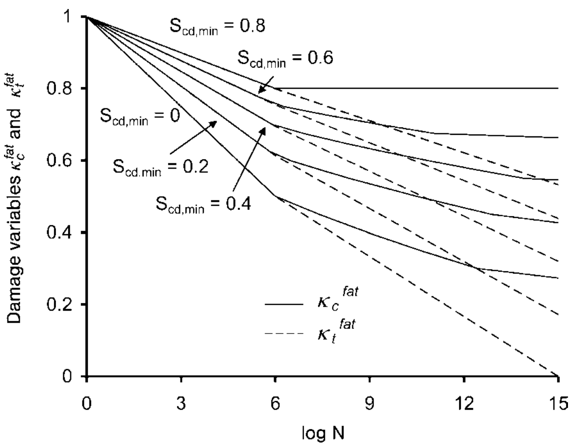

Fig. 4.32 Damage variables κ_c^{fat} and κ_t^{fat}

Conditional equations for damage variable κ_c^{fat}

The courses of the damage variable κ_c^{fat} on the compression meridian are described in Equations 4.20 to 4.25. Based on the S-N curves for uniaxial repeated compressive loads, we get the following ranges:

When $0 < S_{cd,min} < 0.8$, then

$$\log N_1 = (12 + 16 \cdot S_{cd,min} + 8 \cdot S_{cd,min}^2) \cdot (1 - \kappa_c^{fat}) \tag{4.20}$$

$$\log N_2 = 0.2 \cdot \log N_1 \cdot (\log N_1 - 1) \tag{4.21}$$

$$\log N_3 = \log N_2 \cdot (0.3 - 3 \cdot S_{cd,min}/8)/\Delta S \tag{4.22}$$

Specifying the number of fatigue cycles $\log N$ associated with κ_c^{fat}:

$$\begin{aligned}&\text{If } \log N_1 \leq 6, \text{ then}\\ &\log N = \log N_1\end{aligned} \tag{4.23}$$

$$\begin{aligned}&\text{If } \log N_1 > 6 \text{ and } \Delta S \geq 0.3 - 3 \cdot S_{cd,min}/8, \text{ then}\\ &\qquad \log N = \log N_2\end{aligned} \tag{4.24}$$

$$\begin{aligned}&\text{If} \log N_1 > 6 \text{ and } \Delta S < 0.3 - 3 \cdot S_{cd,min}/8, \text{ then}\\ &\qquad \log N = \log N_3\end{aligned} \tag{4.25}$$

$$\text{where } S_{cd,min} = \frac{\sigma_{cd,min}}{f_c(\xi, \rho, \theta)} \tag{4.26}$$

$$\Delta S = \kappa_c^{fat} - S_{cd,min}$$

$$\sigma_{cd,min} = \text{minimum stress}$$

$$f_c(\xi, \rho, \theta) = \text{multi-axial concrete strength according to [93], see also Section 3.6.2}$$

The damage variable κ_c^{fat} can be determined iteratively from Equations 4.20 to 4.25. It is presumed here that we know the number of load cycles $\log N$ for which the damage variable is to be determined. First of all, the damage parameter for the actual minimum stress $S_{cd,min}$ is estimated from Figure 4.32 depending on the number of load cycles $\log N$. The recommendation here is to read off the damage variable κ_c^{fat} for a marginally higher number of load cycles. The value read off is entered into Equations 4.20 to 4.25 and the number of fatigue cycles $\log N$ thus calculated then checked against the initial value. If the number of fatigue cycles calculated is too small, the damage variable κ_c^{fat} must be increased, and if the value calculated is too high, the variable must be reduced. The number of fatigue cycles must be recalculated for the corrected damage variable and again compared with the initial value. This iterative procedure should be repeated until the values coincide with sufficient accuracy.

Conditional equations for damage variable κ_t^{fat}

The courses of the damage variable κ_t^{fat} on the tension meridian are described in Equations 4.27 and 4.28. The equations were developed from the S-N curve for a uniaxial repeated tensile load. The damage variable κ_t^{fat} can be calculated directly from the equations depending on the number of load cycles $\log N$ and the effective minimum stress $S_{cd,min}$.

When $\log N \leq 6$, then

$$\kappa_t^{fat} = 1 - \frac{\log N}{(12 + 16 \cdot S_{cd,min} + 8 \cdot S_{cd,min}^2)} \tag{4.27}$$

When $6 \leq \log N \leq 12$, then

$$\kappa_t^{fat} = \left(1 - \frac{6}{(12 + 16 \cdot S_{cd,min} + 8 \cdot S_{cd,min}^2)}\right) \cdot \frac{(15 - \log N)}{9} \tag{4.28}$$

where $S_{cd,min}$ is in accordance with Equation 4.26.

4.9.4.3 Failure envelope for fatigue load

The failure envelopes for various numbers of fatigue cycles to failure were determined for the minimum stress level shown in Figure 4.32 according to the procedure given in the previous paragraphs. The calculated courses of the triaxial fatigue strength are shown in Figure 4.33 for a minimum stress level of $S_{cd,min} = 0$ according to Equation 4.26 as a principal meridian intersection. The different development of the fatigue strength on the tension and compression meridians can be seen. The fatigue strength for a tension meridian stress decreases faster than for a compression meridian stress. With higher hydrostatic compression components especially, the more ductile material behaviour for a compression meridian stress compared with the more brittle material behaviour for a tension meridian stress is clearly evident.

Figure 4.34 shows the intersection of the deviator with the different strength curves. These clearly reveal the anisotropic course of the calculated triaxial fatigue strength.

The uniaxial compressive strength in both figures is designated f_{c1}. Further calculated principal meridian and deviator intersections are given in [74] for minimum stresses of $S_{cd,min} = 0$ to $S_{cd,min} = 0.6$.

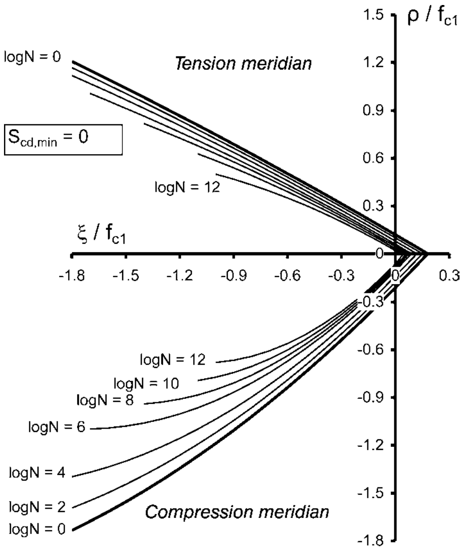

Fig. 4.33 Fatigue curves in the principal meridian intersection

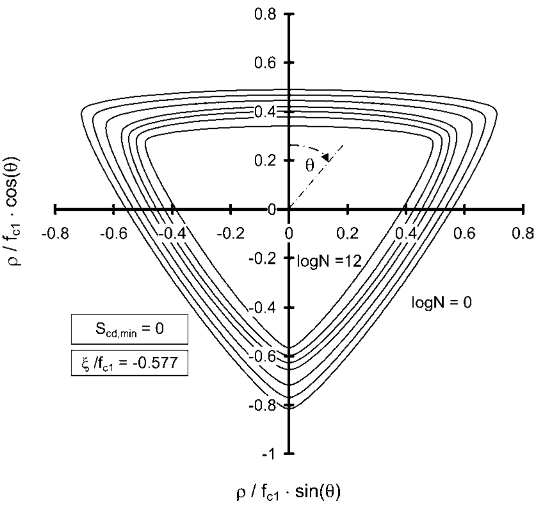

Fig. 4.34 Fatigue curves in the deviatoric plane for $\xi/f_{c1} = -0.57735$

4.9.4.4 Failure curves for biaxial fatigue loads

The numbers of fatigue cycles to failure for biaxial stresses can be determined directly from the calculations for the failure envelopes for various numbers of fatigue cycles. The calculated biaxial failure curves for various minimum stresses $S_{cd,min}$ are given in Figures 4.35 to 4.39.

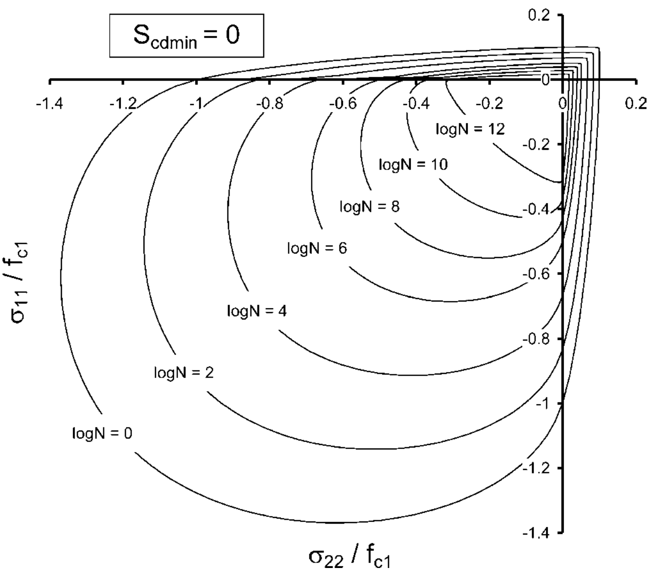

Fig. 4.35 Failure curves for the biaxial stress state $S_{cd,min} = 0$

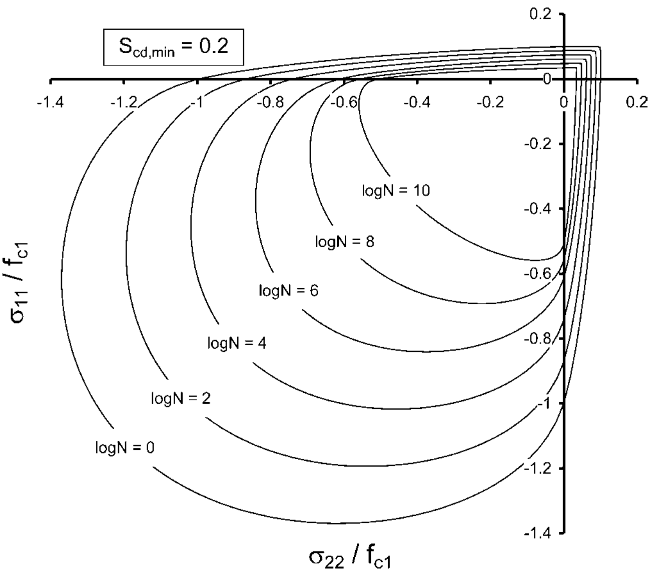

Fig. 4.36 Failure curves for the biaxial stress state $S_{cd,min} = 0.2$

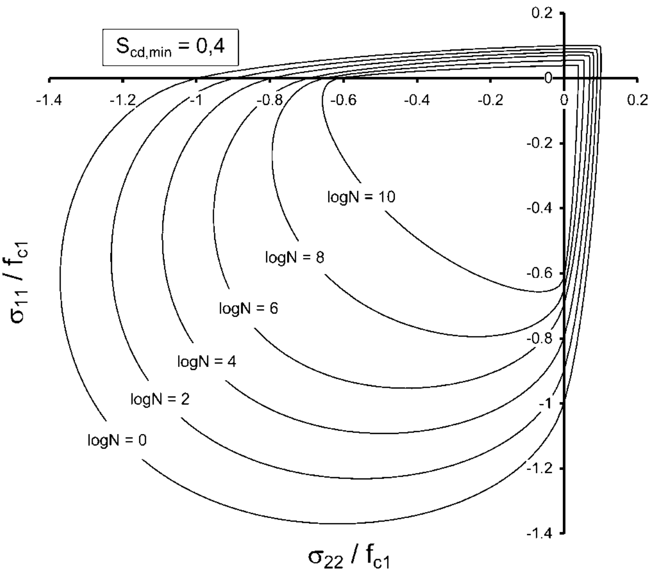

Fig. 4.37 Failure curves for the biaxial stress state $S_{cd,min} = 0.4$

Figure 4.35 clearly indicates how the damage variables (κ_c^{fat} and κ_t^{fat}) influence the forms of the failure curves. The isotropic damage behaviour is recognisable up to $\log N = 6$. The decrease in strength as the number of fatigue cycles increases is identical for uniaxial and biaxial fatigue loads. Subsequently, the decrease in strength

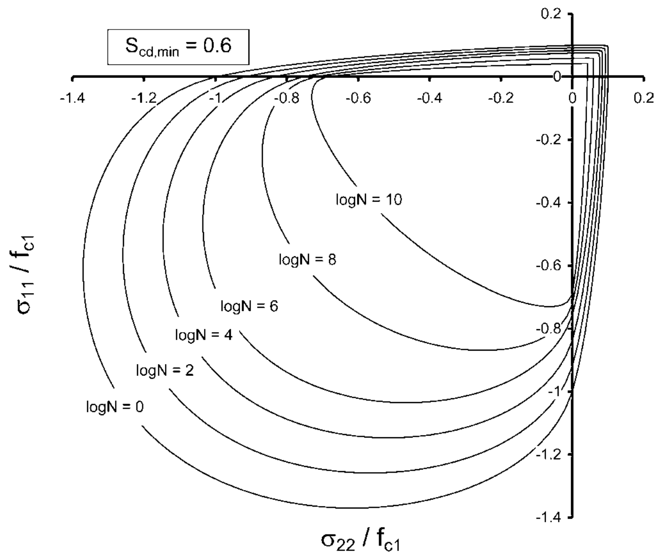

Fig. 4.38 Failure curves for the biaxial stress state $S_{cd,min} = 0.6$

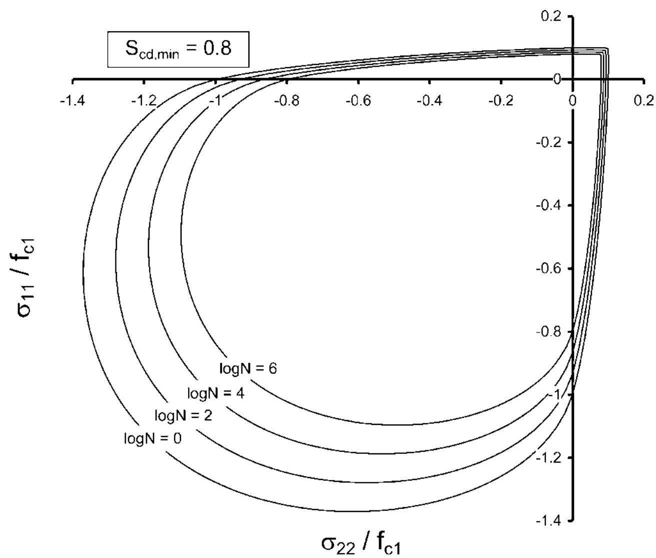

Fig. 4.39 Failure curves for the biaxial stress state $S_{cd,min} = 0.8$

with higher numbers of fatigue cycles is greater for biaxial repeated compressive loads ($\sigma_{11} = \sigma_{22}$) than for uniaxial ones. This can be attributed to the different courses of the damage variables in the high-cycle range. It is obvious that up to approx. $\log N = 8$, the biaxial fatigue strength for repeated compressive loads is greater than the uniaxial fatigue strength. This no longer applies when $\log N = 10$. The failure curve for

$\log N = 12$ just satisfies the convexity condition of the failure model used, which is described in [41].

Furthermore, it is clear in Figure 4.35 that the presence of even just a small transverse tensile action effect leads to a significant decrease in strength with a fatigue load. Failure curves for other minimum stresses are shown in Figures 4.36 to 4.39.

4.9.5 Design proposal for multi-axial fatigue

The use of the extended, energy-based damage model described in [74] is recommended for more accurate fatigue investigations involving multi-stage and multi-axial loads. The non-linear damage process can be ascertained very well with this damage model.

However, its use presumes the iterative calculation of the energy component dissipated in damage in the fatigue process from the monotonic curve. And that requires the use of a computer program.

In addition, the material parameters, for example the volume-specific crushing energy, must be known.

Where the influence of multi-axial fatigue loads is to be estimated with the help of the linear accumulation hypothesis, it is sufficient to determine the numbers of fatigue cycles to failure according to Section 4.9.4.2 and evaluate the individual damage components according to the Palmgren-Miner hypothesis (see Section 4.9.2.2).

4.9.5.1 Procedure for designing on the basis of the linear accumulation hypothesis

If as an approximation the S-N curves for uniaxial repeated compressive loads are presumed for fatigue design in the principal direction of the loading, then the numbers of fatigue cycles to failure can be calculated with Equations 4.7 to 4.13 given in Section 4.9.2.2. However, in doing so, the stresses present must be related to the multi-axial concrete strength. This has to be calculated in each case for the actual loading relationship and can, for example, be determined according to [41].

The alternative for practical applications is to express the multi-axial strength in the form of a modified uniaxial concrete compressive strength. To do this, modification factors λ_{c2} and λ_{c3} are calculated in Sections 4.9.5.2 and 4.9.5.3 respectively, and presented in the form of charts. The modification factors are incorporated directly in the equations for evaluating the S-N curves. The numbers of fatigue cycles to failure can then be determined with the initial values according to Equation 4.29:

$$\begin{aligned} S_{cd,min} &= \gamma_{sd} \cdot \lambda_{c2 \text{ or } c3}(N, \alpha \text{ or } r) \cdot \sigma_{c,min} \cdot \eta_c / f_{cd,fat} \\ S_{cd,max} &= \gamma_{sd} \cdot \lambda_{c2 \text{ or } c3}(N, \alpha \text{ or } r) \cdot \sigma_{c,max} \cdot \eta_c / f_{cd,fat} \end{aligned} \tag{4.29}$$

where

$S_{cd,min}$; $S_{cd,max}$ minimum and maximum repeated compressive loads in the principal direction of the loading related to the uniaxial compressive strength

λ_{c3} (N, r)	modification factor for compression meridian stresss (Section 4.9.5.2)
λ_{c2} (N, α)	modification factor for biaxial action effects (Section 4.9.5.3)
N	actual number of fatigue cycles
$r = (\sigma_{11} = \sigma_{22})/\sigma_{33}$	loading relationship on compression meridian
$\alpha = \sigma_{11}/\sigma_{22}$	loading relationship for biaxial loading

All other designations are as described in Section 4.9.2.

The stresses present in the principal direction of the loading are related to the uniaxial compressive strength. The influence of the multi-axial loading state is taken into account solely by the modification factors. The introduction of the modification factors means it is now possible to avoid a comparatively more involved, direct calculation of the multi-axial concrete strength.

4.9.5.2 Derivation of modification factor λ_{c3} (N, r) for fatigue loads on compression meridian

Comparison of concrete strengths for uniaxial and multi-axial loads

Assuming that fatigue loads on the compression meridian enable the qualitative S-N curves to be used for uniaxial repeated compressive loads allows the modification factor λ_{c3} (N, r) to be determined directly from a comparison of the concrete strengths for uniaxial concrete strength f_{c1} and multi-axial concrete strength f_c (ξ, ρ, θ). This is shown for the effective maximum stress $S_{c33,max}$ and the number of fatigue cycles N = 1; it is also equally valid for higher numbers of fatigue cycles.

Accordingly, the initial equation for the values of the effective maximum stress in the axial direction $S_{c33,max}$ on the compression meridian is

$$S_{c33,max} = \frac{\sigma^{fat}_{c33,max}(r = 0)}{f_{c1}} = \frac{\sigma^{fat}_{c33,max}(r \neq 0)}{f_c(\xi, \rho, \theta)} \tag{4.30}$$

We can use Equation 4.30 to obtain

$$\sigma^{fat}_{c33,max}(r \neq 0) = \sigma^{fat}_{c33,max}(r = 0) \cdot \frac{f_c(\xi, \rho, \theta)}{f_{c1}} \tag{4.31}$$

The modification factor λ_{c3} is defined as

$$\lambda_{c3} = \frac{f_{c1}}{f_c(\xi, \rho, \theta)} \tag{4.32}$$

The modification factor λ_{c3} therefore depends on the triaxial loading state ξ, ρ and θ, which in the case of compression meridian stresss can be expressed by the loading ratio $r = (\sigma_{11} = \sigma_{22})/\sigma_{33}$. The stresses σ_{11} and σ_{22} describe the radial stress, σ_{33} describes the axial stress. In the end, substituting Equation 4.32 in Equation 4.31 leads to

$$\sigma^{fat}_{c33,max}(r = 0) = \lambda_{c3}(r) \cdot \sigma^{fat}_{c33,max}(r) \tag{4.33}$$

We can see from Equation 4.33 that the maximum axial stress for compression meridian stresss can be simplified to the uniaxial compression load by the modification factor λ_{c3} (r). This means that only the axial stresses (maximum and minimum) plus a modification factor λ_{c3} (r) dependent on the loading ratio r have to be known when calculating the number of fatigue cycles to failure for triaxial compression meridian stresss. And this means that within the scope of a fatigue analysis based on the linear accumulation hypothesis, Equation 4.29 can be used to determine the triaxial fatigue strength directly from the uniaxial S-N curves for repeated compressive loads according to Section 4.9.4.2.

Determining the modification factor λ_{c3} (N, r) from the failure hypothesis according to [41]

The calculation of the modification factors λ_{c3} (N, r) is shown below. The yield condition according to [41] gives us (see Section 3.6.2)

$$\frac{\rho}{f_{c1}} = \sqrt{5} \cdot r(\xi, \theta_{INT}) \tag{4.34}$$

Here, the failure curve on the compression meridian ($\theta_{INT} = 60°$) is described by a parabola. Substituting the parabolic equation in Equation 4.34 results in

$$\frac{1}{\sqrt{5}} \cdot \frac{\rho}{f_{c1}} = b_0 + b_1 \cdot \frac{\xi}{f_{c1}} + b_2 \cdot \left(\frac{\xi}{f_{c1}}\right)^2 \tag{4.35}$$

In the case of compression meridian stresss, Equation 4.36 enables the effective deviatoric stress ρ/f_{c1} described by Haigh-Westergaard coordinates to be expressed by the effective principal stress $\sigma^{fat}_{c33,max}(r)/f_{c1}$ and r:

$$\frac{\rho}{f_{c1}} = \sqrt{\frac{2}{3}} \cdot (1 - r) \cdot \frac{\sigma^{fat}_{c33,max}(r)}{f_{c1}} \tag{4.36}$$

Equating Equations 4.35 and 4.36 leads to the following quadratic equation:

$$\begin{aligned} 0 = & \frac{3 \cdot b_0}{b_2 \cdot (2 \cdot r + 1)^2} + \frac{b_1 \cdot \sqrt{3} \cdot (2 \cdot r + 1) + 3 \cdot \sqrt{\frac{2}{15}} \cdot (1 - r)}{b_2 \cdot (2 \cdot r + 1)^2} \\ & \cdot \frac{\sigma^{fat}_{c33,max}(r)}{f_{c1}} + \left(\frac{\sigma^{fat}_{c33,max}(r)}{f_{c1}}\right)^2 \end{aligned} \tag{4.37}$$

The values specified in, for example, [74] enable the parameters of the parabolic equation b_o, b_1 and b_2 to be determined for $N = 1$ and subsequently the calculation of the stress $\sigma^{fat}_{c33,max}(r)$ from Equation 4.37 depending on r.

Equation 4.33 should be used to determine the parameters for the parabolic equations for numbers of fatigue cycles $N > 1$ and to solve Equation 4.37. The modification factor

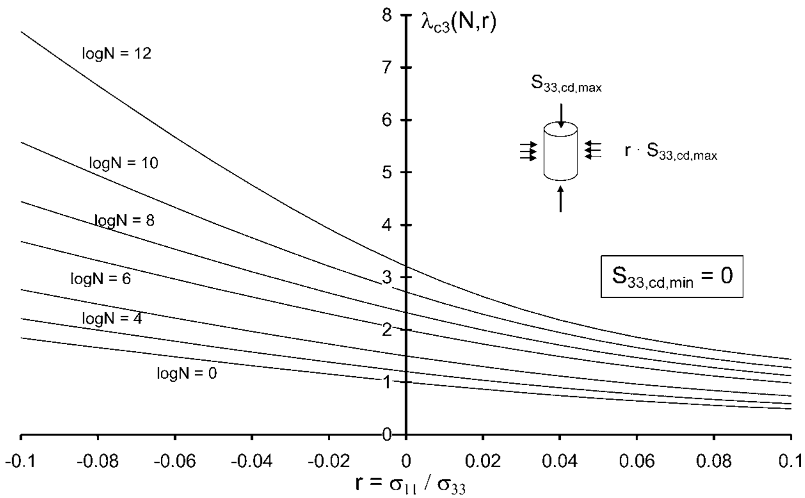

Fig. 4.40 Modification factor λ_{c3} (N, r) for compression meridian stresss and effective minimum stress $S_{33,cd,min} = 0$

λ_{c3} (N, r) therefore depends on the number of fatigue cycles N and is determined as a reciprocal value of $\sigma^{fat}_{c33,max}(N, r)/f_{c1}$:

$$\lambda_{c3}(N, r) = \frac{\sigma^{fat}_{c33,max}(N, r = 0)}{\sigma^{fat}_{c33,max}(N, r)} = \frac{f_{c1}(N, \alpha = r = 0)}{\sigma^{fat}_{c33,max}(N, r)} \tag{4.38}$$

The courses of the modification factor λ_{c3}(N, r) are presented in [74] for practical applications depending on the loading ratio r and the actual number of fatigue cycles N for different effective minimum stresses $S_{c33,min}$. The modification factor λ_{c3} (N, r) can be read off from these charts and used in Equation 4.33. As an example, Figure 4.40 shows the curves for $S_{c33,min} = 0$.

4.9.5.3 Derivation of modification factors λ_{c2} (N, α) for biaxial fatigue loads

Modification factors can also be determined for biaxial fatigue loads for use in Equation 4.29. According to Equation 4.39, these can be obtained directly from failure curves for biaxial fatigue loads. The loading ratio here is described by $\alpha = \sigma_{11}/\sigma_{22}$. The stress in the transverse direction is denoted by σ_{11} and the stress in the principal loading direction by σ_{22}.

$$\lambda_{c2}(N, \alpha) = \frac{\sigma^{fat}_{c22,max}(N, \alpha = 0)}{\sigma^{fat}_{c22,max}(N, \alpha)} = \frac{f_{c,1}(N, \alpha = r = 0)}{S^{fat}_{c22,max}(N, \alpha)} \tag{4.39}$$

For practical applications, Figures 4.41 to 4.45 show the diagrams for λ_{c2} (N, α) depending on the loading ratio α and the actual number of fatigue cycles N for various effective minimum stresses $S_{c22,min}$.

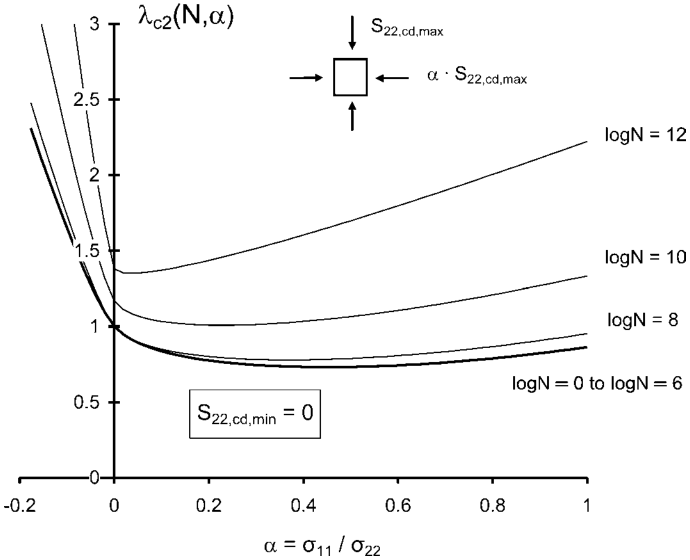

Fig. 4.41 Modification factor λ_{c2} (N, α) for biaxial fatigue load and effective minimum stress $S_{22,cd,min} = 0$

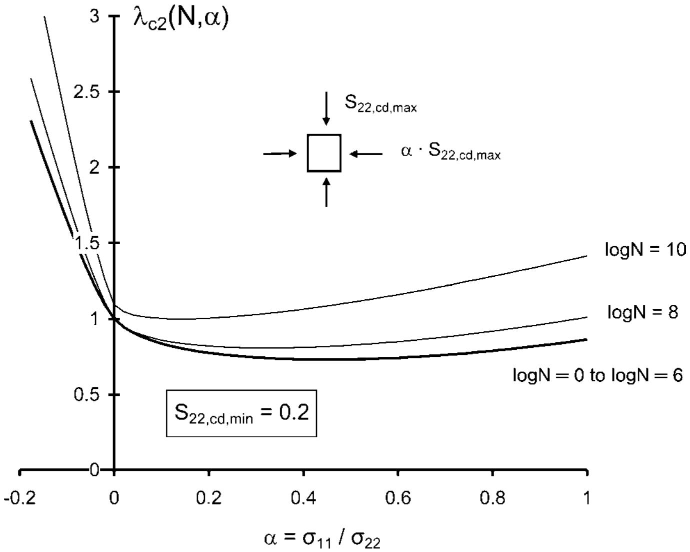

Fig. 4.42 Modification factor λ_{c2} (N, α) for effective minimum stress $S_{cd,min} = 0.2$

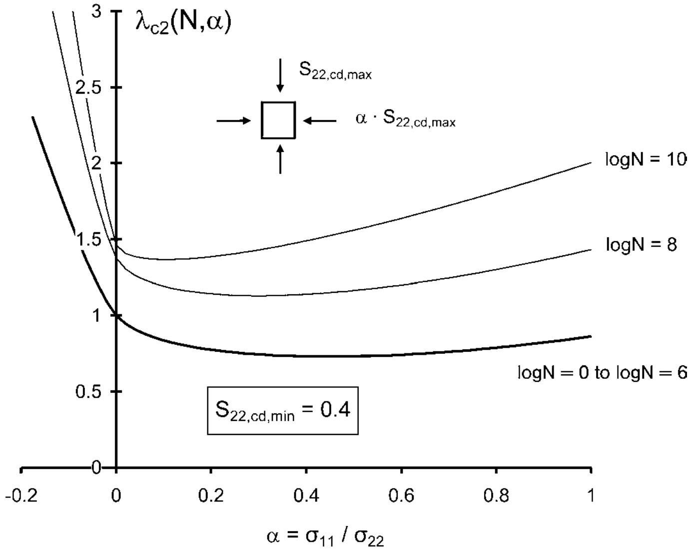

Fig. 4.43 Modification factor λ_{c2} (N, α) for effective minimum stress $S_{cd,min} = 0.4$

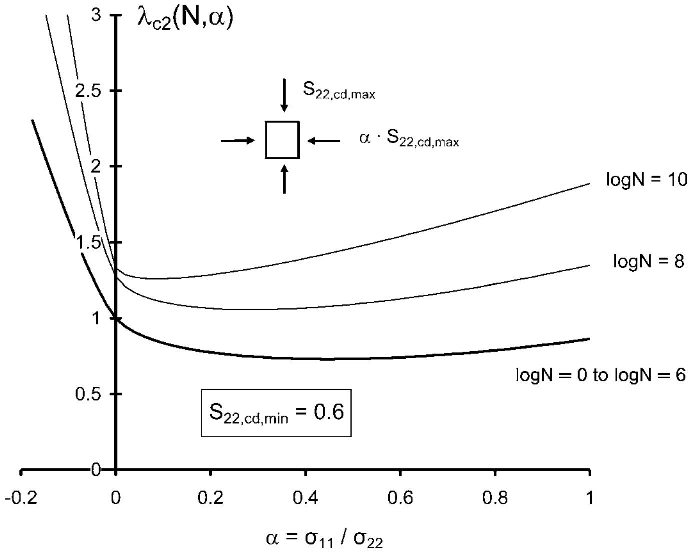

Fig. 4.44 Modification factor λ_{c2} (N, α) for effective minimum stress $S_{cd,min} = 0.6$

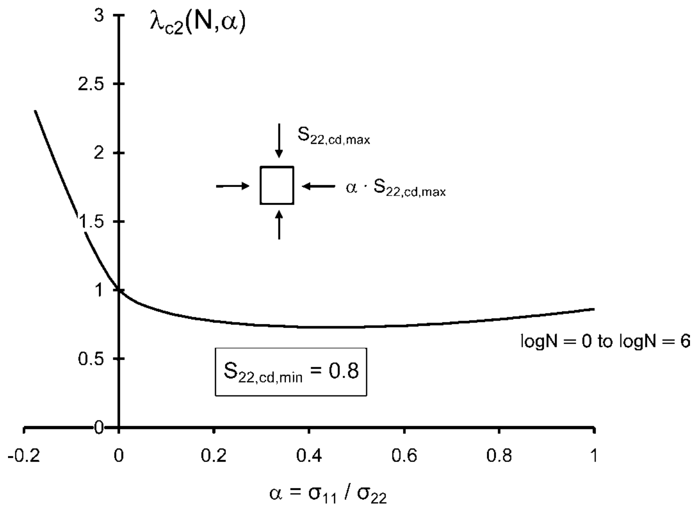

Fig. 4.45 Modification factor $\lambda_{c2}(N,\alpha)$ for effective minimum stress $S_{cd,min} = 0.8$

4.10 Design of construction nodes

Special attention must be paid to the construction nodes during the design. Those include the connections of attached components, for example annular platforms on telecommunications towers. Such items can either be connected directly to the tower shaft or (in the case of large internal forces) via a strong circular ring beam. Examples can be found in [8].

Adapter details are necessary in hybrid towers for wind turbines at the transition from the prestressed concrete tower to the tubular steel segment (Figure 4.46).

4.10.1 Loads on nodes

The abrupt change in the tower diameter leads to high change-of-direction forces (see Figure 4.47). These loads can only be accommodated by circular ring beams with a depth at least equal to their width, preferably 20 to 30% greater! Expressed in more graphical terms: with a square cross-section, the change-of-direction forces to be accommodated by conventional radial reinforcement are equal to the sum of the vertical compression in the shaft wall, the concrete and the reinforcing steel.

4.10.2 Composition of forces at the ultimate limit state

a) Prestressed concrete tower (bar with annular cross-section):

Design values : $N_{Ed}; M_{Ed}; V_{Ed}$

The characteristic values of the internal forces (N_{Gk}, M_{Gk}; $N_{P,k}$; $N_{QN,k}$, $M_{QN,k}$; $V_{QW,k}$, $M_{QW,k}$) result from the equilibrium conditions for the deformed structure with the characteristic values of the actions (G_k, $Q_{N,k}$, $Q_{W,k}$).

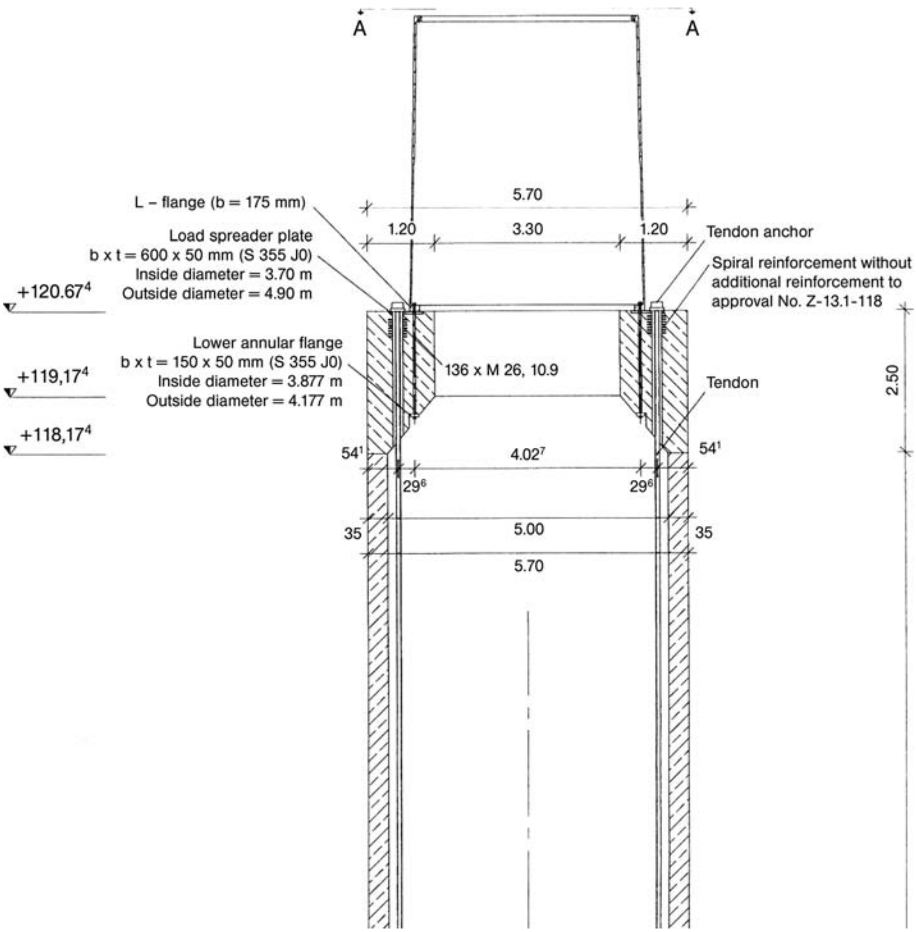

Fig. 4.46 Detail of junction between prestressed concrete tower and tubular steel segment

b) Prestressed concrete tower (cylindrical shell):
Characteristic values of statically indeterminate bending action effects: X_1; X_2
c) Circular ring beam:
Resultant characteristic values: m_R; n_R; v_R

4.10.3 Characteristic values for loads

The characteristic values of the actions on the circular ring beam (m_R; n_R; v_R) are calculated from the characteristic values of the tower internal forces (see above) – separately for symmetrical effects (due to permanent loads and prestress) and antisymmetrical effects (due to wind loads) (Figure 4.48). For simplicity, the symmetrical components of the imposed loads are added to the permanent loads (G_k) and the antisymmetrical components added to the wind loads (Q_{Wk}).

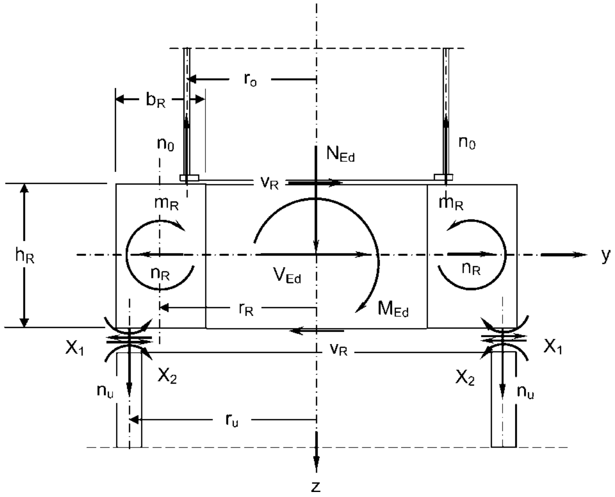

Fig. 4.47 Detail of junction between antenna platform and tower shaft – internal forces

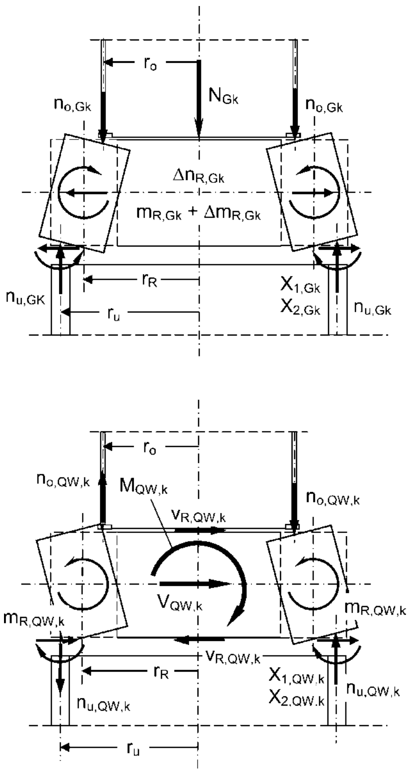

Fig. 4.48 Calculating the actions on a circular ring beam to allow for a sudden change in the tower diameter

First of all we consider the statically determinate primary system. The symmetrical loading results in symmetrical action effects in the circular ring beam ($n_{o,Gk}$, $m_{R,Gk}$ and $n_{0,Gk}$). The antisymmetrical loading results in antisymmetrical action effects in the circular ring beam ($n_{o,QW,k}$, $m_{R,QW,k}$, $n_{0,Gk}$ and $v_{QW,k}$).

Added to this are the effects of the statically indeterminate internal forces. These result from the compatibility between the deformations of the circular ring beam and the adjoining zones of the tower shaft. The latter are considered as cylindrical shells whose bending action effects can be calculated based on [64].

a) Symmetric action effect:
The symmetric loading results in a residual stress state with action effects "short-circuited" at the circular ring beam ($\Delta m_{R,Gk}$ and $\Delta n_{R,Gk}$).

$$n_{o,Gk} = \frac{N_{Gk}}{2 \cdot \pi \cdot r_o}$$

$$m_{R,Gk} = \frac{N_{Gk}}{2 \cdot \pi \cdot r_R} \cdot (r_u - r_o)$$

$$\Delta m_{R,Gk} = \left(X_{1,Gk} \cdot \frac{h_R}{2} - X_{2,Gk} \right) \cdot \frac{r_u}{r_R}$$

$$\Delta n_{R,Gk} = X_{1,Gk} \cdot \frac{r_u}{r_R}$$

$$n_{u,Gk} = \frac{N_{Gk}}{2 \cdot \pi \cdot r_u}$$

b) Antisymmetric action effect (see also [77]):
The antisymmetric loading results in a residual stress state with circumferential harmonic (cosine or sine form) action effects in the circular ring beam.

$$n_{o,QW,k} = \frac{M_{QW,k}}{\pi \cdot r_o^2} \cdot \cos \varphi$$

$$m_{R,QW,k} = \frac{M_{QW,k}}{\pi \cdot r_R^2} \cdot (r_u - r_o) \cdot \cos \varphi$$

$$\Delta m_{R,QW,k} = \left(X_{1,QW,k} \cdot \frac{h_R}{2} - X_{2,QW,k} \right) \cdot \frac{r_u}{r_R} \cdot \cos \varphi$$

$$n_{u,QW,k} = \frac{M_{QW,k}}{\pi \cdot r_u^2} \cdot \cos \varphi$$

$$v_{R,QW,k} = \frac{V_{QW,k}}{\pi \cdot r_R} \cdot \sin \varphi$$

where φ is the rotation angle about the tower axis ($\varphi = 0$ at vertex on flexural compression side).

4.10.4 Example of calculation

A statically indeterminate analysis will be carried out to determine the characteristic values of the loads for the design of the detail in Figure 4.46.

Cross-sectional values:

The stiffness of the tubular steel segment is neglected. Therefore, only the radius is required for the load transfer:

Radius of tubular steel segment : $r_o = 2.10\,\mathrm{m}$

The strengthening to the top of the reinforced concrete tower is idealised as a *circular ring beam* as follows:

Beam radius: $r_R \cong 2.25\,\mathrm{m}$

Beam width: $b_R = 1.20\,\mathrm{m}$

Beam depth $h_R \cong 2.20\,\mathrm{m}$

The annular flange to the tubular steel segment can be considered as part of the circular ring beam, but is neglected here for simplicity, likewise the reinforcement.

Cross-sectional area:
$A_c \cong b_R \cdot h_R = 1.20 \cdot 2.20 = 2.64\ \mathrm{m}^2$

Second moment of area:
$I_R \cong b_R \cdot h_R{}^3/12 = 1.20 \cdot 2.20^3/12 = 1.065\ \mathrm{m}^4$

The reinforced concrete tower itself is idealised as a *cylindrical shell*:

Shell radius: $r_u = 2.675\,\mathrm{m}$

Shell thickness: $t_u = 0.35\,\mathrm{m}$

Shell parameter according to [64]:

$$\kappa_u = \sqrt[4]{3 \cdot (1-\mu^2) \cdot (r_u/t_u)^2} = \sqrt[4]{3 \cdot \left(1 - 0.2^2\right) \cdot (2.675/0.35)^2} = 3.601$$

A *uniform elastic modulus* is used: $E_c = 30\,000$ MPa

Statically determinate primary system:

The statically indeterminate analysis is carried out for a constant unit twisting moment (symmetrical loading: $m_{R0} = +1$ MNm/m).

Unit bending moment in circular ring beam:

$$M_{R0} = m_{R0} \cdot r_R = +1 \cdot 2.25 = +2.25\,\mathrm{MNm}$$

Unit rotation of circular ring beam:

$$\varphi_{R0} = m_{R0} \cdot \pi_R^2/(E_c \cdot I_R) = +1 \cdot 2.25^2/(30 \cdot 1.065) = +0.1585‰$$

Deformation modulus for force method:

$$\delta_{10} = +1 \cdot \varphi_{R0} \cdot h_R/2 = +0.1585 \cdot 2.20/2 = +0.1743\,\text{mm}$$
$$\delta_{20} = -1 \cdot \varphi_{R0} = -0.1585‰$$

Statically indeterminate effects (X_1, X_2, see Figure 4.47):

Unit bending moments in circular ring beam:

$$M_{R1} = +X_1 \cdot h_R/2 = +1[\text{MN/m}] \cdot 2.20/2 = +1.10\,\text{MNm/m}$$
$$M_{R2} = -X_2 = -1.00\,\text{MNm/m}$$

Deformation modulus for force method (cylindrical shell, see [64]):

$$\begin{aligned}\delta_{11} &= M_{R1} \cdot r_R \cdot h_R/2/(E_c \cdot I_R) + 2 \cdot X_1 \cdot r_u \cdot \kappa_u/(E_c \cdot t_u)\\ &= +1.10 \cdot 2.25 \cdot 2.20/2/(30 \cdot 1.065) + 2 \cdot 1.00 \cdot 2.675 \cdot 3.601/(30 \cdot 0.35)\\ &= +0.0852 + 1.8350 = +1.920\,\text{mm}\end{aligned}$$

$$\begin{aligned}\delta_{12} &= M_{R2} \cdot r_R \cdot h_R/2/(E_c \cdot I_R) + 2 \cdot X_2 \cdot \kappa_u^2/(E_c \cdot t_u)\\ &= -1.00 \cdot 2.25 \cdot 2.20/2/(30 \cdot 1.065) + 2 \cdot 1.00 \cdot 3.601^2/(30 \cdot 0.35)\\ &= -0.0775 + 2.4705 = +2.393\,\text{mm}\end{aligned}$$

$$\begin{aligned}\delta_{21} &= -M_{R1} \cdot r_R/(E_c \cdot I_R) + 2 \cdot X_1 \cdot \kappa_u^2/(E_c \cdot t_u)\\ &= -1.10 \cdot 2.25/(30 \cdot 1.065) + 2 \cdot 1.00 \cdot 3.601^2/(30 \cdot 0.35)\\ &= -0.0775 + 2.4705 = +2.393‰\end{aligned}$$

$$\begin{aligned}\delta_{22} &= -M_{R2} \cdot r_R \cdot /(E_c \cdot I_R) + 4 \cdot X_2 \cdot \kappa_u^3/r_u/(E_c \cdot t_u)\\ &= +1.00 \cdot 2.25/(30 \cdot 1.065) + 4 \cdot 1.00 \cdot 3.601^3/2.675/(30 \cdot 0.35)\\ &= +0.0704 + 6.6523 = +6.723‰\end{aligned}$$

Statically indeterminate analysis:

Determinants for deformation modulus:

$$D = \delta_{11} \cdot \delta_{22} - \delta_{21} \cdot \delta_{12} = 1.920 \cdot 6.723 - 2.393^2 = 7.813 \cdot 10^{-3}\,\text{mm}$$

Statically indeterminate internal forces:

$$\begin{aligned}X_1 &= 1.00[\text{MN/m}] \cdot (-\delta_{10} \cdot \delta_{22} + \delta_{20} \cdot \delta_{12})/D\\ &= (-0.1743 \cdot 6.723 - 0.1585 \cdot 2.393)/7.183\\ &= -1.5512/7.183 = -0.2160\,\text{MN/m}\end{aligned}$$

$$\begin{aligned}X_2 &= 1.00[\text{MNm/m}] \cdot (-\delta_{11} \cdot \delta_{20} + \delta_{21} \cdot \delta_{10})/D\\ &= (+1.920 \cdot 0.1585 + 2.393 \cdot 0.1743)/7.183\\ &= +0.7215/7.183 = +0.1005\,\text{MNm/m}\end{aligned}$$

From this we get the following unit differential moment at the circular ring beam:

$$\Delta m_{R0} = \left(X_1 \cdot \frac{h_R}{2} - X_2 \right) \cdot \frac{r_u}{r_R} = \left(-0.2160 \cdot \frac{2.20}{2} - 0.1005 \right) \cdot \frac{2.675}{2.25}$$
$$= (-0.2376 - 0.1005) \cdot 1.189 = -0.402\,\text{MNm/m}$$

Only approx. 10% of the twisting moment acting is carried by the lower tower shell, whereas approx. 60% remains in the circular ring beam and the remaining 30% is carried by way of an eccentric shear force.

In this example the circular ring beam fulfils the stiffening function required.

The **characteristic values of the internal forces** in the circular ring beam (N_{Rk}, M_{Rk}, V_{Rk}, T_{Rk}) and the bending action effects in the adjoining shaft areas below (X_{1k}, X_{2k}) are also calculated separately for symmetrical (permanent) and antisymmetrical (wind) action effects (Figure 4.49).

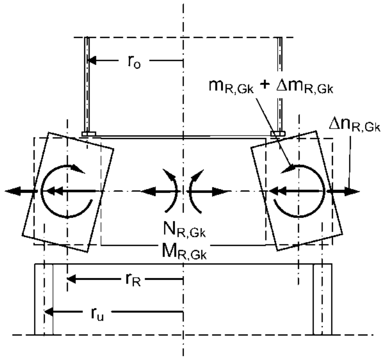

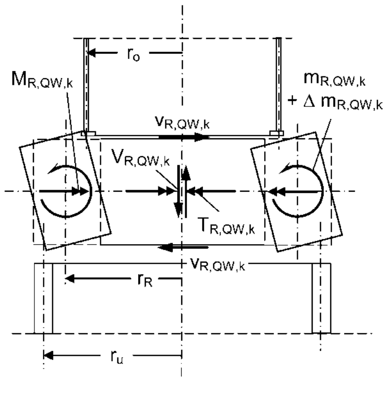

Fig. 4.49 Calculation of the internal forces in a circular ring beam as a result of the actions at an abrupt change in diameter

a) Symmetrical loads:

$$N_{R,Gk} = \Delta n_{R,Gk} \cdot r_R$$
$$M_{R,Gk} = \left(m_{R,Gk} + \Delta m_{R,Gk}\right) \cdot r_R$$
$$V_{R,Gk} = 0$$
$$T_{R,Gk} = 0$$

b) Antisymmetrical loads:

$$N_{R,QW,k} = 0$$
$$M_{R,QW,k} = \left(m_{R,QW,k} + \Delta m_{R,QW,k}\right) \cdot r_R \cdot \beta \cdot \cos\varphi$$
$$V_{R,QW,k} = v_{R,QW,k} \cdot h_R - \left(m_{R,QW,k} + \Delta m_{R,QW,k}\right) \cdot \beta \cdot \sin\varphi$$
$$T_{R,QW,k} = -\left(m_{R,QW,k} + \Delta m_{R,QW,k}\right) \cdot r_R \cdot (1-\beta) \cdot \sin\varphi$$

where

$$\beta = \frac{E \cdot I_B}{E \cdot I_B + G \cdot I_T}$$

4.10.5 Load on circular ring beam at ultimate limit state

The design values of the internal forces ($N_{R,Ed}$; $M_{R,Ed}$; $V_{R,Ed}$; $T_{R,Ed}$) are determined using the same design load cases as for the deformation calculation (see Section 4.7.1). The permanent loads for an unfavourable effect ($\gamma_{G,unf} = 1.35$) are critical for the resultant load:

a) External loading:

$$n_{R,Ed} = 1.35 \cdot \Delta n_{R,Gk}$$
$$m_{R,Ed} = 1.35 \cdot \left(m_{R,Gk} + \Delta m_{R,Gk}\right) + 1.35(\text{or } 1.50) \cdot \left(m_{R,QW,k} + \Delta m_{R,QW,k}\right)$$
$$v_{R,Ed} = 1.35(\text{or } 1.50) \cdot v_{R,QW,k}$$

b) Internal forces:

$$N_{R,Ed} = 1.35 \cdot N_{R,Gk}$$
$$M_{R,Ed} = 1.35 \cdot M_{R,Gk} + 1.35(\text{or } 1.50) \cdot M_{R,QW,k}$$
$$V_{R,Ed} = 1.35(\text{or } 1.50) \cdot V_{R,QW,k}$$
$$T_{R,Ed} = 1.35(\text{or } 1.50) \cdot T_{R,QW,k}$$

c) Internal forces related to the layers of reinforcement:

$$N_{R,Ed} = 1.35 \cdot N_{R,Gk}$$
$$M_{s1,Ed} = M_{R,Ed} - N_{R,Ed} \cdot \left(z_{R,1} - d_{R,1}\right)$$
$$M_{s2,Ed} = M_{R,Ed} + N_{R,Ed} \cdot \left(z_{R,2} - d_{R,2}\right)$$

4.10.6 Design of circular ring beam

The circular ring beam is designed for the resultant tensile forces in the layers of reinforcement at the ultimate limit state. The statically indeterminate forces shown in Figure 4.50 are determined in a similar way to the internal forces in the circular ring beam, that is from the design values of the internal forces at the ultimate limit state.

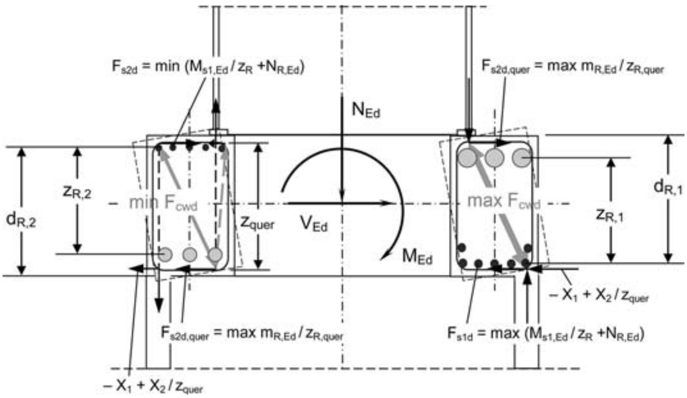

Fig. 4.50 Circular ring beam detail for an abrupt change in tower diameter – internal forces

4.11 Foundation design

4.11.1 Calculating the internal forces

A number of special aspects are relevant when *calculating the internal forces according to second-order theory* in relation to the interaction between tower, foundation and subsoil [78]. Our starting point is the safety concept described in DIN 1055-100 [44]. This is characterised by safety elements (partial safety and combination factors) based on semi-probabilistic methods, also by the fact that we distinguish between the serviceability and ultimate limit states.

Accordingly, we distinguish between three ultimate limit states:

a) Loss of equilibrium of a structure, for example due to uplift, overturning or buoyancy.
b) Failure of the loadbearing structure, one of its parts or the foundation, for example due to rupture, excessive deformation, conversion into a kinematic chain, loss of stability or sliding.
c) Failure of the subsoil, for example due to slope or ground failure; verification of this limit state is to be carried out as an analysis of the overall stability to DIN 1054 [50]!

This distinction results in unambiguous and compatible interfaces between the structural and geotechnical engineering responsibilities. Limit state type (b) governs in all cases in which structure and subsoil act together. The compatibility between the *design situations* to DIN 1055-100 [44] and the traditional load cases 1 to 3 of geotechnical engineering are illustrated in [44] Table A.3.

Whereas in structural engineering the *design load cases* according to [44] apply, some of the design load cases used in geotechnical engineering differ (see DIN 1054 [50]). Consistency is ensured by the fact that the characteristic values of the independent effects are "transferred" at the interfaces, that is the junctions between structure and subsoil. Those are the action effects resulting from the characteristic values of the independent actions (see [58] example A.5, and [78]). Therefore, geotechnical engineering makes use of the design load cases according to DIN 1055-100 [44], but also the cases specific to geotechnical engineering according to DIN 1054 [50].

The design of foundations to loadbearing structures that have to be analysed according to second-order theory must include the second-order components in all the analyses required to satisfy the equilibrium conditions for the deformed structure. Ignoring these could mean that the required structural reliability is not achieved! This applies in particular to the foundations of sway structures and hence also to free-standing towers whose internal forces are calculated according to second-order theory.

In contrast to DIN 1054 [50] 6.1.2, the following procedure is suggested for the conversion into *characteristic internal forces* at the soil/structure interface (for an application see [58] example A.5):

1. Structural Analysis According to Second-Order Theory and Design (see Figure 4.51)
   – Calculation of deformation and internal forces with the design values of the actions (G_d; $Q_{imposed,d}$; $Q_{wind,d}$; . . . etc.) and the resistances specific to the type of construction according to DIN 1045-1 [33] 5 and 8.6.1, plus the soil bearing pressures and uplift resulting from this. In doing so, the equilibrium conditions for the deformed structure have to be satisfied at the ultimate limit state.
   – Calculation of the design values for the subsoil reactions at the underside of the foundation (N_{Ed}; V_{Ed}; M_{Ed}). Design of the loadbearing structure, including the

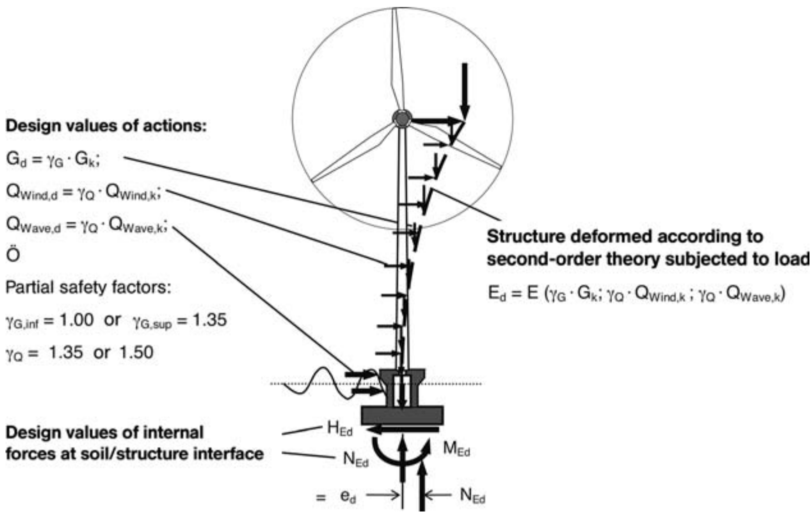

Fig. 4.51 Structural analysis according to second-order theory and design

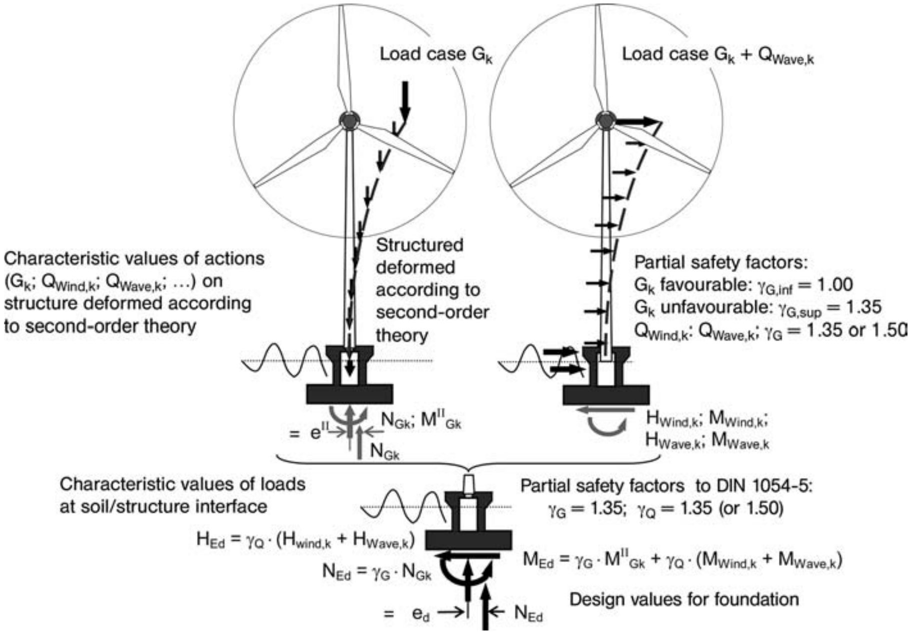

Fig. 4.52 Foundation design

foundation (!), on the basis of DIN 1045-1 [33] in conjunction with DIN 1055-100 [44].

2. Design of Foundation (see Figure 4.52)
   – Calculation of the characteristic values of the independent effects (loads) at the soil/structure interface (N_{Gk}, M_{Gk}, H_{Gk}; $N_{imposed,k}$, $M_{imposed,k}$, $H_{imposed,k}$; $N_{wind,k}$, $M_{wind,k}$, $H_{wind,k}$; . . . etc.) with the equilibrium conditions for the loadbearing structure deformed according to second-order theory.
   – Calculation of the design values of the loads on the subsoil (N_{Ed}; V_{Ed}; M_{Ed} or N_d and T_d) and geotechnical analyses (safety against ground failure, safety against sliding, . . .) according to DIN 1054 [50].

Design of structural components

A compact tower foundation is calculated as a circular or annular slab. In order to avoid lifting of the perimeter and to increase the core radius, a layer of soft material is placed beneath the central area (inside diameter $D_i \cong 1/3 \times$ outside diameter D_a). Further, the aim is to make sure that no uplift occurs at the soil/structure interface under characteristic actions (which traditionally corresponds to a full load made up of permanent, imposed, wind and, if applicable, sea state loads). See [8] for details regarding design, construction details and reinforcement in tower foundations.

5 Construction of prestressed concrete towers

5.1 Introduction

Prestressed concrete towers for onshore wind turbines are constructed using either *in situ* or precast concrete techniques and completed with internal or external prestressing. Hybrid tower forms have proved to be particularly beneficial. Such towers consist of a prestressed concrete shaft and a top segment of steel. In recent years they have turned out to be very economic solutions for turbines of the multi-megawatt class. The detailed design of prestressed concrete towers for wind turbines was covered in detail in Chapter 4.

The choice of a suitable tower design is governed by the conditions at the site (fabrication, transport, erection, etc.) and the number of segments required (precast concrete construction). *Beton-Kalender 2006* [8] contains a comprehensive review of different designs.

Examples of hybrid tower designs and prestressed towers in precast concrete are described in this chapter.

The chapter concludes with a section on concrete foundation designs for offshore wind turbines.

5.2 Hybrid structures of steel and prestressed concrete

Hybrid support structures for wind turbines are characterised by the combination of various individual loadbearing structures of prestressed concrete and steel which carry the load together. The tower consists of a concrete shaft surmounted by a separate steel tower segment that serves as a transition to the nacelle containing the wind turbine itself.

Exclusively tubular steel towers with heights exceeding 100 m and turbine outputs >2.0 MW are practically ruled out because of the transport width of the base segments (>4.30 m). However, the concrete, reinforcing steel and prestressing steel for concrete towers can be easily delivered to the site separately for construction *in situ*.

The hybrid form of construction is frequently the most economic solution for high towers; for details see [8]. Figure 5.1 shows a hybrid design for a 5 MW wind turbine and 130 m hub height. It consists of a prestressed concrete tower (h = 120 m) and a tubular steel top segment that supports the nacelle with the rotor.

The vibration effects for this loadbearing structure were investigated in Section 4.3.2. The aerodynamic force coefficient, the equivalent mass for the prestressed concrete tower and the gust response factor were determined in Section 2.3.1 according to [12] and used as the basis for calculating the wind loads.

A circular ring beam in combination with a steel adapter is provided at the top of the prestressed concrete tower for connecting the tubular steel top segment. The principles for the structural analysis of this structural component can be found in Section 4.10.

Concrete Structures for Wind Turbines. First edition. Jürgen Grünberg, Joachim Göhlmann.

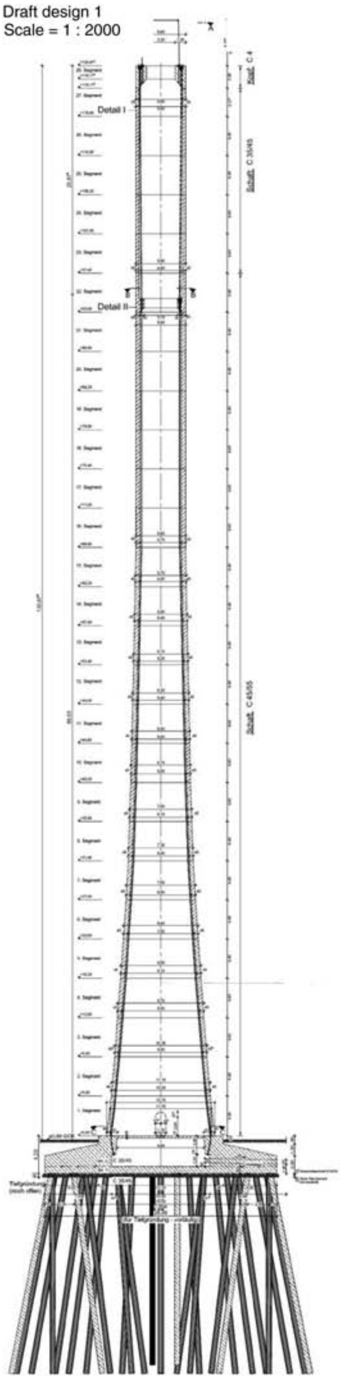

Fig. 5.1 Wind turbine in hybrid form of construction with 130 m hub height © G + S Planungsgesellschaft mbH, Hamburg

5.3 Prestressed concrete towers with precast concrete segments

5.3.1 Examples of design and construction

Towers in reinforced or prestressed concrete are mostly described as *in situ* concrete structures in tenders. Support structures with post-tensioned precast concrete segments are frequently offered as alternatives for towers up to heights of approx. 100 m.

In order speed up operations on site, the Enercon company has developed a design using precast concrete rings for towers with a *hub height of 98 m* (*E-70 turbine*); for details see [8]. Specially fabricated separate internal and external steel moulds are kept in stock for each of the 23 elements of the tapering concrete tower for an E-70 turbine (Figure 5.2). The reinforcement is installed using a winding technique which employs templates fitted to special rotary machines. The precast concrete elements are delivered to the site by road on low-loaders. Owing to their size, the bottommost segments are cast as pairs of half-shells (Figure 5.3).

After arrival on site, these half-shells are assembled with a 300 t telescopic crane. The completed annular segments are then erected with a 600 t crawler-mounted crane. The precast concrete elements are joined together with an epoxy resin

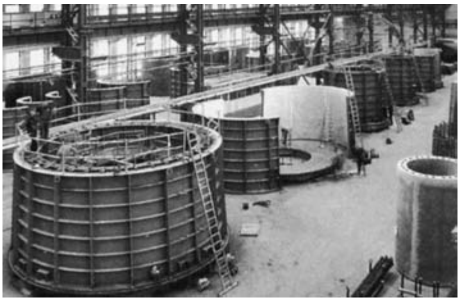

Fig. 5.2 Moulds for tower segments

Fig. 5.3 Half-shell

Fig. 5.4 Enercon E-126 wind turbine

adhesive, and the approx. 800 connections between the ducts for the prestressing tendons with their tubes to protect the couplers must match up exactly. The pockets at the connections, into which the steel U-bars project, are filled with a rapid-hardening grout.

In the meantime, towers with a hub height even higher than 100 m have been built using precast concrete segments. This development, too, can be attributed to Enercon.

The *ENERCON E-126/6 MW* is the *most powerful wind turbine in the world* (Figure 5.4); it generates enough electricity to supply more than 5000 four-person households. The hub height is 135 m, the total height 198 m and the rotor diameter 126 m. Each rotor blade is made in two pieces so that it can be easily transported to the site by road.

The *precast concrete towers* consist of a total of 35 segments with walls up to 45 cm thick. With a base diameter of 14.5 m, each of the first eight segments has to be split into three parts so that transport by road is still feasible (Figure 5.5). Each of the next 22 segments is divided into two parts and only the top five are complete rings. The final segment, on which the nacelle is mounted, is of steel.

All the *tower segments* are cast at the precasting works. The high accuracy of the precast concrete segments is guaranteed by the steel moulds specially built for this work.

The individual tower segments and the foundation are connected by *internal prestressing* tendons which are fed through ducts located on the centre-line of the shaft wall. Although the tendons are fed in from the top, they are prestressed and grouted from a space within the foundation.

The vertical faces between the subdivided segments are in the form of pockets, profiled to handle the shear forces due to transverse loads and torsion and also provided with loop-type starter bars for connecting to the other segments.

The erection procedure involves first positioning and aligning the individual elements. After the structural vertical reinforcement has been installed, the joints are filled with a high-strength grout.

Fig. 5.5 One-third segment

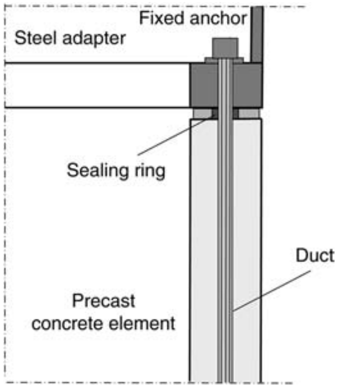

Fig. 5.6 Detail of junction between topmost concrete segment and steel adapter

Each segment is supported and aligned at three points.

The *joints between the segments* take the form of filled joints with spacer blocks. Sealing rings prevent the grout from seeping into the ducts for the prestressing tendons. The joints are prepared with a layer of high-strength mortar and filled completely after each segment has been aligned.

Figure 5.6 shows the junction between the topmost concrete segment and the steel adapter to which the rotor mounting is attached. The steel adapter is fixed and aligned by means of four site bolts. Only after all segments have been erected are the prestressing tendons threaded through from the top. Figure 5.7 shows the junction between the bottommost segment and the foundation with its stressing point in a space within the foundation.

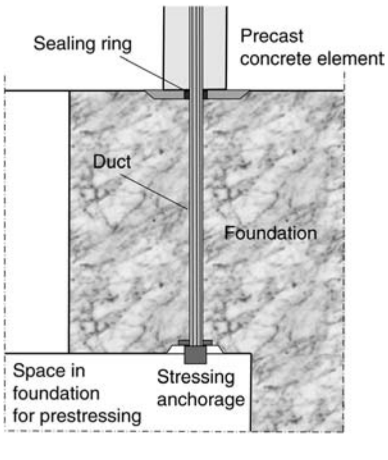

Fig. 5.7 Detail of junction between bottommost segment and foundation

One of the tallest *hybrid towers* built so far is the one erected by the Dutch company *Mecal* on the wind power test site at Grevenbroich near Cologne. The hub height of this 2.3 MW turbine is 133 m. With a rotor diameter of 93 m, that makes the total height about 180 m. The tower foundation is 30 m in diameter and is founded on vibrated stone columns that extend 14 m into the subsoil.

The tower design above this consists of 40 precast concrete elements finished off at the top with an adapter in the form of a single segment. In cross-section, the tower is divided into eight parts: four quarter-circle elements and four straight elements that taper towards the top. It is this design that gives the tower its striking conical form.

Vertically, the tower is subdivided into five levels each 15 m high (Figure 5.8). Transporting and erecting these precast concrete elements presented a challenge in terms of the logistics. Two powerful mobile cranes were needed on site.

Filled mortar joints are used horizontally, whereas the vertical joints are in the form of keyed and reinforced concrete-filled pockets.

The individual phases of the erection of the adapter segment are shown in Figure 5.9. Precision work at a height of 75 m was necessary here in order to fit the threaded bars into the top of the tower. But the prevailing wind conditions allowed this work to be completed in just 15 minutes.

Fig. 5.8 Erecting the 4th level, from 45 to 60 m. (source: ATS Advanced Tower Systems, Enschede, NL)

Fig. 5.9 Erecting the 70 t adapter segment. (source: ATS Advanced Tower Systems, Enschede, NL)

5.3.2 Further developments in precast concrete construction

Tower segments with an annular cross-section are limited to a maximum outside diameter of approx. 4 m owing to the clearances required for road transport. Therefore, the prestressing required to overcompress the joints between segments sufficiently rises rapidly as the height of the tower increases. At the same time, the internal forces due to external loads also increase.

This means that the compressive stresses due to dead loads, the flexural compressive stresses due to wind and also the compressive stresses caused by the concentric prestressing accumulate in the cross-sections and joints of the lower segments, whereas the maximum compression capacity given by the concrete strength is limited. It is for this reason that concretes of strength class B55, even spun concrete of class B65 to DIN 4228 [15], were the types most commonly used in the past.

The introduction of the DAfStb guideline for high-strength concrete, and as a consequence the new DIN 1045-1 [33], means that even higher strengths, for example C 70/85, are being increasingly used for the segments of precast concrete towers. Further developments in the direction of ultra-high-performance concretes (UHPC) are to be expected. One way of ensuring that UHPC mixes comply with requirements regarding sufficient robustness and ductility is to add steel fibres to the mix.

There is considerable room for errors in the design of and workmanship at joints between segments. The danger when applying the grout and subsequently positioning a segment is that the grout can seep into the ducts for the prestressing tendons if the seals have not been properly fitted. On the other hand, any gaps in the grouting at the joints can lead to grout being forced out through the joints when pressure-grouting the ducts.

Such problems are specific to the use of grouted post-tensioned tendons. The alternative is therefore external prestressing with tendons within the interior of the tower shaft, a method that has already been used for a number of wind turbines. However, the special conditions described in Sections 4.7.1, 4.7.5 and 4.8.3 must be taken into account.

Another option is to prestress the segments individually and anchor the tendons in annular structural steel flanges at the horizontal joints. Such annular flanges extend into the interior of the tower shaft in such a way that the segments can be connected on site with high-strength friction-grip (HSFG) bolts. This approach results in a hybrid structure with individual shaft elements of high-strength prestressed concrete and steel connections between those elements. A further possibility with this form of construction is being able to offset the vertical joints between half-shell elements, something that was not possible with the reinforced filled joints used up to now.

Current developments are therefore characterised by innovations on the materials side (HPC, UHPC, fibre-reinforced concrete) on the one hand and by robust design principles (external prestressing, modern connection methods) on the other.

5.4 Offshore substructures in concrete

The offshore wind farms planned for the North Sea and Baltic Sea are up to 40 km from the coast, where the depth of the water varies from 30 to 45 m depending on the particular location. Elsewhere in Europe, the experience with offshore wind farms to date has been limited to much shallower waters and sites much closer to the coast. Design, construction, transportation and erection are four areas where optimisation is crucial if the economic viability of offshore sites in such deep waters is to be guaranteed. Factory-fabrication of individual structural components and the development of prefabricated solutions for the entire structure result in economic benefits and the chance to optimise the construction costs of towers and foundations.

The choice of foundation type, the length of time required for construction and, due to the weather, the limited window for the transportation and on-site erection procedures are further critical factors that influence the costs. Fundamental here for both nearshore and offshore wind turbines are the water depths, the subsoil conditions and the ability to deploy heavy plant, for example pontoons, jack-up barges, heavy-lift crane vessels, drilling and driving equipment, and so on. Another vital aspect for sites near the coast is accessibility for the transport of construction materials and the plant required, see [79].

Current design and construction approaches are described in the following. Earlier projects have already been described in detail in [8].

5.4.1 Compact substructures with ice cones

5.4.1.1 Middelgrunden offshore wind farm

Round substructures topped with ice cones were conceived for this location in shallow waters near Copenhagen.

Comparison of prices for various compact substructures (Figure 5.10):

Steel caisson: € 380 000
Concrete structure: € 315 000
Monopile: € 420 000

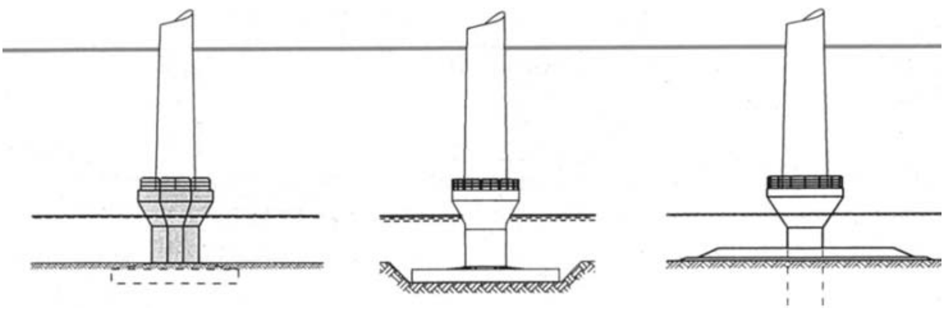

Fig. 5.10 Substructure options. (source: www.middelgrunden.dk)

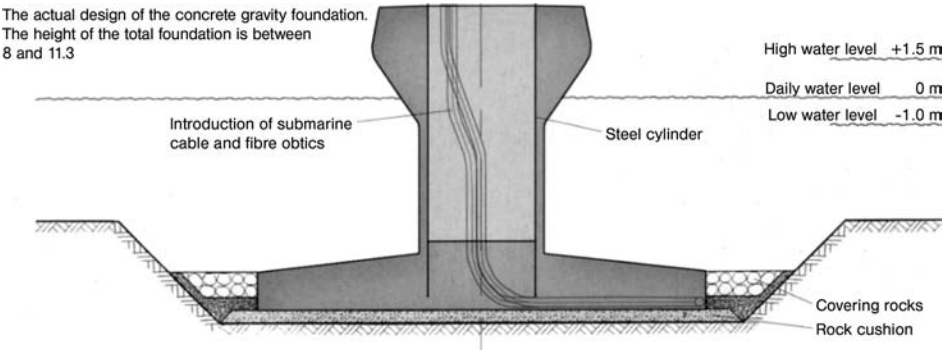

Fig. 5.11 Chosen substructure option. (source: www.middelgrunden.dk)

For details of the design chosen see Figure 5.11 (section) and Figure 5.12 (reinforcement).

Technical specification of foundation:

Water depth: 4 to 8 m
Total height: 8 to 11.3 m
Weight: 1800 t

Fig. 5.12 Fixing the reinforcement in the dry dock. (source: www.middelgrunden.dk)

Fig. 5.13 Fabrication in the dry dock – mounting the steel tower segments. (source: www.middelgrunden.dk)

Figure 5.13 shows the fabrication in the dry dock, which included mounting the bottom section of the steel tower (including transformer and switchgear).

Transport to and erection at the site was undertaken with a heavy-lift crane vessel as shown in Figure 5.14.

Prestressed concrete towers comprising precast concrete segments are also possible offshore. For such structures, the parts below the waterline and in the splash zone should be in the form of a large, compact reinforced concrete substructure. Prestressing is not absolutely essential here. Above the splash zone, the tower can be built using precast concrete segments with external prestressing (Figure 5.15).

Fig. 5.14 Erection operations at sea. (source: www.middelgrunden.dk)

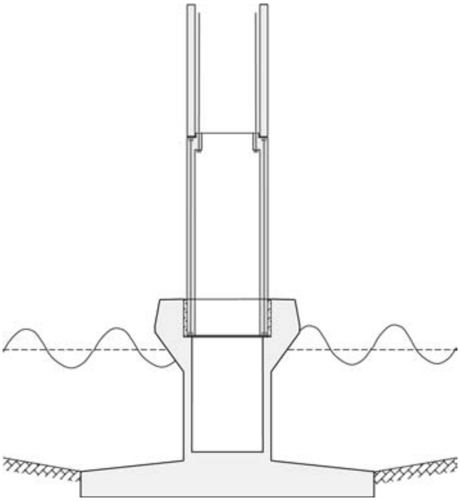

Fig. 5.15 Compact foundation and tower made from prestressed precast concrete elements

5.4.1.2 Sequence of operations on site

1. Installation of foundation with heavy-lift crane vessel
2. Erection of first tower segment, internal prestressing, grouted joint
3. Erection of second tower segment on mortar bed joint, external prestressing
4. Erection of further tower segments with external prestressing

5.4.2 Design, construction, transport and erection of concrete substructures

High-strength lightweight concretes are frequently used for concrete substructures because these represent a weight-saving of approx. 20% over normal-weight concretes. Owing to their very dense microstructure, high-strength lightweight concretes exhibit excellent durability and are therefore particularly suitable for offshore applications. In the past, high-strength lightweight concretes have been successfully used worldwide for oil and gas platforms.

As a rule, the primary loadbearing elements of concrete support structures for wind turbines are prestressed in order to improve the serviceability (to limit cracks, deformations, etc.). The actions due to repeated loads (fatigue) are often especially important when designing the cross-sections (see Section 4.9).

The costs of the materials for and construction of concrete support structures for offshore wind turbines are comparatively low. Moreover, exploiting series production and prefabrication options can make a considerable contribution to optimising the costs. Contrasting with this, however, are the much higher dead loads of such substructures. They frequently weigh between approx. 3000 and 5000 t and are therefore far heavier than steel substructures.

The high self-weight places considerable demands on the fabrication yards and especially the offshore logistics (transport and erection). There are currently only a few offshore rigs available that can handle the lifting, lowering and offshore transport of such heavy loads. Furthermore, the deployment of these rigs is subjected to a global demand that results in high charter prices and timetable constraints. And the fact that the use of such offshore plant is highly dependent on the weather means that calculating the charter costs is a very risky business.

The reduction in costs that can be achieved with concrete designs therefore essentially depends on the logistics concepts and the offshore plant available for those concepts.

5.4.2.1 Special design criteria

Besides the typical design criteria associated with wind turbine support structures, for example the actions due to turbine operation, wind and waves plus the dynamic behaviour of the total structure, the design of concrete substructures calls for other criteria to be considered as well:

– Wave loads on compact concrete designs (Section 2.6)
– Bearing capacity of the subsoil, especially near the surface of the seabed
– Scouring and measures required to prevent scouring
– Offshore logistics concept
– Flotation stability while transporting and lowering float-out substructures
– Behaviour in the event of vessel impact
– Area of seabed sealed
– Number of substructures (exploitation of series effects and use of prefabricated elements)

5.4.2.2 Construction

Concrete substructures can be constructed on land, on a floating pontoon or in a dry dock. When building on land it is generally necessary to ensure that the subsoil is able to bear the high dead loads; the subsoil below the fabrication yard may need to be upgraded. A concrete substructure can be transported to the edge of the quay or a launch barge on skidways or modular heavy-load trailers, for example. Figure 5.16

Fig. 5.16 Gravity bases for the Thorton Bank offshore wind farm. (source: www.c-power.be)

shows an example of the fabrication of concrete substructures and the transfer to a heavy-lift crane vessel for the Thorton Bank offshore wind farm off the Belgian coast.

Carrying out the construction work directly on a floating pontoon requires the different loading situations caused by the progress of the work to be taken into account when checking the stability in the floating condition. In addition, the effects of waves plus the rise and fall of the tide must be considered.

Building the substructure in a dry dock is worth considering when it is to be floated out to its offshore location. However, it should be remembered that in most cases the draught available is limited.

5.4.2.3 Transport and erection

Substructures that do not float are transported with the help of heavy-lift crane vessels or launch barges. The advantage of cranes is that they can position the substructure very accurately at its offshore location and then lower it into position (Figure 5.17).

Alternatively, launch barges can be used for transport, which are often able to carry several substructures to an offshore location simultaneously. Such barges are sometimes fitted with lifting equipment and so a substructure can be lowered into position directly from the vessel. In other cases, a heavy-lift crane vessel will lift the substructure off the ship and lower it into position on the seabed.

Logistics concepts involving semi-submersible vessels have also been used. Such a ship can ballast its bow with water to such an extent that the floating substructure can be floated out of the vessel and picked up by a heavy-lift crane vessel, for example. Substructures can be designed to float and thus avoid the use of expensive heavy-lift crane vessels altogether; several tugs can tow such a substructure from its place of

Fig. 5.17 Transporting a concrete substructure for the Thorton Bank offshore wind farm with a heavy-lift crane vessel. (source: www.c-power.be)

Fig. 5.18 Tugs towing a float-out concrete offshore platform

Fig. 5.19 Controlled sinking of a drilling platform by filling compartments with water

construction to its offshore location. Arranging the tugs in a star formation at the offshore site enables the substructure to be positioned accurately before being ballasted with water and lowered to the seabed. Once on the seabed, the substructure is normally ballasted in its final position with a sand/water mixture. Up until now, such float-out designs have been constructed primarily for the offshore platforms of the oil and gas industry. As an example, Figure 5.18 shows a Russian concrete platform being towed in 2001. The controlled sinking of the platform is shown in Figure 5.19.

5.4.2.4 Spread and deep foundations

Substructure designs in concrete are generally laid flat on the seabed (spread foundation). Irrespective of the construction and transport methods, the seabed will generally have to be prepared for such a foundation. This involves either excavating any seabed soil strata with insufficient bearing capacity or employing soil improvement measures to upgrade the subsoil. A layer of gravel or other filter material should be laid on the prepared seabed to provide a stable base and to prevent erosion.

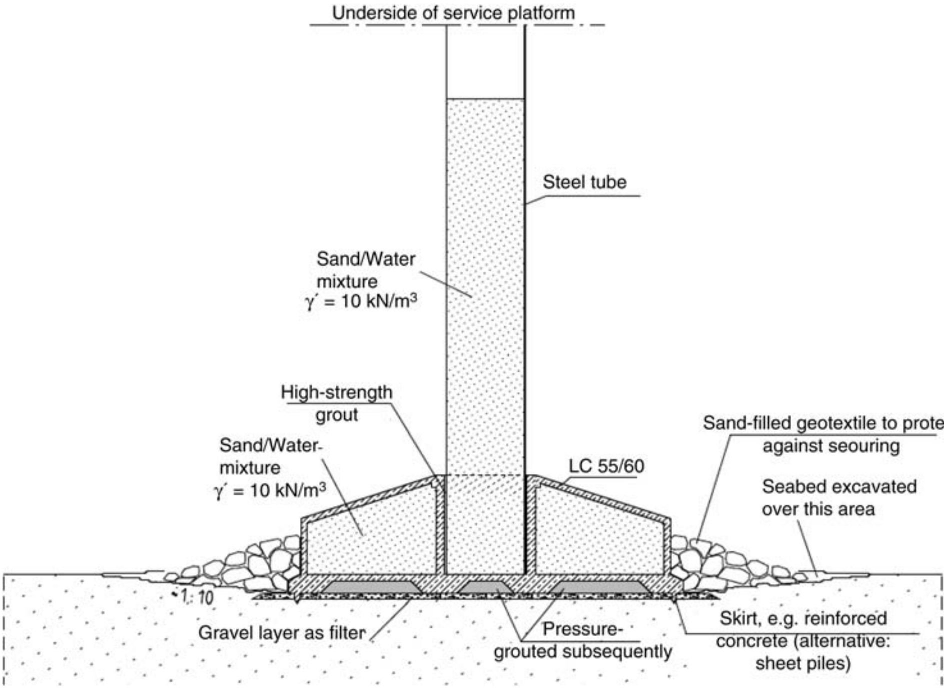

Fig. 5.20 Hybrid gravity base in high-strength lightweight concrete © grbv Ingenieure im Bauwesen GmbH & Co. KG Hannover Germany

Once a spread foundation has been positioned, the surrounding seabed must be protected against scouring, for example with sand-filled geotextiles. Figure 5.20 shows an example of a hybrid gravity base with scouring protection. The logistics concept in such a situation presumes that the concrete substructure is fabricated in a dry dock. After controlled floating of the concrete substructure in the dock, it is attached to heavy-lift pontoons and towed from the dock to a nearby quayside. This is where the steel shaft can be mounted on the concrete foundation, aligned and the space between steel and concrete filled with a high-performance concrete (grouted joint). Alternatively, the tower shaft can be in prestressed concrete.

The hybrid substructure is then towed to its offshore location. The necessary stability during the floating procedure is guaranteed by the heavy-lift pontoons. At the site, the foundation can then be lowered to the seabed in a controlled operation with the system of winches installed on one of the pontoons. Once in position on the seabed and ballasted for the final condition, the anti-scouring measures can be carried out. The extent of the measures necessary to prevent scouring can be estimated by way of numerical analyses and investigated and specified with the help of testing. The geometry of the substructure can have a considerable influence on scouring, or rather the scouring protection measures required. A review of the various anti-scouring measures used for different offshore designs and the experience gained with such measures can be found in, for example, [80]. The reader is referred to [81,82] for the state of the art regarding scouring design.

Where preparation of the seabed and any potential anti-scouring measures are undesirable or there is no subsoil with an adequate bearing capacity near the surface of the seabed, then a deep foundation represents an alternative. Any scouring expected is then taken into account directly in the design of foundation and piles as for steel substructures. Extensive measures to prevent scouring are then unnecessary. On the other hand, a deep foundation involves greater costs for the construction, transport and erection. Therefore, which type of foundation is the best economic answer for a particular offshore location must be determined after taking into account all the specific boundary conditions.

5.4.2.5 Innovations

At the moment, new developments are mainly to be found in the areas of specialising and optimising the offshore logistics, which is the responsibility of individual companies. For example, one logistics concept being pursued by Ed. Züblin AG involves transporting and erecting the concrete support structure, including shaft and wind turbine, as one complete unit [83]. A "special carrier" is being developed for this work, which uses semi-submersible technology and therefore overcomes the weather-related limitations that apply to the heavy-lift crane vessels currently in use. Figure 5.21 shows computer images of the "special carrier" and also the individual steps in the offshore logistics.

Ballast Nedam is currently developing the concept of a prestressed concrete monopile [84]. The idea here is that a concrete monopile consisting of precast concrete rings is assembled on land and prestressed in the longitudinal direction. The monopile is then floated out to its offshore location (towed by tugs) and then installed with a heavy-lift

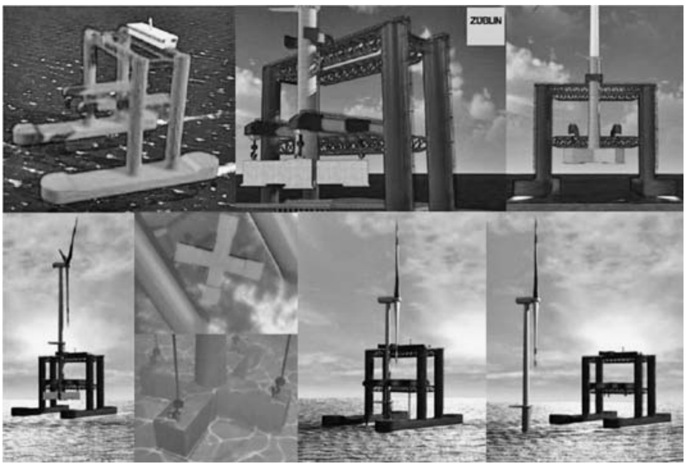

Fig. 5.21 Offshore logistics concept of Ed. Züblin AG. [83]

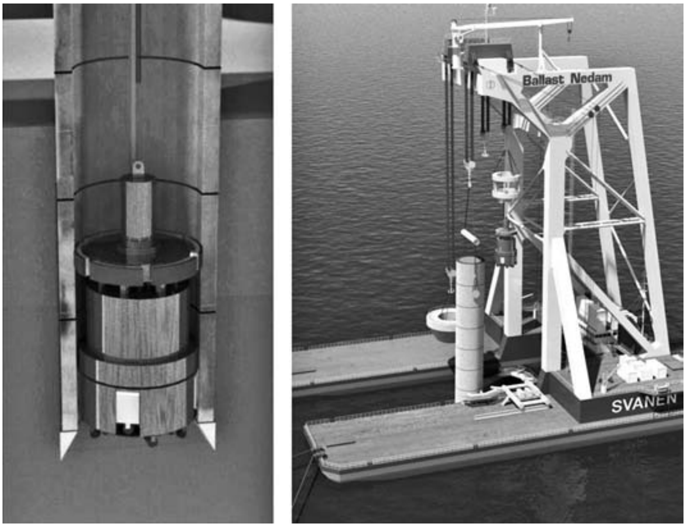

Fig. 5.22 Prestressed concrete monopile

crane vessel. The crane lifts the concrete monopile, aligns it and then lowers a drilling unit through the hollow centre into the subsoil. Drilling a hole in the seabed allows the base of the monopile to sink into the ground and be embedded at the necessary depth (Figure 5.22).

References

1. German Wind Energy Institute (2005) *Wind energy use in Germany – status 31 Dec 2004*. VDMA/BWE/DEWI press release, 24 Jan 2005.
2. Schaumann, P. (2004) [@lang="de"]Einwirkungen und Strukturmechanik bei Windkraftanlagen [actions on and structural mechanics of wind turbines]. *Workshop "Windkraftanlagen – Sicherheit und Zuverlässigkeit" [wind turbines – safety and reliability], VDI Wissensforum, Darmstadt, 4 Nov 2004*.
3. Johnson, B. (2004) DEWI study. [@lang="de"] Das Jahrzehnt der Windenergie beginnt 2006 [the wind energy decade begins in 2006]. *Erneuerbare Energien*, **4**, 18–19.
4. Aydogmus, T., Dohmel, D., and Schümann, C. (2004) [@lang="de"] Zum Einsatz von Geokunststoffen bei der Flachgründung von Windenergieanlagen [Use of geosynthetics for construction of windmills on spread foundation]. *Bautechnik*, **81** (9), 717–724.
5. Merz, K. (2004) [@lang="de"] Näherungsformel zur Bestimmung der Bodenpressung von Turmfundamenten mit unterschiedlichen symmetrischen Querschnitten [approximation formulas for determining the soil pressing of tower foundations with different symmetric cross-sections]. *Bautechnik*, **81** (12), 982–987.
6. Schaumann, P., Kleineidam, P., and Wilke, F. (2004) [@lang="de"] Fatigue Design bei Offshore-Windenergieanlagen [Fatigue design of offshore wind energy conversion systems], *Stahlbau*, **73** (9), 716–726.
7. Liebrecht, K., Loga, A., Förster, K., and Voß, M. (2004) [@lang="de"] *Schwerkraftgründung für eine 5-MW-Offshore-Windenergieanlage [gravity base for 5 MW offshore wind turbine]*. Erneuerbare Energien, 3/2004 & 4/2004.
8. Grünberg, J., Funke, G., Göhlmann, J., and Stavesand, J. (2006) [@lang="de"] *Fernmeldetürme und Windenergieanlagen in Massivbauweise [Concrete Towers for Telecommunications and Wind Turbines]*. (ed. Beton-Kalender), part 1, Ernst & Sohn, pp. 103–223.
9. Deutsches Institut für Bautechnik (DIBt) (2004) [@lang="de"] *Richtlinie Windenergieanlagen. Einwirkungen und Standsicherheitsnachweise für Turm und Gründung [wind turbines guideline – actions on and stability analyses for tower and foundation]* Mar 2004.
10. DIN EN 61400-3 (2010) *Wind turbines – Part 3: Design requirements for offshore wind turbines*. Jan 2010, VDE Verlag GmbH, Berlin.
11. Germanischer Lloyd WindEnergie (2005) *Rules and Guidelines. IV Industrial Services – 2 Guideline for the Certification of Offshore Wind Turbines*.
12. DIN 1055-4 (2005) *Actions on structures – Part 4: Wind loads*, Mar 2005 ed., 1st amendment.

Concrete Structures for Wind Turbines. First edition. Jürgen Grünberg, Joachim Göhlmann.

13. DIN 1056 (2009) *Solid construction, free-standing chimneys – Brick liners – Calculation and design*. Ed. quoted here: Oct 1984 (new ed.: Jan 2009).

14. DIN 4131 (1989) *Steel radio towers and masts*, 1989 ed.

15. DIN 4228 (1989) *Precast concrete lattice towers, masts and columns*, 1989 ed.

16. DIN EN 61400-1 (2007) *Wind turbines – Part 1: Design requirements*. Aug 2007, VDE Verlag GmbH, Berlin.

17. Kokkinowrachos, K. (1980) [@lang="de"] *Hydrodynamik der Seebauwerke [hydrodynamics of marine structures]*. Offprint from "Handbuch der Werften" [shipyards manual], vol. XV.

18. Zielke, W., Mittendorf, K., and Nguyen, B. (1975) [@lang="de"]Seegang und Seegangsbelastung [sea states and sea state loads]. *2nd symposium, Offshore-Windenergie – bau- und umwelttechnische Aspekte [Offshore wind energy – construction and environmental technology aspects]. Hannover, 9 Sept 2002*.

19. Dean, R.G. (1965) Stream function representation of nonlinear ocean waves. *Journal of Geophysical Research*, **70** (18) 4561–4572.

20. Zielke, W., Mittendorf, K., and Nguyen, B. (2004) [@lang="de"]Seegang und Seegangsbelastung [sea states and sea state loads] II. *3rd symposium, Offshore-Windenergie – bau- und umwelttechnische Aspekte. Hannover, 16 Mar 2004*.

21. Hapel, K.-H. (1990) [@lang="de"] *Festigkeitsanalyse Dynamisch Beanspruchter Offshore-Konstruktionen [Strength Analysis of Dynamically Loaded Offshore Structures]*, Vieweg.

22. Clauss, G., Lehmann, E., and Ostergaard, C. (1988) [@lang="de"] *Meerestechnische Konstruktionen*, Springer, [English: *Offshore Structures*, vols. 2, Springer, 1992/1994].

23. Kleineidam, P. (2004) [@lang="de"] *Zur Bemessung der Tragstrukturen von Offshore-Windenergieanlagen gegen Ermüdung [Fatigue design of structures for offshore wind turbines]*. Dissertation, Institute for Steel Construction, University of Hannover.

24. Det Norske Veritas Offshore Standard, DNV-OS-J101 (2004) *Design of Offshore Wind Turbine Structures*, Jun 2004.

25. Grünberg, J. (2007) *Comments on EN 1990 "BASIS of structural design"*. Guidelines for implementation and application. Beuth, Berlin (pub. as electronic book).

26. Recommendations of Committee for Waterfront Structures, Harbours & Waterways (2005) EAU 2004, *Hafenbautechnische Gesellschaft e.V. and Deutschen Gesellschaft für Geotechnik e.V.*, Committee for Waterfront Structures, Harbours & Waterways, Berlin.

27. Hütte (1955) [@lang="de"] *Des Ingenieurs Taschenbuch [Engineer's Manual]*, 28th edn, vol. 1, W. Ernst & Sohn, Berlin.

28. Hager, M. (1991) [@lang="de"] Eisdruck [Ice pressures], in *Grundbau-Taschenbuch [Foundations Manual]*, part 1, 4th edn, Ernst & Sohn, Berlin, pp. 551–564.

29. MacCamy, R.C. and Fuchs, R.A. (1954) *Wave Forces on Piles: A Diffraction Theory*. Tech. Memo. No. 69, Beach Erosion Board.

30. Grünberg, J. (1982) [@lang="de"]Weiterentwicklung eines Computerprogramms für die hydrodynamische Berechnung kompakter, feststehender Offshore-Bauwerke [further development of a computer program for hydrodynamic design of compact, permanent offshore structures]. Presentation at *INTERMARITEC '82, Hamburg (IMT 82–124/01), Sept 1982*.

31. Garrison, C.J. (1980) *Wave loads on large displacement structures with superstructures based on diffraction theory (WAVLODE)*. C. J. Garrison & Associates, Pebble Beach, California, USA. Report No. 76–105, 2 Jun 1980.

32. Kromminga, S., Grünberg, J., and Göhlmann, J. (2008) Wave loads on large-sized concrete foundations. *Proceedings of German Wind Energy Conference, DEWEK 2008, Bremen, 27–28 Nov 2008*.

33. DIN 1045-1 (2008) *Concrete, reinforced and prestressed concrete structures – Part 1: Design and construction*, Aug 2008. Deutsches Institut für Normung, Beuth. (Interpretation of DIN 1045-1 can be found in the Internet at www.nabau.din.de).

34. Kordina, K. and Quast, U. (2001) [@lang="de"] *Bemessung von schlanken Bauteilen für den durch Tragwerksverformungen beeinflussten Grenzzustand der Tragfähigkeit – Stabilitätsnachweis [Design of Slender Components for the Ultimate Limit State Influenced by Structural Deformations – Stability Analysis]*, (ed. Beton-Kalender), part 1, Ernst & Sohn, Berlin, pp. 349–416.

35. Erläuterungen zu DIN 1045-1 (2003) [DIN 1045-1 commentary]. *Deutscher Ausschuss für Stahlbeton, No. 525*. Beuth, Berlin. Amendment 1 to DAfStb No. 525. Sept 2003 ed.

36. DIN EN 1992-1-1/NA (2011) *National Annex – Nationally determined parameters for DIN EN 1992-1-1*, Jan 2011

37. Grünberg, J. and Göhlmann, J. (Mar 2005) [@lang="de"] Versagensmodelle für Beton unter monotoner Beanspruchung und Ermüdung [failure models for concrete subjected to monotonic loading and fatigue]. *Der Bauingenieur*, Springer VDI Verlag, pp. 115.

38. Hofstetter, G. and Mang, H.A. (1995) *Computational Mechanics of Reinforced Concrete Structures*, Vieweg, Braunschweig, Wiesbaden.

39. Kupfer, H. (1973) [@lang="de"] *Das Verhalten des Betons unter mehrachsiger Kurzzeitbelastung unter besonderer Berücksichtigung der zweiachsigen Beanspruchung [Behaviour of Concrete Subjected to Multi-Axial Short-Term Loads, with Special Emphasis on Biaxial Action Effects]*, Deutscher Ausschuss für Stahlbeton, No. 229. Ernst & Sohn.

40. Mehlhorn, G. (ed.) (1996) [@lang="de"] *Der Ingenieurbau, Grundwissen in 9 Bänden: Rechnerorientierte Baumechanik [Construction Engineering, Fundamental Knowledge in 9 volumes: Computer-Based Structural Mechanics]*, Ernst & Sohn, Berlin.

41. Willam, K.J. and Warnke, E.P. (1975) Constitutive Model for the Triaxial Behaviour of Concrete. *IABSE-AIPC-IVBH: Seminar "Concrete Structures subjected to Triaxial Stresses", ISMES, Bergamo, Italy*, vol. 19, p. 174.

42. DIN 1045 (1988) *Concrete, reinforced and prestressed concrete structures*, Jul 1988 ed., Beuth, Berlin/Cologne.

43. Mang, H. A., Lackner, R., Mescke, G., and Mosler, J. (2003) Computational modeling of concrete structures. *Comprehensive Structural Integrity*, **3**. Elsevier Ltd.

44. DIN 1055-100 (2001) *Actions on structures – Part 100: Basis of design, safety concept and design rules*, Mar 2001. Deutsches Institut für Normung, Beuth.

45. DIN EN 1990 (2002) *Eurocode: Basis of structural design*, Oct 2002, Beuth, Berlin.

46. DIN EN 1990/NA 1 (2010) *National Annex – Nationally determined parameters – Eurocode: Basis of structural design;* Amendment A1, Dec 2010.

47. DIN 1055-9 (2003) *Actions on structures – Part 9: Accidental actions*, Aug 2003. Deutsches Institut für Normung, Beuth.

48. DIN EN 1992-1-1 (2005) *Eurocode 2: Design of concrete structures – Part 1-1: General rules and rules for buildings*, Beuth, Berlin.

49. König, G. and Danielewics, I. (1994) [@lang="de"] *Ermüdungsfestigkeit von Stahlbeton- und Spannbetonbauteilen [Fatigue strength of reinforced and prestressed concrete components]*. Deutscher Ausschuss für Stahlbeton, No. 439. Beuth.

50. DIN 1054 (2005) *Subsoil – Verification of the safety of earthworks and foundations – Supplementary rules to DIN EN 1997-1*. Deutsches Institut für Normung, Jan 2005 ed., and amendments Ber1:2005-04, Ber2:2007-04, Ber3:2008-01.

51. Kordina, K. and Quast, U. (1988) [@lang="de"] *Bemessung der Stahlbetonbauteile – Bemessung von schlanken Bauteilen – Knicksicherheitsnachweis [Reinforced Concrete Design – Design of Slender Components – Buckling Analysis]*, (ed. Beton-Kalender), part 1, Ernst & Sohn, Berlin, pp. 549–645.

52. DGGT (2002) [@lang="de"] *Empfehlungen des Arbeitsausschusses "Baugrunddynamik"*. Essen.

53. Rausch, E. (1973) [@lang="de"] *Maschinenfundamente und Andere Dynamisch Beanspruchte Baukonstruktionen [Machine Foundations and Other Dynamically Loaded Structures]*, part 2 (ed. Beton-Kalender), Ernst & Sohn, Berlin, pp. 549–645.

54. Kolymbas, D. (1998) [@lang="de"] *Geotechnik – Grundbau und Bodenmechanik [Geotechnical Engineering – Foundations and Soil Mechanics]*, Springer.

55. Durukal, A. and Batoz, J.-F. (2003) Ultra High Performance Fibre Reinforced Concrete Footbridges. *Ultra-Hochfester Beton. Planung und Bau der ersten Brücke mit UHPC in Europa [ultra-high-strength concrete – design and construction of first UHPC bridge in Europe]. Proceedings, 3rd Kasseler Baustoff- und Massivbautagen [Kassel construction materials & concrete construction conference], 10 Sept 2003*.

56. Grünberg, J. and Göhlmann, J. (2008) [@lang="de"] Tragwerksplanung von Windenergieanlagen in Spannbetonbauweise [structural design of prestressed concrete wind turbine structures]. *Der Bauingenieur*, Springer VDI Verlag. vol. 10, pp. 441–449.

57. BSH, German Maritime & Hydrographic Agency (2007) [@lang="de"] *Standard – Konstruktive Ausführung von Offshore-Windenergieanlagen [design of offshore wind turbines]. Hamburg/Rostock, 12 Jun 2007*.

58. Grünberg, J. (2004) [@lang="de"] *Grundlagen der Tragwerksplanung – Sicherheitskonzept und Bemessungsregeln für den konstruktiven Ingenieurbau [structural engineering basics – safety concept and design rules]*. DIN 1055-100 commentary, Praxis Bauwesen, DIN Deutsches Institut für Normung e.V., Beuth, Berlin/Vienna/Zurich.

59. European Convention for Constructional Steelwork (1996) *Background Documentation to Eurocode 1 (ENV 1991) Part 1: Basis of design*, Mar 1996.

60. Schobbe, W. (1982) [@lang="de"] *Konzept zur Definition und Kombination von Lasten im Rahmen der deutschen Sicherheitsrichtlinie [Concept for Defining and Combining Loads within the Scope of German Safety Guidelines]*, Ernst & Sohn.

61. Spaethe, G. (1992) [@lang="de"] *Die Sicherheit Tragender Baukonstruktionen [Safety of Loadbearing Structures]*, Springer.

62. ForWind (Leibniz University of Hannover), *Probabilistic Safety Assessment of Offshore Wind Turbines. Research project, 2009–2014*.

63. DIN 4227-3 (1983) *Prestressed concrete – Part 3: Segmentised components, design and construction of joints (prestandard)*, Dec 1983 ed.

64. Pflüger, A. (1981) [@lang="de"] *Elementare Schalenstatik [Shell Design]*, 5th edn, Springer.

65. Grasser, E. and Thielen, G. (1991) [@lang="de"] *Hilfsmittel zur Berechnung der Schnittgrößen und Formänderungen von Stahlbetontragwerken [aids for calculating stress resultants and deformations of RC structures]*. Deutscher Ausschuss für Stahlbeton, No. 240. Beuth, Berlin.

66. Comité Euro-International du Béton (1993) *CEB-FIP Model Code 90*. Bulletin d'Information No. 213/214, final draft, Lausanne, Jul 1993.

67. Seidel, M. (2002) [@lang="de"] Auslegung von Hybridtürmen für Windenergieanlagen [Design of hybrid towers for wind turbines]. *Beton- und Stahlbetonbau*, **97**, 564–575.

68. Gasch, R. (2002) [@lang="de"] *Windkraftanlagen: Grundlagen und Entwurf*. Teubner, 2005 [English: *Wind Power Plants: Fundamentals, Design, Construction and Operation*, James & James].

69. Hau, E. (2006) *Wind Turbines*. Springer.

70. Faber, T. and Steck, M. (2005) [@lang="de"] *Windenergieanlagen zu Wasser und zu Lande – Entwicklung und Bautechnik der Windenergie [Onshore and Offshore Wind Turbines – Wind Energy Development and Construction Technology]*. VDI yearbook 2005, VDI-Verlag GmbH, Düsseldorf.

71. Det Norske Veritas Offshore Standard, DNV-OS-J101 (2004) *Design of Offshore Wind Turbine Structures*. Jun 2004.

72. Zilch, K., Zehetmaier, G., and Gläser, C. (2004) [@lang="de"] *Ermüdungsnachweis bei Massivbrücken [Fatigue Analysis for Concrete Bridges]*, part 1: Brücken, Parkhäuser [bridges, multi-storey parking] (ed. Beton-Kalender), Ernst & Sohn.

73. Pfanner, D. (2003) [@lang="de"] *Zur Degradation von Stahlbetonbauteilen unter Ermüdungsbeanspruchung [Degradation of RC Components Subjected to Fatigue Loads]*, Structural Engineering Division, Ruhr-Universität Bochum. VDI Verlag GmbH.

74. Göhlmann, J. (2009) [@lang="de"] *Zur Schädigungsberechnung an Betonkonstruktionen für Windenergieanlagen unter mehrstufiger und mehraxialer Ermüdungsbeanspruchung [calculation of damage to concrete structures for wind turbines subjected to multi-stage and multi-axial fatigue loads]*. Dissertation, Leibniz University of Hannover, IRB Verlag.

75. Su, E. C. (1987) *Biaxial compression fatigue of concrete*. PhD Dissertation, Department of Civil Engineering, University of Houston, Texas.

76. Hsu, T.T.C. (1981) Fatigue of plain concrete. *ACI Journal*, **78**, 292–305.

77. Schlaich, J. (1967) [@lang="de"] Der kontinuierlich gelagerte Kreisring unter antimetrischer Belastung [Continuously supported annulus subjected to antisymmetrical loads]. *Beton- und Stahlbetonbau*, vol. 62, pp. 21ff.

78. Grünberg, J. and Vogt, N. (2009) [@lang="de"] *Teilsicherheitskonzept für Gründungen im Hochbau [Partial Safety Factor Concept for Foundations]*, (ed. Beton-Kalender), part 1, Ernst & Sohn, pp. 555–636.

79. De Gijt, J.G. and Lesny, K. (2009) [@lang="de"] Gründungen im offenen Wasser [foundations in open water], in *Grundbau-Taschenbuch [Foundations Manual]*, part 3, 7th edn, (ed. K.-J. Witt), Ernst & Sohn.

80. Stein, D. (1981) [@lang="de"] *Zur Kolkbildung und ihre Verhinderung an Offshore-Plattformen [Scour on Offshore Platforms and its Prevention]*, Verlag Glückauf GmbH, Essen.

81. Sumer, B.M. and Fredsoe, J. (2002) *The Mechanics of Scour in the Marine Environment*, World Scientific Publishing Co. Pte. org.

82. Whitehouse, R. (1998) *Scour at Marine Structures. A Manual for Practical Applications*, Thomas Telford Ltd, London.

83. Dobrowolsky, M. (2009) Züblin's Gravity Foundation for Offshore Wind Turbines, Presentation at *European Offshore Wind 2009, conference & exhibition, 14–16 Sept 2009, Stockholm*.

84. Ballast Nedam (2009) Presentation at *European Offshore Wind 2009, conference and exhibition, 14–16 Sept 2009, Stockholm*.

85. Comité Euro-International du Béton (1988) Fatigue of concrete structures. State of the Art Report. *Bulletin d'Information*, (188).

86. Holmen, J.O. (1979) *Fatigue of concrete by constant and variable amplitude loading*. Bulletin No. 79-1, Division of Concrete Structures, NTH, Trondheim.

87. Klausen, D. (1978) [@lang="de"] *Festigkeit und Schädigung von Beton bei häufig wiederholter Beanspruchung [Strength of and damage to concrete subjected to frequent repeated loads]*. Dissertation, Technische Hochschule Darmstadt.

88. Mu, B. and Shah, S.P. (2004) Failure mechanisms of concrete under biaxial fatigue load. *Proceedings of 5th International Conference on Fracture Mechanics of Concrete Structures, Colorado (USA), Apr 2004*.

89. Det Norske Veritas Offshore Standard, DNV-OS-502 (2004) *Offshore Concrete Structures*. Jul 2004.

90. Oh, B.H. (1988) Cumulative damage theory of concrete under variable amplitude fatigue loadings. *ACI Material Journal*, **88** (1), 41–48.

91. Pölling, R. (2000) [@lang="de"] *Eine praxisnahe, schädigungsorientierte Materialbeschreibung von Stahlbeton für Strukturanalysen [Practical, damage-based description of the material reinforced concrete for structural analyses]*. Dissertation, Ruhr-Universität Bochum.

92. Richwien, W., Lesny, K., and Wiemann, J. (2002) [@lang="de"] *Gründungen von Offshore-Windenergieanlagen – Gründungskonzepte und geotechnische Grundlagen [Foundations for Offshore Wind Turbines – Concepts and Geotechnical Issues]*. Mitteilungen aus dem Fachgebiet Grundbau und Bodenmechanik der Universität Essen, No. 29, (ed. Prof. Dr.-Ing. W. Richwien), Verlag Glückauf, Essen.

93. RILEM Technical Committee 36 – RDL (1994) Long term random dynamic loading of concrete structures. *Materials and Structures – Research and Testing*, **17**, (97) 1–28.

94. Su, E.C.M. and Hsu, T.T.C. (1988) Biaxial compression fatigue and discontinuity of concrete. *ACI Material Journal*, **85** (3), 178–188.

95. Taliercio, A.L.F. and Gobbi, E. (1998) Fatigue life and change in mechanical properties of plain concrete under triaxial deviatoric cyclic stresses. *Magazine of Concrete Research*, **50** (3), 247–255.

96. Tepfers, R., Fridén, C., and Georgsson, L. (1977) A study of the applicability to the fatigue of concrete of the Palmgren-Miner partial damage hypothesis. *Magazine of Concrete Research*, **29** (100), 123–130.

Index

C

P

W